

## **INFORMATION TO USERS**

This manuscript has been reproduced from the microfilm master. UMI films the text directly from the original or copy submitted. Thus, some thesis and dissertation copies are in typewriter face, while others may be from any type of computer printer.

**The quality of this reproduction is dependent upon the quality of the copy submitted.** Broken or indistinct print, colored or poor quality illustrations and photographs, print bleedthrough, substandard margins, and improper alignment can adversely affect reproduction.

In the unlikely event that the author did not send UMI a complete manuscript and there are missing pages, these will be noted. Also, if unauthorized copyright material had to be removed, a note will indicate the deletion.

Oversize materials (e.g., maps, drawings, charts) are reproduced by sectioning the original, beginning at the upper left-hand corner and continuing from left to right in equal sections with small overlaps. Each original is also photographed in one exposure and is included in reduced form at the back of the book.

Photographs included in the original manuscript have been reproduced xerographically in this copy. Higher quality 6" x 9" black and white photographic prints are available for any photographs or illustrations appearing in this copy for an additional charge. Contact UMI directly to order.

# **UMI**

A Bell & Howell Information Company  
300 North Zeeb Road, Ann Arbor MI 48106-1346 USA  
313/761-4700 800/521-0600



THE UNIVERSITY OF OKLAHOMA  
GRADUATE COLLEGE

SIMULATION OF PENNY-SHAPED HYDRAULIC  
FRACTURING IN POROUS MEDIA

A Dissertation

SUBMITTED TO THE GRADUATE FACULTY

in partial fulfillment of the requirements for the

degree of

DOCTOR OF PHILOSOPHY

By

YANGUANG YUAN

Norman, Oklahoma

1997

**UMI Number: 9719902**

---

**UMI Microform 9719902  
Copyright 1997, by UMI Company. All rights reserved.**

**This microform edition is protected against unauthorized  
copying under Title 17, United States Code.**

---

**UMI**  
300 North Zeeb Road  
Ann Arbor, MI 48103

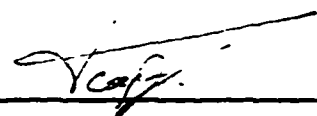
©Copyright by Yanguang Yuan 1997

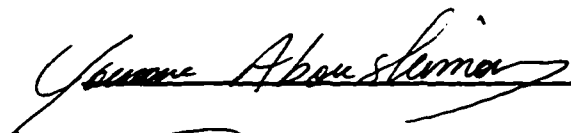
All Rights Reserved

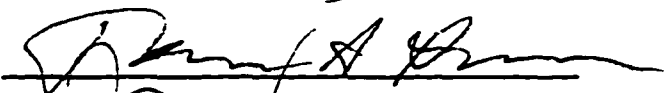
SIMULATION OF PENNY-SHAPED HYDRAULIC  
FRACTURING IN POROUS MEDIA

A DISSERTATION APPROVED  
FOR THE SCHOOL OF PETROLEUM AND GEOLOGICAL  
ENGINEERING

BY

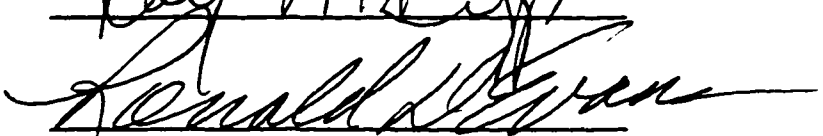
  
\_\_\_\_\_

  
\_\_\_\_\_

  
\_\_\_\_\_

  
\_\_\_\_\_

  
\_\_\_\_\_

  
\_\_\_\_\_

Dedicated to my parents and all the else on that land. Forever, may they live in  
happiness, peace and prosperity up to their intelligence, industriousness.  
persistence and endurance.

# Acknowledgments

Sincerely and gratefully, I would like to acknowledge the general guidance, kind support and enduring encouragement from Drs. J.-C. Roegiers and Y. Abousleiman throughout the course of this study. The OU Rock Mechanics Consortium has provided an unprecedented opportunity to interact with industry. Hereby, I want also to express my admiration and/or gratitude for the vision of the founder — Dr. J.-C. Roegiers whom I fortunately have as my advisor, the support of the participating companies, and the collective effort of my superiors and peers, including my fellow graduate students. Moreover, Dr. Abousleiman needs to be explicitly thanked for his teaching on hypersingular integrals. Thanks are due also to every other member in my Ph.D. advisory committee, including Drs. Faruk Civan, Thomas Dewers, Ron Evans and Roy Knapp, for their help and advice.

The School of Petroleum & Geological Engineering at The University of Oklahoma has provided financial support and assistance in numerous other forms. Support for this research comes from the Rock Mechanics Institute at the same University. All support is gratefully acknowledged.

My past educational and research history bears an important role in the success, if any, of this work. Over the journey, a number of institutions and individuals have provided the opportunities for me to build up and refine my academic knowledge and technical skills. The following need to be mentioned explicitly:



1. the People's Republic of China, which has provided free or greatly subsidized education from kindergarten to M.Sc. graduate studies and then, funding for two research projects that I undertook in China;
2. the Institute of Geology, State Seismological Bureau of China and Profs. Huizhen Song and Shuyan Chen, who have always responded to my needs even after I came to North America;
3. The University of Manitoba, Canada for its generous scholarship and Prof. E.Z. Lajtai at the same University to whom I still feel deeply obliged.

Numerous other individuals have practically lent their hands or influenced my scientific methodologies and personalities. Among them, Drs. Leonid Germanovich, Lev Ring, Dezhang Lin, Lizheng Cui, as well as Ms. Carla Cates and Mr. Don Cruickshan at The University of Oklahoma, USA; Dr. A.H.-D. Cheng at The University of Delaware, USA; Drs. Bruce Carter, Rui Chen and James Ji and Ms. Ingrid Trestrail formerly at The University of Manitoba, Canada; and Mr. Yong Yu at the Ministry of Metallurgy, China, all deserve a special note. Moreover, Dr. Bruce Carter helped in reviewing and editing the manuscript of this dissertation. Dr. Jianxiong Chen provided the prototype  $\LaTeX$  file for the format of this dissertation.

Last, but not the least, I would like to thank my parents who endured the hardship of having not seen me in six years, but always communicated a happy and understanding mood. I also want to thank my father-in-law who finally got "frustrated" with the slow pace of my career and came to this very unfamiliar culture to help us. Thanks also inevitably go to my wife, who put aside her promising career and spared no efforts in bringing up our little daughter.

# Abstract

This dissertation presents a mathematical study and numerical procedure to simulate penny-shaped hydraulic fracture (HF) propagation in porous media. It accounts for the two-dimensional (2-D) pressure-dependent leakoff and poroelastic backstress contributions. It allows for multiple fracture propagation/closure/re-opening (PCR) events during multiple injection/shut-in/flow-back (ISF) pumping cycles.

However, this work is not a simple application of a standard numerical method to the general governing equations. Instead, it first proceeds to derive analytical expressions for the early- and late-time asymptotic poroelastic responses of a pressurized fracture. It then builds a composite approximate analytical formula to cover the interim transient poroelastic response between the two asymptotic time regimes. When compared against the numerical computations using commercial FEM software for the full mechanical model, the simplified model is shown to involve less than 10% relative error in the significant part of the poroelastic domain. Therefore, an adequately accurate mathematical accuracy exists.

A Duhamel's theorem-like principle is further derived to extend the foregoing stationary fracture-based simplified 2-D model to a propagating fracture. The only assumption used is that the pore pressure ahead of the fracture tip remains at the *in-situ* pore pressure level. When the fracture propagation speed is much faster

than fluid diffusion rate, this assumption is valid. Several examples are computed. Analyses of the computations show the physical validity of the extension principle and the mathematical accuracy in the limiting cases. Moreover, the computation shows that the 1-D poroelastic model underestimates the poroelastic effect when the fracture propagates a considerable distance.

In another major step, this work derives a pseudo-explicit finite difference scheme (PEFD) to compute the nonlinear, coupled problem of modeling the HF propagation. It is fully implicit in the time marching and is thus stable. But it solves one point at one time, i.e., it is explicit in the solution of the discretized equations. Furthermore, the Newton-Raphson method for a system of nonlinear equations is applied to speed up the convergence. Numerical tests verify its stability and consistency as well as mathematical accuracy. Many other numerical strategies are presented to compute the multiple PCR fracturing events during multiple ISF pumping cycles. Examples are run to verify overall performance of the resultant HF simulator and to show its computational capabilities.

More examples are computed to exemplify the poroelastic effect. The computations suggest that the poroelastic effect increases the wellbore pressure response and reduces both the fracture aperture and radius. In the computed examples, a maximum of 150% increase in the wellbore pressure is registered as compared to the purely elastic case. The magnitude of the poroelastic effect is linearly proportional to the *in-situ* minimum stress and pore pressure difference. It is also a positive power function of the formation permeability. The magnitude also increases with the number of pumping cycles.

# Contents

<b>Acknowledgments</b>	<b>v</b>
<b>Abstract</b>	<b>vii</b>
<b>List of Figures</b>	<b>xii</b>
<b>List of Tables</b>	<b>xviii</b>
<b>Nomenclature</b>	<b>xx</b>
<b>1 General Introduction</b>	<b>1</b>
1.1 Simulation of Discrete Fracture Propagation . . . . .	2
1.2 Simulation of HF Propagation . . . . .	6
1.3 Penny-shaped HF Model . . . . .	8
1.4 Critical Review on HF Simulation . . . . .	10
1.5 Poroelastic Effects in the HF Process . . . . .	11
1.6 Conjectures, Objectives and Approaches . . . . .	14
1.7 Organization of the Work . . . . .	19
1.8 Summary . . . . .	20
<b>2 1-D Transient and 2-D Steady-State Poroelastic Response</b>	<b>24</b>
2.1 Governing Equations in Poroelastic Domain . . . . .	24
2.2 General Discussion on Poroelastic Effect . . . . .	27

2.3	A 1-D Poroelastic Model . . . . .	30
2.4	2-D Steady-State Poroelastic Response . . . . .	34
2.4.1	Computation of Poroelastic Displacements . . . . .	36
2.4.2	Computation of the Pressure Derivative . . . . .	40
2.5	Summary . . . . .	44
<b>3</b>	<b>A Simplified 2-D Poroelastic Model</b>	<b>51</b>
3.1	Non-dimensionalization of the Governing Equations . . . . .	53
3.2	Computed Poroelastic Response . . . . .	56
3.3	A Simplified 2-D Poroelastic Model . . . . .	58
3.3.1	Cubic Spline Interpolation for $w^p$ . . . . .	58
3.3.2	Simple Superimposition for $u$ . . . . .	60
3.3.3	Comparison of the Simplified 2-D Poroelastic Model with the True 2-D Computations . . . . .	61
3.4	Extension of the Simplified 2-D Model to a Propagating Fracture . .	62
3.4.1	Derivation of the Extension Principle . . . . .	62
3.4.2	Discussion about the Extension Principle . . . . .	66
3.5	Summary . . . . .	70
<b>4</b>	<b>A Pseudo-Explicit Finite Difference Scheme</b>	<b>86</b>
4.1	Governing Equations in McFrac . . . . .	87
4.2	Non-Dimensionalization of the Governing Equations . . . . .	90
4.3	A Pseudo-Explicit Finite Difference Scheme . . . . .	93
4.3.1	Discretization of Fluid Flow Equations . . . . .	96
4.3.2	The PEFD Algorithm. . . . .	99
4.4	Qualitative Validation of the PEFD . . . . .	103
4.4.1	Fluid Flow inside the Fracture. . . . .	103

4.4.2	Convergence of the PEFD . . . . .	105
4.5	Newton-Raphson Scheme . . . . .	106
4.5.1	Effect of the PEFD Simplifications . . . . .	106
4.5.2	Derivation of NR Algorithm . . . . .	108
4.5.3	Relationship between PEFD and NR Schemes . . . . .	110
4.6	Quantitative Validation of the PEFD . . . . .	111
4.6.1	Similarity Solution at Late Times . . . . .	112
4.6.2	Stability and Consistency . . . . .	113
4.7	Power-law Fluid Rheology . . . . .	114
4.8	Implementation of the Poroelastic Effects . . . . .	117
4.9	Summary . . . . .	121
<b>5</b>	<b>Simulation of Fracture Propagation/Closure/Re-opening</b>	<b>141</b>
5.1	Fracture Propagation . . . . .	142
5.1.1	Calculation of the Stress Intensity Factor . . . . .	142
5.1.2	$\Delta R$ -based Fracture Propagation Scheme . . . . .	144
5.1.3	Calculation of the Temporal Derivatives . . . . .	145
5.1.4	Validation Examples . . . . .	146
5.2	Fracture Closure . . . . .	148
5.2.1	$\Delta t$ -based Fracture Propagation Scheme . . . . .	148
5.2.2	Determining Carter's Leakoff Coefficient from Pressure-Decline Curves . . . . .	149
5.2.3	Fracturing Behavior after the Shut-in . . . . .	151
5.3	Fracture Re-opening . . . . .	154
5.3.1	Carter's Leakoff Calculation in Multiple Fracturing Events . .	155
5.3.2	1-D Pressure-dependent Leakoff Calculation in Multiple Frac- turing Events . . . . .	157

5.3.3	An Example . . . . .	157
5.4	Poroelastic Effects in HF Fracture Propagation . . . . .	160
5.4.1	Poroelastic Effect During the Monotonic Fracture Propagation	160
5.4.2	Poroelastic Effects during Fracture Propagation/ Closure/Re- opening . . . . .	161
5.5	Summary . . . . .	162
<b>6</b>	<b>Conclusions and Recommendations for Future Work</b>	<b>177</b>
<b>A</b>	<b>Proof of the 1-D Poroelastic Formulae</b>	<b>180</b>
<b>B</b>	<b>Proof of the Steady-State Poroelastic Displacement Formula</b>	<b>183</b>
<b>C</b>	<b>Equations for Power-law Fluid Flow inside Fractures</b>	<b>187</b>
<b>D</b>	<b>Matrix Coefficients in NR Algorithm</b>	<b>190</b>
	References . . . . .	194

# List of Figures

1.1	Simulation of discrete fracture propagation. . . . .	22
1.2	In-plane and out-of-plane fracture propagation. . . . .	22
1.3	The complicated physics involved in a HF process. . . . .	23
2.1	1-D poroelastic model and its loading mode decomposition. . . . .	48
2.2	Comparison of the leakoff rate, $u$ , and the poroelastic displacement, $w^p$ , under mode 1 and mode 2 loading. . . . .	48
2.3	Penny-shape pressurized fracture model. . . . .	49
2.4	ABAQUS's computations vs. analytical predictions at the steady state. See Chapter 3 for the non-dimensionalization details. . . . .	49
2.5	Comparison of the computed elastic fracture deformation with the corresponding analytical results. . . . .	50
2.6	Comparison of the computed pressure derivative with the corresponding analytical or other numerical results. . . . .	50
3.1	Computational model of the penny-shaped pressurized fracture. . . . .	73
3.2	The computed example pressure profiles. . . . .	73
3.3	Comparison of $w^p$ between mode 1 and 2 loading in the non-dimensionalized domain. . . . .	74
3.4	Comparison of $w^p$ between mode 1 and 2 loading in the dimensional domain. . . . .	74



3.5	Evolution of the poroelastic displacement, $w^p(s, t)$ and its comparison with the 1-D transient and 2-D steady-state solutions. Uniform pressure profile. . . . .	75
3.6	Evolution of the leakoff rate, $u(s, t)$ and its comparison with the 1-D transient and 2-D steady-state solutions. Uniform pressure profile. . .	75
3.7	Profiles of the computed $w^p$ and $u$ along the fracture and their comparison with the asymptotic 1-D analytical results. Uniform pressure profile. . . . .	76
3.8	Evolution of the poroelastic displacement, $w^p(s, t)$ , during the early time period. Uniform pressure profile. . . . .	76
3.9	Comparison of the simplified 2-D model with the true 2-D computations. Poroelastic displacement, $w^p$ , and uniform pressure profile. . .	77
3.10	Comparison of the simplified 2-D model with the true 2-D computations. leakoff rate, $u$ , and uniform pressure profile. . . . .	77
3.11	Comparison of the simplified 2-D model with the true 2-D computations. Poroelastic displacement, $w^p$ , and elliptic-like pressure profile. .	78
3.12	Comparison of the simplified 2-D model with the true 2-D computations. Leakoff rate, $u$ , and elliptic-like pressure profile. . . . .	78
3.13	Distribution of the relative error of the simplified 2-D model as compared to the true 2-D computations. Poroelastic displacement, $w^p$ . . .	79
3.14	Distribution of the relative error of the simplified 2-D model as compared to the true 2-D computations. Leakoff rate, $u$ . . . . .	79
3.15	Physical description of the simple step-rate fracture propagation history.	80
3.16	Mathematical realization of the simple step-rate fracture propagation history. . . . .	80

3.17	$w^p$ evolution and its comparison with the analytical results for a stationary fracture under the linearly decreasing pressure. . . . .	81
3.18	$w^p$ evolution during the simple step-rate fracture propagation history.	81
3.19	Evolution of the $w^p$ profiles along the fracture during its simple step-rate propagation history. . . . .	82
3.20	The steady-state $w^p$ profiles for the original and propagated fracture geometries and their comparison with the analytical predictions. Simple step-rate fracture propagation history. . . . .	82
3.21	The fracture radius and pressure histories during the real propagation case. . . . .	83
3.22	$w^p$ evolution at the typical physical coordinates on the fracture during the real propagation history. . . . .	83
3.23	Evolution of $w^p$ profiles along the fracture and comparison between the 1-D and the simplified 2-D poroelastic models. The real fracture propagation history. . . . .	84
3.24	Comparison between the 1-D and the simplified 2-D poroelastic models in the $w^p$ evolution. The real fracture propagation history. . . . .	84
3.25	Parametric dependence on $\kappa$ or $K_r$ of the 1-D vs. 2-D comparison in the $w^p$ evolution. The real fracture propagation history. . . . .	85
3.26	Evolution of the leakoff rate, $u$ and the comparison between the 1-D and 2-D models. The real propagation history. . . . .	85
4.1	Sketch of the penny-shaped HF propagation. . . . .	129
4.2	Nodal distribution of the Chebyshev grid. . . . .	129
4.3	Fracture aperture profiles at early times before the fluid reaches the fracture tip. . . . .	130

4.4	Fluid front position, measured in distance from the well, vs. time after different numbers of the Chebyshev grid nodes. . . . .	130
4.5	Pressure profiles along the fracture at late times. . . . .	131
4.6	Fracture aperture profiles along the fracture at late times. The unmarked dotted lines are the predicted elliptical profiles based on the computed average pressures. . . . .	131
4.7	Evolution of the fracture aperture, $w_{wb}$ and fluid pressure, $p_{wb}$ at the wellbore; average pressure along the fracture, $p_{avg}$ and stress intensity factor, $K_I$ . . . . .	132
4.8	Evolution of $R_f$ and $R_{mas}$ during the iterations for time step no. 2. .	132
4.9	Evolution of $R_f$ and $R_{mas}$ during the iterations for time step no. 45. .	133
4.10	Number of iterations required for each time step if computed by the different numerical schemes. . . . .	133
4.11	Evolution of the wellbore pressure computed by NR alone based on the different initial guesses for the pressure profile. . . . .	134
4.12	Relationship between the PEFD and NR algorithms. . . . .	134
4.13	Influence of the time stepping size, $\Delta t$ on the computed wellbore pressures, $p_{wb}$ . . . . .	135
4.14	Influence of the different number of the Chebyshev nodes, $N$ , on the computed wellbore pressure, $p_{wb}$ . . . . .	135
4.15	Influence of the different iteration measure values, $\epsilon_f$ , on the computed wellbore pressure, $p_{wb}$ . . . . .	136
4.16	Distribution of the effective viscosity, $\mu_e$ , along the fracture at different times. . . . .	136
4.17	Fracture aperture profiles at early times and the comparison between the power-law and Newtonian rheology cases. . . . .	137

4.18	The wellbore responses for the power-law fluid cases. . . . .	137
4.19	Poroelastic effect on fracture deformation as displayed by its profile along the fracture at $t = 100s$ . . . . .	138
4.20	Pressure response due to the poroelastic effect as illustrated by its profile along the fracture at $t = 100s$ . . . . .	138
4.21	Evolution of the accumulated leakoff volume, $V_{lek}$ and the created fracture volume, $V_{crk}$ . . . . .	139
4.22	Comparison of the leakoff flux, $u$ , with the fracture aperture change, $w' = \frac{\partial w}{\partial t}$ , in the fluid mass balance equation. . . . .	139
4.23	Poroelastic effect influenced by the $\sigma_0 - p_0$ difference and the for- mation permeability as typified by the fracture aperture profile at $t = 200s$ . . . . .	140
5.1	Evolution of the pressure profiles along the fracture. . . . .	167
5.2	Computed wellbore pressure, aperture and fracture radius as well as their comparison with the similarity solution. . . . .	167
5.3	Comparison of pressure and aperture profiles between high and low fracture toughnesses. . . . .	168
5.4	Fracture propagation history projected in the dimensionless coordi- nates. . . . .	168
5.5	Evolution of the post-shut-in wellbore pressure and fracture radius. Carter's leakoff. . . . .	169
5.6	Nolte's pressure decline curve. . . . .	169
5.7	Zoom-up of Figure 5.5 near $t = 100 s$ to show the continuous fracture propagation after shut-in. . . . .	170
5.8	Evolution of the pressure profiles immediately after shut-in. . . . .	170
5.9	Evolution of the aperture profiles during the fracture closure. . . . .	171

5.10 Comparison of the fracture radius among the different leakoff coefficients and/or fracture toughnesses. . . . .	171
5.11 Zoom-up of the wellbore pressure evolution near the shut-in time to show up the $p_{isip}$ . . . . .	172
5.12 $p_{foc}$ point on the wellbore pressure logs as reflected by its second time derivatives. . . . .	172
5.13 Calculating pressure-dependent leakoff in multiple fracturing events. .	173
5.14 Evolution of fracture radius and wellbore pressure under multiple pumping cycles. . . . .	173
5.15 Poroelastic effect on wellbore pressure response and its parametric dependence. . . . .	174
5.16 Poroelastic effect on the created fracture radius and its parametric dependence. . . . .	174
5.17 Poroelastic effect on wellbore fracture aperture and its parametric dependence. . . . .	175
5.18 Effect of the <i>in-situ</i> stress and pore pressure difference, $\sigma_0 - p_0$ , via the poroelastic mechanism. . . . .	175
5.19 Effect of the formation permeability, $k$ , via the poroelastic mechanism.	176
5.20 Evolution of wellbore pressure response during multiple pumping cycles under pressure-dependent leakoff. . . . .	176
C.1 Sketch of an elementary volume to derive: (a). the momentum equation and (b). mass balance equation for fluid flow inside parallel plates.	189

# List of Tables

2.1	Poroelastic material properties of some typical rocks. . . . .	47
2.2	Poroelastic material properties used for the computations. . . . .	47
4.1	Material properties for the stationary fracture. . . . .	123
4.2	Comparison of the $w_{wb}$ and $p_{wb}$ between the different $\Delta t$ s. Early time.	123
4.3	Comparing the analytical results with the computed $w_{wb}$ and $p_{wb}$ by the different $\Delta t$ s. Late times. . . . .	124
4.4	$w_{wb}$ and $p_{wb}$ between the different Chebyshev grid points, $N$ . Early time. . . . .	126
4.5	$w_{wb}$ and $p_{wb}$ by the different Chebyshev grid points, $N$ . Late times. .	127
5.1	Material properties for the propagating fracture. . . . .	165
5.2	Some characteristic values on the computed wellbore pressure log in pertinence to HF stress measurement. . . . .	165
5.3	Material Properties for the Examples with Multiple Pumping Cycles .	165
5.4	Poroelastic effect on the wellbore pressure response. . . . .	166
5.5	Comparison of Wellbore Pressures during the Multiple Pumping Cy- cles. Poroelastic ( $\eta = 0.3$ ) vs. Leakoff-only Cases ( $\eta = 0.$ ). . . . .	166

# Nomenclature

1-D	= one-dimensional
2-D	= two-dimensional
ABAQUS	= a commercial finite element software from HKS
$B$	= Skempton's pore pressure coefficient, [1]
BEM	= boundary element method
$c$	= poroelastic diffusivity coefficient, $[LT^{-2}]$
$c_{ij}^p$	= fluid pressure matrix coefficients to relate the elastic normal fracture displacement at node, $j$ , in the Chebyshev grid system to the fluid pressure inside the fracture at node, $i$
$c_{ij}^u$	= leakoff rate matrix coefficients to relate the fluid pressure inside the fracture at node, $j$ , in the Chebyshev grid system to the leakoff rate at node, $i$
$c_{ij}^w$	= elastic displacement matrix coefficients to relate the fluid pressure inside the fracture at node, $j$ , in the Chebyshev grid system to the normal fracture displacement at node, $i$
$C_{ijkl}$	= solid deformational constitutive tensor, $[ML^{-1}T^{-2}]$
$C_l$	= Carter's leakoff coefficient, $[LT^{-1/2}]$
DF	= discrete fracture
$E$	= drained Young's modulus, $[ML^{-1}T^{-2}]$
$E_u$	= undrained Young's modulus, $[ML^{-1}T^{-2}]$
FD	= finite difference
FEM	= finite element method
$f_w$	= approximate transient 2-D poroelastic model defined by the cubic spline polynomial. Eqn. (3.21), $[L]$
$G$	= shear modulus, $[ML^{-1}T^{-2}]$
HF	= hydraulic fracture
ISF	= injection/shut-in/flowback
$i, j, k, l$	= coordinate axis index or the nodal index the discretized grid system

$k$	= intrinsic permeability of the porous media, [ $L^2$ ]
$K$	= bulk modulus, [ $ML^{-1}T^{-2}$ ]; or the consistency index in the power law fluid rheology, [ $ML^{n-1}T^{-2}$ ] where $n$ is the flow behavior index
$K_f$	= bulk modulus of the pore fluid in the porous media, [ $ML^{-1}T^{-2}$ ]
$K_I, K_{II}, K_{III}$	= $I, II, III$ –mode stress intensity factor, [ $ML^{-1/2}T^{-2}$ ]
$K_{Ic}$	= fracture toughness, [ $ML^{-1/2}T^{-2}$ ]
$K_s$	= bulk modulus of the solid grains in the porous media, [ $ML^{-1}T^{-2}$ ]
L.H.S.	= left-hand side
$M$	= Biot's modulus, = $KB/\alpha$ , [ $ML^{-1}T^{-2}$ ]
McFrac	= the HF simulator developed in this work
$N$	= the total number of nodes in the Chebyshev grid system along the fracture, [1]
NR	= Newton-Raphson method
$n_i$	= directional cosine component, [1]
$p$	= pore fluid pressure in the porous media, [ $ML^{-1}T^{-2}$ ]
PCR	= propagation/closure/re-opening
PEFD	= pseudo-explicit finite difference
$p_0$	= virgin formation pore pressure, [ $ML^{-1}T^{-2}$ ]
$p_{0+}$	= undrained pore pressure response of the porous media due to the mechanical loading, [ $ML^{-1}T^{-2}$ ]
$p_f$	= fracturing fluid pressure inside the HF, [ $ML^{-1}T^{-2}$ ]
$p_{foc}$	= fracture closure pressure, [ $ML^{-1}T^{-2}$ ]
$p_{f,j}$	= fracturing fluid pressure at node, $j$ , in the Chebyshev grids on the fracture, [ $ML^{-1}T^{-2}$ ]
$\bar{p}_i$	= the prescribed boundary traction force in the $i$ -th axis direction, [ $MLT^{-2}$ ]
$p_{isip}$	= instantaneous shut-in pressure, [ $ML^{-1}T^{-2}$ ]
$p_{wb}$	= fracturing fluid pressure at the wellbore, [ $ML^{-1}T^{-2}$ ]
$q$	= fluid flux across the fracture, [ $L^2T^{-1}$ ]
$q_i$	= pore fluid flux in the $i$ -th direction of the porous media, [ $LT^{-1}$ ]
$Q$	= volumetric flow rate of fluid flowing inside the fracture, [ $L^3T^{-1}$ ]



$Q_0$	= volumetric injection rate of the fracturing fluid. [ $L^3T^{-1}$ ]
$r$	= distance from the wellbore, or the coordinate axis along the fracture, [ $L$ ]
$R$	= the radius of a propagating fracture. [ $L$ ]
R.H.S.	= right-hand side
$R_0$	= the radius of a stationary fracture. [ $L$ ]
$R_f$	= ratio of the accumulative unbalanced fluid volume in the calculation to the injected volume, $V_{inj}$ . [1]
$R_{mas}$	= ratio of $(V_{crk} + V_{lek})$ to $V_{inj}$ . [1]
$s$	= normalized coordinate along the fracture direction. = $r/R_0(, R)$ . [1]
$t$	= time, [ $T$ ]
$t_c$	= characteristic time, [ $T$ ]
$t_{foc}$	= the time when the fracture starts to close, [ $T$ ]
$t_i$	= shutin time, [ $T$ ]; or dimensionless time at the inner end point in the simplified 2-D poroelastic model <i>prior</i> to which, the 1-D analytical poroelastic model is assumed to be valid. Currently set at $10^{-3}$ . [1]
$t_o$	= dimensionless time at the outer end point in the simplified 2-D poroelastic model beyond which, the 2-D steady-state analytical poroelastic solution is assumed to be valid. Currently set at 10. [1]
$T_k$	= $k$ -order Chebyshev polynomial function, [1]
$u$	= leakoff rate from the fracture into the formation. [ $LT^{-1}$ ]
$u_i$	= displacement in the $i$ -th axis direction, [ $L$ ]
$\bar{u}_i$	= the prescribed boundary displacement component, [ $L$ ]
$u_{mddf}$	= simplified 2-D leakoff rate model defined by Eqn. (3.38), [ $LT^{-1}$ ]
$u_r$	= displacement component in the radial direction, $r$ , of the axisymmetric configuration. [ $L$ ]
$u_z$	= displacement component in the axial direction, $z$ , of the axisymmetric configuration. [ $L$ ]
$V_{crk}$	= crack volume, [ $L^3$ ]
$V_{inj}$	= accumulative injected fluid volume, [ $L^3$ ]
$V_{lek}$	= accumulative leaked fluid volume, [ $L^3$ ]
$w$	= total fracture aperture, [ $L$ ]

w.r.t	= with respect to
$w^e$	= instantaneous elastic displacement normal to the fracture. [L]
$w^p$	= displacement normal to the fracture, induced by the poroelastic mechanism. [L]
$w^p(r, t; R)$	= operator showing the parametric dependence of the poroelastic displacement at position, $r$ , and time, $t$ , on the fracture radius, $R$ , in the dimensional simplified 2-D poroelastic model. [L]
$w_{1D}^p$	= analytical 1-D poroelastic model defined by Eqn. (2.32). [L]
$w_{mfd}^p$	= simplified 2-D poroelastic model defined by Eqn. (3.37) or Eqn. (3.39), [L]
$w_{stdy}^p$	= analytical 2-D steady-state poroelastic solution defined by Eqn. (2.64), [L]
$w_{wb}$	= fracture aperture at the wellbore, [L]
$x, y, z$	= $x, y, z$ - axis in the general three-dimensional Cartesian coordinate system
$\alpha$	= Biot's coupling coefficient, [1]
$\alpha_d$	= representative driving force for the fracture propagation
$\beta_r$	= representative resistance force for the fracture propagation
$\delta_{ij}$	= Kronecker's delta function, = 0 if $i \neq j$ and =1 if $i = j$
$\delta w_{j,n}^m$	= increment normal fracture displacement at node, $j$ , during iteration step, $m$ , of time step, $n$ , [L]
$\epsilon_f$	= maximum allowable relative error tolerance during the iterations in PEFD as shown in Eqn. (4.56), [1]
$\epsilon_\mu$	= maximum allowable relative error tolerance during the iterations for the power-law fluid rheology as shown in Eqn. (4.86), [1]
$\epsilon_{K_I}$	= maximum allowable relative error tolerance during the iterations for fracture propagation/closure/re-opening as shown in Eqn. (5.5), Eqn. (5.15), Eqn. (5.17) or Eqn. (5.18), [1]
$\epsilon$	= volumetric strain, [1]
$\epsilon_{ij}$	= strain component, [1]
$\zeta$	= variation of the pore fluid volume per unit volume of the porous media due to the diffusive mass transport, [1]
$\eta$	= poroelastic stress coefficient, [1]
$\kappa$	= permeability coefficient, = $k/\mu$ with $k$ being the intrinsic permeability of the porous media and $\mu$ the viscosity of the pore fluid. [ $M^{-1}L^3T$ ]
$\mu$	= Newtonian fluid viscosity, [ $ML^{-1}T^{-1}$ ]

$\mu_e$	= effective Newtonian fluid viscosity of the non-Newtonian fluid. [ $ML^{-1}T^{-1}$ ]
$\nu$	= drained Poisson's ratio, [1]
$\nu_u$	= undrained Poisson's ratio. [1]
$\sigma_0$	= <i>in-situ</i> minimum principal stress. [ $ML^{-1}T^{-2}$ ]
$\sigma_{ij}$	= stress component, [ $ML^{-1}T^{-2}$ ]
$\sigma_{kk}$	= the sum of the principal stresses, [ $ML^{-1}T^{-2}$ ]
$\phi$	= porosity of the porous media, [1]
$\psi$	= geometric factor in the fluid momentum equation inside the fracture. = $n/(2(2n+1))$ with $n$ being the flow behavior index in the power-law fluid rheology, [1]
$\nabla^2$	= Laplacian operator
$\Gamma_c$	= surfaces of the discrete fractures as boundaries to the deformational solid
$\Gamma_p$	= portion of the boundary where the tractions are prescribed
$\Gamma_u$	= portion of the boundary where the displacements are prescribed

# Chapter 1

## General Introduction

Hydraulic fracturing (HF) has been widely used in the petroleum industry to create additional hydraulic conduits between the petroleum reservoir in the formation and the production wells. It is also utilized to measure the formation leakoff characteristics and the *in-situ* stresses. In addition, the HF technique has been applied in liquid waste disposal, contaminant recovery and geothermal production. Knowledge of the fracture dimensions (length/width) is crucial for design as well as evaluation of the field operation. When used for formation testing, the HF operations are deliberately manipulated to extract as much information as possible. The procedure ranges from single cycle of injection/shut-in/flow-back (ISF) to multiple cycles. The formation information is extracted from the recorded history of the wellbore pressure. Insight into the influence of the formation characteristics on such a pressure record is vital for the inversion. Therefore, it is of practical importance to characterize a HF process, including its geometry and wellbore pressure response.

The task of characterization is tackled via various means including direct observation and mechanistic studies. While many geophysical observation methods have been applied to pinpoint the fracture geometry, the ultimate burden often falls on mechanistic study. In theory, the mechanistic study should be able to predict the fracture geometry before the operation starts. It, therefore, provides a design tool.

For the purpose of formation testing, mechanistic studies are the only means to relate formation characteristics to the wellbore pressure response.

In general, a mechanistic study includes two aspects: physical testing and mathematical analysis. The former provides constitutive theories and the relevant material properties. The latter provides a forecasting tool to infer the physical process under general conditions. As will be discussed below, any HF process, even in its simplest form, simultaneously involves several sub-processes which often interact with each other. The solution of such a coupled system normally relies on numerical methods. This dissertation is a mechanistic study of HF by means of numerical simulations. It particularly focuses on the penny-shaped fracture geometry in porous media, multiple ISF cycles and the associated poroelastic effects in a 2-D, pressure-dependent leakoff environment.

## **1.1 Simulation of Discrete Fracture Propagation**

Simulation of HF propagation falls within the category of modeling discrete fracture (DF) propagation which has comprised a distinctive branch in engineering fracture mechanics, particularly in geomechanics. Using a static linear elastic problem as an example, this section sets off to mathematically formulate the problem of modeling DF propagation and elucidate the difficulties involved. It is hoped to set the general mathematical framework about modeling HF propagation. Precise definition of a fracture is not necessary for the purpose of the following description. In numerical simulation, a fracture is a special geometric and mechanical entity. In HF, the fracture also has its hydraulic characteristics.

Acting both as friends and foes, fractures are of vital interest to the scientific and engineering community. In many cases, such as in fragmentation, blasting and HF, fractures are the goal that is being sought; the design index here is to create the

desired fracture (length, aperture or density, and direction) at the lowest possible cost. In many other cases where fractures are detrimental, like in engineering stability, it has been recognized that it is neither possible nor cost-effective, to eliminate the initiation of fractures. A feasible way is to tolerate fracture nucleation while monitoring its evolution so that the growth is stable and controllable. Even if it is impossible to control fracture initiation and propagation such as during earthquakes, the study of fracture progression is the key for insight into its mechanisms and its successful forecast. Therefore, it is important to trace the whole life-cycle of a fracturing event, including initiation, propagation, arrest and re-mobilization as well as interaction of multiple fractures.

Physically, the goal of modeling fracture growth is to answer questions like *where*, *when* and *how* a fracture is nucleated/propagated. Mathematically, it involves solving a system of equations governing the continuum deformation and under the constraint of fracture conditions. While physical modeling provides the insight, in particular about the failure criterion, mathematical modeling is an efficient way to rehearse the fracture growth details.

In general, two fracture models are used in the literature: one is deformation-discontinuous, such as strain localization, e.g. [1, 2]; the other is displacement-discontinuous, i.e. DF, e.g. [3]. The former is more commonly used in soil mechanics for granular and soft materials whereas the latter is more often seen in rock mechanics. Having a distinctive fracture opening, a HF is displacement-discontinuous; and, therefore, belongs to the DF type.

In general, simulation of DF propagation can be formulated into the following set of displacement,  $u_i$ -based differential equations:

$$G\nabla^2 u_i + \frac{G}{1-2\nu}\varepsilon_{,i} = 0 \quad i = x, y, z \quad (1.1)$$

in which the Laplacian operator,  $\nabla^2$ , and the volumetric deformation,  $\varepsilon$ , are defined

by:

$$\nabla^2 = \frac{\partial^2}{\partial x^2} + \frac{\partial^2}{\partial y^2} + \frac{\partial^2}{\partial z^2} \quad (1.2)$$

$$\varepsilon = \frac{\partial u_x}{\partial x} + \frac{\partial u_y}{\partial y} + \frac{\partial u_z}{\partial z} \quad (1.3)$$

The corresponding boundary conditions are as follows:

$$\sigma_{ij}n_j = \bar{p}_i \quad \text{prescribed traction along } \Gamma_p; \text{ and,} \quad (1.4)$$

$$u_i = \bar{u}_i \quad \text{prescribed displacement along } \Gamma_u \quad (1.5)$$

where the stresses,  $\sigma_{ij}$ , are related to the displacement via the constitutive law:

$$\sigma_{ij} = C_{ijkl}\varepsilon_{kl} \quad (1.6)$$

and the strain-displacement relation:

$$\varepsilon_{ij} = \frac{1}{2} \left( \frac{\partial u_i}{\partial x_j} + \frac{\partial u_j}{\partial x_i} \right) \quad (1.7)$$

if small deformations are assumed.

The DF's are treated as boundaries to the deformation system (Figure 1.1<sup>1</sup>). For example, if a crack is open, a zero or prescribed-value boundary traction is imposed along the crack surface. The crack path,  $\Gamma_c$ , is equivalent to the prescribed-traction boundary,  $\Gamma_p$ .

In addition to the prescribed-displacement and traction boundary conditions, for modeling fracture propagation, the deformation everywhere inside the solid has to satisfy the non-fracture condition as well:

$$f(\alpha_d, \beta_r) > 0 \quad (1.8)$$

where  $\alpha_d$  is the driving force for the fracture propagation which can be quantified by the state of stresses as in stress-based fracture criteria or by stress intensity factors,  $K_I, K_{II}, K_{III}$ , as in fracture mechanics theories. The  $\beta_r$  is the resistance force to the

---

<sup>1</sup>Tables and figures are all listed at the end of the corresponding chapters.

fracture propagation often described by material properties such as the compressive or tensile strengths,  $\sigma_c$  or  $\sigma_t$ , or the fracture toughness,  $K_{Ic}$ . Eqn. (1.8) is just the fracture criterion written in an inequality under which no fracture occurs, such as  $K_{Ic} - K_I > 0$ . If Eqn. (1.8) is violated, i.e.  $f(\alpha_d, \beta_r) \leq 0$ , a fracture has to nucleate or propagate in order to dissipate the energy and render a stable condition. If no stable condition is possible, the fracture continues to propagate and an unstable fracture propagation or uncontrollable structural failure results.

Introduction of fractures into the general solid mechanics problem causes certain difficulties:

1. A fracture criterion is required to determine *where* and *when* a fracture is nucleated/propagated.
2. After a fracture is detected to nucleate or propagate, an explicit fracture will be inserted into the mathematical modeling. Therefore, an appropriate mathematical description of the fracture is needed.
3. Stress often concentrates around the fracture tip, such as the tip stress singularity in the fracture mechanics theories. This rapidly varying stress field often breaks the capacity of conventional numerical modeling tools for accurate computations. It also requires special attention to the possible fracture criteria.
4. Before load is added to the structure, the *where*, *when* questions of the fracture behavior are generally unknown, which is tackled by a "snap-shot" scheme. That is once the fracture violates the non-fracture condition, Eqn. (1.8), the fracture is extended by a certain amount. Iterations are then performed to adjust the basic controlling variable to render the newly-propagated fracture tip to be at the critical condition again. In HF, this basic control variable



is the injection time. During each of these iterations, a stationary fracture is computed. The same scheme applies for simulation of fracture closure. This scheme has been proven theoretically for elastic materials, e.g. [4]. It also works for nonlinear materials if the loading is monotonic, similar to the validity domain of the J-integral [5]. A similar approach was also used in modeling HF propagation in poroelastic media.

## 1.2 Simulation of HF Propagation

Herein, the earlier description about the four tasks in modeling DF propagation is extended to the simulation of HF propagation. As will be clear, some special features, mainly in the geometry of a HF, lead to a simplification of the general problem while the physics makes the problem more complex.

In general, the procedure of HF starts with injecting fluid down the wellbore to the desired depth where the section to be fractured is packed off. There, a fracture is created along a certain direction. Fluid enters into the opened aperture, driving the fracture and propagating it further. In the micro/mini-HF jobs, the fluid injection is stopped or possibly the injected fluid is pumped back to allow the wellbore pressure to fall off. During these operations, the fracture may stay stationary, propagate or recede. In the stimulation and environmental applications, proppants are also pumped in to hold the opened width after the pumping stops. Therefore, the unique features associated with a HF as compared to the general DFs are two-fold: it is driven by the injected fluid and it proceeds in porous media. These features lead to a simple geometry, but complicated physics.

Besides being driven by the fluid pressure inside the fracture, a HF grows perpendicular to the direction of the minimum *in-situ* stress once it propagates away from the influential domain of a borehole<sup>2</sup>. This combined loading condition makes

---

<sup>2</sup>In general, for deviated boreholes and within the influential stress domain of the boreholes.

the HF behave as a mode-I crack [13, 14]. Propagation of the mode-I fracture is along the fracture itself, i.e. in-plane fracture propagation (Figure 1.2). The resultant geometry is planar. Therefore, the *where* question in the general problem of modeling DF propagation, i.e. direction of fracture propagation, is answered. Associated with the mode-I crack type of the HF, the fracture condition for HF propagation can be adequately quantified by the fracture toughness criterion:

$$K_I = K_{Ic} \quad (1.9)$$

i.e. the *when* question is resolved as well<sup>3</sup>. Moreover, HF has created a distinctive fracture opening and therefore, two planes with a narrow aperture and a displacement discontinuity suffice to describe the fracture.

The complicated physics involved in a HF process can be explained by several co-existing and mutually influential sub-models in the deformation system (Figure 1.3). The injected fluid flows inside the fracture and is governed by the *fluid mechanics theory*. The fluid pressure deforms the fracture, which is described by the *solid deformation theory*. When the fracture deformation reaches a critical point in terms of the material strength, propagation of the fracture ensues, which is within the domain of *fracture mechanics*. Furthermore, fluid inside the fracture can leak into the surrounding porous formation, resembling *fluid flow in porous media*. The leaked fluid builds up pore pressure within the formation, causing it to expand. This

---

the local minimum principal stress direction the HF responds may not coincide with the far-field minimum *in-situ* stress direction. The fracture undergoes turning and twisting after its initiation at the borehole before it finally becomes normal to the minimum *in-situ* stress direction, e.g. [6]. Therefore, in this region, the fracture is subject to a mixed-mode loading condition and its propagation cannot be planar according to fracture mechanics theories, e.g. [7, 8, 9]; Instead, an out-of-plane geometry is often caused (Figure 1.2). This near-wellbore out-of-plane geometry limits the entry of particle-laden packing fluid into the fracture which could cause the early screenout problems in the HF stimulation [6, 10, 11, 12]

<sup>3</sup>Note that behind the superficial simplicity manifested by Eqn. (1.9) lies a great difficulty in quantifying the  $K_{Ic}$  for the *in-situ* rock materials. It has been argued that the *in-situ* values of  $K_{Ic}$  are influenced by the complicated tip behavior (to be elaborated below), e.g. [10]. It has been reported that the *in-situ* values of  $K_{Ic}$  could be orders larger than the laboratory-measured ones, e.g. [15]

expansion tends to close the fracture, which falls into the discipline of *poroelasticity*. Therefore, a comprehensive analysis of HF should at least include the foregoing five physical submodels, i.e. fluid mechanics, solid deformation, fracture mechanics, poroelasticity and fluid flow in porous media. Some other physical complexities include, though not exclusively, multiphase flow in the formation, temperature effects, tip behavior as well as nonlinear deformation of the formation.

Mathematically, the HF growth is strongly nonlinear because of the intimate coupling between these various physical processes. The strongest nonlinearity comes from the coupling between fracture deformation and flow inside the fracture. The fluid flow follows the Poiseuille law if a parallel plate model is used. The flow rate is proportional to the *cubic* of the fracture aperture if a Newtonian fluid is considered. Thus, any small change in the aperture could induce large changes in the fracture conductivity, which in turn disturbs the fluid pressure distribution inside the fracture. On the other hand, the pressure change affects the fracture deformation, including the fracture aperture. Some other couplings include the one between flow and deformation in the formation, and the one between fluid leakoff into the formation and fluid flow inside the fracture.

In summary, a relieving factor in modeling HF is the relatively simple planar geometry. The challenge mainly comes from the complicated physics, specifically, the nonlinear, coupled system including the at least the five physical submodels as described.

### 1.3 Penny-shaped HF Model

Among the four commonly-referred HF models — KGD (Khristianovich-Geertsma-Daneshy), PKN (Perkins-Kern-Nordgren), penny-shaped and quasi-3D<sup>4</sup>, the penny-

---

<sup>4</sup>In the petroleum engineering literature, the quasi-3D model is commonly termed as 3D model. In this model, the fracture is assumed and forced to remain planar. However, in engineering

shaped model along with the quasi-3D are most mechanically sound. No mechanical assumption is needed therein.

Both KGD and PKN models are constrained by the pay zone, i.e. having a constant height. The KGD model assumes a rectangular section perpendicular to the fracture direction [18, 19, 20]. A plane strain crack is assumed to prevail along the fracture direction. The fracture shape is governed by fracture deformation, fluid flow inside the fracture and leakoff from the fracture. In contrast, the PKN model takes an elliptical section perpendicular to the fracture direction [21, 22]. The cross-sections are assumed to be mutually independent. No rigorous deformation mechanism is assumed along the fracture direction. The fracture geometry along this direction is solely determined by fluid flow equations.

The penny-shaped model [23, 24, 21, 19, 25] is contained within the pay zone. It is equi-dimensional in all directions. The quasi-3D model allows the fracture to grow up or downwards beyond the pay zone in addition to propagating laterally into the formation. It has been modeled by pseudo-3D [26, 27, 28, 29, 30, 57, 32, 33, 34] and true-3D simulators [35, 36, 37, 38, 39, 40, 41, 42, 43].

The validity range of the various models are not strictly defined. Both KGD and PKN models represent the first generation of HF simulators. Their advantage is in their simplicity. While they are still used as design tools, their role is gradually giving way to the quasi-3D models according to the latest survey [44].

The penny-shaped model is valid when the created fracture lies within the uniform area of either material properties or *in-situ* stresses. This condition holds when the formation to be fractured is relatively large, i.e. in HF stimulation of massive formations. This condition also exists in micro-/mini-fracturing jobs when

---

mechanics, a 3-D crack growth may undergo twisting and turning, e.g. [6] and its shape is thus curved and out-of-plane. To differentiate these two models, the planar 3D is denoted as quasi-3D while the curved-3D is called full-3D. Simulation of the full-3D model is theoretically and computationally challenging. There have been a few attempts [16, 17]. However, none of them have reported specific results about the out-of-plane propagation.

the injected fluid is small and the propagated fracture does not approach the bounding layers. This practice has been deliberately employed in diagnosis of formation leakoff properties and in measuring the *in-situ* stresses. The penny-shaped model also prevails in hydraulic fracturing of shallow formations where the created fracture is horizontal, such as in environmental applications or stimulation of the Canadian tar sands.

## 1.4 Critical Review on HF Simulation

Since the onset of the HF concept, intensive efforts have been spent to simulate its propagation either as a predictive tool or as a post-frac checkup. Volumous literature exists and, consequently, a comprehensive review is out of the scope of this dissertation. Several review papers also appear in the literature [45, 46, 47, 48, 49, 50]. Two SPE monographs were dedicated to this subject [51, 52]. At least, one dedicated textbook has been published to this topic [53]. The intention of this section is to summarize the state of the art in accounting for the complicated physics. Some other aspects, such as modeling methodology, are to be covered in the subsequent chapters when they become relevant.

Most of the existing hydraulic simulators account only for flow inside the fracture, deformation of the fracture, and fluid leakage into the formation. Flow inside the fracture is formulated by the Poiseuille law. Both Newtonian and non-Newtonian, particularly power-law, fluid rheology has been considered. The fluid leakage has been accounted for by Carter's leakoff model [54] which is 1-D and pressure-independent. Computation of the fracture deformation is based on the elasticity theory.

Carter's leakoff model is independent of any fluid pressure condition in the formation/fracture. A pressure-dependent leakoff mechanism has been considered in

studying water- or steam-flood induced fracture propagation [55, 56, 57, 58] and in the conventional HF simulation [59, 60]. Thermal effects as well as multiphase flow in the reservoir have also been considered when analyzing the flooding-induced fracture in conventional or tar-sand reservoirs, e.g. [61, 58, 62], or in the conventional HF simulation where large temperature contrasts exist between the fracturing fluid and the formation [63, 64, 65]. Moreover, in order to explain the discrepancy between the higher observed wellbore pressure and lower simulated value, near-tip behavior has been investigated [10]. The near-tip process includes the near-tip fluid lag [66, 67] and nonlinear deformation and dilatancy in the formation around the tip [26, 68, 66, 69].

## 1.5 Poroelastic Effects in the HF Process

The role of the flow-deformation coupling, i.e. the poroelastic effect, on HF has also been brought to attention. The theory of poroelasticity was established in 1940's to study coupled flow-deformation behavior of porous media [70]. In the theory, volumetric deformation triggers fluid flow and flow induces solid dilation. The first insight into the poroelastic effect in general fracturing behavior was made in 1970's [71, 72, 73]. Particular implication of the poroelastic effect in HF was first noted also around the 70's [74, 75, 76, 77]. More detailed studies have continued [78, 79, 80, 81, 82]. Cleary (1980, 1983) [83, 84] considered the flow-induced rock dilation and suggested that its effect on the HF propagation is similar to the fracture closure exerted by an additional compressive stress acting normal to the fracture surface which he coined as *back-stress*. Settari (1980) [55] followed a similar procedure when accounting for the poroelastic effect in his hydraulic fracturing simulation. Detournay et. al (1990) [85] implemented the poroelastic effect into the PKN model based on Carter's leakoff model. Abousleiman [60] extended it by

including a pressure-dependent leakoff model. Clifton and Wang [86] included the poroelastic effect into a 3-D HF simulator. More recently, Ghassemi (1996) [17] coded the 3-D poroelastic fundamental solutions into a boundary element method algorithm.

Theoretical findings on poroelastic effects in HF propagation can be summarized as follows:

1. It raises considerably the wellbore pressure response; as much as a 60% increase as compared to non-poroelastic cases has been reported based on numerical studies [82].
2. The shut-in pressure can be higher than the *in situ* minimum principal stress, e.g. [87].
3. The fracture dimensions (length/width) depend on the fluid leakoff model. The pressure-independent Carter's leakoff model gives little difference in fracture dimension between the poroelastic and non-poroelastic cases, e.g. [85]. Otherwise, if the leakoff is pressure-dependent, the fracture dimension can be altered by the poroelastic effect [60, 88].
4. With the fluid flow included in the poroelasticity theory, additional factors, such as injection rate, injected fluid viscosity and dilatancy around the fracture tip, can influence the already complicated HF process, e.g. [89].

Some of these theoretical findings have been backed by laboratory and field observations. For example, field evidence has indicated that fracture closure pressure increases with injection time [90, 91]. Fracturing pressures have also been found to depend on the reservoir pressure change during production [92, 93]. Summarizing the numerous microfrac tests, Kry (1989) [94] reported that the instantaneous shut-in pressure,  $p_{isip}$ , and fracture closure pressure,  $p_{foc}$ , were significantly less in high

injection rate tests than when using low rates. In their numerical simulations, Boone et al. (1991) [95] attributed this difference to the poroelasticity. Several laboratory tests [91, 96, 97, 98] have indicated that  $p_{i,si}$  was greater than the known or expected value of the *in-situ* minimum principal stress. Boone et al. (1990) [87] found that the cause to this discrepancy is due to the poroelastic effect.

More broadly, physical tests as run by Haimson and Fairhurst (1969) [75] and Zoback et al. (1977) [99] pointed out that the breakdown pressure in HF is rate-dependent, whose origin was again traced to the poroelastic effect [100, 101, 87]. Some other well-established field examples about the poroelastic effect can be found in other geomechanics fields, such as the reverse consolidation (i.e. time-dependent borehole closure) [102], Mandel-Cryer effect (i.e. non-monotonic pressure history) [103, 104], and Noordbergum effect (i.e. rise of groundwater table in the observation wells during initial stage of pumping nearby) [105].

Development of poroelastic effects depends on the material properties and operation time scale, which are lumped into a characteristic dimensionless time variable,  $\tau = ct^2/L$ . For a Griffith crack, if  $\tau$  is greater than 0.001, the poroelastic effect is expected to become influential, e.g. [95]. In this formula,  $c$  is the poroelastic diffusivity coefficient (to be defined in the following chapter).  $t$  can be broadly defined as the time period over which the porous formation has undergone fluid exchange with the external system.  $L$  is a characteristic length. In HF,  $t$  is the injection time and  $L$  is the fracture length. Low diffusivities such as in gas-dissolved reservoirs, low permeability, high fluid viscosity as well as short operation time scale all lead to a small  $\tau$  which therefore hampers the development of the poroelastic effect in the field. Of course, the material properties also influence the magnitude of the poroelastic effect even after it has been fully fledged. A small magnitude makes the poroelastic effect obscure in the already complicated field practices. Furthermore, if



the leakoff is considered to be pressure-dependent, the contrast between the *in-situ* stress and reservoir pore pressure also affects the significance of poroelastic effect. If the contrast is large, the poroelastic effect becomes more pronounced.

## 1.6 Conjectures, Objectives and Approaches

Scientific research is motivated by conjectures and proceeds towards certain objectives via systematic approaches. Based on the foregoing discussion, the conjectures for this dissertation are as follows:

1. Poroelastic effects are important for HF of porous media. The penny-shaped HF model needs to be specifically studied. As pointed out before, the penny-shaped model is applicable in HF stimulation of massive or shallow formations, or in the early stages of HF jobs for formation testing and in *in-situ* stress measurements. In all these occasions, poroelastic effects are expected to be significant. In the first case, a long period of fluid injection is inevitable as it is required to create large fractures. In the second and third cases, the fracturing fluid is often operated through the multiple ISF cycles. The repeated ISF cycles extend the operation time. On the other hand, the repeated cycles result in complicated pressure histories inside the fracture, which in turns affects the fluid leakoff and fracture propagation history. All these circumstances facilitate the generation of the fully-fledged poroelastic effects. Notably, the penny-shaped geometry has been out of the picture in the literature for consideration of the poroelastic effect. The majority of the published works have focused on the PKN, e.g. [85, 60] and one was on the KGD [82].
2. Analyses of the complicated PCR fracturing behavior during the multiple ISF pumping cycles is helpful in the interpretation of the mini/micro-HF jobs for the formation properties and *in-situ* stress. More information and/or a

more accurate determination could be obtained from the wellbore pressure response if the effects of the various *in-situ* conditions during the fracturing process were investigated. Rigorous simulation of the fracturing behavior, particularly the involved poroelastic effects, during multiple ISF cycles have not been attempted in the literature and, therefore, warrant serious scientific investigation.

3. The fluid leakoff module should have pressure-dependent capabilities in addition to the pressure-independent Carter's leakoff model. When incorporated with pressure-dependent leakoff, poroelastic effects have been shown to be broader: it changes not only the wellbore pressure response, but also the fracture dimensions. In addition, the filtercake, which causes the leakoff to be pressure-independent, often does not exist if the injected fluid is of low viscosity as in the micro-HF jobs and/or if the reservoir to be stimulated is of high permeability such as naturally fractured reservoirs, e.g. [51, 49]. In these situations, the leakoff depends on the pressure difference between the reservoir pore fluid and the fracturing fluid.
4. In consideration of the poroelastic effects, a realistic 2-D model is important. The 1-D leakoff assumption in the context of Carter's leakoff model underestimates the leakoff value at low fluid injection rates [58]. Significant difference between the 1-D and 2-D leakoff models has also been reported in [84].
5. A fast, PC-based HF simulator is more appealing not only for field design and interpretation purposes, but also for academic research. This idea happens to agree with the spirit of the current momentum-gaining on-site real-time simulation of HF jobs, e.g. [50, 106]. With the sacrifice of being constrained to a particular idealized geometry (penny-shaped), it is possible to responsibly

simplify the complicated physics and make them amendable.

The primary objective of this dissertation is to build a penny-shaped HF simulator, which considers the pressure-dependent leakoff and poroelastic effect in the context of multiple ISF cycles and in the 2-D configuration; and which is PC-based, fast-run and real time analysis-oriented. For this mission, the following specific goals are set:

1. Construct a simplified 2-D poroelastic model which balances the complicated physics and intensive computational effort. Specifically, this model should be computationally comparable to the simple 1-D poroelastic model while it mechanically covers the true physics in the 2-D poroelastic domain.
2. Develop an efficient numerical solver to simulate the HF propagation of a penny-shaped geometry.
3. Implement the pressure-dependent leakoff and poroelastic effect into the penny-shaped model in the context of multiple PCR fracturing events during the multiple ISF cycles.
4. Build up a PC-based, fast-run simulator. Extensively validate the numerical algorithms as well as the computer program.

Therefore, this work is not a simple application of a certain standard numerical method to the governing equations followed by coding and validating the computer program. Instead, it makes rational simplifications and invents an efficient numerical algorithm particularly appropriate to the model.

The foregoing tasks are accomplished via the following approaches:

1. Analyze the 1-D transient and 2-D steady-state poroelastic models. Acting as the asymptotic behavior, these two models bound the full 2-D poroelastic response from the early and late times, respectively,

2. Investigate the transient poroelastic response of a penny-shaped fracture and apply a cubic spline scheme to interpolate the transient response based on the early- and late-time analytical predictions. Thereby, a simplified 2-D poroelastic model is constructed. Comparisons between the simplified model and the original model are made. The error domain induced therein is specified.
3. Derive a pseudo-explicit finite difference (PEFD) algorithm which is fast as equivalent to the purely explicit FD scheme, but unconditionally stable like the fully-implicit FD method. Furthermore, the Newton-Raphson (NR) scheme for a system of nonlinear equations is applied to further speed up the computations. Their combination has successfully and efficiently solved the mathematical system arising from modeling the HF fracture propagation. The stability, consistency and computational accuracy of the combined PEFD-NR scheme has been numerically tested.
4. Implement the combined PEFD-NR algorithm in the context of multiple PCR fracturing events during the multiple ISF cycles. Further validate the computer program.
5. Perform a series of parametric analyses about the poroelastic effects in HF propagation, including the multiple PCR events during the multiple ISF pumping cycles.

Inclusion of the poroelastic effects in the HF simulation dramatically complicates the numerical calculations. The necessity to simplify the poroelastic response can be illustrated by taking a plane strain fracture as an example. The governing equation for fluid flow inside the fracture is of the following form [82]:

$$\frac{\partial q}{\partial x} + \frac{\partial w}{\partial t} + u = 0 \quad (1.10)$$

in which  $w$  is the fracture aperture and  $u$  is the fluid leakoff flux. The fluid flux,  $q$ , is related to the pressure distribution by:

$$q = -\frac{w^3}{12\mu} \frac{\partial p_f}{\partial x} \quad (1.11)$$

if a Newtonian fluid rheology is used. In the poroelastic domain and if the leakoff is pressure-dependent,  $w$  and  $u$  depend on the deformation and fluid flow in the formation. The dependency can be cast into the following integral form [82]:

$$\begin{aligned} \sigma_0 - p_f(x, t) = & -\frac{G}{2\pi(1-\nu_u)} \int_{\Omega} \frac{\partial}{\partial x} (\ln R) \frac{\partial w(x', t)}{\partial x'} dx' \\ & - \int_{\Omega} \int_{t'(x')}^t \left[ H_{11}(\xi) \frac{x' - x}{R^4} \frac{\partial w(x', \tau)}{\partial x'} + H_{12} \frac{u(x', \tau)}{R^2} \right] d\tau dx' \end{aligned} \quad (1.12)$$

$$\begin{aligned} p_f(x, t) - p_0 = & -\frac{3c(\nu_u - \nu)}{2\pi B\kappa(1 + \nu_u)(1 - \nu)} \int_{\Omega} \frac{\partial}{\partial x} (\ln R) \frac{\partial w(x', t)}{\partial x'} dx' \\ & - \int_{\Omega} \int_{t'(x')}^t \left[ H_{21}(\xi) \frac{x' - x}{R^4} \frac{\partial w(x', \tau)}{\partial x'} + H_{22} \frac{u(x', \tau)}{R^2} \right] d\tau dx' \end{aligned} \quad (1.13)$$

where  $t'(x')$  is the arrival time of the fracture tip at which, the position  $x'$  is first exposed to the fracturing fluid.  $\Omega$  is the whole fracture surface.  $R = |x' - x|$ . Functions of  $H_{ij}(\xi)$  can be found in [82] and contain both spatial and temporal variables.

Direct discretization of the coupled equations, (1.10) - (1.13), as done in [82], involves integrations in both time and space domains. Solution at the current time depends on the pressure or deformation history along the fracture back to the fracture arrival time. Therefore, it inevitably slows down the calculation.

On the other hand, if a 1-D model is used, there is only a point-wise relationship between the poroelastic response and the fluid pressure, e.g. [60]; i.e. no spatial integration is needed. This significantly speeds up the calculations. The goal of the current study is to express the general poroelastic response, i.e. Eqn. (1.12) and

Eqn. (1.13), in terms of a quasi-point-wise explicit relationship, whose consumed computational effort is much less than the full implementation as done via Eqn. (1.12) and Eqn. (1.13) but retains the full physics and an adequate mathematical accuracy of the true 2-D poroelastic model.

## 1.7 Organization of the Work

By reviewing some generalities and the state-of-art in HF simulation, this general introduction has laid out the objectives and approaches for this dissertation work. After reviewing the theory of poroelasticity, the second chapter studies the 1-D transient and 2-D steady-state poroelastic responses. They bound the full transient 2-D poroelastic response in the early- and late-time regions, respectively. Some mathematical axioms have been proven which are to be used in the subsequent development.

The third chapter is devoted to a study of the full transient poroelastic response and seeks ways to simplify the general 2-D response. Using a commercial finite element (FEM) software, ABAQUS, it first examines the full history of the poroelastic response of a penny-shaped fracture pressurized by two example pressure profiles. It is found that the 1-D transient and 2-D steady state poroelastic models, as studied in Chapter 2, indeed act as the asymptotic behavior to the full transient process. A composite formula, covering the interim transient poroelastic response, is developed by using the cubic spline interpolation based on the analytical results of the two asymptotic models. With these, a simplified transient 2-D poroelastic response is constructed, which is to be used to simulate the penny-shaped fracture propagation and is expected to greatly alleviate computational burden.

The fourth and fifth chapters concentrate on the development of a numerical solution strategy (McFrac) to simulate the PCR of a penny-shaped HF. The dedicated

governing equations are described based on the simplified 2-D poroelastic model as developed in Chapter 3. Extensive example problems are computed to examine the stability, convergence and computational accuracy of the numerical means as well as to demonstrate the capacity of the numerical simulator. The fourth chapter focuses on the simulation of a stationary fracture. The fifth chapter extends to a propagating fracture, particularly in the multiple fracturing events during the multiple ISF cycles. In the fifth chapter, some parametric analyses are also run to exemplify the poroelastic effect in HF propagation, including during the multiple ISF pumping cycles.

The final chapter serves to summarize major findings of this work and to suggest areas of further study. Usage of mathematical symbols are intended to be systematic and are tabulated in the nomenclature. Duplication of symbols are to be specifically mentioned when they occur. This study focuses on isotropic, linear elastic deformations and one-phase Darcy flow in the porous formation. The system is isothermal. The leaked fracturing fluid is assumed to be fully miscible with the *in-situ* reservoir fluid. The mixture has the same viscosity as the virgin reservoir fluid.

## 1.8 Summary

The primary objective of this work is to build up a fast-run, PC-based, field analysis-oriented HF simulator (McFrac) for the penny-shaped geometry. It accounts for the pressure-dependent leakoff and poroelastic effect in the 2-D domain. It simulates multiple ISF cycles and the associated multiple PCR fracturing events.

Simple application of a standard numerical method to the general governing equations cannot achieve the objective because it is computationally-expensive. Instead, this work proceeds to reasonably simplify the mathematical description which retains the physics, does not lose much of the computational accuracy, but greatly

reduces the computational effort. Behind this approach lies the serious analytical effort this dissertation undertakes to investigate the full poroelastic response of a pressurized penny-shaped fracture. Furthermore, an efficient numerical algorithm is created to solve the resultant governing equations. The numerical solver combines the advantages of explicit and implicit F.D. schemes as well as the Newton-Raphson scheme for nonlinear equations: fast and unconditionally stable.

Ultimately, this dissertation will help the industry in the interpretation of the mini/micro-HF jobs for measurements of the *in-situ* stresses and leakoff characteristics. The current HF *in-situ* stress measurement technique relies on the recognition of the so-called instantaneous shut-in pressure or fracture closure pressure on the wellbore pressure log curves. In permeable formations, the pressure-dependent leakoff and poroelastic effects make both characteristic pressures obscure and difficult to pinpoint. Moreover, they vary with the injection rate and the number of the ISF cycles. In permeable formations where the filtercake cannot fully developed, Carter's leakoff coefficient is a fictitious man-added constant. The leakoff depends on the pressure difference between the reservoir and the fracturing fluid. In all these occasions, McFrac provides a modeling tool to further investigate the influential factors as well as to history-match the observed pressure history and therefrom, to make inferences about the *in-situ* stresses and the leakoff features.



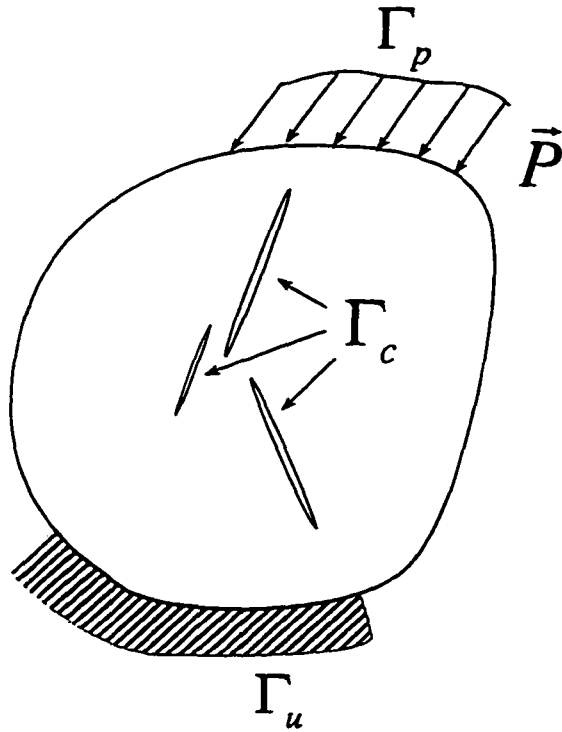


Figure 1.1: Simulation of discrete fracture propagation.

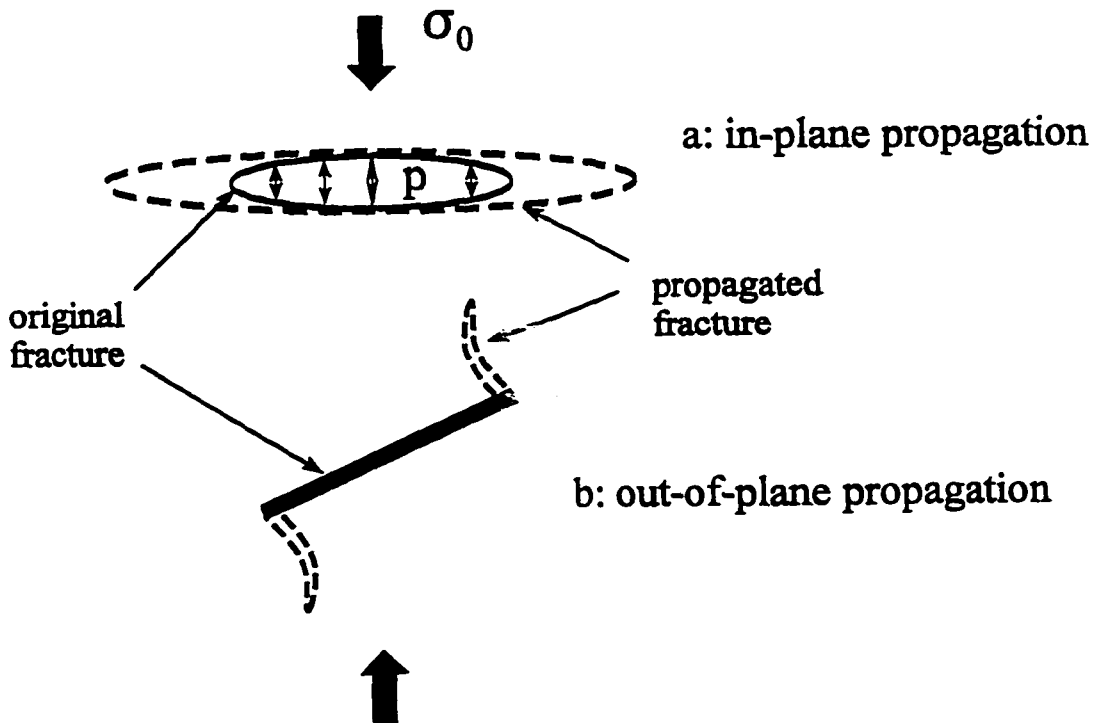


Figure 1.2: In-plane and out-of-plane fracture propagation.

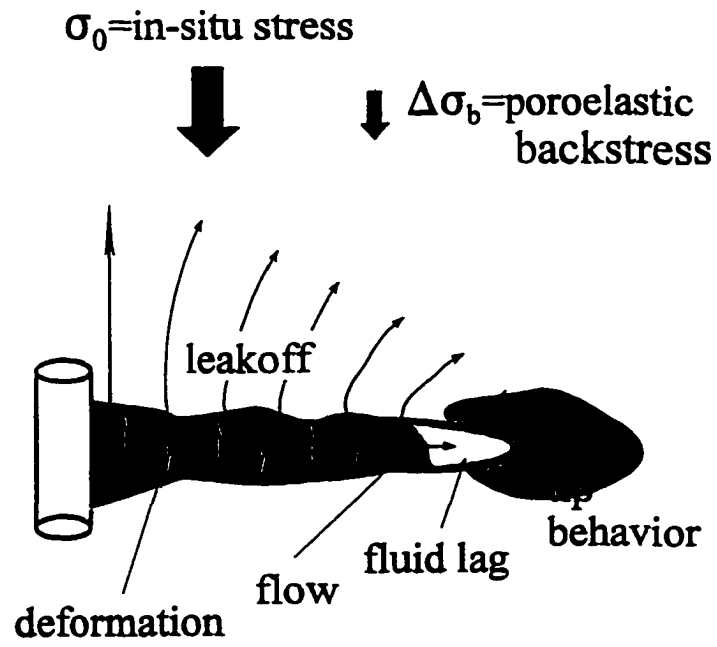


Figure 1.3: The complicated physics involved in a HF process.

## Chapter 2

# 1-D Transient and 2-D Steady-State Poroelastic Response

Fluid-saturated porous rock behaves mechanically different than its dry state. Flow-deformation coupling is the key factor. The theory of poroelasticity is the mathematical framework to describe this coupled system in the linear elastic regime. Physically, two mechanisms are involved: volumetric deformation causes an instantaneous pore pressure increment; an increment in the pore pressure triggers rock dilation. This chapter summarizes the governing equations and investigates 1-D transient and 2-D steady-state poroelastic responses. Typically, a complete history of the poroelastic response is bounded in the beginning by the 1-D model and at the end by the steady state. Therefore, observations made herein serve further development in the following chapters which study the full transient poroelastic behavior of a penny-shaped fracture in the porous media.

### 2.1 Governing Equations in Poroelastic Domain

Although analyses about the role of the flow-deformation coupling can be traced back to Terzaghi (1923)[107], the modern poroelasticity theory was initiated by Biot (1941, 1955, 1962) [70, 108, 109]. Rice and Cleary (1976) [71] reformulated the

theory in terms more familiar to the rock and soil mechanics community. Alternatively, the theory of poroelasticity was derived within the framework of the mixture theory. e.g. [110, 111, 112, 113]. A more physically straightforward version of the mixture theory, i.e. the micromechanical approach [114, 115, 116, 117, 118] breaks the continuum behavior of the porous media into those of its constituents, i.e. solid, pores and fluid. Therefore, it is more helpful to gain insight into the basic physics of the poroelastic behavior. Following a similar approach, Yew and Liu (1992) [119] have also derived the poroelasticity theory with different expressions for the material parameters.

In order to fully describe the poroelastic problems, two independent material constants, which could be the Biot's coupling coefficient,  $\alpha$ , and Skempton's pore pressure coefficient,  $B$ , are needed, in addition to the two elastic (e.g, Young's modulus,  $E$  and Poisson's ratio,  $\nu$ ) and a fluid flow (permeability coefficient,  $\kappa^1$ ) properties. The micromechanical approach relates the poroelastic constants to the mechanical properties of the individual constituents as follows:

$$\alpha = 1 - \frac{K}{K_s} \quad (2.1)$$

$$B = \frac{\frac{1}{K} - \frac{1}{K_s}}{\phi \left( \frac{1}{K_f} - \frac{1}{K_s} \right) + \frac{1}{K} - \frac{1}{K_s}} \quad (2.2)$$

in which  $K$  is the elastic bulk modulus of the porous media.  $K_f$  and  $K_s$  are the bulk modulus of the fluid and solid phase, respectively. Therefore,  $\alpha$  depends only on the solid properties while  $B$  is influenced by the fluid property as well as the formation porosity. The governing equations in the poroelastic domain can be organized into the following forms:

---

<sup>1</sup> $\kappa$  relates to the intrinsic permeability of the formation,  $k$  (with a dimension of length squared) via  $\kappa = k/\mu$ .  $\mu$  is the formation fluid viscosity.

1. equilibrium equation:

$$\frac{\partial \sigma_{ij}}{\partial x_j} = 0 \quad i, j = x, y, z \quad (2.3)$$

in which, quasi-static deformation and no body force are assumed.

2. constitutive equation:

$$\sigma_{ij} = 2G\varepsilon_{ij} + \frac{2G\nu}{1-2\nu}\varepsilon\delta_{ij} + \alpha p\delta_{ij} \quad (2.4)$$

where compression is taken as positive. This equation, together with the small deformation assumption, Eqn. (1.7), ensures the kinematic determinativity and geometric compatibility of the deformation system.

3. mass conservation equation for fluid flow:

$$\frac{\partial \zeta}{\partial t} + \frac{\partial q_i}{\partial x_i} = 0 \quad i = x, y, z. \quad (2.5)$$

Here, no fluid source/sink is introduced. The fluid content term,  $\zeta$ , is related to the fluid pressure,  $p$ , and solid mean stresses,  $\sigma_{kk}$ , by:

$$\zeta = \frac{\alpha}{K} \left( \frac{p}{B} - \frac{\sigma_{kk}}{3} \right) \quad (2.6)$$

or is related to the fluid pressure and solid volumetric deformation,  $\varepsilon$ , via:

$$\zeta = \frac{p}{M} - \alpha\varepsilon \quad (2.7)$$

in which  $M$  is Biot's modulus,  $M = KB/\alpha$ .  $q_i$  is the fluid flux given by the Darcy's law as follows.

4. fluid momentum equation as described by Darcy's law:

$$q_i = -\kappa \left( \frac{\partial p}{\partial x_i} \right) \quad i = x, y, z \quad (2.8)$$

in which, the fluid body force is not included.  $\kappa$  is the dynamic conductivity of the porous formation defined by  $k/\mu$  with  $k$  being the formation permeability and  $\mu$  the pore fluid viscosity.

Assumptions behind these governing equations include: (1) quasi-static small deformations; (2) isothermal system and (3) single-phase Darcy flow. Dynamic excitation induces more sophisticated fluid-solid coupling. *“It is therefore in the modeling of quasi-static processes that the Biot model finds its full justification”* [89]. Inclusion of thermal effects should not cause serious difficulties. Consideration of multiple phase flow depends on the correlation of the phacial fluid pressures to describe the pore space deformations.

Combining Eqn. (2.3) to Eqn. (2.8) could yield the following field equations of the poroelasticity theory:

$$G\nabla^2 u_i + \frac{G}{1-2\nu} \left( \frac{\partial \varepsilon}{\partial x_i} \right) - \alpha \left( \frac{\partial p}{\partial x_i} \right) = 0 \quad i = x, y, z \quad (2.9)$$

$$\frac{\partial p}{\partial t} - \kappa M \nabla^2 p - \alpha M \frac{\partial \varepsilon}{\partial t} = 0 \quad . \quad (2.10)$$

## 2.2 General Discussion on Poroelastic Effect

Within the existence of a freely-moving fluid in the porous medium, the solid deformations become time-dependent even though the mechanical loading may not change over time. This time-dependence may be described by the variation of the elastic parameters in the coupled system. Instantaneously upon the exertion of the mechanical loading, the material responds undrained in that the fluid has no time to flow, i.e.  $\zeta = 0$ . A pore pressure field is induced according to Eqn. (2.6):

$$p_{0+} = \frac{B\sigma_{kk}}{3} \quad (2.11)$$

Substituting Eqn. (2.11) into Eqn. (2.4) gives:

$$\sigma_{ij} = 2G\varepsilon_{ij} + \frac{2G\nu_u}{1-2\nu_u} \varepsilon \delta_{ij} \quad (2.12)$$

in which,

$$\nu_u = \frac{3\nu + \alpha B(1 - 2\nu)}{3 - \alpha B(1 - 2\nu)} \quad (2.13)$$

called the undrained Poisson's ratio. The shear modulus is independent of the fluid flow.<sup>2</sup> Therefore, there is a corresponding undrained Young's modulus:

$$E_u = \frac{3E}{3 - \alpha B(1 - 2\nu)} \quad (2.14)$$

When the induced pore pressure disturbance,  $p_{0+}$ , diffuses to zero everywhere, i.e. the material becomes drained, the stress-strain relation returns to its original equilibrium (dry) state. The material deformation at this stage is characterized by the usual (drained) Young's modulus and Poisson's ratio,  $E, \nu$ .

It can be easily proven that  $\nu_u > \nu$  and  $E_u > E$ <sup>3</sup>, i.e. the material at the undrained state is volumetrically stiffer as compared to the drained<sup>4</sup>. As the fluid, which has previously shared part of the external loading, is now escaping from the pores, the solids become more stressed and experience more deformation as the material approaches the drained state. The time scale from the undrained state to the drained is determined by the diffusivity coefficient as discussed below.

In the poroelastic domain, the pore pressure invokes rock dilation. Therefore, fluid flow can induce a non-zero state of stress or displacement field. The magnitude

---

<sup>2</sup>Simply taking  $i \neq j$  in Eqn. (2.4) reveals that in the stress-strain relation under shear, there is no pore pressure involved, i.e. the shear modulus remains independent of the pore pressure.

<sup>3</sup>Rearranging Eqn. (2.13) and Eqn. (2.14) gives:

$$\begin{aligned} \nu_u &= \nu + \frac{\alpha B(1 - 2\nu)(1 + \nu)}{3 - \alpha B(1 - 2\nu)} \\ \frac{E_u}{E} &= 1 + \frac{\alpha B}{3 - \alpha B(1 - 2\nu)} \end{aligned}$$

The limiting analyses have shown that  $0 \leq \alpha, B \leq 1$  and  $0 \leq \nu \leq 0.5$ , e.g. [120]. Therefore, the second term on the R.H.S. of the above two equations are all larger than zero. Thus,  $\nu_u \geq \nu$  and  $E_u \geq E$ .

<sup>4</sup>Although both  $E$  and  $\nu$  change, their combination in the shear modulus,  $G$ , does not depend on the pore pressure diffusion, i.e. the shear deformation does not vary.

of such an effect is characterized by the poroelastic stress coefficient,  $\eta$ :

$$\eta = \frac{\alpha(1 - 2\nu)}{2(1 - \nu)} \quad (2.15)$$

Note that like  $\alpha$ ,  $\eta$  depends on the solid properties only.

In poroelasticity, the temporal variation of the pore pressure is no longer a pure diffusion process. The pure diffusion equation applies only to the fluid content,  $\zeta$ , e.g. [89]:

$$\nabla^2 \zeta = \frac{1}{c} \frac{\partial \zeta}{\partial t} \quad (2.16)$$

in which  $c$  is called the poroelastic diffusivity coefficient; i.e.

$$c = \frac{2\kappa G(1 - \nu)(\nu_u - \nu)}{\alpha^2(1 - 2\nu)^2(1 - \nu_u)} \quad (2.17)$$

It is the diffusivity coefficient,  $c$ , which controls the evolution of the poroelastic effect. A higher value of  $c$  causes the poroelastic effect to show up earlier. A permeable rock and/or low viscosity fluid corresponds to a higher  $\kappa$ , thus facilitating the development of the poroelastic effect because it gives a higher value of  $c$ . Stiffer grains and/or more compliant solid skeleton, such as a soft formation, give a smaller  $\alpha$  and thus, a lower  $c$  value, impeding the maturity of the poroelastic effect. But its magnitude, when fully developed, may be large because it gives a higher  $\nu_u$  or  $\eta$  value. Furthermore, the fluid compressibility for a gas-dissolved reservoir is high. As a result, it gives a low  $B$  and small  $\nu_u$  and  $c$  values in the chain rule. Therefore, this kind of reservoir delays the full development of the poroelastic effect and its magnitude is small as well.

When considered in modeling HF propagation, the poroelastic effect shows up in the following two competing aspects: the mechanically-induced deformation of the pressurized fracture is smaller at the beginning, determined by the undrained elastic properties, and increases later on to the drained state. The increment is



controlled by the drained and undrained Poisson's ratios,  $\nu$  and  $\nu_u$ , as well as the stress difference:  $(p_f - \sigma_0)$  with  $\sigma_0$  being the *in-situ* minimum stress component. On the other hand, as the fracturing fluid leaks into the formation, it increases the pore pressure and induces rock dilation, tending to close the fracture. The corresponding magnitude is directly proportional to the stress coefficient,  $\eta$ , and the difference,  $(p_f - p_0)$ , in which  $p_0$  is the *in-situ* pore pressure. In most practical situations,  $\sigma_0$  is much larger than  $p_0$ ; and; therefore, the second effect, which reduces the fracture opening, is expected to be much larger than the first one in HF.

## 2.3 A 1-D Poroelastic Model

In this section, a 1-D poroelastic model is analyzed. This example serves as an illustration for the poroelasticity theory. More importantly, a 1-D model is justifiable to describe the early-time poroelastic response of the geometries larger than 1-D, e.g. [89]. A sketch of the problem is shown in Figure 2.1. Physically, it is equivalent to an infinitely long strip of porous material saturated with an initial pore pressure,  $p_0$  and subject to a far-field normal stress,  $\sigma_0$ . Fluid pressure,  $p_f(t)$ , which may be time-dependent, is applied at surface  $x = 0$ . It serves as both mechanical and hydraulic loading conditions.

The governing equations for the current 1-D model can be greatly simplified from the general poroelastic equations, (2.3) to (2.8). Specifically, they can be written as:

1. Equilibrium equation:

$$\sigma_{xx} = C(t) \quad x, t > 0 \quad (2.18)$$

i.e. it is constant spatially, but could vary in time.

2. Constitutive equation combined with the small deformation assumption:

$$\frac{\partial w}{\partial x} = \frac{\eta}{G}p + \frac{\eta}{G\alpha}\sigma_{xx} \quad x, t > 0 \quad (2.19)$$

$w$  is the displacement component along the  $x$ -direction.

3. Diffusion equation:

$$c \frac{\partial^2 p}{\partial x^2} - \frac{\partial p}{\partial t} = \frac{B(1 + \nu_u)}{3(1 - \nu_u)} \frac{d\sigma_{xx}}{dt} \quad x, t > 0 \quad (2.20)$$

The original problem is decomposed into two modes (Figure 2.1), which cover the perturbation caused by the pressurization. Mode 1 represents the mechanical loading condition at  $x = 0$ :

$$\begin{cases} \sigma_{xx}(x, t) = p_f(t) - \sigma_0 \\ p(x, t) = 0 \end{cases} \quad x = 0, t > 0 \quad (2.21)$$

Mode 2 makes up the hydraulic flow part with the boundary condition as:

$$\begin{cases} \sigma_{xx}(x, t) = 0 \\ p(x, t) = p_f(t) - p_0 \end{cases} \quad x = 0, t > 0 \quad (2.22)$$

Combination of Eqn. (2.18) and Eqn. (2.21) or Eqn. (2.22) yields the following state of stress:

$$\sigma_{xx}(x, t) = p_f(t) - \sigma_0 \quad x > 0, t > 0 \quad (2.23)$$

for mode 1, and:

$$\sigma_{xx}(x, t) = 0 \quad x > 0, t > 0 \quad (2.24)$$

for mode 2. At the beginning, i.e.  $t = 0^+$ , the non-zero stress field in mode 1 causes an instantaneous pore pressure field,  $p(x, t = 0^+)$ , which can be easily computed from Eqn. (2.6) by setting  $\zeta = 0$ , so that:

$$p(x, t) = \frac{B(1 + \nu_u)}{3(1 - \nu_u)} [p_{f0} - \sigma_0] \quad t = 0 \quad (2.25)$$

where  $p_{f0} = p_f(t = 0)$ <sup>5</sup>. Afterwards, this pore pressure field diffuses through the surface  $x = 0$  as dictated by the pore pressure boundary condition, Eqn. (2.21), i.e. the diffusion is governed by Eqn. (2.20) and Eqn. (2.25) as:

$$\begin{cases} c \frac{\partial^2 p}{\partial x^2} - \frac{\partial p}{\partial t} = -\frac{B(1+\nu_u)}{3(1-\nu_u)} \frac{dp_f}{dt} & x > 0, t > 0 \\ p(x, t) = \frac{B(1+\nu_u)}{3(1-\nu_u)} [p_{f0} - \sigma_0] & x > 0, t = 0 \\ p(x, t) = 0 & x = 0, t > 0 \end{cases} \quad (2.26)$$

With a zero stress field, Eqn. (2.24), the diffusion problem in mode 2 can now be simplified to:

$$\begin{cases} c \frac{\partial^2 p}{\partial x^2} - \frac{\partial p}{\partial t} = 0 & x > 0, t > 0 \\ p(x, t) = 0 & x > 0, t = 0 \\ p(x, t) = p_f(t) - p_0 & x = 0, t > 0 \end{cases} \quad (2.27)$$

Based on the above equations, the following three formulae can be proven which is detailed in Appendix A:

1. *The poroelastic displacement at  $x = 0$ ,  $w^p(t)$ , can be expressed as time integration of the leakoff rate,  $u(t)$ , at the surface  $x = 0$ :*

$$w^p(t) = -\frac{\eta c}{G \kappa} \int_0^t u(\tau) d\tau \quad (2.28)$$

2. *The pressure-dependent leakoff rate at  $x = 0$  is given by:*

$$u^1(t) = -\frac{B(1+\nu_u)}{3(1-\nu_u)} \frac{\kappa}{\sqrt{\pi c}} \left[ \frac{p_{f0} - \sigma_0}{\sqrt{t}} + \int_0^t \frac{dp_f}{d\tau} \frac{d\tau}{\sqrt{t-\tau}} \right] \quad (2.29)$$

*for mode 1 loading; or;*

$$u^2(t) = \frac{\kappa}{\sqrt{\pi c}} \left[ \frac{p_{f0} - p_0}{\sqrt{t}} + \int_0^t \frac{dp_f(\tau)}{d\tau} \frac{d\tau}{\sqrt{t-\tau}} \right] \quad (2.30)$$

*for mode 2 loading.*

---

<sup>5</sup>The time factor is included in all the expressions herein. However, it is not necessary in the actual mathematical manipulations. The boundary condition may be first assumed to be time-independent. The thus derived results can be easily extended to the general time-varying boundary condition by utilization of Duhamel's principle, e.g. [121].

Eqn. (2.28) implies that  $w^p(t)$  is proportional to the total fluid leakoff volume into the media through  $x = 0$  until the current time,  $t$ . To arrive at Eqn. (2.28), the pressure boundary condition at  $x = 0$ , i.e.  $p(x, t) = 0$  or  $p(x, t) = p_f - p_0$ , is not required. Therefore, if the boundary condition there changes to a leakoff rate-prescribed boundary such as in Carter's leakoff model,  $u(x = 0, t) = u_0(t)$ , Eqn. (2.28) still holds.

Combining Eqn. (2.28) with Eqn. (2.29) or Eqn. (2.30) gives the pressure-dependence of the poroelastic displacement:

$$w^{1,p}(t) = \left[ \frac{B(1 + \nu_u)}{3(1 - \nu_u)} \right] \left( \frac{\eta}{G} \sqrt{\frac{c}{\pi}} \right) \left[ 2(p_{f0} - \sigma_0)\sqrt{t} + \int_0^t d\tau \int_0^\tau \frac{dp_f(s)}{ds} \frac{ds}{\sqrt{\tau - s}} \right] \quad (2.31)$$

for mode 1; or,

$$w^{2,p}(t) = -\frac{\eta}{G} \sqrt{\frac{c}{\pi}} \left[ 2(p_{f0} - p_0)\sqrt{t} + \int_0^t d\tau \int_0^\tau \frac{dp_f(s)}{ds} \frac{ds}{\sqrt{\tau - s}} \right] \quad (2.32)$$

for mode 2.

Comparing mode 1 and 2 values, i.e. Eqn. (2.29) and Eqn. (2.30) or Eqn. (2.31) and Eqn. (2.32), shows:

$$\frac{u^1}{u^2} \left( \text{or } \frac{w^{1,p}}{w^{2,p}} \right) \propto \frac{B(1 + \nu_u) p_{f0} - \sigma_0}{3(1 - \nu_u) p_{f0} - p_0} \quad (2.33)$$

Theoretically, the combined poroelastic constant,  $B(1 + \nu_u)/3(1 - \nu_u)$  ranges from 0 to 1. In practice, this combined constant falls within the range (0.3, 0.7) (Table 2.1). More significantly, the *in-situ* stress,  $\sigma_0$ , is much larger than the *in-situ* pore pressure,  $p_0$ . Therefore, the mechanical (mode 1) loading-induced leakoff or poroelastic effect is much smaller than the flow-triggered one (mode 2). Similar assertion has been made by many other researchers, e.g. [80, 60]. Figure 2.2 exemplifies this comparison. The material properties are from Table 2.2. The *in-situ* stress and pore pressure data are from [123].

## 2.4 2-D Steady-State Poroelastic Response

The pore fluid, whether it is generated by the mechanical loading (mode 1) or by the imposed hydraulic flow boundary condition (mode 2), all diffuses to reach steady state. Therefore, the steady-state poroelastic solution is representative of the full poroelastic response at late times. The steady state under mode 1 loading is equivalent to the drained state. Its mechanical behavior is quantified by the drained response, which is given by the conventional elasticity theory and is, therefore, not analyzed herein.

Mathematically, the steady state under mode 2 loading for a pressurized fracture in an infinite media may not be possible. However, after a relatively long diffusion time, the temporal variation of the pore pressure (under a time-independent fluid pressure condition on the fracture surface) in the neighborhood of the fracture surface becomes so small that the steady state practically has been reached. This will be now shown by several example problems.

Solution to the steady-state poroelastic response is much easier because the deformation and flow now become decoupled. This is evident by eliminating the temporal variation in the general poroelastic governing equations, (2.9) and (2.10), which becomes:

$$G\nabla^2 u_i + \frac{G}{1-2\nu} \left( \frac{\partial \epsilon}{\partial x_i} \right) - \alpha \left( \frac{\partial p}{\partial x_i} \right) = 0, \quad i = x, y, z \quad (2.34)$$

$$\nabla^2 p = 0 \quad . \quad (2.35)$$

This is equivalent to the steady-state thermoelastic equations, e.g. [124] with the pressure being substituted by the temperature and the Biot's coupling coefficient,  $\alpha$ , replaced by  $3K\gamma$  in which  $\gamma$  is the linear thermal expansion coefficient and  $K$  is the bulk modulus of the elastic material. Therefore, the

many available solutions in thermoelasticity can be applied to the current steady-state poroelastic problems.

Now, consider a penny-shaped fracture of radius,  $R_0$ , in an infinite poroelastic domain which is subject to a pure pore pressure boundary condition,  $p_f(r)$ , along the fracture (Figure 2.3):

$$p = -p_f(r) ; \quad \sigma_{zz} = 0 \quad 0 \leq r \leq R_0; \quad z = 0 \quad . \quad (2.36)$$

The minus sign is added to allow for the fracture to open. The far-field boundary condition as well as the initial conditions are all natural, i.e. zero. The similar problem was originally solved in thermoelasticity by Olesiak and Sneddon (1961) [125] and can also be found in [126]. In our interest, the normal displacement along the fracture can be expressed by the following formula:

$$w(s) = \int_0^\infty \psi(\eta) J_0(s\eta) d\eta \quad , \quad 0 < s = r/R_0 < 1 \quad (2.37)$$

where  $\eta$  is an integration variable, and:

$$\psi(\eta) = \frac{2}{\pi} \int_0^1 \sin(\eta v) dv \int_0^v \frac{x f(x) dx}{\sqrt{v^2 - x^2}} \quad (2.38)$$

with  $f$  given by:

$$f(x) = \frac{(1 + \nu)\alpha R_0^2}{3K} \int_0^\infty q(\eta) J_0(x\eta) d\eta \quad (2.39)$$

in which  $J_0$  is the zero-order Bessel function of the first kind, and:

$$q(\eta) = \frac{2}{\pi R_0} \left[ \cos \eta \int_0^1 \frac{y p_f(y) dy}{\sqrt{1 - y^2}} + \eta \int_0^1 \frac{y dy}{\sqrt{1 - y^2}} \int_0^1 u p_f(yu) \sin(yu) du \right] \quad .(2.40)$$

Furthermore, the pressure derivative,  $\frac{\partial p}{\partial z}$ , normal to the fracture on the fracture surface, which is related to the leakoff rate across the fracture surface, is computed via:

$$\left. \frac{\partial p_f(s, z)}{\partial z} \right|_{z=0} = \int_0^\infty \eta q(\eta) J_0(s\eta) d\eta \quad , \quad 0 < s < 1 \quad . \quad (2.41)$$

In the following, these complicated formulae are analyzed. Numerical means are developed to calculate them under general pressure profiles,  $p_f(r)$ .

### 2.4.1 Computation of Poroelastic Displacements

First of all, the following statement can be reached:

*The steady-state poroelastic displacement on the fracture induced by a pure pore pressure boundary condition,  $p_f(r)$ , along the fracture in an infinite poroelastic domain is equivalent to the purely drained elastic response to a mechanical loading condition,  $\sigma_{zz} = \eta p_f(r)$ , on the fracture surface, i.e.*

$$w_{steady}^p(s) = \frac{2(1-\nu)R_0}{\pi G} \int_s^1 \frac{d\xi}{\sqrt{\xi^2 - s^2}} \int_0^\xi \frac{[\eta p_f(v)]v dv}{\sqrt{\xi^2 - v^2}} \quad (2.42)$$

whose proof is described in Appendix B.

Some simple pressure profiles can be computed analytically to give the explicit relationship between the steady-state poroelastic displacement,  $w_{steady}^p$ , and the pressure profile. For example,

$$w_{steady}^p(s) = \frac{2(1-\nu)\eta p_{f0} R_0}{\pi G} \sqrt{1-s^2} \quad (2.43)$$

for a uniform pressure profile,

$$p_f(s) = p_{f0} ; \quad (2.44)$$

or,

$$w_{steady}^p(s) = \frac{2(1-\nu)\eta p_{f0} R_0}{\pi G} \left[ \left(1 - \frac{\pi}{8}\right) \sqrt{1-s^2} - \frac{s^2 \pi}{8} \ln \left( \frac{1 + \sqrt{1-s^2}}{s} \right) \right] \quad (2.45)$$

for a linear pressure profile,

$$p_f(s) = p_{f0}(1-s) ; \quad (2.46)$$

or,

$$w_{stdy}^p(s) = \frac{\pi(1-\nu)\eta p_{f0} R_0}{4G} (1-s^2) \quad (2.47)$$

for an elliptic-like pressure profile:

$$p_f(s) = p_{f0} \left[ \frac{1+s^2}{1+s} K(k) - K(s) - (1+s)E(k) \right] \quad (2.48)$$

with  $k = 4s/(1+s)^2$  and  $K, E$  are the complete elliptical integrals of the first and second kinds, respectively.

In the above, Eqn. (2.43) and Eqn. (2.45) can be computed easily while Eqn. (2.47) is from the purely elastic solution [128]. Figure 2.4 shows the coincidence of the analytical predictions, Eqn. (2.43) or Eqn. (2.45) or Eqn. (2.47), with the late-time computations for the penny-shaped fracture under the corresponding pressure profiles. The computations come from a commercial FEM software and will be detailed in Chapter 3. Therefore, Axiom 2.3 is numerically verified.

The expression for  $w_{stdy}^p$  under a uniform pressure profile was derived elsewhere [125, 126, 129]. However, all of their final results except the one in [126] were wrong due to errors in the intermediate steps of derivation.

For more complicated pressure profiles, a numerical scheme is needed to compute the integral in Eqn. (2.42). In view of the fact that this integral also gives the purely elastic response of the fracture deformation to a mechanical pressure profile, the following derivation is based on replacing  $\eta p_f(r)$  with a more general profile,  $p_f(r)$ :

$$w(s) = \frac{2(1-\nu)R_0}{\pi G} \int_s^1 \frac{d\xi}{\sqrt{\xi^2-s^2}} \int_0^\xi \frac{vp_f(v)dv}{\sqrt{\xi^2-v^2}} \quad (2.49)$$



For the convenience of numerical calculation, the double-integral in Eqn. (2.49) is divided into single integrals via the following exercise. Consider the following prototype form:

$$I(\theta) = \int_{\theta}^1 \frac{d\xi}{\sqrt{\xi^2 - \theta^2}} \int_0^{\xi} \frac{\eta p_f(\eta) d\eta}{\sqrt{\xi^2 - \eta^2}} \quad (2.50)$$

which can be divided into the sums of the following  $I_1$  and  $I_2$ :

$$\begin{aligned} I_1 &= \int_{\theta}^1 \frac{d\xi}{\sqrt{\xi^2 - \theta^2}} \int_0^{\theta} \frac{\eta p_f(\eta) d\eta}{\sqrt{\xi^2 - \eta^2}} \\ &= \int_0^{\theta} \eta p_f(\eta) d\eta \left[ \int_{\theta}^1 \frac{d\xi}{\sqrt{(\xi^2 - \theta^2)(\xi^2 - \eta^2)}} \right] \\ &= \int_0^{\theta} \eta p_f(\eta) d\eta \left[ \frac{1}{\theta} F(\phi_1, \kappa_1) \right] \end{aligned} \quad (2.51)$$

The integral in the bracket comes after [130], which reads as:

$$\int_a^u \frac{dx}{\sqrt{(x^2 - a^2)(x^2 - b^2)}} = \frac{1}{a} F(\phi, \kappa) \quad (2.52)$$

for  $u > a > b > 0$  and with:

$$\phi = \arcsin \sqrt{\frac{u^2 - a^2}{u^2 - b^2}} ; \quad \kappa = \frac{b}{a} \quad (2.53)$$

Presently,  $u = 1, a = \theta, b = \eta$ ; and,

$$\phi_1 = \arcsin \sqrt{\frac{1 - \theta^2}{1 - \eta^2}} ; \quad \kappa_1 = \frac{\eta}{\theta} \quad (2.54)$$

$F$  is the elliptical integral of the first kind,

$$F(\phi, \kappa) = \int_0^{\phi} \frac{d\alpha}{\sqrt{1 - \kappa^2 \sin^2 \alpha}} = \int_0^{\sin \phi} \frac{dx}{\sqrt{(1 - x^2)(1 - \kappa^2 x^2)}} \quad (2.55)$$

Furthermore,

$$\begin{aligned} I_2 &= \int_{\theta}^1 \frac{d\xi}{\sqrt{\xi^2 - \theta^2}} \int_{\theta}^{\xi} \frac{\eta p_f(\eta) d\eta}{\sqrt{\xi^2 - \eta^2}} \\ &= \int_{\theta}^1 f(1, \eta) \eta p_f(\eta) d\eta - \int_{\theta}^1 f(\xi, \xi) \xi p_f(\xi) d\xi \end{aligned} \quad (2.56)$$

in which  $f$  is defined by:

$$\begin{aligned} f(1, \eta) &= \int_{\eta}^1 \frac{ds}{\sqrt{(s^2 - \theta^2)(s^2 - \eta^2)}} + f(\eta, \eta) \\ &= \frac{1}{\eta} F(\phi_2, \kappa_2) + f(\eta, \eta) \end{aligned} \quad (2.57)$$

which is again from Eqn. (2.52) with  $u = 1, a = \eta, b = \theta$ ; and,

$$\phi_2 = \arcsin \sqrt{\frac{1 - \eta^2}{1 - \theta^2}} ; \quad \kappa_2 = \frac{\theta}{\eta} \quad (2.58)$$

Therefore,

$$I_2 = \int_{\theta}^1 F(\phi_2, \kappa_2) p_f(\eta) d\eta \quad (2.59)$$

The elliptic integral,  $F(\phi, \kappa)$ , has a logarithmic singularity as  $\phi \rightarrow \pi/2$  and  $\kappa \rightarrow 1$ , which is the case when  $\eta \rightarrow \theta$  in the both integrals of  $I_1$  and  $I_2$ . In the numerical calculation, this singularity is singled out by adjusting the  $F$  function to:

$$F(\phi, \kappa) = \bar{F}(\phi, \kappa) - \frac{1}{2} \ln(1 - \kappa) \quad (2.60)$$

$\bar{F}(\phi, \kappa) = F(\phi, \kappa) + \frac{1}{2} \ln(1 - \kappa)$  is regular. The logarithmic singular integral,  $\int_{\theta}^{\theta(1)} f(\eta) \ln(1 - \kappa) p_f(\eta) d\eta$ , is calculated using special Gaussian quadratures [131]. Herein,  $f(\eta)$  represents the remainder in the integrand of  $I_1$  and  $I_2$ .

In the numerical implementation, the pressure profile,  $p_f(\eta)$ , is interpolated by the Chebyshev polynomial of the first kind of order,  $N$ , from its values at the Chebyshev grid points,  $p_{f,n}$ :

$$p_f(v) = \frac{2}{N} \sum_{n=1}^N p_{f,n} \left[ \sum_{k=1}^N T_{k-1}(v_n) T_{k-1}(v) - \frac{1}{2} \right] , \quad -1 \leq v \leq 1 \quad (2.61)$$

in which:

$$v = 2\eta - 1 ; \quad T_k(x) = \cos(k \cos^{-1} x) ; \quad v_n = \cos \left[ \frac{(n - \frac{1}{2}) \pi}{N} \right] \quad (2.62)$$

Substituting Eqn. (2.61) into  $I_1$  and  $I_2$  and carrying out the regular integration part by normal Gaussian quadratures and the logarithmically singular integration part by the special Gaussian quadratures, as discussed above, gives the discretized elastic deformation equation, (2.49), as follows:

$$w_i = \frac{2(1-\nu)R_0}{\pi G} c_{ij}^w p_{f,j} \quad . \quad (2.63)$$

Here, the subscript “ $i, j$ ” refer to the nodal point with the repetitive index implying summation over  $[1, N]$ . Note that the matrix  $c_{ij}^w$  only depends on the Chebyshev polynomial grids. Therefore, once the grid points are fixed at the beginning of the simulation, it remains unchanged even after the fracture propagates. Substituting  $p_j$  in Eqn. (2.63) with  $\eta p_j$  gives the numerical formula to compute the steady-state poroelastic displacement,  $w^p$ ,

$$w_i^p = \frac{2\eta(1-\nu)R_0}{\pi G} c_{ij}^w p_{f,j} \quad . \quad (2.64)$$

In order to check Eqn. (2.63) or Eqn. (2.64), the three pressure profiles, Eqn. (2.44), Eqn. (2.46) and Eqn. (2.48), are computed by Eqn. (2.64) using a Chebyshev order of  $N = 10$ . The computations are compared with the corresponding analytical results, Eqn. (2.43), Eqn. (2.45) and Eqn. (2.47). Figure 2.5 shows a very good agreement between them.

## 2.4.2 Computation of the Pressure Derivative

For simple pressure profiles, analytical expressions can be developed to calculate the fluid leakoff rate along the fracture, or, the pressure derivative, Eqn. (2.41). For example, for the uniform pressure profile, Eqn. (2.44), the pressure derivative is:

$$\left. \frac{\partial p_f(s, z)}{\partial z} \right|_{z=0} = \frac{2p_{f0}}{\pi R_0 \sqrt{1-s^2}} \quad ; \quad (2.65)$$

or for a linear profile, Eqn. (2.46),

$$\left. \frac{\partial p_f(s, z)}{\partial z} \right|_{z=0} = \frac{p_{f0}}{R_0} \left[ \left( \frac{2}{\pi} - 1 \right) \frac{1}{\sqrt{1-s^2}} + \ln \left( \frac{1 + \sqrt{1-s^2}}{s} \right) \right] \quad (2.66)$$

The following is to develop a numerical scheme to compute the leakoff rate for more complicated pressure profiles.

Substituting Eqn. (B.2) into Eqn. (2.41) and eliminating the Bessel function,  $J_0$ , which is often problematic in its numerical integration, gives:

$$\left. \frac{\partial p_f(s, z)}{\partial z} \right|_{z=0} = \frac{2}{\pi R_0} \left[ \frac{1}{\sqrt{1-s^2}} \int_0^1 \frac{y g_1(y) dy}{\sqrt{1-y^2}} - \int_0^1 \frac{y^2 dy}{\sqrt{1-y^2}} \int_s^1 \frac{g_2(yu) du}{\sqrt{u^2-s^2}} \right] \quad (2.67)$$

As done with the elasticity equation, (2.49), the double integral in Eqn. (2.67) can be divided into single integrals via the following manipulations. First, making the change of integration variable,  $v = yu$  transforms this integral to:

$$I = \int_0^1 \frac{y^2 dy}{\sqrt{1-y^2}} \int_{ys}^y \frac{g_2(v) dv}{\sqrt{v^2 - y^2 s^2}} \quad (2.68)$$

Defining:

$$f(y, v) = f(0, v) + \int_0^y \frac{r^2 dr}{\sqrt{(1-r^2)(v^2 - r^2 s^2)}} \quad (2.69)$$

and integrating Eqn. (2.68) by parts gives:

$$I = \int_s^1 f(1, v) g_2(v) dv - \int_0^s f_1(y, y) g_2(y) dy - \int_s^1 f_2(y, y) g_2(y) dy + s \int_0^1 f(y, ys) g_2(ys) dy \quad (2.70)$$

It can be easily shown that a specific form of function,  $f(0, s)$ , in Eqn. (2.69) is irrelevant and is, therefore, taken to be zero. The various functions,  $f(1, s)$ ,  $f_{1(2)}(y, y)$

and  $f(y, ys)$  involve elliptical integrals, which can be found in [130] as:

$$f(1, v) = \frac{1}{vk_1^2} \left[ F\left(\frac{\pi}{2}, k_1\right) - E\left(\frac{\pi}{2}, k_1\right) \right] \quad (2.71)$$

$$f_1(y, y) = \frac{y^3}{s^3 k_{y1}^2} [F(\phi_{y1}, k_{y1}) - E(\phi_{y1}, k_{y1})] \quad (2.72)$$

$$f_2(y, y) = \frac{1}{yk_{y2}^2} [F(\phi_{y2}, k_{y2}) - E(\phi_{y2}, k_{y2})] \quad (2.73)$$

$$f(y, ys) = \frac{y^2}{sk_{ys}^2} [F(\phi_{ys}, k_{ys}) - E(\phi_{ys}, k_{ys})] \quad (2.74)$$

with the various coefficients given by:

$$\begin{aligned} k_1 &= s/v \\ \phi_{y1} &= \sin^{-1} s, \quad k_{y1} = y/s \\ \phi_{y2} &= \sin^{-1} y, \quad k_{y2} = s/y \\ \phi_{ys} &= \sin^{-1} s, \quad k_{ys} = y \end{aligned} \quad (2.75)$$

$F$  has been defined by Eqn. (2.55) and  $E$  is the elliptical integral of the second kind, defined by:

$$E(\phi, k) = \int_0^\phi \sqrt{1 - k^2 \sin^2 \alpha} d\alpha = \int_0^{\sin \phi} \frac{\sqrt{1 - k^2 x^2} dx}{\sqrt{1 - x^2}} \quad (2.76)$$

A similar numerical procedure as used in computing the integrals of Eqn. (2.51) and Eqn. (2.59), can be utilized to compute the integrals in Eqn. (2.70). Some of the differences are elaborated here. As shown in Eqn. (B.3) and Eqn. (B.4),  $g_1$  contains  $p'_f(v)$ , the first derivative of the pressure profile w.r.t. the fracture direction. And  $g_2$  involves up to the 2nd derivative,  $p''_f(v)$ . In one way, the  $p'_f(v)$  or  $p''_f(v)$  can be estimated by computing the derivative,  $\frac{dT_{k-1}(v)}{dv}$  in the Chebyshev polynomial for the original pressure profile, Eqn. (2.61), i.e.

$$p'_f(v) = \frac{2}{N} \sum_{n=1}^N p_n \left\{ \sum_{k=1}^N T_{k-1}(v_n) \left[ \frac{dT_{k-1}(v)}{dv} \right] \right\}, \quad -1 \leq v \leq 1 \quad (2.77)$$

or,

$$p_f''(v) = \frac{2}{N} \sum_{n=1}^N p_n \left\{ \sum_{k=1}^N T_{k-1}(v_n) \left[ \frac{d^2 T_{k-1}(v)}{dv^2} \right] \right\} \quad , \quad -1 \leq v \leq 1 \quad .(2.78)$$

On the other way,  $p_f'(v)$  and  $p_f''(v)$  can be interpolated by the Chebyshev polynomial based on their corresponding values at the grid points,  $p_f'(v_n)$  and  $p_f''(v_n)$  ( $n = 1, 2, \dots, N$ ). Experience has shown that the former approach greatly exaggerates the sinusoidal oscillation intrinsic to the Chebyshev function and is, therefore, very inaccurate. The latter approach gives smooth variation and much better accuracy as compared to the analytical results, and is thus employed for this study. In computing the derivatives, the following F.D. discretization is used:

$$\left. \frac{dp_f}{dv} \right|_{v=v_i} = \frac{p_{f,i+1} - p_{f,i-1}}{v_{i+1} - v_{i-1}} \quad (2.79)$$

$$\left. \frac{d^2 p_f}{dv^2} \right|_{v=v_i} = \frac{2 [p_{f,i+1}(v_i - v_{i-1}) + p_{f,i-1}(v_{i+1} - v_i) - p_{f,i}(v_{i+1} - v_{i-1})]}{(v_{i+1} - v_{i-1})(v_{i+1} - v_i)(v_i - v_{i-1})} \quad (2.80)$$

for  $i = 2, 3, \dots, N - 1$ ; or,

$$\left. \frac{dp_f}{dv} \right|_{v=v_1} = \frac{p_{f,2} - p_{f,1}}{v_1 + v_2} \quad (2.81)$$

$$\left. \frac{d^2 p_f}{dv^2} \right|_{v=v_1} = \frac{2(p_{f,2} - p_{f,1})}{v_2^2 - v_1^2} \quad (2.82)$$

at the first grid point,  $i = 1$ ; and,

$$\left. \frac{dp_f}{dv} \right|_{v=v_N} = \frac{(p_{f,N} - p_{f,N-2})(v_N - v_{N-1})(v_N + v_{N-1} - 2)}{(v_N - v_{N-1})(v_N - v_{N-2})(v_{N-1} - v_{N-2})} - \frac{(p_{f,N} - p_{f,N-1})(v_N - v_{N-2})(v_N + v_{N-2} - 2)}{(v_N - v_{N-1})(v_N - v_{N-2})(v_{N-1} - v_{N-2})} \quad (2.83)$$

$$\left. \frac{d^2 p_f}{dv^2} \right|_{v=v_N} = \frac{(p_{f,N} - p_{f,N-1})(v_N - v_{N-2}) - (p_{f,N} - p_{f,N-2})(v_N - v_{N-1})}{(v_N - v_{N-1})(v_N - v_{N-2})(v_{N-1} - v_{N-2})} \quad (2.84)$$

at the end point,  $i = N$ . In computing the derivatives at the first grid point,  $i = 1$ , the symmetric property of the pressure profile w.r.t. the symmetric axis,  $z = 0$ , is used so that  $p'_f(v) = 0$  at  $v = 0$ . At the end point,  $i = N$ , the pressure profile is locally fitted to a parabolic curve based on the immediately adjacent three nodal values,  $p_{f,N}$ ,  $p_{f,N-1}$  and  $p_{f,N-2}$ .

Carrying out the foregoing numerical procedures finally gives a discretized relationship between the pressure and the pressure derivative as:

$$\left. \frac{\partial p_f(s, z)}{\partial z} \right|_{z=0} = c_{ij}^u p_{f,j} \quad (2.85)$$

with  $i, j = 1, \dots, N$ . Comparison of the computations based on Eqn. (2.85) with other solutions for the example pressure profiles, Eqn. (2.44) and Eqn. (2.48), are shown in Figure 2.6. Good agreement has been reached. For the uniform profile, Eqn. (2.44), the other solution is analytically obtained as in Eqn. (2.65). For the elliptic-like profile, Eqn. (2.48), however, an analytical solution is not possible and shown in Figure 2.6 are the ABAQUS's computations as to be detailed in the subsequent chapter. The linear pressure profile, Eqn. (2.46), which does have the analytical expression for the pressure derivative, Eqn. (2.66), however, does not satisfy  $p'_f(v) = 0$  at  $v = 0$ . Therefore, this profile is not computed by Eqn. (2.85).

## 2.5 Summary

In its first innovative contribution, this chapter has shown, based on the penny-shaped fracture geometry, that the steady-state poroelastic deformation along the fracture under mode 2 loading (pure fluid flow condition) is simply equivalent to the purely elastic deformation of the same fracture loaded by a fluid pressure of  $\eta p(r)$  on the fracture surface, i.e. Eqn. (2.42). This conclusion has

been analytically proven and numerically verified by comparing the analytical predictions with the computations from a commercial FEM software.

The practical significance of Eqn. (2.42) lies in that it characterizes the late-time asymptotic poroelastic response using the relatively simple elastic formula. To the author's knowledge, there has been no similar assertion proven in the literature for the general pressure profile. For the simple uniform pressure profile, Eqn. (2.42) has been implicitly used without proof on several occasions [81, 126]. For the same simple pressure profile, however, the steady state poroelastic, or equivalently the thermoelastic, solution about the fracture deformation was given mistakenly in some other published works [125, 129].

Secondly, the procedure outlined in this chapter to convert a double integral into single ones provides an efficient and accurate numerical means to compute the double integrals. Based on the conversion, two numerical algorithms have been developed to compute the elastic deformation of the fracture (or the steady-state poroelastic deformation) and the steady-state leakoff rate along the fracture. The logarithmic singularity involved therein is adjusted to a regular integral, which can be computed by the normal Gaussian quadratures, plus a purely logarithmic part, which is numerically calculated by the special Gaussian quadratures. Using a Chebyshev polynomial to interpolate the pressure variation along the fracture, the resultant matrices that relate the pressure profile to the deformations or leakoff rate do not depend on the propagation of the fracture. Therefore, once the Chebyshev grid is set at the beginning, the matrix equation does not need to be re-computed as the fracture propagates. In so doing, a considerable computational effort is saved.

The 1-D transient poroelastic model is also analyzed. The 1-D model represents the early-time asymptotic behavior of a full poroelastic response. The



various mathematical formulae arrived at herein serve different purposes in the subsequent chapter and further development in McFrac. Particularly, it assures that the same equation, 2.28, holds for the pressure-independent Carter's leakoff model, which has not been explicitly pointed out in the literature.

Table 2.1: Poroelastic material properties of some typical rocks.

material	$E$ (GPa)	$\nu$	$k$ (md)	$\phi$	$\alpha$	$B$	Var1
Ruhr sandstone	29	0.12	0.2	0.02	0.65	0.88	0.56
Tennessee marble	20	0.25	$1 \times 10^{-4}$	0.02	0.19	0.51	0.30
charcoal granite	28	0.27	$1 \times 10^{-4}$	0.02	0.27	0.55	0.34
Berea sandstone	14	0.20	190	0.19	0.79	0.62	0.41
Westerly granite	38	0.25	$4 \times 10^{-4}$	0.01	0.47	0.85	0.57
Weber sandstone	28	0.15	1	0.06	0.64	0.73	0.44
Ohio sandstone	16	0.18	5.6	0.19	0.74	0.50	0.30
Pecos sandstone	14	0.16	0.8	0.20	0.83	0.61	0.39
Boise sandstone	-	-	200	0.26	0.85	0.50	
coarse sand	0.25	0.30	3,600	0.48	0.98	0.73	0.62

Note:  $\text{Var1} = B(1 + \nu_u)/3(1 - \nu_u)$ . Data compiled from [120].

Table 2.2: Poroelastic material properties used for the computations.

$E$ (GPa)	$\nu$	$k$ (md)	$\mu$ (cp)	$\phi$	$\alpha$	$B$
10	0.25	35	1	0.20	0.798	0.687

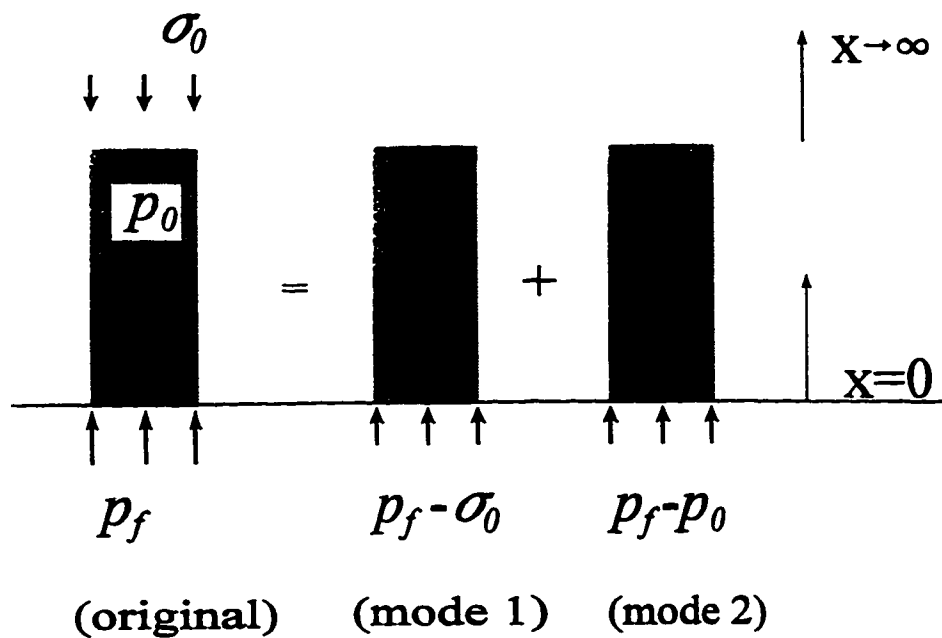


Figure 2.1: 1-D poroelastic model and its loading mode decomposition.

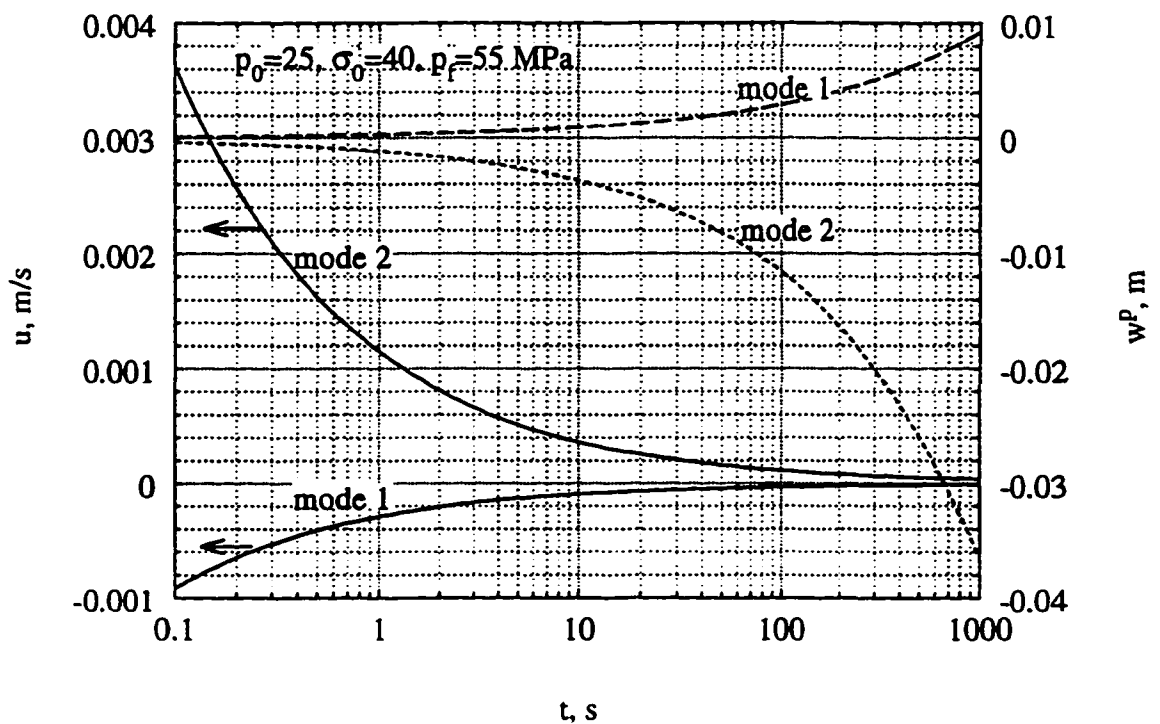


Figure 2.2: Comparison of the leakoff rate,  $u$ , and the poroelastic displacement,  $w^p$ , under mode 1 and mode 2 loading.

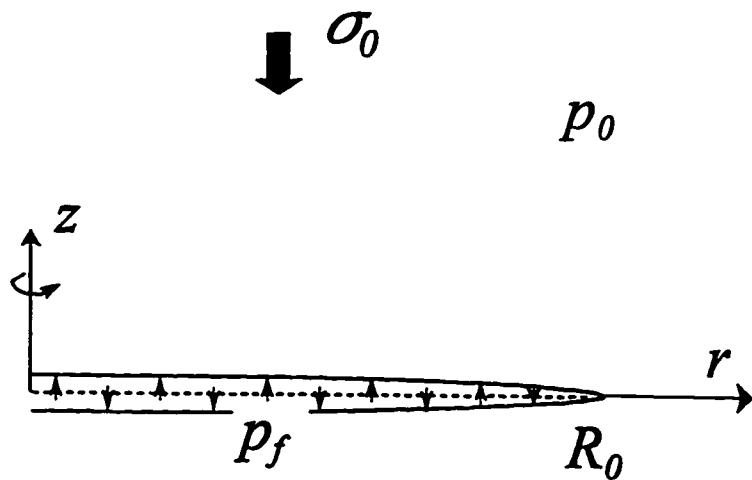


Figure 2.3: Penny-shape pressurized fracture model.

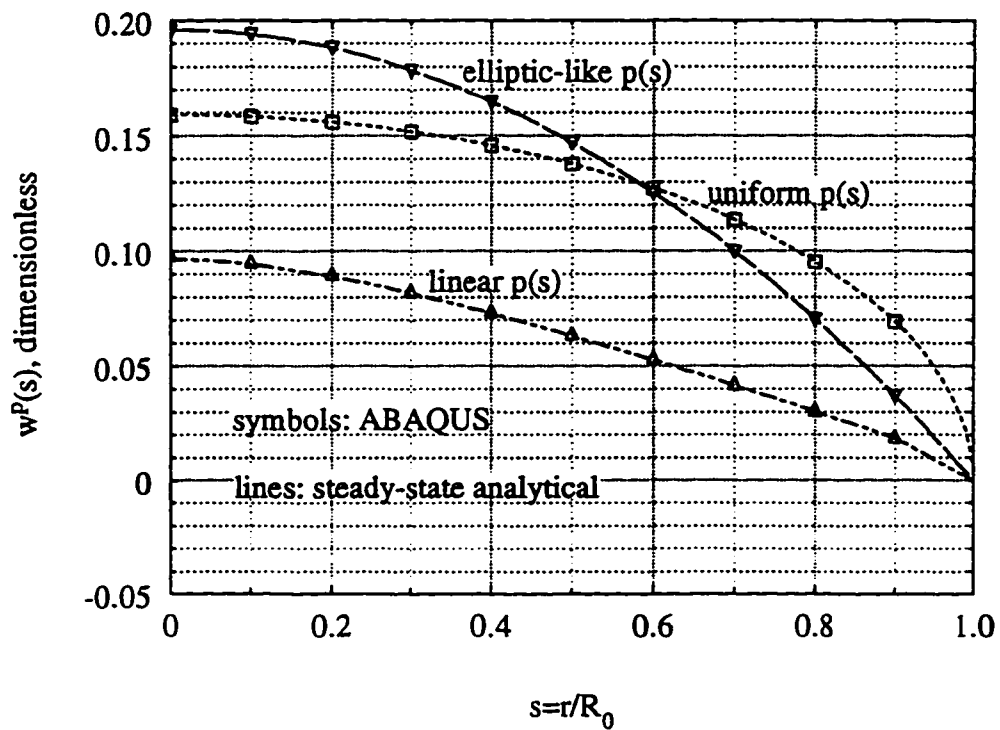


Figure 2.4: ABAQUS's computations vs. analytical predictions at the steady state. See Chapter 3 for the non-dimensionalization details.

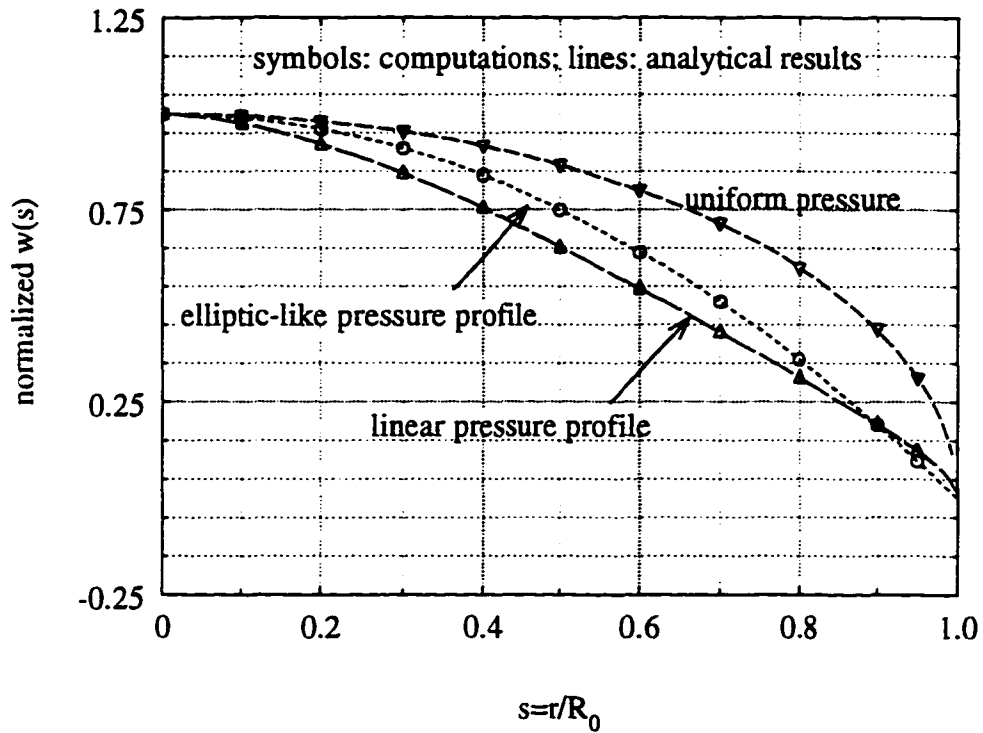


Figure 2.5: Comparison of the computed elastic fracture deformation with the corresponding analytical results.

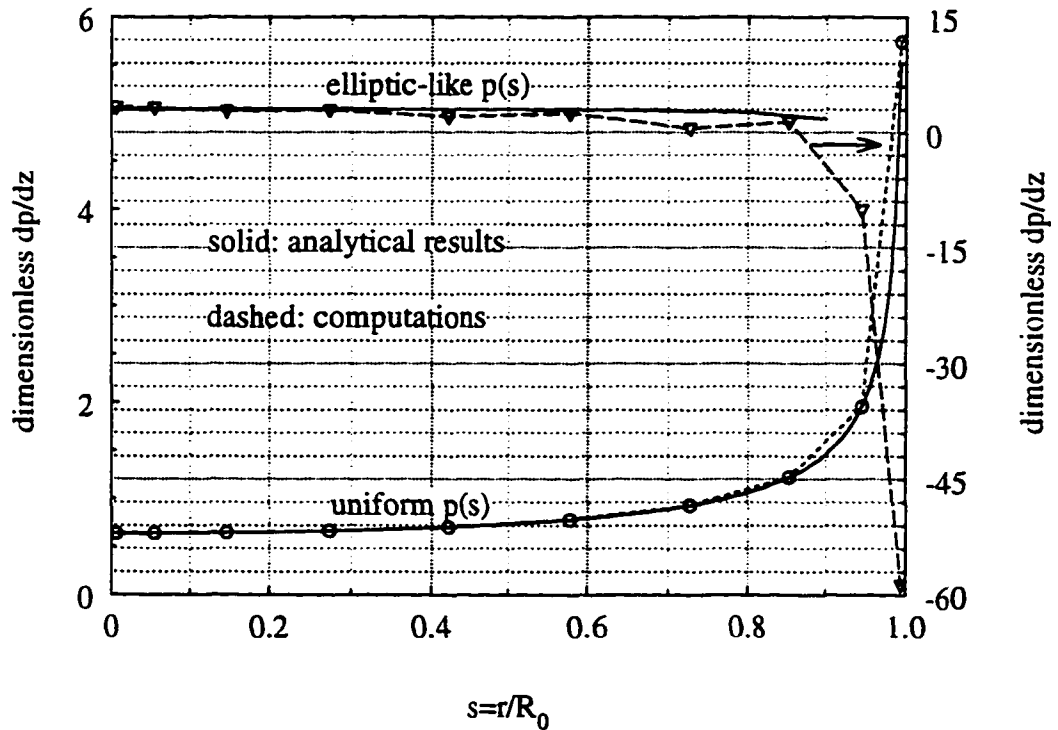


Figure 2.6: Comparison of the computed pressure derivative with the corresponding analytical or other numerical results.

## Chapter 3

# A Simplified 2-D Poroelastic Model

In the previous chapter, it was concluded that the full poroelastic response of a hydraulically-driven fracture is bounded by the 1-D poroelastic model at the early times and by the steady-state solution at the late times. Analytical expressions or numerical formulae have been derived to compute their values. This chapter is dedicated to the investigation of this transient region between these two asymptotic regimes for a penny-shaped fracture configuration. Ways are sought to simplify the transient poroelastic response so that there is no need to compute the complicated temporal and spatial integrations that is used by general HF simulators and discussed in Chapter 1. Only with this simplification can the goal of developing a fast HF simulator be realized.

Because of the strong flow-deformation coupling, very few problems of practical significance have explicit analytical solutions in the full poroelastic domain. The analytical means include the various decomposition techniques, i.e. (1) to decompose the general loading condition into mode 1 and 2 as exemplified in [100], or (2) to decompose the general coupled field equations into uncoupled ones each of which governs a particular sub-function, e.g. McNamee and Gib-

son's displacement functions (1960) [132], or Biot's decomposition functions (1956) [133, 134]. In order to make these analytical methods work, further conditions have to be met in regards to the problem geometry and/or initial and boundary conditions. The summary by Detounary and Cheng (1993) [89] provides an excellent coverage on this subject.

General solutions to poroelastic problems rely on various numerical techniques. Finite element (FEM) [135, 136, 137, 78, 138], boundary element (BEM) [139, 140] and even finite difference (FD) [141] methods have been used. Particular to the current task of analyzing the poroelastic response of a pressurized fracture, a commercial FEM software, ABAQUS, was used. Derivation of the equivalence of the ABAQUS's formulations with the poroelasticity theory and validation of its sensitivity to the mesh size and time step increment has been documented by Yuan and Abousleiman (1993) [142].

The computed model is axi-symmetrical (in  $r, z$  coordinates), containing a pressurized fracture of radius,  $R_0$ , lying in a plane  $z = 0$  (Figure 2.3). The model is embedded in an *in-situ* pore pressure field,  $p_0$ , and is subject to a *in-situ* stress,  $\sigma_0$ , perpendicular to the fracture. The fracture surface is loaded with a fluid pressure,  $p_f(r)$ , which serves as both mechanical and hydraulic boundary conditions. The loading condition is again decomposed into mode 1 and 2. Although the 1-D poroelastic analysis carried out in the previous chapter has already concluded that the mode 1-induced poroelastic effect is negligibly small and thus can be ignored, the mode 1 loading is retained here. It helps offer further support to the previous assertion. The relevant material properties are listed in Table 2.2.

The model boundary is set sufficiently far away from the fracture to represent the infinite geometry (Figure 3.1). Fluid should not diffuse to the boundary

during the solution time. The outside boundaries are, thus, set impermeable and pinned in deformation with zero displacements. Due to the symmetry, only one quarter of the model is computed.

In the following, the governing equations for a stationary penny-shaped hydraulic fracture are first reviewed and non-dimensionalized. The computations are then analyzed in the second section in terms of the poroelastic displacements and leakoff rate along the fracture. In the third section, a simplified 2-D poroelastic model is developed and compared with the computations for two example pressure profiles. The fourth section extends the mathematical analysis from a stationary fracture to a propagating one. A Duhamel's theorem-like extension principle is derived.

### 3.1 Non-dimensionalization of the Governing Equations

In order to reveal the controlling parameters, the mathematical problem is non-dimensionalized. Particular to the axisymmetric configuration, the general governing equations can be reduced to:

$$G\nabla^2 u_r + \frac{G}{1-2\nu} \frac{\partial \varepsilon}{\partial r} - \frac{u_r}{r^2} - \alpha \left( \frac{\partial p}{\partial r} \right) = 0 \quad (3.1)$$

$$G\nabla^2 u_z + \frac{G}{1-2\nu} \frac{\partial \varepsilon}{\partial z} - \alpha \left( \frac{\partial p}{\partial z} \right) = 0 \quad (3.2)$$

$$\frac{\partial p}{\partial t} - \alpha M \frac{\partial \varepsilon}{\partial t} - \kappa M \nabla^2 p = 0 \quad (3.3)$$

with the Laplace operator and the volumetric strain given by:

$$\nabla^2 = \frac{1}{r} \frac{\partial}{\partial r} \left( r \frac{\partial}{\partial r} \right) + \frac{\partial^2}{\partial z^2} \quad (3.4)$$

$$\varepsilon = \frac{\partial u_r}{\partial r} + \frac{u_r}{r} + \frac{\partial u_z}{\partial z} \quad (3.5)$$



The initial and far-field boundary conditions are taken to be homogeneous. i.e. zero. The remaining boundary condition takes place along the fracture as follows:

$$\begin{cases} \sigma_{zz}(r, t) = p_{f0}H(t) - \sigma_0 \\ p(r, t) = 0 \end{cases} \quad r \in [0, R_0], t > 0 \quad (3.6)$$

for mode 1 loading; and,

$$\begin{cases} \sigma_{zz}(r, t) = 0 \\ p(r, t) = p_{f0}H(t) - p_0 \end{cases} \quad r \in [0, R_0], t > 0 \quad (3.7)$$

for mode 2 loading. In the above,  $H(t)$  denotes the Heaviside function. Without loss of generality, the pressure profile is assumed to be uniform and constant. More complicated pressure distributions can be easily substituted and in fact, have been computed as shown below.

Substituting the following dimensionless variables:

$$s(, h) = \frac{r(, z)}{R_0} \quad (3.8)$$

$$\sigma'_{ij}(, p') = \frac{\sigma_{ij}(, p)}{p_{f0} - p_0} \quad (3.9)$$

$$u_s(, u_h) = \frac{u_r(, u_z)}{u_c}; \quad u_c = \frac{\alpha(p_{f0} - p_0)R_0}{G} \quad (3.10)$$

$$t' = \frac{t}{t_c}; \quad t_c = \frac{R_0^2}{\kappa M} \quad (3.11)$$

into Eqn. (3.1) to Eqn. (3.3) and carrying out the algebraic manipulations gives the following dimensionless governing equations:

$$\nabla^2 u_s + \frac{1}{1 - 2\nu} \frac{\partial \varepsilon}{\partial s} - \frac{u_s}{s^2} - \frac{\partial p}{\partial s} = 0 \quad (3.12)$$

$$\nabla^2 u_h + \frac{1}{1 - 2\nu} \frac{\partial \varepsilon}{\partial h} - \frac{\partial p}{\partial h} = 0 \quad (3.13)$$

$$\frac{\partial p}{\partial t} - \frac{\alpha^2 M}{G} \frac{\partial \varepsilon}{\partial t} - \nabla^2 p = 0 \quad (3.14)$$

with the prime denoting the dimensionless sense being dropped; and,

$$\nabla^2 = \frac{1}{s} \frac{\partial}{\partial s} \left( s \frac{\partial}{\partial s} \right) + \frac{\partial^2}{\partial h^2} \quad (3.15)$$

$$\varepsilon = \frac{\partial u_s}{\partial s} + \frac{u_s}{s} + \frac{\partial u_h}{\partial h} \quad (3.16)$$

which is subject to the following boundary condition:

$$\begin{cases} \sigma_{hh}(s, t) = H(t) \\ p(s, t) = 0 \end{cases} \quad s \in [0, 1], t > 0 \quad (3.17)$$

for mode 1 loading; and,

$$\begin{cases} \sigma_{hh}(s, t) = 0 \\ p(s, t) = H(t) \end{cases} \quad s \in [0, 1], t > 0 \quad (3.18)$$

for mode 2.

The physical variables,  $\kappa M$  and  $\alpha^2 M/G$ , are functions of the drained and undrained Poisson's ratios:

$$\kappa M = \left[ \frac{(1-2\nu)(1-\nu_u)}{(1-2\nu_u)(1-\nu)} \right] c \quad (3.19)$$

$$\frac{\alpha^2 M}{G} = \frac{2(\nu_u - \nu)}{(1-2\nu_u)(1-2\nu)} \quad (3.20)$$

Therefore, the solution to the current problem in the dimensionless domain is solely controlled by  $\nu$  and  $\nu_u$ . In addition, the non-dimensionless formulae, Eqn. (3.8) to Eqn. (3.11) are particular for mode 2 loading only. In computing the mode 1, the  $(p_{f0} - p_0)$  term should be replaced with  $(p_{f0} - \sigma_0)$ .

The pressure distribution along the fracture also influences the computations. In this chapter, two example profiles have been computed, i.e. the uniform profile, Eqn. (2.44), and the elliptical-like profile, Eqn. (2.48) (Figure 3.2). As will be shown in Chapters 4 and 5, the former corresponds to the case of very large fracture toughness and the latter is more like the cases when the fracture toughness is small.

## 3.2 Computed Poroelastic Response

The computational results are analyzed for the profiles of leakoff rate,  $u(s, t)$  and poroelastic displacement,  $w^p(s, t)$ , perpendicular to the fracture on the fracture surface. The following major observations can be reached:

- (a) The 2-D computations again support the previous conclusion that mode 2 loading dominates both the leakoff rate and poroelastic effect. This dominance stems from the large difference in  $p_0$  and  $\sigma_0$  as observed in practice. In the non-dimensionalized domain, the mode 1 effect is smaller than but still comparable to the mode 2 effect (Figure 3.3). In the dimensional sense, i.e. when the practical values of  $p_0$  and  $\sigma_0$  are taken into account, the mode 1 effect is indeed much smaller than the mode 2 effect (Figure 3.4). This agrees with the earlier 1-D prediction and other researcher's conclusion, e.g. [80, 60]. Therefore, the mode 1-induced poroelastic effect is ignored throughout the sequel of this dissertation. Its induced mechanical behavior is described by the drained elastic deformation theory. The loading data used in Figure 3.4 are as follows:  $p_0 = 25$  MPa and  $\sigma_0 = 40$  MPa as from [123]; and  $p_{f0}$  is set at 55 MPa.

- (b) The 1-D transient and 2-D steady-state poroelastic models, as discussed in the previous chapter, are clearly shown in the computations as the asymptotic behavior during the early and late times, respectively.

Take the uniform pressure profile for example. Figure 3.5 shows the evolution of the poroelastic displacement,  $w^p(s, t)$ , at several typical locations along the fracture. Also displayed there are the asymptotic 1-D poroelastic response, Eqn. (2.32), and the steady-state solution, Eqn. (2.43). Clearly, the computations at late times and the analytical results

at the steady state coincide. Similar observations can be reached for the leakoff rate,  $u(s, t)$ , based on Figure 3.6 which displays the evolution of  $u(s, t)$  for the same uniform pressure profile.

As shown in Figure 3.7, large disagreement is visible between the analytical predictions and the numerical computations during the early-time period, particularly in the leakoff rate. This inaccuracy is associated with ABAQUS in computing the early-time poroelastic response or the pressure derivative. The analytical models should not share the blame.

Any numerical means, including the current ABAQUS, are not adequate to yield accurate results for the early-time poroelastic response due to the skin effect caused by the Heaviside temporal function in the boundary condition [143]. Moreover, calculations of the leakoff rate involve pressure derivatives which are computed by numerically differentiating the computed nodal pressure values along the  $z$ -direction. Computational error is inevitable in this transformation process <sup>1</sup>.

- (c) The transient response in the poroelastic displacement,  $w^p(s, t)$ , between the two asymptotic time regimes takes the typical diffusion form: increasing rapidly at the beginning from the 1-D response, then gradually slowing down and approaching the steady-state solution (Figure 3.8). At the dimensionless time of  $t = 1$ ,  $w^p$  has taken over 80% of the full response, i.e. the steady-state value (Figure 3.5).

The leakoff rate decreases exponentially (linearly in the log-log plot with a slope of -0.5) nearly till  $t = 1$  and then, turns to the constant value associated with the steady state (Figure 3.6). The early-time values are

---

<sup>1</sup>A good analogy to this point is to compare the stress and displacement computations. It is widely observed and accepted that in the displacement-based FEM computations, the accuracy for stresses at nodal points, which involves displacement derivatives, is not as good as for the displacement.

orders larger than the late-time ones, such as the steady-state constant.

### 3.3 A Simplified 2-D Poroelastic Model

Between the two asymptotic time regions, there is no explicit analytical expression to cover the transient poroelastic response. Several avenues exist in singular perturbation theories to build up composite mathematical expressions to bridge the outer and inner expansions [144, 145]. In this section, the cubic spline interpolation scheme is used to create an approximate analytical formula covering the interim for the poroelastic displacement. The interim leakoff rate is based on a simple superimposition principle. The reason for using the cubic spline scheme is that the first derivatives at both ends of the transition period are known. The same interpolation scheme could be applied to the leakoff rate. However, it has been found that doing so does not significantly enhance the accuracy, but considerably complicates the numerical calculation.

#### 3.3.1 Cubic Spline Interpolation for $w^p$

The cubic spline interpolation principle is detailed, e.g. by Press et. al. (1990) [146], whose derivation is applied herein. Given the end points,  $t_{i(o)}$ , the end-point values,  $y_{i(o)}$  and the first derivative values,  $y'_i, y'_o$ , we set off to find the coefficients for the cubic polynomial resulting from the interpolation:

$$y = y_0 + y_1x + y_2x^2 + y_3x^3 \quad (3.21)$$

in which,  $x = \log(t)$  and  $y = w^p$  since it is found that the best fit can be realized in the semi-logarithmic plot. Based on the steady state property,  $y'_o = 0$ .

After lengthy algebraic exercises, the coefficients in Eqn. (3.21) have been found in the following form:

$$y_0 = \frac{x_o y_i}{\Delta x} - \frac{x_i y_o}{\Delta x} + \frac{C_c}{6\Delta x} [x_i x_o (2x_o - x_i)] + \frac{C_d}{6\Delta x} [x_i x_o (x_o - 2x_i)] \quad (3.22)$$

$$y_1 = \frac{y_o}{\Delta x} - \frac{y_i}{\Delta x} - \frac{C_c}{6\Delta x} (2x_o^2 + 2x_i x_o - x_i^2) + \frac{C_d}{6\Delta x} (2x_i^2 + 2x_i x_o - x_o^2) \quad (3.23)$$

$$y_2 = \frac{C_c x_o}{2\Delta x} - \frac{C_d x_i}{2\Delta x} \quad (3.24)$$

$$y_3 = \frac{C_d}{6\Delta x} - \frac{C_c}{6\Delta x} \quad (3.25)$$

where,

$$\Delta x = \log \left( \frac{t_o}{t_i} \right) \quad (3.26)$$

$$C_c = \frac{6(y_o - y_i)}{(\Delta x)^2} - \frac{4y'_i}{\Delta x} \quad (3.27)$$

$$C_d = \frac{2y'_i}{\Delta x} - \frac{6(y_o - y_i)}{(\Delta x)^2} \quad (3.28)$$

with,

$$y_i = \left[ \frac{2\eta R_o p_f}{G} \sqrt{\frac{(1-2\nu_u)(1-\nu)}{\pi(1-2\nu)(1-\nu_u)}} \right] \sqrt{t_i} \quad (3.29)$$

$$y'_i = \left[ \frac{\eta R_o p_f}{G} \sqrt{\frac{(1-2\nu_u)(1-\nu)}{\pi(1-2\nu)(1-\nu_u)}} \right] \sqrt{t_i} \ln 10 \quad (3.30)$$

and  $y_o$  from Eqn. (2.64). Eqn. (3.29) is from Eqn. (2.32) with  $t_i$  as the dimensionless time.

In general, it is reasonable to truncate the transient poroelastic response before  $t_i = 0.001$  for the 1-D poroelastic model and after  $t_o = 10$  for the steady state solution. With  $t_i = 10^{-3}$  and  $t_o = 10$  being dictated so, the best fit can be achieved for the computed example pressure profiles. The various coefficients in Eqn. (3.22) to Eqn. (3.25) are thus reduced to:

$$y_0 = \frac{1}{8} (2 y_i + 6 y_o - 5 C_c - 7 C_d) \quad (3.31)$$

$$y_1 = \frac{1}{24} (6 y_o - 6 y_i + 13 C_c + 11 C_d) \quad (3.32)$$

$$y_2 = \frac{1}{8}(C_c + 3C_d) \quad (3.33)$$

$$y_3 = \frac{C_d - C_c}{24} \quad (3.34)$$

with,

$$C_c = \frac{3}{8}(y_o - y_i) - y'_i \quad (3.35)$$

$$C_d = \frac{1}{8}[4y'_i - 3(y_o - y_i)] \quad (3.36)$$

The transient poroelastic response thus developed by Eqn. (3.21) is denoted by  $f_w$ . Therefore, a complete description of the simplified 2-D poroelastic model can be formulated as follows:

$$w_{mfd}^p(s, t) = \begin{cases} w_{1D}^p(s, t) & t \leq 10^{-3} \\ f_w(s, t) & 10^{-3} < t < 10 \\ w_{stdy}^p(s, t) & t \geq 10 \end{cases} \quad (3.37)$$

with  $w_{1D}^p$  and  $w_{stdy}^p$  being given by Eqn. (2.32) or Eqn. (2.64), respectively.

### 3.3.2 Simple Superimposition for $u$

Overall, simply adding the steady-state leakoff value to the 1-D leakoff formula, Eqn. (2.30), fits the transient response reasonably well for the leakoff rate. This simple scheme works because the 1-D leakoff prevails for a relatively long time, e.g. until  $t = 1$  in the case of uniform pressure profile (Figures 3.6). Moreover, the magnitude of the leakoff rate decreases exponentially and its early time values, which are more akin to the 1-D model, are several orders larger than the late-time values. The simplified 2-D leakoff model formulated this way has the following form:

$$u_{mfd}(r, t) = \frac{\kappa}{\sqrt{\pi c}} \frac{p_{f0}(r, t) - p_0}{\sqrt{t}} + u_{stdy}(r, t) \quad (3.38)$$

in which,  $u_{stdy} = -\kappa \frac{\partial p}{\partial z}$  with the pressure derivative given by Eqn. (2.85) for the general pressure profile or analytically by Eqn. (2.65) for the simple

uniform pressure profile. Eqn. (3.38) is written in dimensional form but assuming the pressure profile to be constant in time. For the time-varying pressures, Duhamel's principle can be used as to be discussed below.

### **3.3.3 Comparison of the Simplified 2-D Poroelastic Model with the True 2-D Computations**

Figures 3.9-3.14 extensively document the comparison for the two computed sample pressure profiles together with the distribution of the relative errors. Some major observations can be made:

- (a) In general, the simplified model catches the transient nature of the poroelastic response very well. Particular for the displacements,  $w^p$ , the relative error is below 10% in the significant part of  $w^p$  where  $t > 10^{-2}$  and  $w^p$  attains a large magnitude (Figure 3.13).
- (b) A relatively larger error of 10-20% occurs at early times:  $t < 10^{-2}$  (Figure 3.13) where the  $w^p$  is small as compared to its full, steady-state value. Therefore, this error is acceptable and not expected to affect the whole deformation system very much.
- (c) Moreover, as much as 70% relative error is registered at  $s = 0.9$  under the elliptic-like pressure profile in the analytical 1-D region, i.e.  $t < 10^{-3}$  (Figure 3.13). This is caused by the steep pressure gradient near the fracture tip in this particular example. The pressure gradient in the fracture direction at the tip is negatively infinite, as described by Eqn. (2.48) and shown in Figure 3.2. In this case, the 1-D poroelastic response assumption may have already lost its validity near  $t = 10^{-3}$ . In addition, the ABAQUS inaccuracy in computing the early-time response, as discussed earlier, may become even worse near this rapidly-changing



pressure region.

- (d) The agreement for the leakoff rate is generally in the range of 30-40 % (Figure 3.14), i.e. not as good as for the poroelastic displacement. Two factors are likely causer. One is the computational inaccuracy in ABAQUS's computing the early-time response or the pressure derivative as discussed earlier. The other factor is the simple superimposition interpolation scheme, which is responsible for the large errors during the transition period from the exponential decrease to the steady-state constant. Again, this inaccuracy, however, should not affect the whole system very much because the leakoff rate during this period is orders smaller than its early time values.

### **3.4 Extension of the Simplified 2-D Model to a Propagating Fracture**

The simplified 2-D poroelastic model Eqn. (3.37) or Eqn. (3.38) is based on a stationary fracture of a constant radius,  $R_0$ . When applied to the simulation of a propagating fracture, a primary issue to be dealt with is the changing fracture radius,  $R$ . There is no ready mathematical theory to extend the stationary case to that of propagation. In the following, a Duhamel's theorem-like extension principle is derived based on physical arguments.

#### **3.4.1 Derivation of the Extension Principle**

Before going into the details, let us examine the parametric dependence of the simplified poroelastic model, such as Eqn. (3.37) or Eqn. (3.38). Firstly, transforming the dimensionless form of the equations into the dimensional one

gives:

$$w_{mfd}^p(r, t) = \begin{cases} \frac{2\eta}{\pi G} \sqrt{\frac{c}{\pi \kappa M}} [p_f(r) R_0 \sqrt{t'}] & t' \leq 10^{-3} \\ f_w(r, t') & 10^{-3} < t' < 10 \\ \frac{2(1-\nu)\eta}{\pi G} (R_0 c_{ij}^w p_{f,j}) & t' > 10 \end{cases} \quad (3.39)$$

in which,  $p_f$  should be viewed as relative to the reservoir pressure,  $p_0$ .  $p_f$  is assumed to be constant in time although it may vary along the fracture.  $t'$  is the dimensionless time. Obviously,  $w^p(r, t)$  depends on the fracture radius,  $R_0$ , and the pressure distribution,  $p_f(s)$  (we use  $s$  here to cover all along the fracture and to differentiate from  $r$  where we seek the  $w^p$  solution.). The  $p_f(s)$  influence on  $w^p$  is linear. Explicitly, we use  $p(s)w^p(r, t; R_0)$  to denote this parametric dependence.

Now, consider a simple fictitious fracture propagation history (Figure 3.15): the fracture has a radius,  $R_0$ , over  $t \in [t_0, t_1]$ . At  $t = t_1$ , the fracture suddenly extends to a new radius,  $R_1$  and thereafter, remains stationary at  $R_1$ . To simplify the description, the pressure profile along the fracture is assumed to be uniform and constant at  $p_{f0}$  even after the fracture propagation. We need to compute the poroelastic response, say  $w^p$ , at location,  $r$ , on the fracture and at the current time,  $t$ .

For the convenience of the mathematical analysis, the same problem is depicted a little differently (Figure 3.16). Instead let  $R = R_0$  during  $t \in [t_0, t_1]$ ; let us attach an additional fracture segment to  $R_0$  so that the total fracture radius during  $[t_0, t_1]$  has the same radius,  $R_1$  as during  $t \in [t_1, t]$ . The boundary condition for both deformation and flow over this additional segment during  $[t_0, t_1]$  is maintained so that it is just like in the continuum. i.e.

$$u_z(r, t) = 0, \quad \sigma_{rz}(r, t) = 0, \quad q_z(r, t) = 0; \quad r \in [R_0, R_1], \quad z = 0, \quad t \in [t_0, t_1] \quad (3.40)$$

Therefore, the mathematical solution to this modified problem with a fracture radius,  $R_1$  is the same as the one with a radius,  $R_0$ .

As a result of the boundary condition, Eqn. (3.40), the fluid pressure over the fracture segment,  $[R_0, R_1]$ , during  $t \in [t_0, t_1]$ , is unknown and changes both temporally and spatially. In any case, let us denote it as  $p_{R_0 R_1}(r, t)$ . With this, the boundary condition to this segment can be re-expressed in terms of this pressure function, i.e.

$$p_f(r, t) = p_{R_0 R_1}(r, t) : \quad r \in [R_0, R_1] , \quad z = 0 , \quad t \in [t_0, t_1] \quad . \quad (3.41)$$

During the fracture propagation, the fluid pressure condition along the fracture has experienced the following change:

$$\Delta p_f(r, t = t_1) = \begin{cases} 0 & r \in [0, R_0] \\ p_{f_0} - p_{R_0 R_1}(r, t_1) & r \in [R_0, R_1] \end{cases} \quad (3.42)$$

With the modification, the fracture has an identical fracture radius,  $R_1$ , over the whole time domain:  $[t_0, t]$ . Therefore, the conventional Duhamel's principle is applicable, i.e. the  $w^p$  solution at  $r, t$  can be given by:

$$w^p(r, t) = p_{f_0} w^p(r, t - t_0; R_0) + \Delta p_f(r, t_1) w^p(r, t - t_1; R_1) \quad (3.43)$$

So far, no other assumption has been made except the linearity of the problem which is guaranteed by the theory of poroelasticity. The fracture propagation, however, introduces an intermediate unknown,  $p_{R_0 R_1}(r, t_1)$ , into Eqn. (3.42), which needs to be solved from the pressure solution based on the boundary condition, Eqn. (3.40). Physically, the pressure over  $r \in [R_0, R_1]$ , follows the diffusion process (Figure 3.16): at  $t = t_0$  instantly upon the fracture of  $R_0$  in radius being created, the pressure over there is equal to the formation pore pressure,  $p_0$ . As the fluid diffuses (assume  $p_{f_0} > p_0$ ) into the formation,

the pressure gradually rises towards  $p_{f0}$ . Therefore, if the fracture propagates faster than the fluid diffusion rate, the pressure over  $[R_0, R_1]$  is always at the early stage of the diffusion process and can be reasonably approximated by  $p_0$ , i.e.  $p_{R_0 R_1}(r, t_1) = p_0$  for  $r \in (R_0, R_1]$ . Similar conditions have been applied in all other researches explicitly or implicitly whenever the  $p_{R_0 R_1}$  value is needed. e.g. [60, 82].

Now, let us extend the above simple propagation history to a continuous fracture propagation history,  $R(t)$ . Look at a point at a fixed physical distance from the wellbore,  $r$ . At time,  $\tau(r)$ , the fracture first extends beyond this point whose radius is denoted as  $R_\tau$ . To compute the poroelastic response at the current time,  $t$ , let us divide the time period,  $[\tau, t]$ , into a number of small intervals:  $[\xi_k, \xi_{k+1}]$ . During the each time increment,  $\Delta\xi = \xi_{k+1} - \xi_k$ , the fracture radius increases from  $R_{\xi_k}$  to  $R_{\xi_{k+1}}$  and the fluid pressure changes from  $p(\xi_k)$  to  $p(\xi_k) + \Delta p_f(\xi_k)$ . The contribution from this time subinterval to the poroelastic effect at  $r, t$  can be computed by:

$$\Delta w^p(r, t) = \Delta p_f(s, \xi_k) w^p(r, t - \xi_k; R_{\xi_{k+1}}) \quad (3.44)$$

One may sum the elemental contributions corresponding to each subinterval as described by Eqn. (3.44), and pass to the limit by taking the subintervals to zero and their number to infinity. In this way, the following formulae for a propagating fracture can be reached:

$$\begin{aligned} w^p(r, t) &= p_f(s, \tau) w^p(r, t - \tau; R_\tau) + \\ &\quad \lim_{\substack{\max \Delta \xi_k \rightarrow 0 \\ n \rightarrow \infty}} \sum_{k=1}^n \left\{ \left[ \frac{\Delta p_f(\xi_k)}{\Delta \xi_k} \Delta \xi_k \right] w^p(r, t - \xi_k; R_{\xi_{k+1}}) \right\} \\ &= p_f(s, \tau) w^p(r, t - \tau; R_\tau) + \int_\tau^t \left[ \frac{\partial p_f(s, \xi)}{\partial \xi} \right] w^p(r, t - \xi; R_\xi) d\xi \end{aligned} \quad (3.45)$$

This equation is similar to Duhamel's principle except that the fundamental function,  $w^p$ , depends on both  $\xi$  and  $R$ . The pressure appears in this equation as its profile along the fracture, i.e.  $s \in (0, 1)$ . Therefore, the fracture propagation may also induce a non-zero time derivative of the fluid pressure,  $\frac{\partial p_f}{\partial \xi}$ . If the fracture is stationary at  $R_0$ , Eqn. (3.45) recovers the conventional Duhamel's principle for a time-varying pressure profile.

Similarly, the leakoff rate can be computed for a propagating fracture as follows:

$$u(r, t) = -\frac{1}{\kappa} \left\{ u(r, t - \tau; R_\tau) p_f(\tau) + \int_\tau^t \left[ \frac{\partial p(s, \xi)}{\partial \xi} \right] u(r, t - \xi; R_\xi) d\xi \right\} \quad (3.46)$$

in which,  $u(r, t - \xi; R_\xi)$  is given by Eqn. (3.38) with  $R_\xi$  as the non-dimensionalizing fracture radius,  $R_0$ .

### 3.4.2 Discussion about the Extension Principle

A rigorous proof of the extension principle can only be obtained by solving the case of a propagating fracture and comparing the results with the ones based on Eqn. (3.45). Unfortunately, this cannot be carried out because the solution of a propagating fracture in poroelastic media requires a numerical tool which neither exists in the literature nor can be readily developed. In this section, we attempt to check its performance in some limiting cases. The needed material properties are listed in Table 2.2.

Firstly, let us consider the case of a stationary fracture. For simplicity, take a spatially uniform and temporally linearly decreasing pressure profile, for example,

$$p_f(s, t) = p_{f0}(1 - t/t_0) \quad . \quad (3.47)$$

An analytical solution can be easily derived based on Eqn. (3.45). Figure 3.17 shows the comparison between the numerical prediction by Eqn. (3.45) and the analytical ones. Obviously, an almost identical agreement results. The poroelastic displacement,  $w^p$ , increases initially till  $t = 10$  seconds even though the pressure continuously decreases. Starting from  $t = t_c = 24$  seconds, the  $w^p$  decreases linearly with time. In Figure 3.17,  $t_0 = 100$  seconds and  $p_{f0} = 1$ .

Next, let us consider a simple propagation history:

$$R(t) = \begin{cases} 1. & t < 10s \\ 1. + 0.5(t - 10) & 10 \leq t \leq 11 \\ 1.5 & t > 11s \end{cases} \quad (3.48)$$

in which, the specific numbers are chosen arbitrarily and have no physical meaning.  $R$  has a unit of meter. Figure 3.18 shows the evolution of the poroelastic displacement at several particular physical locations on the fracture. Before  $t = 10$  s, the poroelastic response coincides with the stationary fracture case with its radius equal to 1 meter. At  $t = 10$  s, it has already attained the steady state. The fracture propagation perturbs the steady state so that after  $t = 10$  s, the fracture experiences an abrupt, rapid increase in its deformation and then again, slowly approaches the new steady state based on the propagated fracture geometry of 1.5 m in radius.

Figure 3.19 shows the evolution of the  $w^p$  profiles along the fracture. The fracture propagation causes a cusp in the  $w^p$  profiles near the previous fracture tip; the newly propagated fracture segment has a smaller fracture opening because it is exposed to the fracturing fluid later. As the diffusion continues, the kink is gradually smoothed out and the whole  $w^p$  profile finally becomes the steady-state elliptical shape.

Due to its history-independence, the final steady state should not feel the influence of the fracture propagation except its created new fracture radius.

It is therefore expected that the final computed steady state values of  $w^p$  by Eqn. (3.45) should coincide with the analytical predictions based on Eqn. (2.43) if substituted with the appropriate fracture radius values. Figure 3.20 indeed shows this observation. At  $t = 10$  s before the fracture propagation, the  $w^p$  profile is elliptical, corresponding to the steady state based on the non-propagated fracture geometry of 1 m in radius. At  $t = 100$ s when the propagated fracture reaches the steady state, another elliptical-shape for the fracture aperture appears, which corresponds to the propagated fracture radius of 1.5 m.

Finally, let us consider a real fracture propagation history in which the fracturing pressure decreases as the fracture propagates (Figure 3.21):

$$R(t) = 3.74 t^{0.4} \quad (3.49)$$

$$p(t) = 11.49 t^{-0.2} \quad (3.50)$$

where  $R$  is in meters and  $p$  in MPa. Eqn. (3.49) and Eqn. (3.50) are based on a similarity solution of a penny-shaped fracture propagation in purely elastic media of high fracture toughnesses (to be discussed in the next chapters).

Figure 3.22 displays the  $w^p$  evolution at some particular physical coordinates on the fracture. The abrupt change in  $w^p$  due to the fracture propagation, which is observable in the above simple step-rate fracture propagation history, Eqn. (3.48), does not exist for the current continuous propagation history, Eqn. (3.49). As shown in Figure 3.23, the  $w^p$  profiles along the fracture appear linear and do not have the cusps (except at early times) which are visible for the step-rate fracture propagation history as discussed earlier (Figure 3.19).

Figure 3.24 plots the comparison between the 1-D transient model, Eqn. (2.32), and the simplified 2-D model, Eqn. (3.45). At the very early times

when the fracture is first exposed to the fracturing fluid, the 1-D and 2-D results are comparable. Shortly after the fracture arrival, however, the 1-D results start to exceed the 2-D as the fluid penetrates deeper into the formation in 1-D (in 2-D, the lateral diffusion takes portion of the diffused fluid). However, the 1-D model cannot feel the structural influence, i.e. the fracture radius, induced by the fracture propagation. As the fracture propagates to a certain length, the structural effect intrinsic to the 2-D model eventually overtakes the penetrating diffusion predominance of the 1-D model. As a result, the 2-D  $w^p$  values go beyond the 1-D. Similar observation can be made in the  $w^p$  profiles (Figure 3.23); the fracture aperture near the fracture tip is larger in the 1-D prediction than in the 2-D because the fracturing fluid just reaches that point; whereas away from the tip, the  $w^p$  results in the 2-D model are larger than in the 1-D model because the structural effect has already surpassed the diffusion effect.

Based on the above reasoning about the competition between the structural effect in the 2-D model and the penetrating diffusion advantage of the 1-D model, a smaller permeability,  $\kappa$ , of the poroelastic media is expected to prolong the time period when both models are comparable and reduces the predominance of the 1-D over 2-D, i.e. enhances the structural dominance. Moreover, a faster fracture propagation rate, i.e. a higher  $K_r$  value in Eqn. (3.49), should strengthen the 2-D response, causing it to exceed the 1-D results at earlier times. The parametric study as shown in Figure 3.25 indeed predicts this trend.

As a separate note, we computed the CPU time taken to compute Figure 3.24 based on the 1-D and 2-D models, respectively. The 1-D model consumes 11 seconds on IBM PC 486 66 MHz while the 2-D model spends 32 seconds on



the same machine. We believe this is comparable. Therefore, the advantage of the 2-D model being physically realistic and computationally efficient is shown here.

The above exercises point to the conclusion that all the computations based on Eqn. (3.45) are physically valid and mathematically accurate in the limiting cases, including the cases of a stationary fracture and the final steady-state solution during the simple step-rate propagation history, Eqn. (3.48).

Similar exercises have been applied to compute the leakoff rate based on Eqn. (3.46) and its validity has been proven as well. As an illustration, Figure 3.26 shows the comparison of the leakoff rate evolution between the 1-D analytical model, Eqn. (2.30), and the simplified 2-D model, Eqn. (3.46), during the realistic propagation history, Eqn. (3.49) and Eqn. (3.50). It suggests that the 1-D model underestimates the leakoff rates if compared to the 2-D model, which is in agreement with other researchers' findings (e.g. Settari and Warren, 1994).

### **3.5 Summary**

In this chapter, a simplified 2-D poroelastic model has been developed. In the existing literature, poroelastic effects have been considered by either a full model or a 1-D model. The full model is very computationally intensive as briefly discussed in Chapter 1 of this dissertation. The 1-D model consumes much less calculation effort, but loses the true 2-D or 3-D nature which introduces large errors, particularly, in the poroelastic displacements as shown, for example, in this chapter. The simplified 2-D model eliminates the disadvantages of both models. It retains the realistic physics and reasonably good mathematical accuracy as compared to the true 2-D model. However, it is

computationally efficient and comparable to the 1-D explicit analytical model. Only with this simplified model is it possible to have a fast, yet accurate, HF simulator that accounts for the poroelastic effect.

The simplified model is reached by first building up the model for the case of stationary fractures and then, deriving a Duhamel's theorem-like principle to extend it to propagating fractures. The stationary fracture-based model is created by interpolating the transient interim behavior of the 2-D poroelastic response based on the early- and late-time asymptotic results. A cubic spline interpolation scheme is used for the poroelastic displacement,  $w^p$ ; and a simple superimposition technique summing the 1-D transient and 2-D steady-state predictions is applied to the pressure-dependent leakoff rate,  $u$ .

The mathematical accuracy of the simplified 2-D model for stationary fractures has been checked by comparing its predictions with the commercial FEM's computations based on the full 2-D model for two example pressure profiles. In the significant part of the poroelastic domain, e.g. for  $t > 10^{-2}$ , less than 10% relative error is reported for  $w^p$ . In some situations, larger errors, e.g. 20% relative error for  $w^p$  and 30-40% for  $u$ , do occur in the comparison. Partly, they can be attributed to the FEM's inherent inaccuracy in early-time calculation or in the calculation of pressure gradient. The cases where the simplified model is the main source of the error, happen to be those when the  $w^p$  or  $u$  values are insignificantly small; therefore, a relatively large error in the prediction does not affect the whole system very much.

Based on the physical arguments, an extension principle has been derived to apply the stationary fracture-based simplified 2-D model to a propagating fracture. The resultant mathematical formula happens to appear like Duhamel's theorem and in fact, it strictly can be reduced to Duhamel's theorem for a

stationary fracture and time-varying pressure history. Besides the linearity requirement which is guaranteed by the theory of poroelasticity, the derivation also assumes that the pore pressure ahead of the fracture tip along the fracture direction remains at the *in-situ* reservoir pore pressure value. This assumption has been used explicitly or implicitly in all other researches whenever it is needed. It is valid when the fracture propagation rate is much faster than the fluid diffusion rate in the porous media. Although vigorous proof of this extension principle has not been attempted, computations for several representative fracture propagation histories using the extension principle have revealed that it captures all the physics, and in the limiting behavior, it is identical to the corresponding analytical results.

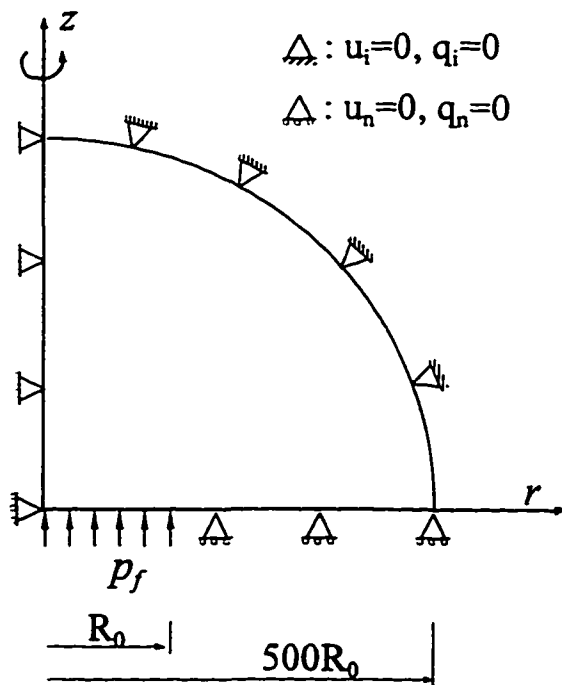


Figure 3.1: Computational model of the penny-shaped pressurized fracture.

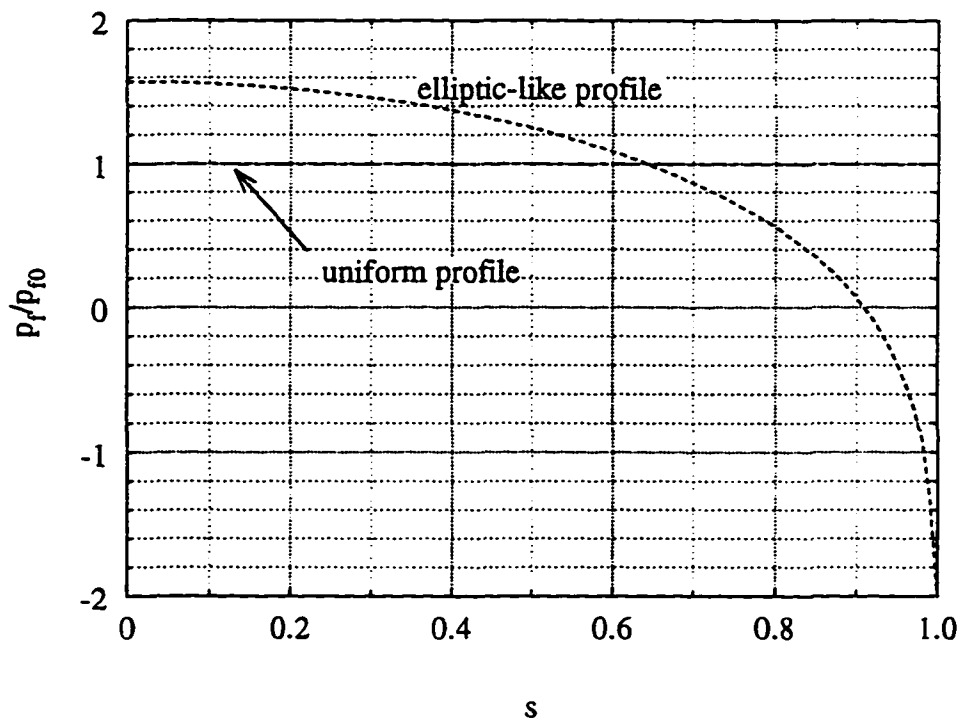


Figure 3.2: The computed example pressure profiles.

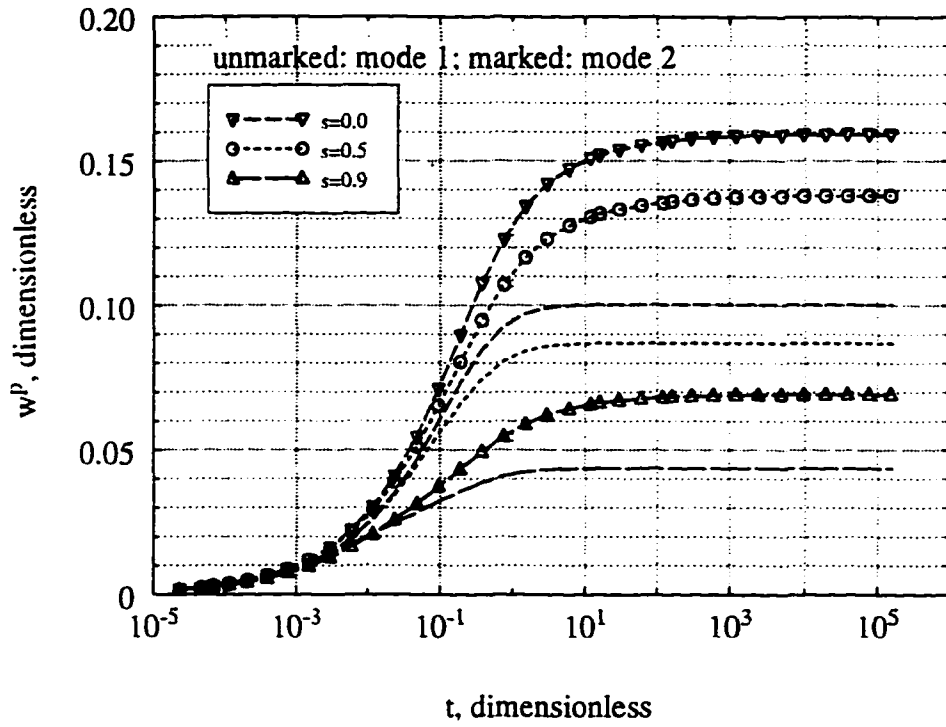


Figure 3.3: Comparison of  $w^p$  between mode 1 and 2 loading in the non-dimensionalized domain.

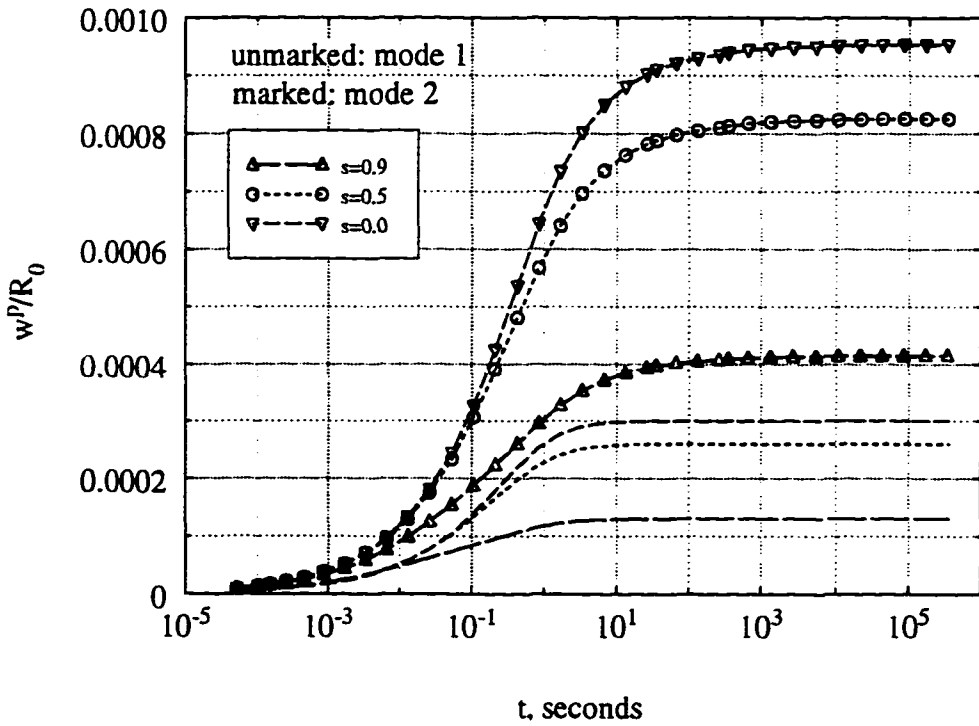


Figure 3.4: Comparison of  $w^p$  between mode 1 and 2 loading in the dimensional domain.

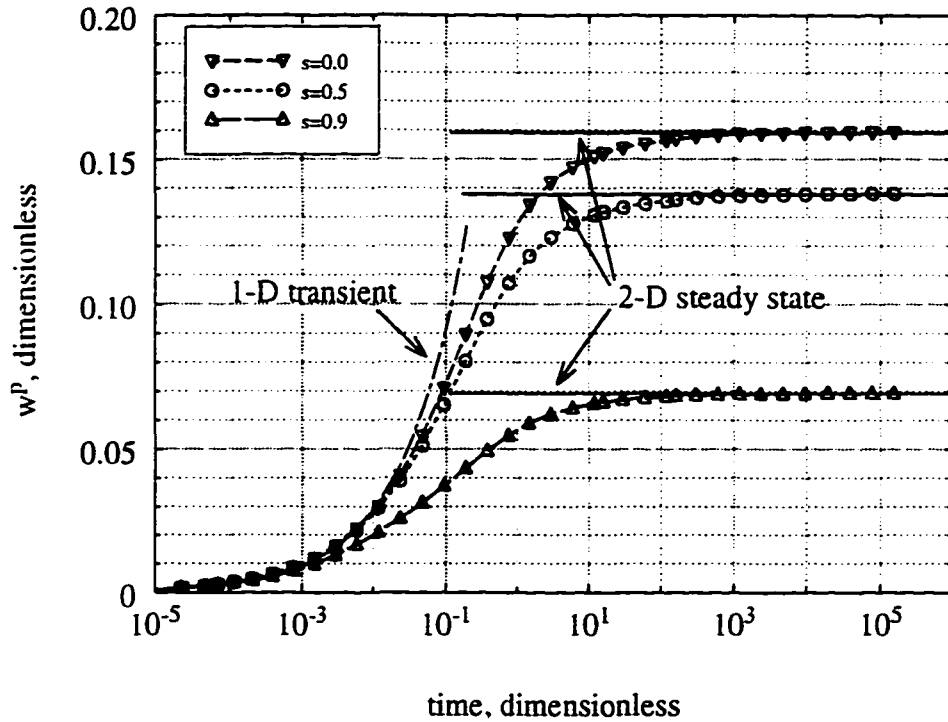


Figure 3.5: Evolution of the poroelastic displacement,  $w^p(s, t)$  and its comparison with the 1-D transient and 2-D steady-state solutions. Uniform pressure profile.

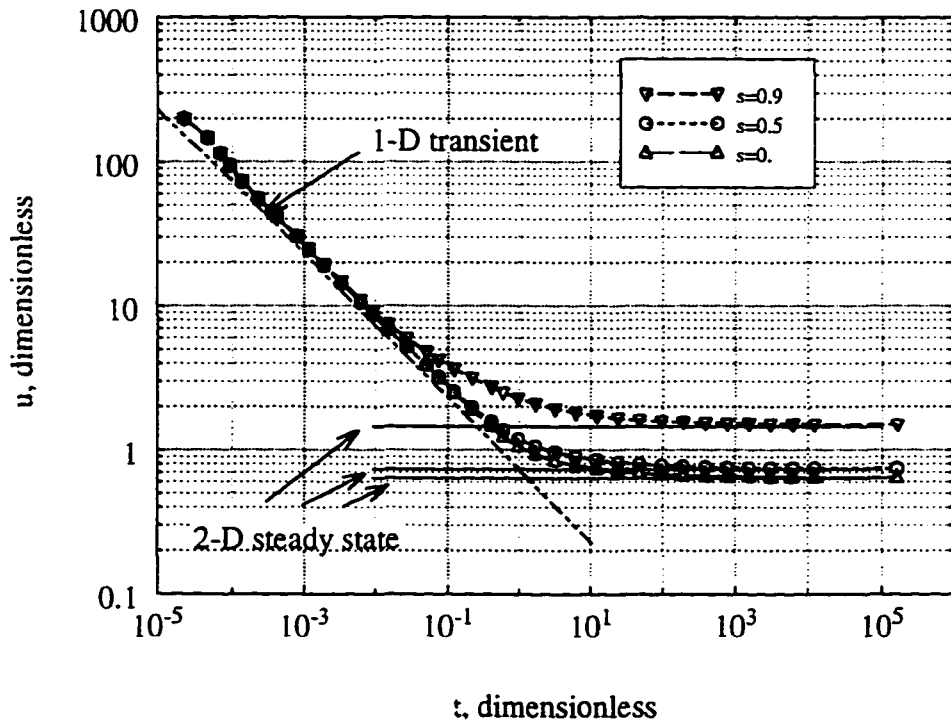


Figure 3.6: Evolution of the leakoff rate,  $u(s, t)$  and its comparison with the 1-D transient and 2-D steady-state solutions. Uniform pressure profile.

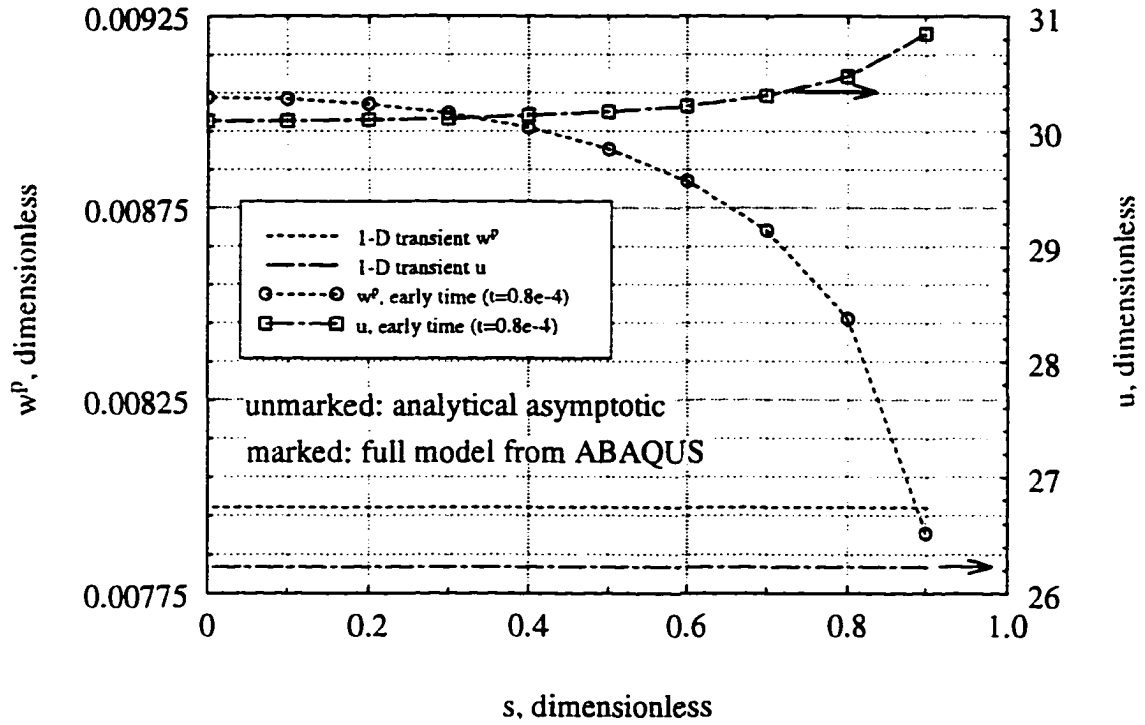


Figure 3.7: Profiles of the computed  $w^p$  and  $u$  along the fracture and their comparison with the asymptotic 1-D analytical results. Uniform pressure profile.

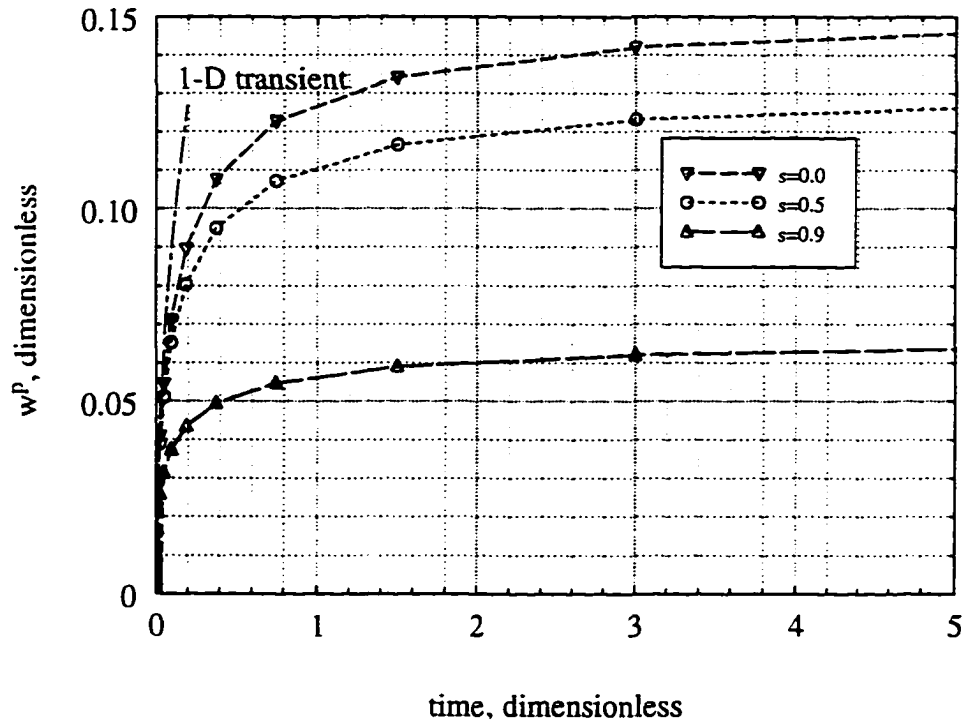


Figure 3.8: Evolution of the poroelastic displacement,  $w^p(s, t)$ , during the early time period. Uniform pressure profile.

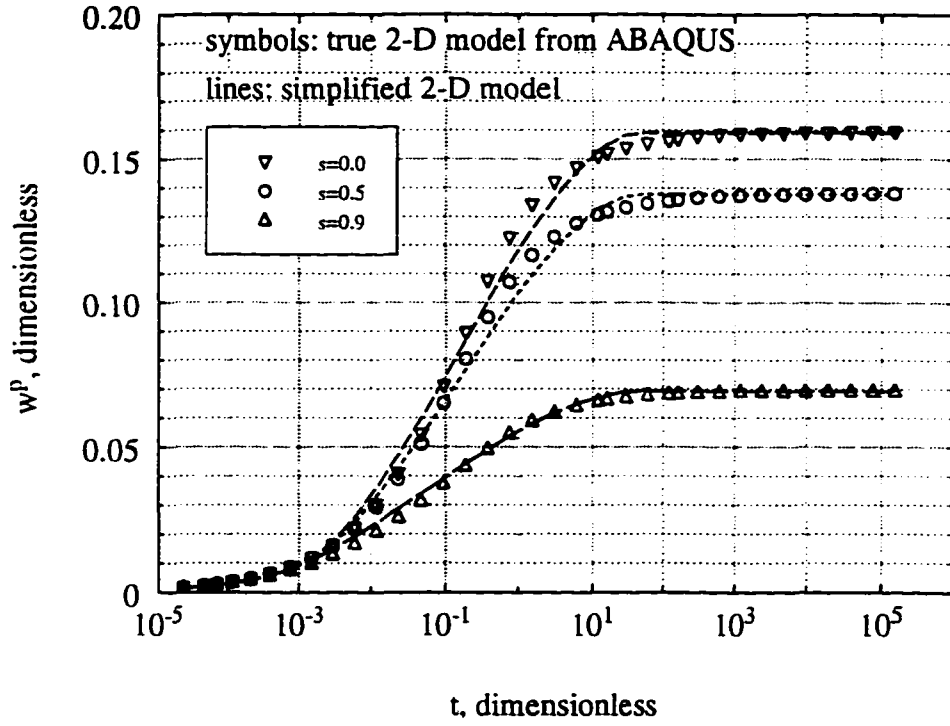


Figure 3.9: Comparison of the simplified 2-D model with the true 2-D computations. Poroelastic displacement,  $w^p$ , and uniform pressure profile.

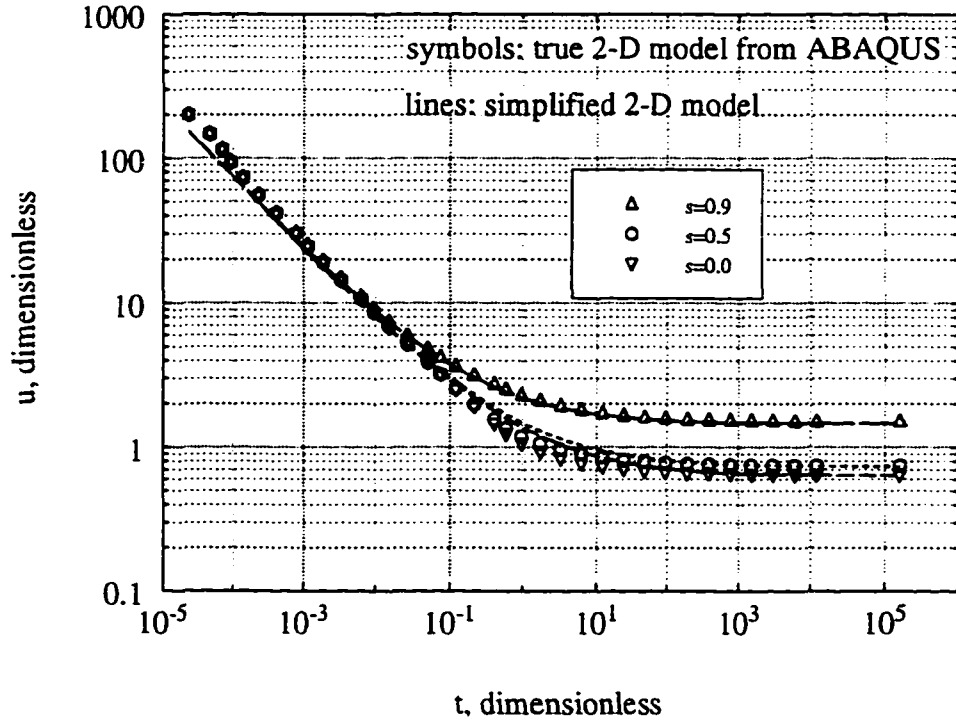


Figure 3.10: Comparison of the simplified 2-D model with the true 2-D computations. Leakoff rate,  $u$ , and uniform pressure profile.



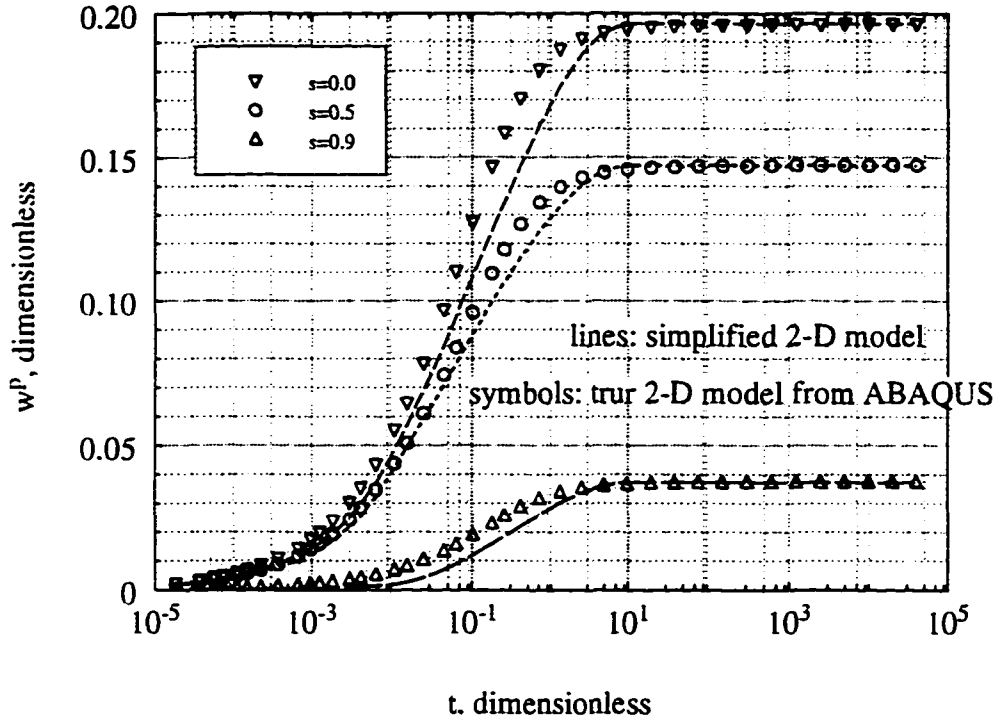


Figure 3.11: Comparison of the simplified 2-D model with the true 2-D computations. Poroelastic displacement,  $w^p$ , and elliptic-like pressure profile.

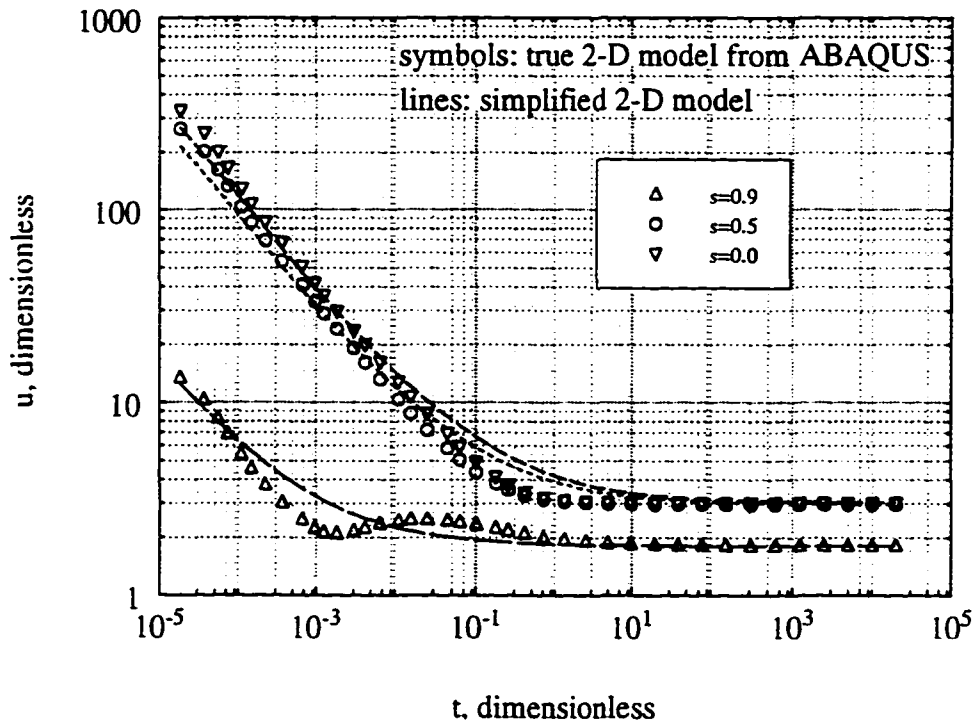


Figure 3.12: Comparison of the simplified 2-D model with the true 2-D computations. Leakoff rate,  $u$ , and elliptic-like pressure profile.

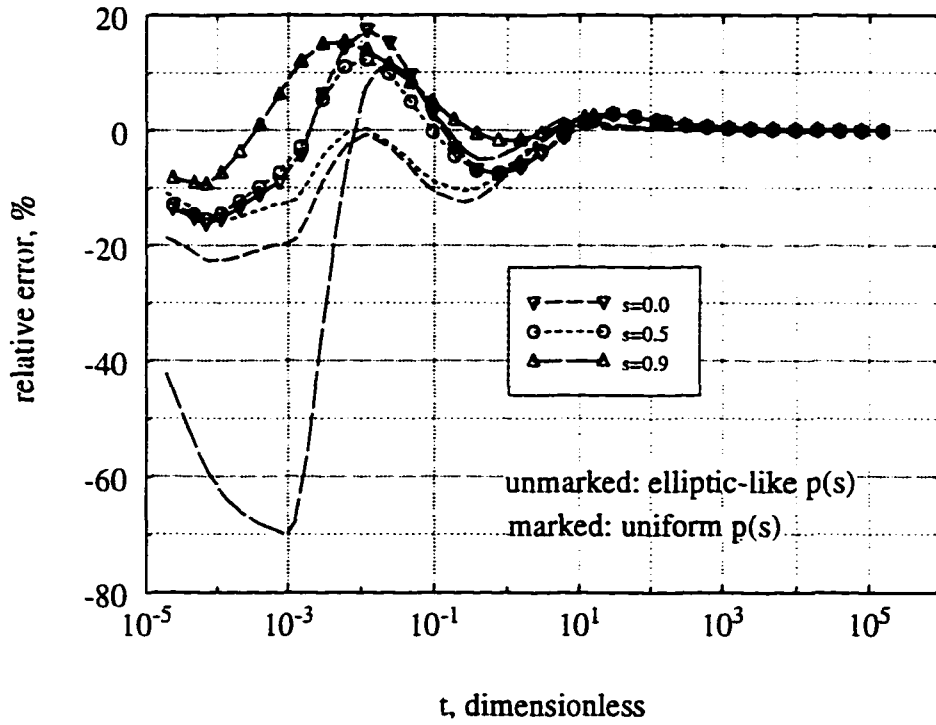


Figure 3.13: Distribution of the relative error of the simplified 2-D model as compared to the true 2-D computations. Poroelastic displacement,  $w^p$ .

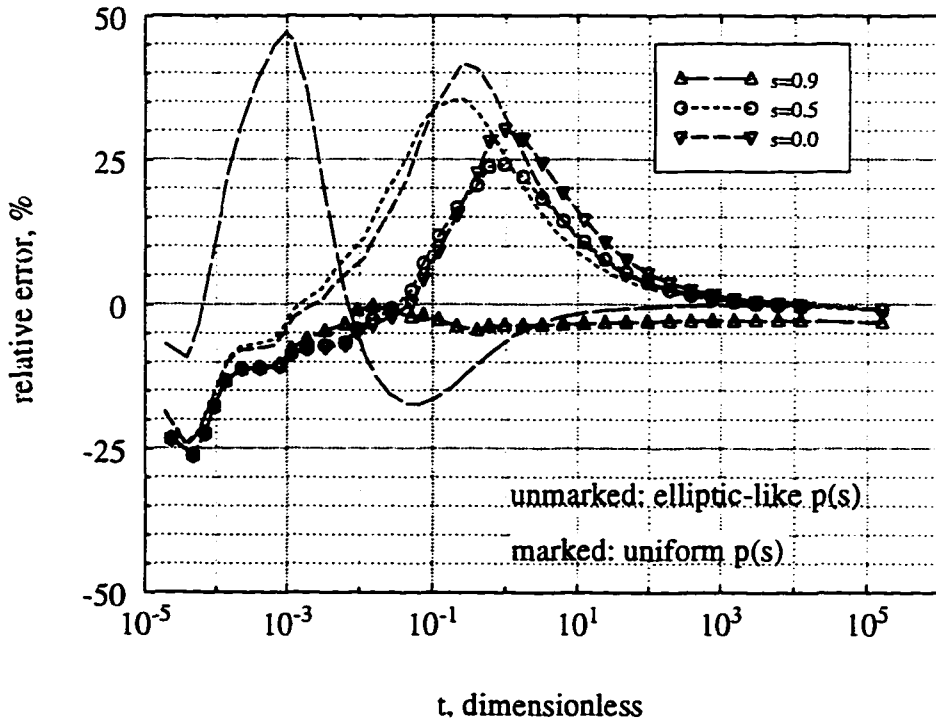


Figure 3.14: Distribution of the relative error of the simplified 2-D model as compared to the true 2-D computations. Leakoff rate,  $u$ .

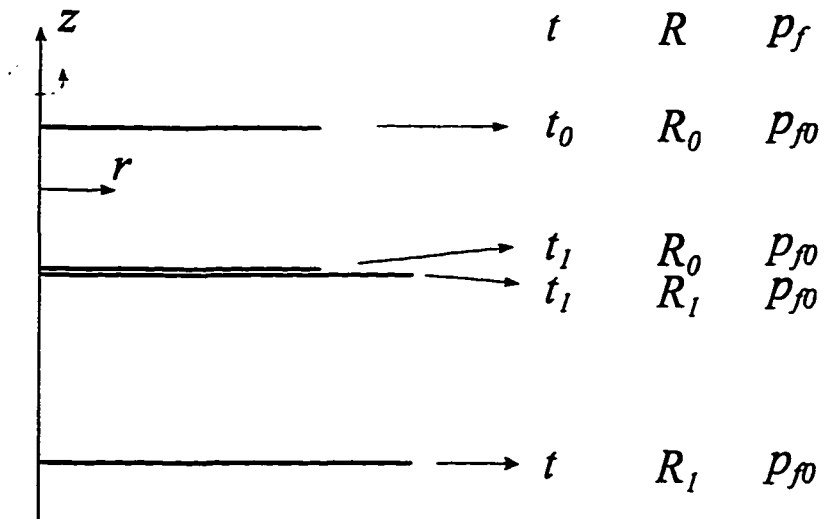


Figure 3.15: Physical description of the simple step-rate fracture propagation history.

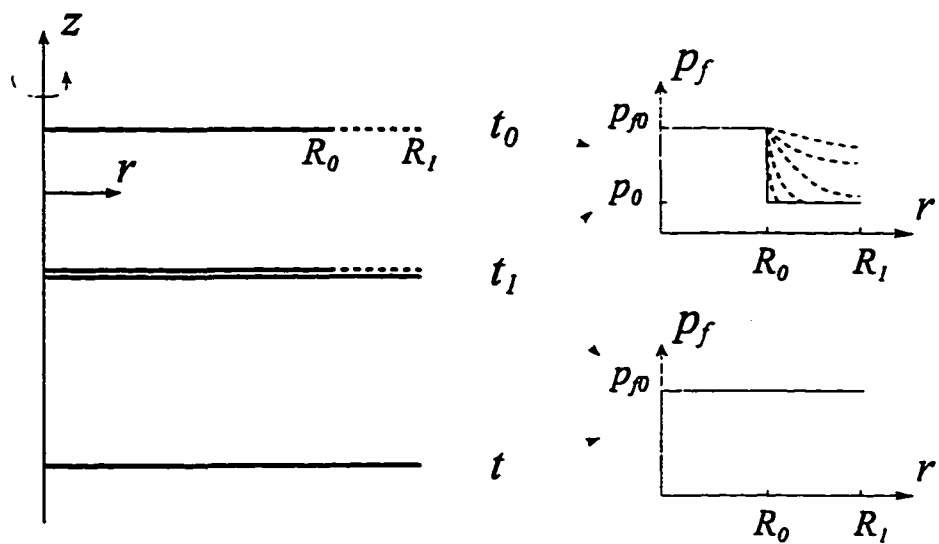


Figure 3.16: Mathematical realization of the simple step-rate fracture propagation history.

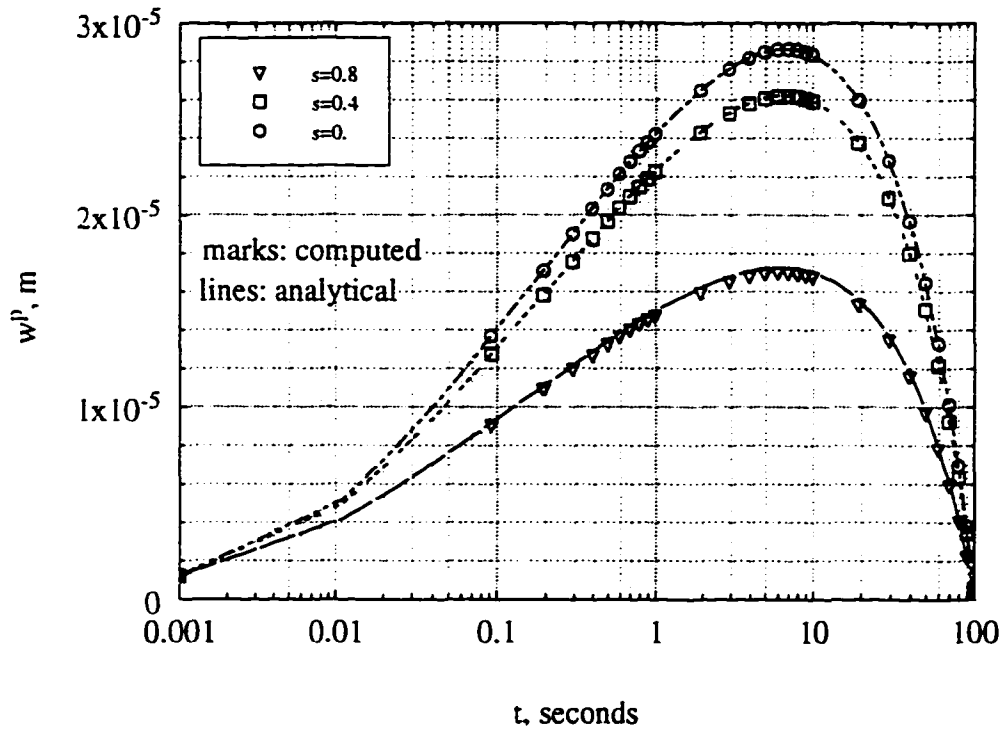


Figure 3.17:  $w^p$  evolution and its comparison with the analytical results for a stationary fracture under the linearly decreasing pressure.

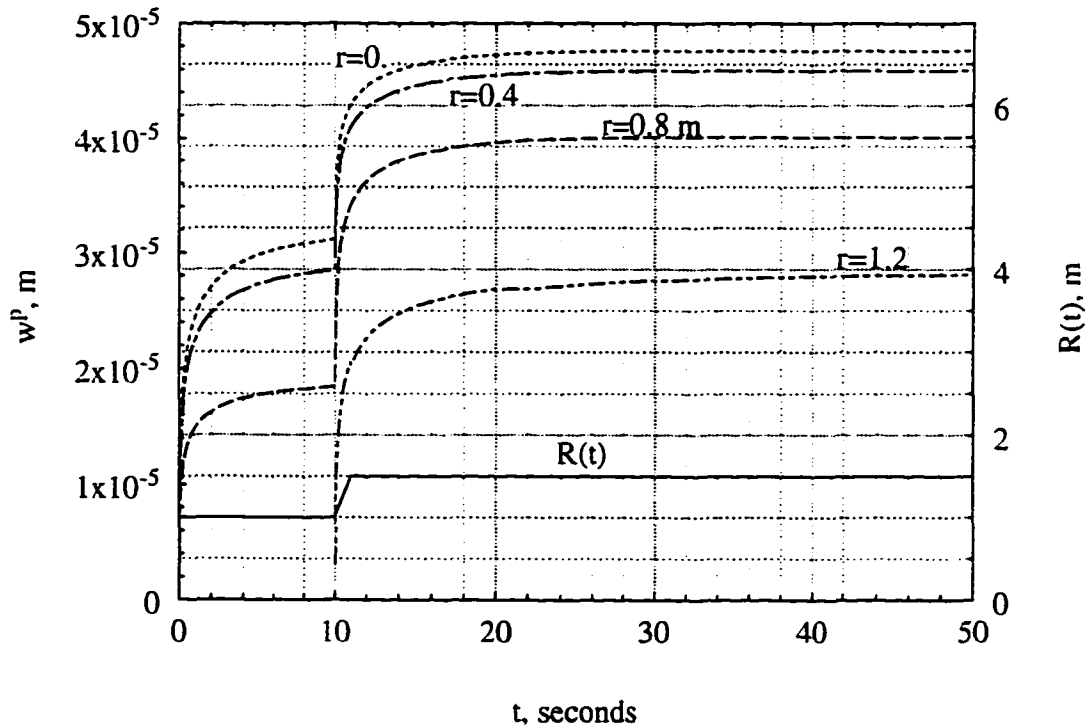


Figure 3.18:  $w^p$  evolution during the simple step-rate fracture propagation history.

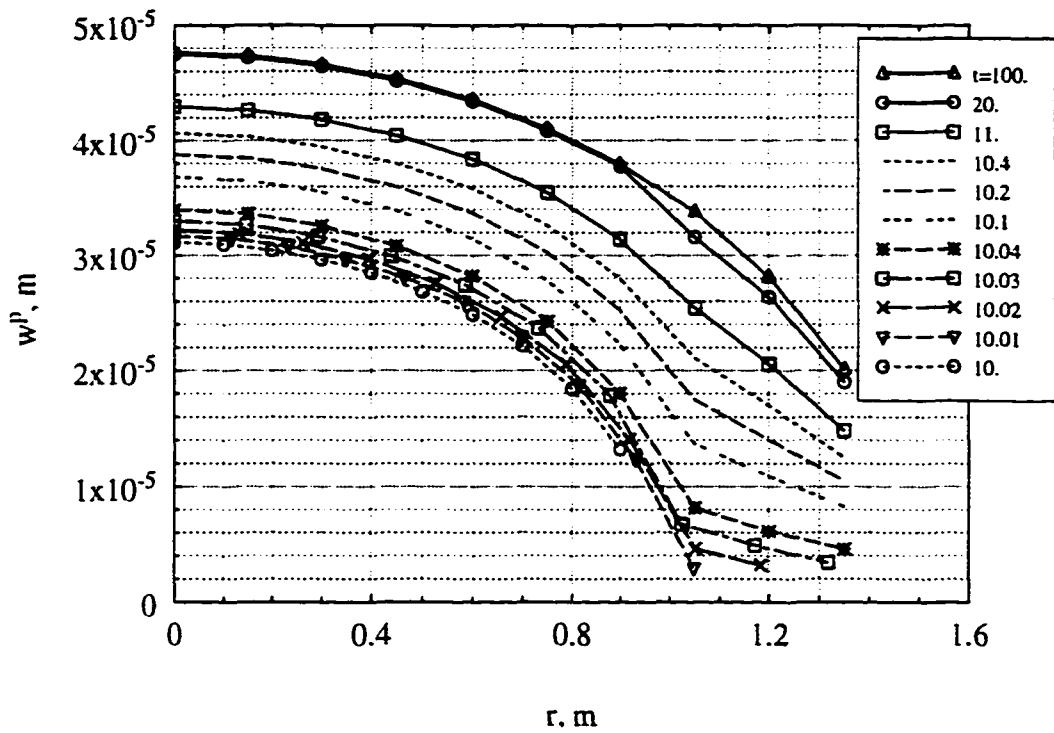


Figure 3.19: Evolution of the  $w^p$  profiles along the fracture during its simple step-rate propagation history.

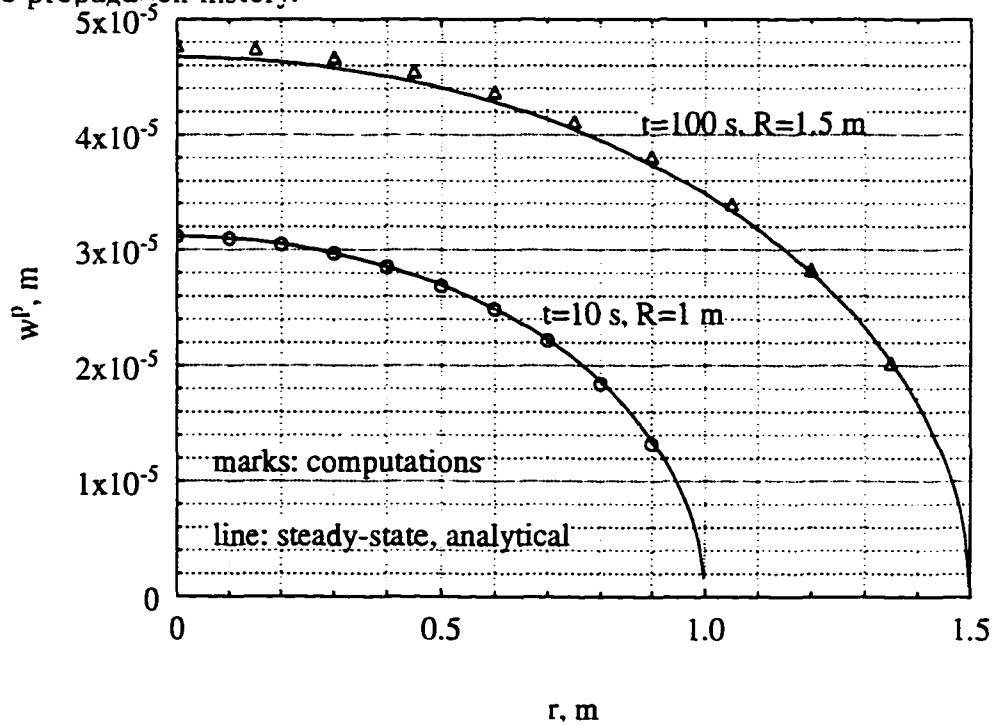


Figure 3.20: The steady-state  $w^p$  profiles for the original and propagated fracture geometries and their comparison with the analytical predictions. Simple step-rate fracture propagation history.

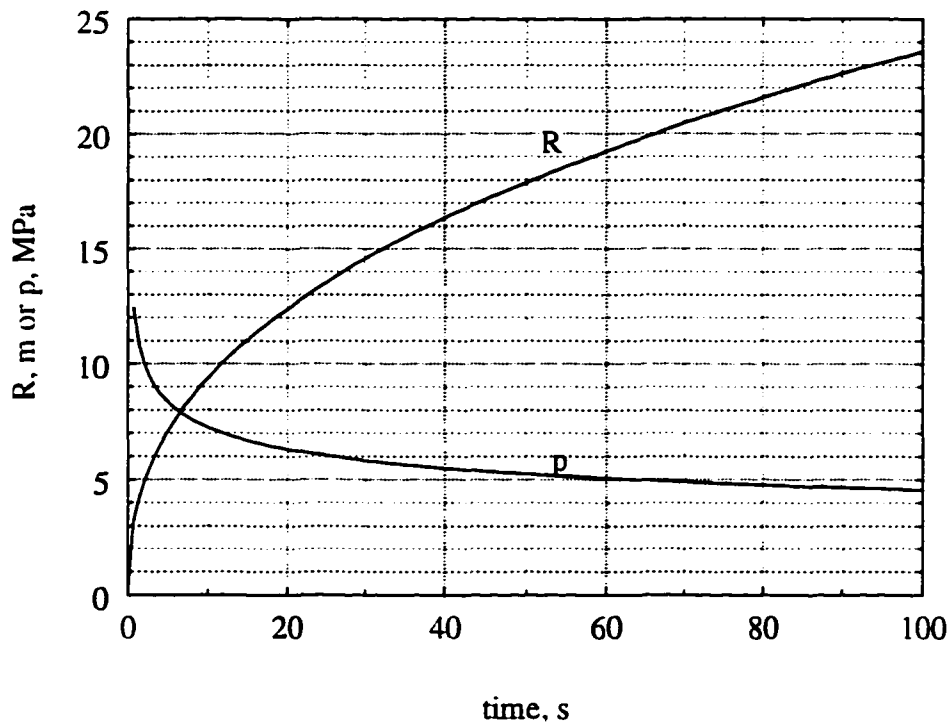


Figure 3.21: The fracture radius and pressure histories during the real propagation case.

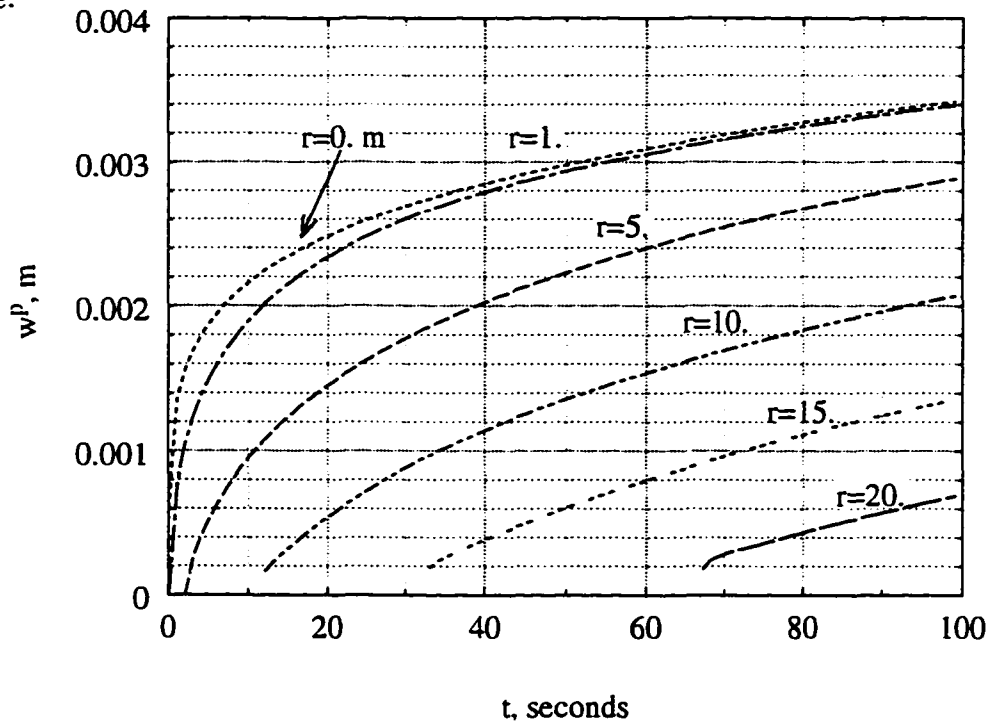


Figure 3.22:  $w^p$  evolution at the typical physical coordinates on the fracture during the real propagation history.

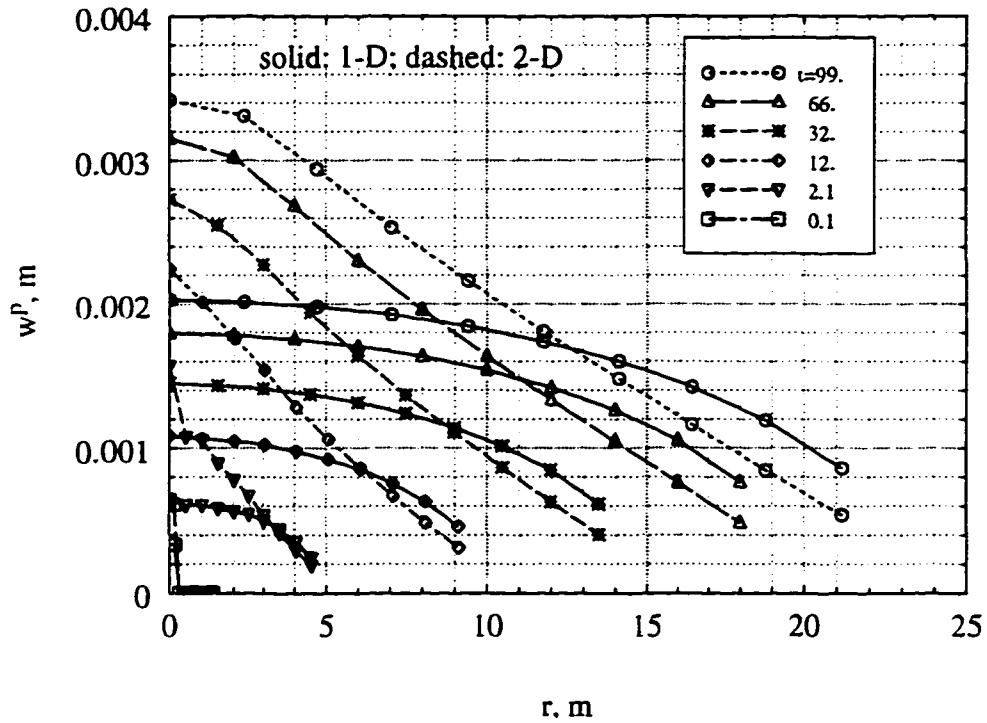


Figure 3.23: Evolution of  $w^p$  profiles along the fracture and comparison between the 1-D and the simplified 2-D poroelastic models. The real fracture propagation history.

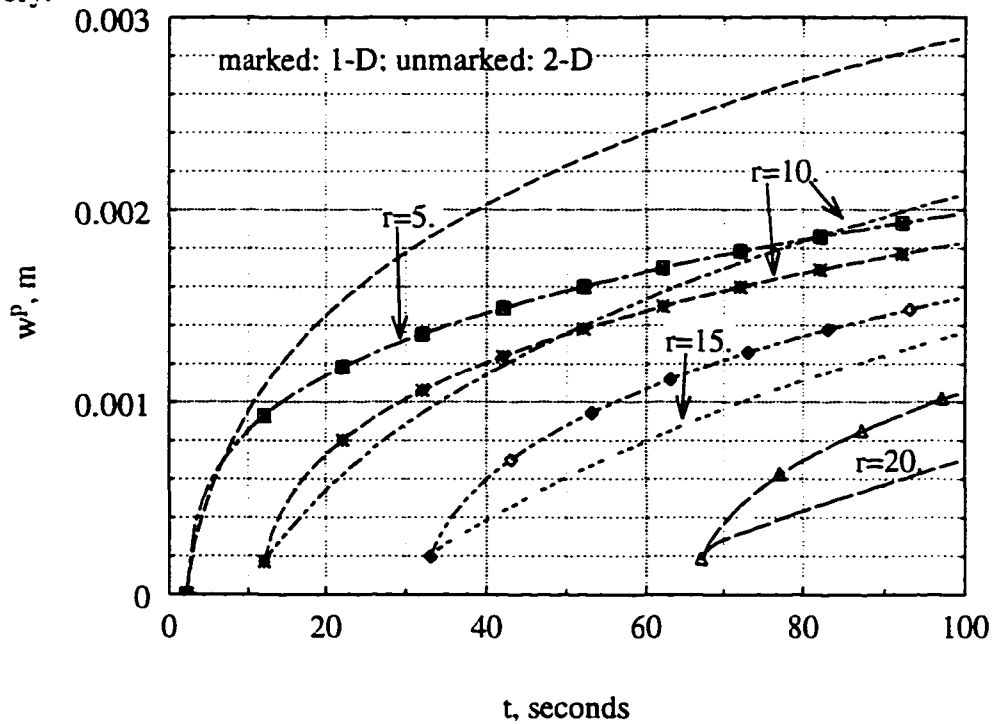


Figure 3.24: Comparison between the 1-D and the simplified 2-D poroelastic models in the  $w^p$  evolution. The real fracture propagation history.

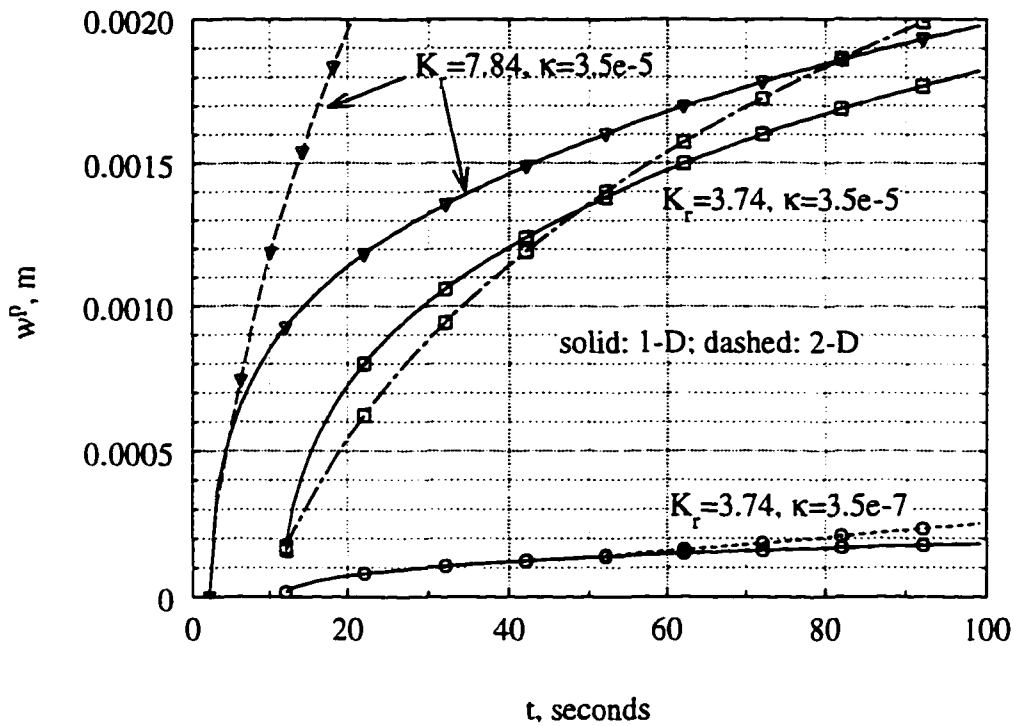


Figure 3.25: Parametric dependence on  $\kappa$  or  $K_r$  of the 1-D vs. 2-D comparison in the  $w^p$  evolution. The real fracture propagation history.

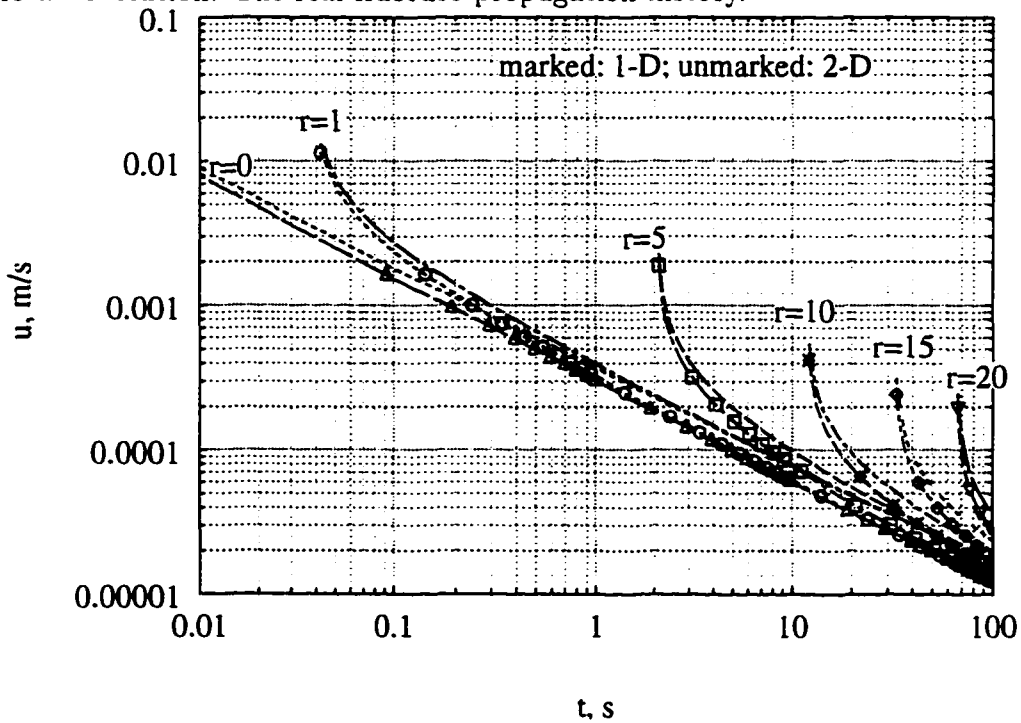


Figure 3.26: Evolution of the leakoff rate,  $u$  and the comparison between the 1-D and 2-D models. The real propagation history.



## Chapter 4

# A Pseudo-Explicit Finite Difference Scheme

This and the following chapters deal with the simulation of penny-shaped HF propagation. A numerical algorithm was derived and tested to couple the various physical sub-processes during the fracture propagation, including fracture deformation, flow inside the fracture, fracture propagation, fluid leakage into the formation and the associated poroelastic effect. Numerically, the fracture propagation is often accomplished via the snap-shot scheme. In each snap-shot, a stationary fracture is calculated. Therefore, one of the keys is the strategy to compute the stationary fracture, which is the focus of this chapter. The subsequent chapter extends this concept to a propagating fracture. Particularly, it describes the computation of the fracture propagation/closure/re-opening.

Herein, the governing equations to model the penny-shaped HF propagation are first summarized and non-dimensionalized. Thereafter, a pseudo-explicit finite difference (PEFD) scheme is derived and qualitatively tested for its computational and convergence performance. The Newton-Raphson (NR) method is then applied to aid the PEFD in speeding up the convergence. Finally, the

stability, consistency and accuracy of the current combined PEFD-NR algorithm are checked via various examples in the context of a stationary fracture.

## 4.1 Governing Equations in McFrac

Consider a penny-shaped fracture of radius  $R$  in an infinite and permeable formation (Figure 1). Given the injection rate,  $Q_0$ , from the wellbore, the fluid properties, the flow and deformation properties of the porous rock, the *in situ* stress,  $\sigma_0$ , and pore pressure,  $p_0$ , the goal is to determine the evolution of the fracture dimension (radius/width) and the pressure profile along the fracture, including the pressure response at the wellbore. The fracture is assumed to propagate equi-dimensionally, i.e. possessing an axial symmetry. The mathematical model is constructed as follows.

The fluid flow inside the fracture follows the Poseuille's law:

$$\frac{\partial p_f}{\partial r} = -\frac{2Kq|q|^{n-1}}{\psi^n w^{2n+1}} \quad (4.1)$$

and is also governed by the mass balance:

$$\frac{1}{r} \frac{\partial (rq)}{\partial r} + \frac{\partial w}{\partial t} + u = 0 \quad (4.2)$$

where  $p_f$  is the fluid pressure inside the fracture;  $r$  is the radial distance from the wellbore;  $\psi = \frac{n}{2(2n+1)}$  is a geometric factor for the current axisymmetric configuration;  $q$  is fluid flux, defined as the volumetric flow rate,  $Q$ , through a unit circumference at distance,  $r$ , from the wellbore, i.e.  $q = Q/2\pi r$  and, thus, has a dimension of  $L^2/T$ ;  $w$  is the fracture aperture;  $u$  is the rate of the fluid leakoff from both fracture surfaces. Eqn. (4.1) is written for the power-law fluid rheology with  $K$  being the consistency index and  $n$  is the flow behavior

index. For a Newtonian fluid,  $n = 1$ ,  $K = \mu$  — the fluid dynamic viscosity. Eqn. (4.1) thus becomes:

$$\frac{\partial p_f}{\partial r} = -\frac{12\mu q}{w^3} \quad (4.3)$$

which is the well known cubic law. Eqn. (4.1) and Eqn. (4.2) are derived in Appendix C. Therefrom, it is clear that the major assumption for Eqn. (4.1) is its small Reynolds number so that a laminar flow exists and the inertial force can be ignored. For Eqn. (4.2), the fluid is assumed to be incompressible.

Primarily, the fluid leakoff is assumed to be pressure-dependent, which is described by the modified 2-D model, Eqn. (3.38)<sup>1</sup>. However, allowance for the Carter's leakoff model is also provided:

$$u(r) = \frac{2C_l}{\sqrt{t - \tau(r)}} \quad (4.4)$$

in which,  $C_l$  is the Carter's leakoff coefficient;  $\tau(r)$  is the fracture arrival time when the position,  $r$ , is first exposed to the fracturing fluid.

According to the loading modal decomposition as exemplified in Chapters 2 and 3, the fracture aperture,  $w$ , consists of two contributions:

$$w = w_1 + w_2 \quad (4.5)$$

in which,  $w_1$  reflects the fracture deformation induced by the mechanical loading condition,  $p = p_f - \sigma_0$ , while  $w_2$  represents the contribution from the hydraulic loading condition,  $p = p_f - p_0$ .  $w_2$  is purely time-dependent and caused by the poroelastic mechanism, which is therefore re-denoted by  $w^p$ . In

---

<sup>1</sup>A factor, "2", has to be added to account for the contribution from the upper and lower fracture surfaces. The same applies to the poroelastic displacement,  $w^p$ , to be described below.

the poroelastic domain,  $w_1$  comprises the time-independent undrained elastic response and the time-dependent poroelastic part as the deformation approaches the drained state. However, the earlier discussion has pointed out that this time-dependence of mode 1 is negligibly small as compared to mode 2 and thus, can be ignored.  $w_1$  can be adequately quantified by the purely elastic deformation characterized by the drained state. For this reason,  $w_1$  is re-written as  $w^e$ , and the total fracture deformation now becomes:

$$w = w^e + w^p \quad (4.6)$$

with  $w^e$  given by Eqn. (2.49) and  $w^p$  by Eqn. (3.37).

The fracture propagation is governed by the fracture toughness criterion:

$$K_I = \frac{1}{\pi} \sqrt{\frac{2}{R(t)}} \int_0^{R(t)} \frac{p_f(\xi, t) - \sigma_o}{\sqrt{R^2(t) - \xi^2}} \xi d\xi = \beta K_{Ic} \quad (4.7)$$

in which,  $\beta$  is introduced to quantify the poroelastic influence on the dry fracture toughness,  $K_{Ic}^2$

The boundary condition to the above mathematical system is dictated by the injection rate,  $Q_0$ , from the fracture inlet, i.e. at the wellbore,  $r = R_w$ :

$$q(0, t) = \lim_{R_w \rightarrow 0} \frac{Q_0}{2\pi R_w}; \quad t > 0 \quad (4.8)$$

Theoretically, the initial conditions are specified as:

$$R(0) = 0 \quad \text{and} \quad p(0, 0) = 0 \quad (4.9)$$

---

<sup>2</sup>The tip region around a fast propagating fracture is always near the undrained state. Therefore, the material there behaves stronger. The fracture toughness of the poroelastic media is expected to be larger than its dry value and depends on the fracture propagation rate [147].  $\beta$  describes the ratio of the fracture toughness at the wet state to its dry value. Because there is no explicit relationship between  $\beta$  and the fracturing speed,  $\beta$  is conveniently given a unit value. For a given material, the associated poroelastic effect can be approximately analyzed by changing its  $K_{Ic}$  value.

The system of equations 4.1.4.2, 3.38, 4.6, 2.49, 3.37, and 4.7, supplemented by the above boundary and initial conditions constitutes a well-posed mathematical model to predict the evolution of the fracture radius  $R(t)$  and the field variables:  $w(r, t)$ ,  $p(r, t)$ ,  $u(r, t)$  and  $q(r, t)$ .

## 4.2 Non-Dimensionalization of the Governing Equations

For the non-dimensionalization, the following dimensionless variables are introduced:

$$r' = r/L_c, \quad R' = R/L_c, \quad t' = t/t_c, \quad p_f = p'_f \sigma_0 + \sigma_0 \quad (4.10)$$

in which,

$$L_c = \frac{\pi^2 K_{Ic}^2}{2\sigma_0^2} \quad (4.11)$$

so that, the fracture propagation equation, (4.7), is reduced to

$$\sqrt{R'} \int_0^1 \frac{p_f(s, t') s ds}{\sqrt{1-s^2}} = 1 \quad (4.12)$$

Following [148, 149],  $t_c$ , as a characteristic time, is an unknown constant for the time being and is to be specified as explained in the following. Correspondingly, the various governing equations can be expressed in their dimensionless counterparts via the following relations:

$$w^e(r', t') = w_c^e w'_e(r', t') \quad (4.13)$$

$$u(r', t') = u_c u'(r', t') \quad (4.14)$$

$$w^p(r', t') = w_c^p w'_p(r', t') \quad (4.15)$$

$$w(r', t') = w_c^e w'(r', t') \quad (4.16)$$

$$q(r', t') = q_c q'(r', t') \quad (4.17)$$

with

$$w_c^e = \frac{4(1-\nu)L_c\sigma_0}{\pi G} \quad (4.18)$$

$$u_c = \frac{2\kappa\sigma_0}{L_c} \quad (4.19)$$

$$w_c^p = \frac{2\alpha\sigma_0L_c}{G} \quad (4.20)$$

$$q_c = \left[ \frac{w(w_c^e)^{2+1/n}}{(2K)^{1/n}} \right] \left( \frac{\sigma_0}{L_c} \right)^{1/n} \quad (4.21)$$

and

$$w'_e(r', t') = R' \int_{\theta}^1 \frac{d\xi}{\sqrt{\xi^2 - \theta^2}} \int_0^{\xi} \frac{\eta p'_f(r', t') d\eta}{\sqrt{\xi^2 - \eta^2}} \quad (4.22)$$

$$w'(r', t') = w'_e - \left( \frac{w_c^p}{w_c^e} \right) w'_p \quad (4.23)$$

$$q'(r', t') = -(w')^{2+1/n} \left( \frac{\partial p'_f}{\partial r'} \right)^{1/n} \quad (4.24)$$

Formulation for  $u'$  or  $w'_p$  is the dimensional form, Eqn. (3.38) or Eqn. (3.37), divided by  $u_c$  or  $w_c^p$ , respectively.

Substituting the relevant variables as listed in the above into Eqn. (4.2) yields the following dimensionless fluid mass balance equation:

$$\frac{1}{r'} \frac{\partial(r'q')}{\partial r'} + \frac{w_c^e L_c}{q_c t_c} \left( \frac{\partial w'_e}{\partial t'} - \frac{w_c^p}{w_c^e} \frac{\partial w'_p}{\partial t'} \right) + \left( \frac{u_c L_c}{q_c} \right) u' = 0 \quad (4.25)$$

which can be further simplified by defining the characteristic time,  $t_c$ , by dictating

$$\frac{w_c^e L_c}{q_c t_c} = 1 \quad (4.26)$$

Therefrom,  $t_c$  is solved as

$$t_c = \frac{2^{1/n}}{\psi} \left[ \frac{\pi}{4(1-\nu)} \right]^{1+1/n} \left( \frac{K}{G} \right)^{1/n} \left( \frac{G}{\sigma_0} \right)^{1+2/n} \quad (4.27)$$

i.e.

$$t_c \propto \left(\frac{K}{G}\right)^{1/n} \left(\frac{G}{\sigma_0}\right)^{1+2/n} \quad (4.28)$$

which happens to agree with Cleary's definition [77, 26].

The simplified version of Eqn. (4.25) now becomes:

$$\frac{1}{r} \frac{\partial(rq)}{\partial r} + \frac{\partial w^e}{\partial t} + \frac{\alpha\pi}{2(1-\nu)} \frac{\partial w_p}{\partial t} + \left\{ \left[ \frac{\pi}{2(1-\nu)} \right] \left( \frac{\kappa G t_c}{L_c^2} \right) \right\} u = 0 \quad (4.29)$$

in which the prime denoting the dimensionless sense is dropped.

The concerned non-trivial dimensionless boundary/initial conditions to the above mathematical system are located at the wellbore:

$$q(0, t') = \lim_{r_w \rightarrow 0} \frac{Q_{0c}}{2\pi r_w} \quad (4.30)$$

in which,

$$Q_{0c} = \frac{Q_0}{q_c L_c} \quad (4.31)$$

Physically,  $t_c$  characterizes the time for the injected fluid to reach the fracture tip of radius,  $L_c$ ; and; furthermore, for the pressure inside the fracture to become uniform at  $\sigma_0$  if its pressure at the wellbore is maintained at the constant value,  $\sigma_0$ . Currently, the injection rate is used as the boundary condition at the wellbore. Thus, the resultant wellbore pressure does not remain constant. Therefore,  $t_c$  may not be very useful herein. However, for the purely elastic case without leakoff, the fluid mass balance equation can be reduced to the following simple dimensionless form:

$$\frac{1}{r} \frac{\partial(rq)}{\partial r} + \frac{\partial w^e}{\partial t} = 0 \quad (4.32)$$

which implies that in the purely elastic regime without leakoff, the fracture propagation in the dimensionless regime is dependent only on the non-dimensionalized injection rate,  $Q_{0c}$ . Any set of material and operation parameters should give an identical solution provided their corresponding  $Q_{0c}$  values are equal. As will be discussed in the subsequent chapter, this notion provides another means to check the numerical algorithm.

### 4.3 A Pseudo-Explicit Finite Difference Scheme

A number of papers have studied the penny-shaped HF propagation to different degrees of complexities. The earlier works, e.g. [23, 24, 21, 19], initialized the penny-shaped fracture configuration in HF simulation. Abe et al. (1976) [25] addressed the need to implement temporal variation of the fracture width, i.e. the unsteady flow. Zazovskii (1979) [150, 151] studied *separately* the influence of leak-off and the unsteady flow inside the fracture. Cleary and Wong (1985) [152] considered fluid lag, but no fluid leakoff. The penny-shaped fracture has also been modeled in the defense industry to investigate the explosive gas dynamics-induced fracture propagation [153, 154].

All the researchers show that the difficulty involved in modeling the HF is the nonlinear coupling between the two major mechanisms: fracture deformation and fluid flow inside the fracture. Experience indicates that the key in coping with the nonlinear coupling is to solve for the fluid flow and fracture deformation *simultaneously*. Cleary and Wong (1985) [152] achieved this by solving a matrix equation resulting from a fully-implicit FD discretization of both the fluid flow and elasticity equations. The integral method [153] and similarity solution method [26, 155, 154] semi-analytically combined these two submodels together. The successive approximations [150, 151] condensed the



various unknowns into two; thus, the coupling is closely simulated. To accommodate the various physical processes, including unsteady flow inside the fracture, pressure-dependent leakoff and poroelastic effects, these methods appear neither applicable nor efficient.

The finite difference method has the advantages of being physically straightforward and thus versatile in considering complicated physical processes. If an explicit scheme can be used, FD can be very efficient. This is especially true for McFrac because, mathematically, it is a 1-D problem. Indeed, these advantages of the explicit FD's have been witnessed in computing the PKN models that accounts for pressure-dependent leakoff and/or poroelastic effect [85, 60].

The key to success of an explicit FD method is the derivation of a universal adaptive time-marching criterion to ensure the stability of the solution. For the PKN model, an explicit point-wise relationship between the fracture aperture and the fracturing pressure can be derived because of the plane strain assumption perpendicular to the fracture (also the fluid flow) direction [85]. There is a direct proportionality between them:

$$w \propto p_f \tag{4.33}$$

in which,  $w$  and  $p_f$  are the aperture and pressure values at the same location. Although the resulting fluid mass balance equation is still highly nonlinear, a heuristic approach was proposed in [85] to derive an approximate time-stepping criterion:

$$\Delta t_c^{k+1} = \min \left[ \frac{\Delta \theta_i^2}{2(c_w)_i^k} \right]; \quad i = 1, \dots, N - 1 \tag{4.34}$$

$c_w$  comes from the diffusion part of the mass balance equation:

$$\frac{\partial w}{\partial t} = c_w \frac{\partial^2 w}{\partial \theta^2} + \frac{(2n+1)c_w}{w} \left( \frac{\partial w}{\partial \theta} \right)^2 + \frac{\theta}{L} \frac{dL}{dt} \frac{\partial w}{\partial \theta} \quad (4.35)$$

in which, the leakoff and poroelastic terms have already been ignored. For detailed explanation to Eqn. (4.34) and Eqn. (4.35), please refer to [85]. At least, Eqn. (4.34) has been shown to break down during fracture recession [60]. An *ad hoc* adaptive scheme was thus proposed by controlling "the time step size" calculated after Eqn. (4.34) "so that the variation of the width and its spatial derivative do not exceed a prescribed magnitude at each time step" [60]. Therefore, it is proper to say that Eqn. (4.34) is not universally adaptive as generally required by an explicit FD scheme.

More importantly, the above heuristic or *ad hoc* approach cannot be applied to the penny-shaped HF model because the pointwise relation of  $w$  vs.  $p_f$ . Eqn. (4.33), no longer holds for the penny-shaped configuration. Instead, an integral equation takes its place so that the fracture aperture at one point,  $i$ , is a function of the fracturing pressure at all the points along the fracture as shown in Eqn. (2.63).

The PEFD scheme is proposed to overcome the difficulty in deriving a universal adaptive time marching criterion for the penny-shaped model while retaining advantages of an explicit FD method. It is implicit in that it uses the implicit F.D. scheme to obtain the time marching. It is explicit, however, in that it does not need to solve a matrix equation; instead it solves one point at one time. The payoff is to iterate to get the convergence.

### 4.3.1 Discretization of Fluid Flow Equations

The numerical calculation of the fracture deformation,  $w^c$ , fluid leakoff,  $u$ , and poroelastic displacement,  $w^p$ , has been detailed in the previous chapters. Therein, a Chebyshev grid in the normalized coordinate system,  $s = r/R \in [0, 1]$ , is distributed along the fracture. In so doing, the various matrix equations relating the foregoing variables to the fluid pressure are independent of the fracture propagation. Once established at the beginning, they do not need to be re-computed throughout the fracture propagation steps.

The Chebyshev grid offers another advantage in discretizing the fluid mass balance equation, Eqn. (4.2). From Eqn. (2.62), the Chebyshev grid has a dense distribution of nodes near the ends of the fracture (Figure 4.2). This happens to provide more leverage to model the rapid variation there. Near the wellbore, as fluid is injected into the fracture, rapid variation in the field variables is expected. Within the fracture tip region, a dense mesh is desired because the tip is a mathematically singular point. Note that the two end nodes, 1 and  $N$ , do not coincide with the wellbore point or the fracture tip. A small but non-zero distance spans them, respectively (Figure 4.2).

Without loss of generality, an example of pure elasticity, Newtonian fluid, and no leakoff is cited here to describe the FD discretization and the PEFD scheme. Inclusion of the power-law fluid rheology, fluid leakoff, and the associated poroelastic effect will be detailed later. In this simplified case, the fluid mass balance at node “ $i$ ” can be written as:

$$\frac{1}{sR_0} \frac{\partial(sq)}{\partial s} + \frac{\partial w_i^c}{\partial t} = 0 \quad (4.36)$$

in which,  $s = r/R_0$  and the fracture radius is explicitly denoted by  $R_0$  to imply that currently, one only deals with a stationary fracture.

Numerically, Eqn. (4.36) is equivalent to:

$$\frac{1}{s_i R_0} \frac{s_{i+1/2} q_{i+1/2} - s_{i-1/2} q_{i-1/2}}{s_{i+1/2} - s_{i-1/2}} + \frac{w_{i,n}^m - w_{i,n-1}^m}{\Delta t} + \frac{\delta w_{i,n}^m}{\Delta t} = 0$$

$$i = 1, 2, 3, \dots \quad (4.37)$$

which is written for an iteration step,  $m + 1$ , in time step,  $n$ , in the incremental form as:

$$w_{i,n}^{m+1} = w_{i,n}^m + \delta w_{i,n}^m \quad (4.38)$$

with  $\delta w_{i,n}^m$  as the basic unknown. The subscripts ' $i \pm 1/2$ ' refer to the mid-positions between  $i$  and  $i \pm 1$ , respectively.

Special attention is needed for the near-boundary nodes in order to implement the boundary conditions. At node '1' which is the nearest to the wellbore (Figure 4.2),

$$2\pi R_0 s_{1-1/2} q_{1-1/2} = Q_0(t) \quad (4.39)$$

as from Eqn. (4.8), which gives:

$$s_{1-1/2} q_{1-1/2} = Q_0(t) / 2\pi R_0 \quad (4.40)$$

At node ' $N$ ', the nearest to the fracture tip,

$$q_{N+1/2} = 0 \quad (4.41)$$

since the fracture aperture at the tip is zero. Note that in these implementations, subscripts ' $1 - 1/2$ ' and ' $N + 1/2$ ' refer to the wellbore point and the fracture tip, respectively. Their corresponding coordinates are:

$$s_{1-1/2} = 0 ; \quad s_{N+1/2} = 1 \quad (4.42)$$

The flux,  $q$ , depends on the fluid pressure,  $p$ , and fracture width,  $w$ , via the cubic law, Eqn. (4.3), for the current Newtonian fluid rheology:

$$q_{i\pm 1/2} = -\frac{w_{i\pm 1/2}^3}{12\mu R_0} \left. \frac{\partial p}{\partial s} \right|_{s=s_{i\pm 1/2}} \quad (4.43)$$

The pressure derivative can be computed by:

$$\left. \frac{\partial p}{\partial s} \right|_{s=s_{i+1/2}} = \frac{p_{i+1} - p_i}{s_{i+1} - s_i} \quad (4.44)$$

and  $w_{i\pm 1/2}$  is taken as the corresponding arithmetic mean:

$$w_{i\pm 1/2} = \frac{w_i + w_{i\pm 1}}{2} \quad (4.45)$$

The fracturing pressure is related to the fracture width via the elasticity equation:

$$\delta p_{i,n}^m = c_{i,j}^p \delta w_{j,n}^m \quad i = 1, 2, 3, \dots, N \quad (4.46)$$

which is written in terms of increments.  $c_{i,j}^p$  is the inverse of matrix  $c_{ij}^w$  as defined in Eqn. (2.63). The repetitive index,  $j$ , in Eqn. (4.46) implies its summation over 1 to  $N$ .

As described earlier, there are two essential complicating factors in computing the penny-shaped propagation: one is the nonlinear coupling between the fracture deformation and fluid flow inside the fracture, which dictates that the fracture deformation and fluid flow be solved simultaneously. However, if the foregoing relevant equations are directly, without any tactic modifications, substituted into the discretized fluid mass balance equation, Eqn. (4.37), a set of nonlinear equations results in terms of the incremental width variables,  $\delta w_{i,n}^m$ . This is the other troublesome factor in modeling the penny-shaped fracture propagation, which is referred herein as the integro-differential nature

of the governing equations. The PKN model is not troubled by this factor because its  $w$  vs.  $p$  relation is directly proportional and point-wise [85, 60].

Solution of such a set of nonlinear equations is neither theoretically mature nor practically feasible. “*There are no good, general methods for solving systems of more than one nonlinear equation*” [146]. The only available method, the Newton-Raphson method, strongly depends on the initial guess about the solution, which is detrimental to a flexible program like McFrac. In view of this situation, the following pseudo-explicit FD (PEFD) scheme is proposed. The two troublesome factors, as discussed in the above, are all accounted for, but less strictly.

### 4.3.2 The PEFD Algorithm.

In PEFD, the fluid momentum equation, (4.43), is deliberately written as:

$$q_{i\pm 1/2} = C_{i\pm 1/2}^q w_{i\pm 1/2}^{m+1} \left. \frac{\partial p}{\partial s} \right|_{s=s_{i\pm 1/2}} \quad (4.47)$$

with,

$$C_{i\pm 1/2}^q \approx -\frac{(w_{i+1/2, \pi}^m)^2}{12\mu R_0} \quad (4.48)$$

using the fracture aperture value at the immediately previous iteration step,  $m$ .

In solving for node ‘ $i$ ’, PEFD further simplifies the momentum equation, (4.47), by assuming that width increments at nodes other than ‘ $i$ ’ are all zero, i.e.

$$\delta p_i = c_{ij} \delta w_j \quad (4.49)$$

in which, the repetitive  $j$  does not mean summation. In so doing, Eqn. (4.47)

becomes:

$$q_{i+1/2} \approx C_{i+1/2}^q \left[ \frac{1}{2}(w_{i,n}^m + w_{i+1,n}^m) + \frac{\delta w_{i,n}^m}{2} \right] \left[ \frac{p_{i+1,n}^m - p_{i,n}^m}{s_{i+1} - s_i} + \frac{(c_{i+1,i}^p - c_{i,i}^p)\delta w_{i,n}^m}{s_{i+1} - s_i} \right] \quad (4.50)$$

or,

$$q_{i+1/2} \approx C_{i+1/2}^q \left[ w_{i+1/2} + \frac{\delta w_i}{2} \right] \left[ \left. \frac{\partial p}{\partial s} \right|_{i+1/2} + \frac{(c_{i+1,i}^p - c_{i,i}^p)\delta w_i}{s_{i+1} - s_i} \right] \quad (4.51)$$

$$= c_{0,i+1/2}^q + c_{1,i+1/2}^q \delta w_i + c_{2,i+1/2}^q (\delta w_i)^2 \quad (4.52)$$

where the indices for time and iteration steps are dropped. The coefficients  $c_{0(1,2),i+1/2}^q$  come from the associated factorization of Eqn. (4.51) and the expressions are not given here.

Therefore, the fluid mass balance equation, (4.37), is reduced to:

$$\begin{aligned} & \frac{\theta_{i+1/2} \left[ c_{0,i+1/2}^q + c_{1,i+1/2}^q \delta w_i + c_{2,i+1/2}^q (\delta w_i)^2 \right]}{R(\theta_{i+1/2} - \theta_{i-1/2})} \\ & - \frac{\theta_{i-1/2} \left[ c_{0,i-1/2}^q + c_{1,i-1/2}^q \delta w_i + c_{2,i-1/2}^q (\delta w_i)^2 \right]}{R(\theta_{i+1/2} - \theta_{i-1/2})} \\ & + \frac{w_i - w_i^0}{\Delta t} + \frac{\delta w_i}{\Delta t} = 0 \end{aligned} \quad (4.53)$$

or,

$$c_{0i}^m + c_{1i}^m \delta w_i + c_{2i}^m (\delta w_i)^2 = 0 \quad (4.54)$$

Again, the various  $c_{0(1,2),i}^m$ 's are after the factorizing procedure. Therefore, the PEFD has finally given a single equation for a single unknown,  $\delta w_{i,n}^m$ , similar to the fully-explicit FD scheme. Eqn. (4.54) is a quadratic equation; the choice of the appropriate solution from the two roots can be made easily by using physical intuition. That is, the total fracture aperture must be positive or at least zero.

After solving for node 'i', the pressure profile is updated using the updated width profile before proceeding to solve for the next node 'i + 1'.

To get a converging solution, iterations are performed. The whole process, as outlined above, is repeated until the following convergence check variable:

$$R_f = \frac{1}{V_{in,j}} \int_0^t d\lambda \left[ 2\pi R^2(\lambda) \int_0^1 r_f(s, \lambda) s ds \right] \quad (4.55)$$

meets the convergence condition:

$$R_f \leq \epsilon_f \quad (4.56)$$

in which,  $\epsilon_f$  is a given small number. In Eqn. (4.55),  $V_{in,j}$  is the total injected fluid volume. In general, i.e. for the case of a propagating fracture in poroelastic media,  $r_f$  is the unbalanced local fluid mass, i.e. the non-zero L.H.S. value of Eqn. (4.2) in the discretized form which is computed after all the nodes have been solved during each iteration step. The time integral in Eqn. (4.55) is approximated by the simple accumulation of the spatial integral within each time step,  $k$ , i.e.

$$\int_0^t d\lambda \left[ 2\pi R^2(\lambda) \int_0^1 s r_f(s, \lambda) ds \right] \approx \sum_{k=0}^n (t_{k+1} - t_k) (R_f^{k+1} + R_f^k) \quad (4.57)$$

with,

$$\begin{aligned} R_f^k &= \pi R^2(t_k) \int_0^1 s r_f(s, t_k) ds \\ &\approx \left( \frac{\pi R_0^2}{2} \right) \sum_{j=1}^N \left[ r_{f,j}(t_k) (s_{j+1/2}^2 - s_{j-1/2}^2) \right] \end{aligned} \quad (4.58)$$

in which,  $r_{f,j}(t_k)$  is the corresponding unbalanced local fluid mass at node,  $j$ , and at time,  $t_k$ , i.e. the L.H.S. value of Eqn. (4.37) at this particular location in case of pure elasticity without leakoff.



The definition of  $R_f$  in Eqn. (4.55) comes from taking both the temporal and spatial integral on the local fluid mass balance equation, e.g. Eqn. (4.2), so that:

$$\int_0^t d\lambda \int_0^1 \left[ \frac{\partial(sq)}{\partial s} + sR(\lambda) \frac{\partial w(s, \lambda)}{\partial \lambda} + sR(\lambda)u(s, \lambda) \right] ds = \int_0^t d\lambda R(\lambda) \int_0^1 sr_f(s, \lambda) ds \quad (4.59)$$

in which, the unbalanced mass,  $r_f$ , is inserted to account for the inaccuracy caused by the numerical discretization, including the PEFD procedure. Carrying out the integrations in Eqn. (4.59) yields the following physically self-evident equation:

$$-V_{inj} + V_{crk} + V_{lek} = V_{inj}R_f \quad (4.60)$$

measured at the current time,  $t$ . In Eqn. (4.60),  $R_f$  is defined by Eqn. (4.55) and  $V_{crk}$  is the current crack volume,

$$V_{crk}(t) = 2\pi R^2(t) \int_0^1 w(s, t) s ds \quad ; \quad (4.61)$$

and  $V_{lek}$  is the accumulated leakoff volume through the propagating fracture:

$$V_{lek} = \int_0^t d\lambda 2\pi R^2(\lambda) \int_0^1 su(s, \lambda) ds \quad . \quad (4.62)$$

Therefore, Eqn. (4.60) implies that the convergence check variable,  $R_f$ , represents the total unbalanced global mass portion so far among the total injected fluid:

$$R_f = \left| 1 - \frac{V_{crk} + V_{lek}}{V_{inj}} \right| \quad . \quad (4.63)$$

Theoretically,  $R_f$  should be zero when convergence is strictly fulfilled. In the numerical calculation, a small threshold value,  $\epsilon_f$ , is permitted.

## 4.4 Qualitative Validation of the PEFD

In this section, an example is used to exemplify the PEFD's performance. Analyses are carried out in regards to the fluid front progression inside the fracture, evolution of the wellbore response and profiles of pressure/fracture aperture as well as the global mass balance based on the convergence measure,  $R_f$ . Therefore, it provides a means to validate the PEFD in a qualitative sense. It also reveals the necessity to develop a supplementary algorithm to enhance the PEFD's convergence rate when the fluid pressure inside the fracture becomes uniform.

In this example, fluid is pumped into a pre-existing fracture of a constant length. As a benchmark case, a fracture 10 m long is discretized by a 10-order Chebyshev grid. A constant time step of 1 second is used. The iteration tolerance is set at  $\epsilon_f = 1\%$ . The other relevant material and operational parameters are listed in Table 4.1.

### 4.4.1 Fluid Flow inside the Fracture.

In Figure 4.3, the fracture aperture profiles at earlier times illustrate the fluid front advancement inside the fracture. Fluid progresses gradually toward the fracture tip. In the present case, it takes about 13 seconds for the fluid to reach there. The advancing rate is not uniform, initially rapid and then approaching zero (Figure 4.4). The fluid front in Figure 4.4 is taken as the first node where the fracture aperture still remains at zero.

After the fluid reaches the fracture tip, its further movement beyond is prevented. Fluid accumulates inside the fracture and its pressure builds up and becomes uniform as suggested in Figure 4.5. Correspondingly, the fracture

aperture profiles become more like an elliptic shape (Figure 4.6). This stage is reached after about 40 seconds of pumping. Thereafter, the computations agree well with the similarity solution to be discussed later (Figure 4.7).

Figure 4.7 displays the evolution of the global variables, including the fluid pressure and fracture aperture at the wellbore, the stress intensity factor as well as the average pressure along the fracture. At least, three periods can be distinguished:

- (a) *Period 1.*  $0 \leq t < 13$  s. Fluid has not advanced to the fracture tip. Fracture aperture at the wellbore increases, but the increasing rate gradually slows down. The stress intensity factor remains at zero. Initially, pressure at the wellbore decreases rapidly. Then, the decrease gradually slows down. However, the average pressure along the fracture increases almost linearly. During this period, the similarity solution does not hold. Therefore, large differences exist between the analytical results and the computations (Figure 4.7).
- (b) *Period 2.*  $13 \leq t \leq 40$  s. Fluid has reached the fracture tip, but the pressure has not built up to the extent that its profile has become uniform. During this period, the increasing rate of the fracture aperture at the wellbore is raised to a new level and extends to the linear range in the subsequent Period 3. The stress intensity factor rises rapidly and approaches a constant rate. During this period, pressure at the wellbore initially continues its decreasing trend inherited from Period 1, but later begins to increase. The average pressure continues its linear increasing trend.
- (c) *Period 3.*  $t > 40$  s. The injected fluid uniformly raises the pressure inside the fracture. An elliptical shape of the fracture opening results. All the

global variables show a linear increasing trend. The wellbore pressure and the average pressure emerge together, representing the uniform pressure profile.

#### 4.4.2 Convergence of the PEFD

At early times before the fluid pressure inside the fracture becomes uniform, the PEFD algorithm works very efficiently. Each iteration takes about  $10^{-9}$  seconds of CPU time on an IBM 486 66MHz PC. A few hundreds of such iterations generally achieve the convergence for a given time step. For example, Figure 4.8 shows the evolution of the iteration convergence measure,  $R_f$ , and the global mass balance check.

$$R_{mas} = \frac{V_{crk} + V_{lek}}{V_{inj}} \quad (4.64)$$

after each iteration step during time step no. 2, i.e. at  $t = 2$  s.  $V_{lek}$  in Eqn. (4.64) represents the leaked fluid volume, which is zero for the current no-leakoff case.

Theoretically, at convergence, the injected fluid volume,  $V_{inj}$  is expected to be 100% occupied by the current crack volume,  $V_{crk}$  and the local fluid mass balance equation, Eqn. (4.37) is rigorously met, i.e.,  $R_{mas} = 1$  and  $R_f = 0$ . Indeed, Figure 4.8 shows this trend. The mass balance is rapidly met either locally or globally with  $R_f$  approaching zero and  $R_{mas}$  increasing towards unity. A total of 120 iterations suffice to bring the iteration convergence to the prescribed level.

However, Figures 4.9-10 reveal one of the drawbacks with the PEFD scheme, i.e. as the fluid pressure inside the fracture builds up to be relatively uniform, the PEFD convergence becomes very slow and it takes over several thousands

iterations to arrive at the converged solution (Figure 4.9). As a result, the number of iterations taken for each time step, if computed by PEFD alone, increases exponentially (Figure 4.10). In the following section, a new algorithm is derived to assist PEFD in overcoming the difficulty of slow convergence at late times.

## 4.5 Newton-Raphson Scheme

In this section, the cause of the slow convergence in PEFD at later time is first analyzed. The Newton-Raphson (NR) scheme for a system of nonlinear equations is implemented. Such a combined NR-PEFD algorithm solved the slow convergence problem.

### 4.5.1 Effect of the PEFD Simplifications

There have been two key steps in the PEFD algorithm. One is to retain both linear terms of  $w$  and  $p$  in the fluid momentum equation, 4.47, so that both the elastic deformation and the fluid flow are accounted for simultaneously. This step is essential to tackle the strong nonlinearity involved. Then, as done in Eqn. (4.50), the fluid flux,  $q_{i\pm 1/2}$ , is further simplified to be dependent on  $\delta w_{i,n}^m$  only by introducing Eqn. (4.49). This step is to avoid solving a set of nonlinear equations. These simplifications break down the local fluid mass balance, which in turn affects the global mass balance. In order to clarify the effect, let us compare the local mass balance equation with and without the simplifications. Obviously, all the exercises center around the term  $I = w^3 \frac{\partial p}{\partial \theta}$ . With the simplifications,  $I$  becomes:

$$I_{PEFD,i+1/2} = (w_{i+1/2})^2 \left[ w_{i+1/2} + \frac{\delta w_i}{2} \right] \left[ \left. \frac{\partial p}{\partial \theta} \right|_{i+1/2} + \frac{(c_{i+1,i}^p - c_{i,i}^p) \delta w_i}{\theta_{i+1} - \theta_i} \right]$$

$$\begin{aligned}
&= (w_{i+1/2})^3 \frac{\partial p}{\partial \theta} \Big|_{i+1/2} + \left[ \frac{(w_{i+1/2})^3 (c_{i+1,i}^p - c_{i,i}^p)}{\theta_{i+1} - \theta_i} \right. \\
&+ \left. \frac{(w_{i+1/2})^2}{2} \frac{\partial p}{\partial \theta} \Big|_{i+1/2} \right] \delta w_i + \left[ \frac{(w_{i+1/2})^2}{2} \frac{c_{i+1,i}^p - c_{i,i}^p}{\theta_{i+1} - \theta_i} \right] (\delta w_{i+1}) \quad (4.65)
\end{aligned}$$

Without the simplifications.

$$I_{exact,i+1/2} = I_{PEFD,i+1/2} + R_{i+1/2} \quad (4.66)$$

i.e.  $R_{i+1/2}$  represents the error introduced in the PEFD scheme. Ignoring width increments with powers higher than second-order,  $R_{i+1/2}$  can be written as:

$$\begin{aligned}
R_{i+1/2} &\approx \bar{w}^3 \sum_{j=1, j \neq i}^N \frac{c_{i+1,j} - c_{i,j}}{\theta_{i+1} - \theta_i} \delta w_j + \bar{w}^2 \left( \delta w_i + \frac{3}{2} \delta w_{i+1} \right) \frac{\partial p}{\partial \theta} \Big|_{i+1/2} \\
&+ \frac{3}{4} \bar{w} (\delta w_i + \delta w_{i+1})^2 \frac{\partial p}{\partial \theta} \Big|_{i+1/2} + \frac{\bar{w}^2}{2} \sum_{j=1, j \neq i}^N \frac{c_{i+1,j} - c_{i,j}}{\theta_{i+1} - \theta_i} \delta w_j \delta w_j \\
&+ \bar{w}^2 \left( \delta w_i + \frac{3}{2} \delta w_{i+1} \right) \frac{\partial p}{\partial \theta} \Big|_{i+1/2} \sum_{j=1}^N \frac{c_{i+1,j} - c_{i,j}}{\theta_{i+1} - \theta_i} \delta w_j \quad (4.67)
\end{aligned}$$

The overbar denotes the arithmetic average between nodes  $i$  and  $i+1$ . It is thus clear that the coefficients of the width increment terms in both  $I_{PEFD,i+1/2}$  and  $R_{i+1/2}$  are comparable. For the material properties as listed in Table 4.1, the order of magnitudes of the various terms can be estimated as:

$$I_{PEFD,i+1/2} \sim 10^{-5} + 10^{-1} \delta w_i + 10 (\delta w_i)^2 \quad (4.68)$$

$$R_{i+1/2} \sim \sum_{j=1, j \neq i}^N 10^{-1} \delta w_j + \sum_{j=1, j \neq i}^N 10 \delta w_i \delta w_j \quad (4.69)$$

At early times, the fracture aperture near the fracture tip are either zero or very small as the fluid has not reached the tip or the fluid pressure has not built up so much therein. During this period, dropping the width increments at nodes in this region does not result in a large error. Expectedly, the convergence is fast as shown in Figure 4.8. On the other hand, however, when

the fluid pressure approaches a uniform distribution inside the fracture, all the nodes experience a comparable width increment,  $\delta w$ . By dropping the  $\delta w$  for other than the current node, large errors result. This causes the slow convergence as witnessed in the current example at late times when the pressure profile becomes uniform (Figure 4.9). In order to circumvent this difficulty, the algorithm must incorporate as much nodal information as possible in the solution procedure. In the following, a strategy is implemented which does not make the simplification of Eqn. (4.49); instead, the full relationship, Eqn. (4.46), is applied. The Newton-Raphson method is employed to solve the resultant system of nonlinear equations with the required initial guess about the solution provided by PEFD.

#### 4.5.2 Derivation of NR Algorithm

The Newton-Raphson scheme for finding the root(s) of a nonlinear equation system has been described in [146]. The following is its straightforward application to the current task of modeling the penny-shaped HF propagation. Given the general power-law fluid rheology, the fluid momentum equation, (4.1), can be re-written as:

$$\begin{aligned} q &= -\text{Sign} \left( \frac{\partial p}{\partial \theta} \right) \left( \frac{\psi^n}{2K R_o} \right)^{1/n} w^{2+1/n} \left( \left| \frac{\partial p}{\partial \theta} \right| \right)^{1/n} \\ &= C^q w^{2+1/n} \left( \left| \frac{\partial p}{\partial \theta} \right| \right)^{1/n} \end{aligned} \quad (4.70)$$

in which,  $C^q$  now changes to:

$$C^q = -\text{Sign} \left( \frac{\partial p}{\partial \theta} \right) \left( \frac{\psi^n}{2K R_o} \right)^{1/n} \quad (4.71)$$

and  $\text{Sign}(x)$  function denotes the sign of  $x$ :

$$\text{Sign}(x) = \begin{cases} 1 & \text{if } x > 0 \\ -1 & \text{if } x < 0 \end{cases} \quad (4.72)$$

If discretized at node ' $i + 1/2$ ', Eqn. (4.70) becomes:

$$q_{i+1/2} = C_{i+1/2}^q (w_{i+1/2})^{2+1/n} \left( \frac{p_{i+1} - p_i}{\theta_{i+1} - \theta_i} \right)^{1/n} \quad (4.73)$$

in which the sign for the absolute value of the pressure gradient is omitted for simplicity.

In NR, the pressures are taken as the basic unknowns and the elastic fracture aperture,  $w^e$ , is expressed as the function of the pressures by Eqn. (2.63). Finally, after substituting Eqn. (4.73) into Eqn. (4.37) results in the following set of nonlinear equations:

$$F_i(p_1, p_2, \dots, p_N) = 0 \quad i = 1, 2, \dots, N \quad (4.74)$$

In solving for time step,  $n$ , and proceeding from iteration step,  $m$  to  $m+1$ , Eqn. (4.74) can be expanded into a Taylor series around the solution at iteration step,  $m$ :

$$F_i(\mathbf{P}_n^{m+1}) = F_i(\mathbf{P}_n^m) + \sum_{j=1}^N \frac{\partial F_i}{\partial p_j} \delta p_{j,n}^m + O[(\delta \mathbf{P}_n^m)^2] \quad i = 1, 2, \dots, N \quad (4.75)$$

where the bold symbols represent the vector of the corresponding variables. Truncating the terms higher than the first-order yields the following linear equation for  $\delta p_{j,n}^m$ :

$$\sum_{j=1}^N \alpha_{ij} \delta p_j = \beta_i \quad i = 1, 2, \dots, N \quad (4.76)$$

The coefficients,  $\alpha$  and  $\beta$ , are listed in Appendix D.

After the current iteration, the total solution is updated to:

$$p_{i,n}^{m+1} = p_{i,n}^m + \delta p_{i,n}^m \quad (4.77)$$



At the beginning of each time step, the initial guess for the solution is solved by PEFD. The iteration ends when Eqn. (4.56) is met. The NR algorithm, if provided with a good initial guess, is very efficient at arriving at the true solution. The example in Figure 4.7, if calculated by the combined PEFD-NR algorithm, takes only 2 seconds of the CPU time on IBM 486 66 MHZ PC while the PEFD alone consumes much more, i.e. over 1,000 seconds. The results from the two methods are essentially identical.

### 4.5.3 Relationship between PEFD and NR Schemes

Inevitably, the remarkable efficiency of the NR scheme may cause one to wonder why the PEFD scheme is needed. The answer is that PEFD is needed to provide a correct initial guess for NR. Also, as pointed out in [146], the NR method “*gives you a very efficient means of converging to the root, if it exists, or of spectacularly failing to converge, indicating that your putative root does not exist nearby.*” Therefore, the issue is to identify the appropriate neighborhood of a root in which the solution to be sought is guaranteed to exist. In our experience, if the NR is used alone, its solution is either found dependent on the initial guess; or it simply cannot converge. For example, if NR is used alone, Figure 4.11 shows the computed pressure response at the wellbore for the same problem as in Figure 4.7 using different initial guesses for the pressure profile at the beginning of the solution, i.e. at the beginning of time step no. 1. Obviously, the final computations deviate significantly among the various initial guessed pressure profiles.

Fortunately, the PEFD can correctly approximate the root within the range around the correct solution. For each time step, PEFD is first invoked to predict the solution for NR. If NR has not converged after 100 iteration steps,

the PEFD subroutine is called back, this time for more steps before handing the solution procedure to NR. In general, with this precaution, NR will indeed yield a converged solution. If still not, PEFD is mobilized again for more steps (Figure 4.12). Such a combination of PEFD and NR has successfully solved all of our computed examples.

Figure 4.10 also shows the number of iterations taken by the NR-enhanced PEFD algorithm for each time step. With PEFD first called only once, NR then correctly locates the solution. And all the computations given by the combined PEFD-NR scheme based on the different initial guesses are identical.

## **4.6 Quantitative Validation of the PEFD**

In Section 4, the PEFD has been qualitatively examined for its computed fluid flow pattern inside the fracture and its convergence performance. Therefrom, it can be concluded that all the computations are at least physically valid. It is also shown that the PEFD converges and preserves the mass balance.

This section extends the validation to the qualitative comparison. The lack of decent comparison examples makes the full quantitative verification difficult. The various solutions for the similar penny-shaped fracture configuration are based on different simplifications. All the results are obtained by complicated numerical methods. Neither the assumptions nor the results are ready to be repeated. Fortunately, at late times when the fluid pressure inside the fracture becomes relatively uniform, there is an analytical similarity solution. In this section, the late-time computations are compared to this analytical prediction. The stability and consistency of the PEFD scheme is then numerically examined.

### 4.6.1 Similarity Solution at Late Times

For a stationary penny-shaped fracture of radius,  $R_0$ , within a pure elastic medium, a similarity solution exists if the pressure profile within the fracture is assumed to be uniform at  $p_f(t)$ . The elastic fracture aperture profile is elliptic:

$$w(s, t) = \frac{4(1 - \nu)p_f(t)R_0}{\pi G} \sqrt{1 - s^2} \quad (4.78)$$

The corresponding crack volume is given by:

$$V_{crk} = \frac{8(1 - \nu)p_f(t)R_0^3}{3G} \quad (4.79)$$

Based on the global mass balance, i.e.  $Q_0 t = V_{crk}$  if a constant injection rate,  $Q_0$  and no fluid leakoff are assumed, the pressure and fracture aperture profiles as well as the stress intensity factor are derived as follows:

$$p_f(t) = \frac{3Q_0 G}{8(1 - \nu)R_0^3} t \quad (4.80)$$

$$w(s, t) = \frac{3Q_0}{2\pi R_0^2} t \sqrt{1 - s^2} \quad (4.81)$$

$$K_I(t) = \left( \frac{\sqrt{2R_0}}{\pi} \right) p_f(t) \quad (4.82)$$

As shown in Figure 4.5, the fluid pressure inside the fracture is indeed uniform at late times, e.g.  $t > 40$  s. Thus, it is expected that the computations will then agree well with Eqn. (4.80)-Eqn. (4.82). The comparison is indeed very good as shown in Figure 4.7 and Tables 4.3 and 4.5. Both tables show that the relative error decreases with time. Table 4.5 further indicates that the best agreement has less than 0.5% relative error.

### 4.6.2 Stability and Consistency

Next, the time stepping size,  $\Delta t$ , is varied to check the stability of the algorithm. Figure 4.13 and Tables 4.2-3 show that stability is realized. One order of difference in the time stepping gives identical wellbore responses at late times, and only a little difference exists at earlier times between the various  $\Delta t$ s (Figure 4.13). Table 4.2 details the comparison by listing the difference between the neighboring time steps for the early-time results; and Table 4.3 gives the computational error relative to the late-time analytical results. In Table 4.2,  $\delta w$  or  $\delta p$  for  $\Delta t = 1.0$  comes after taking the difference between  $\Delta t = 1.0$  and 0.5; for  $\Delta t = 5.0$ , it is the difference between  $\Delta t = 5.0$  and 1.0; for  $\Delta t = 10$ , it is between  $\Delta t = 10$  and 5. The difference calculated this way shows a decreasing trend as  $\Delta t$  decreases (Table 4.2). This means that the time stepping effect is consistent — — — a smaller difference in the time stepping gives smaller difference in the computations or vice versa. Table 4.3 shows that the different  $\Delta t$ s give an identical computed relative error at the same time. It therefore suggests the stability.

Consistency of the algorithm is checked by varying the number of Chebyshev grid points,  $N$ . As shown in Figure 4.14 and Tables 4.4-5, the early-time computations are indeed very much affected by the grid discretization. However, as the grids become denser, i.e. as  $N$  increases, the computations differ less. The early-time inaccuracy diminishes with time and does not propagate to the late-time period. This observation has been graphically shown in Figure 4.14. It is further supported by the more detailed quantitative comparison in Tables 4.4-5.

Table 4.4 is constructed similar to Table 4.2 except the varying parameter now changes to the Chebyshev nodal number,  $N$ , i.e. the difference,  $\delta w$  or

$\delta p$ , is after the subtraction between the neighboring  $N$ s. Unlike for  $\Delta t$ , the  $N$ s now increases from 5 to 20 by a constant increment. Table 4.4 shows that the difference decreases as the Chebyshev grid becomes denser, i.e.  $N$  increases. Therefore, it suggests that further increasing  $N$  could yield an identical result, i.e. the consistency of changing the grid discretization is realized. This conclusion has its further support, perhaps even more clearly, from Table 4.5 where the late-time computations are listed and compared with the analytical solutions, Eqn. (4.81) or Eqn. (4.80), to give the relative error measurement. Therefrom, it is obvious that the denser discretization, i.e. a larger  $N$ , yields better computational accuracy.

The keen sensitivity of early-time computations to the discretization is mostly caused by the inaccuracy in computing the fluid front before the fluid moves to the tip. Different numbers of grid points give different movement patterns for the fluid front (Figure 4.4). The denser grids give closer patterns, thus, the computations differ less.

The consistency is also checked by varying the iteration convergence threshold value,  $\epsilon_f$ . Figures 4.15 show that with a decreasing  $\epsilon_f$ , i.e. as the fluid mass balance is more strictly enforced, the computations moves closer to the analytical solutions. After  $\epsilon_f \leq 1\%$ , reducing  $\epsilon_f$  further does not have significant effect.

## 4.7 Power-law Fluid Rheology

Allowance of power-law fluid rheology can easily be made with the NR algorithm. As derived in Section 4.5, the power-law parameters are directly entered into the expressions and, therefore, no iterations are necessary. This is, however, under the condition that the pressure gradient remains unchanged

in sign during each iteration for pressure increments. In the power-law expression, Eqn. (4.73), it is implied that the pressure gradient is taken as its absolute value so that its derivative with respect to the pressures can be written as:

$$\frac{\partial \left( \frac{p_{i+1} - p_i}{\theta_{i+1} - \theta_i} \right)}{\partial p_j} = S_{i+1/2}^p \left( \frac{\delta_{i+1,j} - \delta_{i,j}}{\theta_{i+1} - \theta_i} \right) \quad (4.83)$$

$S_{i+1/2}^p$  denotes the sign of the pressure gradient and  $\delta_{i,j}$  is the Kronecker delta.

In most cases, the pressure gradient does not change in sign during consecutive iterations. However, during the multiple ISF cycles and at the time when pumping-in stops or is followed by pumping-back (or vice versa), pressure gradients at some points no longer hold the same sign as in the previous iteration step. In McFrac, allowance is made for this situation by an iterative procedure for the power-law fluid. This procedure is evoked in the early 10 time steps (the "10" is essentially arbitrary) of each new pumping event. In this procedure, the fluid momentum equation is written as the Newtonian fluid form:

$$q = -\frac{\psi^n}{2R\mu_e} w^3 \frac{\partial p}{\partial \theta} \quad (4.84)$$

in which  $\mu_e$  is called effective Newtonian viscosity and computed by:

$$\mu_e = K \left( \frac{|q|}{w^2} \right)^{n-1} \quad (4.85)$$

using the solution at the immediately previous iteration step. Doing so, the computation of fracture width and pressure is based on an equivalent Newtonian fluid and it is not necessary to distinguish the pressure gradient sign. An iteration loop is enforced to ensure converged power-law fluid properties. That is, prior to each current iteration,  $l$ , for the power-law fluid, the effective

Newtonian viscosity,  $\mu_e$ , is updated based on the solution at the end of previous iteration,  $l - 1$ . At the end of the current iteration, a new set of  $\mu_e$  values are computed based on the current results and compared with the previous  $\mu_e$ . Convergence is met if:

$$\sum_{i=1}^N \left| \frac{\mu_{e,i}^l - \mu_{e,i}^{l-1}}{\mu_{e,i}^{l-1}} \right| \leq \epsilon_u \quad . \quad (4.86)$$

At the beginning of each new time step, the  $l - 1$  iteration steps are taken at the end of the previous time step. At the beginning of time step 1, the fluid flux,  $q$ , is estimated from the given pumping rate,  $Q$ , so that:

$$\mu_e = K \left( \frac{10Q}{w^2} \right)^{n-1} \quad (4.87)$$

in which the factor “10” comes from a rough estimate about the effect of wellbore radius on conversion from  $Q$  to  $q$ .  $w$  is computed under the assumption of a uniform pressure profile.

The previous example listed in Table 4.1 is re-computed by changing the fluid rheology to power-law in which  $K = 2.5 \times 10^{-7}$  MPa.s <sup>$n$</sup>  and  $n = 0.8$ . Figure 4.16 displays the effective viscosity,  $\mu_e$ , of the fluid moving inside the fracture. Due to the shear-thinning, the fluid viscosity is reduced as compared to the Newtonian one ( $\mu = 250$  cp and the solid line in Figure 4.16). Relatively, the viscosity attains the smallest value near the wellbore and the largest near the fracture tip. This corresponds well to the fact that the fluid moves fastest near the wellbore and staggers near the fracture tip because it is prevented from moving further. Owing to the reduced viscosity, the fluid flows faster in the fracture. The fracture aperture profile is flatter, i.e. smaller near the wellbore, but larger towards the fracture tip, as compared to the Newtonian case (Figure 4.17). By the same token, the fluid reaches the fracture tip earlier so that its

computations start earlier to agree with the similarity solution (Figure 4.18). Note that the fluid rheology plays no role at late times when the pressure profile becomes uniform (Figure 4.18). This is predicted by the analytical solution, Eqn. (4.80)-Eqn. (4.82). Figure 4.18 also includes an example which further reduces the power-law flow behavior index,  $n$ , to 0.2. This enhances the shear-thinning effect, i.e. further lowers the fluid viscosity. As a result, the fluid reaches the tip and its pressure profile becomes uniform at even earlier times. The computed wellbore response agrees with the analytical results almost instantly upon starting the pumping.

## 4.8 Implementation of the Poroelastic Effects

When the poroelastic effect is considered, the fluid mass balance contains two additional contributions: one is the poroelastic fracture closure,  $w^p$  and the other is the fluid leakoff,  $u$ . Their calculation has already been given in Chapter 3 by two formulae, Eqn. (3.37) and Eqn. (3.38), and their extensions to a propagating fracture, Eqn. (3.45) and Eqn. (3.46).

At the current time,  $t$  which corresponds to the  $n$ -th time step, Eqn. (3.45) tells that  $w^p$  can be broken into the following two parts:

$$w^p(r, t) = w_n^{0,p}(r, t) + \Delta w_n^p(r, t) \quad (4.88)$$

with,

$$w_n^{0,p}(r, t) = p_f(s, \tau)w^p(r, t - \tau; R_\tau) + \sum_{k=1}^{n-1} \left\{ \int_{t_{k-1}}^{t_k} \left[ \frac{\partial p_f(s, \xi)}{\partial \xi} \right] w^p(r, t - \xi; R_\xi) d\xi \right\} \quad (4.89)$$

$$\Delta w_n^p(r, t) = \int_{t_{n-1}}^t \left[ \frac{\partial p_f(s, \xi)}{\partial \xi} \right] w^p(r, t - \xi; R_\xi) d\xi \quad (4.90)$$



in which,  $t_0 = \tau$ .  $w_n^{0,p}(r, t)$  is known since the pressure and fracture propagation history before the current  $n$ -th time step has been solved. However,  $\Delta w_n^p(r, t)$  contains the unknown pressure,  $p_f(s, t)$ . Physically, this integral represents the contribution from the current time step,  $t \in [t_{n-1}, t]$ . To simplify the calculation, the time stepping size,  $\Delta t = t - t_{n-1}$ , is constrained by the following condition:

$$\Delta t \leq \frac{t_{1D} R_n^2}{\kappa M} \quad (4.91)$$

so that  $\Delta w_n^p$  can be adequately represented by the 1-D poroelastic model, Eqn. (2.32), i.e.

$$\Delta w_n^p(r) = \frac{2\eta \sqrt{c}}{G \sqrt{\pi}} \left[ \int_0^{\Delta t} d\tau \int_0^r \frac{dp_f(r, \xi)}{d\xi} \frac{d\xi}{\sqrt{\tau - \xi}} \right] \quad (4.92)$$

in which, a factor, "2", is added to the original equation, Eqn. (2.32), to count for the upper and lower fracture surfaces (the same applies to the following leakoff rate formula). Eqn. (4.91) simply comes from the 1-D validity range as shown in Eqn. (3.37) (where  $t_{1D}$  is taken as  $10^{-3}$ ). Similarly, the leakoff rate can be decomposed into:

$$u(r, t) = u_n^0(r, t) + \Delta u_n(r, t) \quad (4.93)$$

with,

$$u_n^0(r) = p_f(s, \tau) u(r, t - \tau; R_\tau) + \sum_{k=1}^{n-1} \left\{ \int_{t_{k-1}}^{t_k} \left[ \frac{\partial p_f(s, \xi)}{\partial \xi} \right] u(r, t - \xi; R_\xi) d\xi \right\} \quad (4.94)$$

$$\Delta u_n(r) = \frac{2\kappa}{\sqrt{\pi c}} \int_0^{\Delta t} \frac{1}{\sqrt{\Delta t - \xi}} \frac{\partial p_f(r, \xi)}{\partial \xi} d\xi \quad (4.95)$$

In the numerical discretization,  $\Delta u$  can be approximated via the following exercise:

$$\Delta u_{i,n}^{m+1,p} \approx \frac{2\kappa}{\sqrt{\pi c}} \frac{\Delta p_{f,i}}{\Delta t} \int_0^{\Delta t} \frac{1}{\sqrt{\Delta t - \xi}} d\xi$$

$$= \frac{4\kappa}{\sqrt{\pi}c\Delta t} \left[ (p_{i,n}^m - p_{i,n-1}) + \delta p_{i,n}^m \right] \quad (4.96)$$

Similarly,

$$\Delta w_{i,n}^{m+1,p} \approx \frac{8\eta\sqrt{\Delta t}}{3G} \sqrt{\frac{c}{\pi}} \left[ (p_{i,n}^m - p_{i,n-1}) + \delta p_{i,n}^m \right] \quad (4.97)$$

Here,  $p_{i,n}^m$  and  $p_{i,n-1}$  are all known at the current iteration step.  $\delta p_{i,n}^m$  is the unknown, dependent on the width increments as shown in Eqn. (4.46) or Eqn. (4.49), if the PEFD simplification is used.

With the poroelastic effects included, the discretization of the fluid mass balance equation, (4.2), changes to:

$$\frac{1}{s_i R_0} \frac{s_{i+1/2} q_{i+1/2} - s_{i-1/2} q_{i-1/2}}{s_{i+1/2} - s_{i-1/2}} + \frac{w_{i,n}^{m,e} - w_{i,n-1}^e}{\Delta t} - \frac{w_{i,n}^{0,p} - w_{i,n-1}^p}{\Delta t} + \frac{\delta w_{i,n}^{m,e}}{\Delta t} - \frac{\Delta w_{i,n}^p}{\Delta t} + u_{i,n}^0 + \Delta u_{i,n} = 0 \quad i = 1, 2, 3, \dots, N \quad (4.98)$$

However,  $\frac{\Delta w_{i,n}^p}{\Delta t}$  can be computed by taking the time derivative of Eqn. (2.28) so that:

$$\frac{\Delta w_{i,n}^p}{\Delta t} = \frac{\partial w^p(t)}{\partial t} = \left( \frac{\eta c}{G\kappa} \right) u(t) \quad (4.99)$$

in which, the minus sign in the original equation, (2.28), is dropped since in the above derivations,  $w^p$  has been taken as an absolute value. Thus, Eqn. (4.98) becomes:

$$\frac{1}{s_i R_0} \frac{s_{i+1/2} q_{i+1/2} - s_{i-1/2} q_{i-1/2}}{s_{i+1/2} - s_{i-1/2}} + \frac{w_{i,n}^{m,e} - w_{i,n-1}^e - w_{i,n-1}^p}{\Delta t} + u_{i,n}^0 + \frac{\delta w_{i,n}^{m,e}}{\Delta t} + \left( 1 - \frac{\eta c}{G\kappa} \right) \Delta u_{i,n} = 0 \quad i = 1, 2, 3, \dots, N \quad (4.100)$$

in which,  $w_{i,n-1}$  now stands for the total fracture aperture at the end of the  $(n-1)$ -th time step. The corresponding coefficients in the NR algorithm are listed in Appendix D.

The same benchmark example (Table 4.1) is computed here by setting the corresponding poroelastic constants as non-zero. i.e,  $\alpha = 0.798$ ,  $B = 0.678$ ,  $\kappa = 3.5 \times 10^{-5} \text{ m}^2/\text{MPa.s}$ , which gives  $\nu_u = 0.376$ ;  $\eta = 0.266$  and  $c = 0.266 \text{ m}^2/\text{s}$ . Because the current chapter is confined to the subject of a stationary fracture, the calculation is started when the fluid has flowed to the tip of the fracture and occupied the whole fracture space therein. Figures 4.19-20 show the profiles of pressure and fracture aperture at  $t = 100\text{s}$  among the cases of pure elastic without leakoff, leakoff only without poroelastic backstress contribution and the full poroelastic case. Figure 4.19 shows that the fluid leakoff plays a dominant role in depleting the injected fluid volume so that when propagation takes place, much less fluid is available to prop-up the fracture and the resultant fracture aperture is much less when compared to the no-leakoff situation. Correspondingly, the dominant leakoff mechanism lowers the well-bore pressure considerably (Figure 4.20). The poroelastic effect increases the pressure as it resists the poroelastic closure, but the aftermath is not enough to raise the pressure to a level comparable to the purely elastic case. Moreover, the raised pressure level due to the poroelastic mechanism increases the fluid leakoff, which further reduces the fracture aperture from its no-leakoff counterpart (Figure 4.19).

Figure 4.21 displays the evolution of the accumulated leakoff volume,  $V_{lek}$ , and the created fracture volume,  $V_{crk}$ . Again, it shows that a larger portion of the injected fluid is leaked into the formation. Moreover, it shows that the various mass distributions in the computations are balanced. The sum of  $V_{crk} + V_{lek}$  is equal to the injected fluid volume,  $V_{inj}$ .

Figure 4.22 illustrates the profiles of the temporal derivative of the fracture aperture,  $w' = \frac{\partial w}{\partial t}$ , and the fluid leakoff flux,  $u$ , along the fracture at  $t =$

100s. It more clearly characterizes the mass distribution among the leakoff and fracture aperture change. From Eqn. (4.2), the fluid transport,  $\partial(rq)/r\partial r$ , supplies the fluid source to create the additional fracture aperture,  $w'$ , and to meet the leakoff demand,  $u$ . With leakoff, the fracture aperture increment rate,  $w'$ , is very much reduced as compared to the case without leakoff. The leakoff term,  $u$ , takes the majority of the injected fluid as it is much larger than  $w'$ . Even more fluid escapes into the formation when the poroelastic backstress is allowed to develop (as denoted by the superscript, '2', in Figure 4.21. The superscript "0" or "1" denotes the purely elastic case without leakoff or the leakoff-only, respectively.).

Being pressure-dependent, the leakoff now is controlled by the pressure difference between the *in-situ* stress,  $\sigma_0$ , and the reservoir pore pressure,  $p_0$ , as well as the formation permeability,  $k$ . Expectedly, a larger difference of  $\sigma_0 - p_0$  and/or a more permeable formation facilitates the fluid leakoff and thus, results in a smaller fracture aperture (Figure 4.23).

## 4.9 Summary

In the first place, this chapter contributes an efficient numerical algorithm, PEFD, for the simulation of fluid flow inside the fracture coupled with the fracture deformation in the context of pressure-dependent leakoff, poroelastic effect and power-law fluid rheology. The validity of the computations has been first qualitatively checked by observing the convergence and global mass balance. The stability and consistency of the algorithm has been numerically verified. Its mathematical accuracy has been validated by comparing the computations with the associated analytical results.

An explicit FD method is well-known for its efficiency and flexibility. These

advantages have been keenly felt in computing the PKN HF model [60, 85]. For the penny-shaped HF fracture, the explicit FD scheme was attempted for the relatively simple elastic situation without leakoff [156]. However, it was later given up because of the resultant severe numerical instability problem. Indeed, our previous experience with McFrac [157] did agree with their notion: if one directly applies the traditional explicit FD scheme, it is very difficult, if not impossible, to derive an adaptive time marching criterion. No fruitful efforts has been reported in the literature to overcome this difficulty. The PEFD algorithm proposed in this dissertation has successfully circumvented this deadlock by using a fully implicit time marching scheme.

However, computationally, the PEFD scheme is fully explicit. It solves one point at one time, needing no matrix inversion. The reason for invoking such an algorithm is the nonlinear, coupled and integro-differential nature of the governing equation system. The way to achieve it is to isolate one point at one iteration. Qualitatively, this is similar to the Alternative Direction Implicit (ADI) method [158, 159]. The latter isolates one direction at one time of the solution.

One advantage of this explicit nature is the efficiency, which has been demonstrated by the CPU time. Although there is no comparison with other methods because of the lack of their data, it is believed that the present method is the fastest. Another advantage is the flexibility. With few additional difficulties, the pressure-dependency of the leakoff and the induced poroelastic effects have been included into the HF simulation. It is anticipated that it would be also relatively easy to implement other physical aspects such as the temperature effects.

Table 4.1: Material properties for the stationary fracture.

$K$	$n$	$E$	$\nu$	$\sigma_0$	$Q_0$
250 cp	1	3.0E4 MPa	0.25	10.0, MPa	0.03 m <sup>3</sup> /s

Table 4.2: Comparison of the  $w_{wb}$  and  $p_{wb}$  between the different  $\Delta t$ s. Early time.

$t, s$	$\Delta t$	$w_{wb}, \times 10^{-2} m$	$\delta w_{wb}, \times 10^{-4} m$	$p_{wb}, MPa$	$\delta p_{wb}, MPa$
1.	0.1	0.212680		14.665480	
	1.0	0.188306	2.437422	14.189700	-.475780
5.	0.1	0.255450		8.793759	
	1.0	0.246896	0.855416	8.720428	0.073332
	5.0	0.226218	2.067734	8.863718	0.143291
10.	0.1	0.271678		7.162381	
	1.0	0.269506	0.217199	7.141482	0.020898
	5.0	0.257977	1.152885	7.156686	0.015203
	10.	0.244727	1.324975	7.361680	0.204994
15.	0.1	0.286668		6.248361	
	1.0	0.284159	0.250879	6.242867	0.005494
	5.0	0.279036	0.512335	6.255274	0.012407
20.	0.1	0.318444		5.653008	
	1.0	0.318690	0.024617	5.656522	0.003514
	5.0	0.319551	0.086036	5.668419	0.011898
	10.	0.319641	0.009038	5.670056	0.001637
25.	0.1	0.378281		5.701672	
	1.0	0.378299	0.001818	5.702083	0.000412
	5.0	0.378457	0.015786	5.705551	0.003468
30.	0.1	0.444919		6.163538	
	1.0	0.444923	0.000396	6.163641	0.000103
	5.0	0.444950	0.002682	6.164333	0.000692
	10.	0.445020	0.007055	6.166118	0.001785
35.	0.1	0.514440		6.830737	
	1.0	0.514442	0.000113	6.830769	0.000031
	5.0	0.514448	0.000674	6.830954	0.000185
40.	0.1	0.585330		7.601273	
	1.0	0.585330	0.000036	7.601284	0.000011
	5.0	0.585333	0.000221	7.601346	0.000062
	10.	0.585337	0.000458	7.601476	0.000131

Table 4.3: Comparing the analytical results with the computed  $w_{wb}$  and  $p_{wb}$  by the different  $\Delta t$ s. Late times.

$t, s$	$\Delta t$	$w_{wb}, \times 10^{-2} m$	rel. error. %	$p_{wb}, MPa$	rel. error. %
30.	0.1	0.444919	3.54	6.163538	14.14
	1.0	0.444923	3.54	6.163641	14.14
	5.0	0.444950	3.54	6.164333	14.15
	10.	0.445020	3.56	6.166118	14.19
	analy.	0.429717		5.400000	
35.	0.1	0.514440	2.61	6.830737	8.42
	1.0	0.514442	2.61	6.830769	8.42
	5.0	0.514448	2.62	6.830954	8.43
	analy.	0.501337		6.300000	
	40.	0.1	0.585330	2.16	7.601273
1.0		0.585330	2.16	7.601284	5.57
5.0		0.585333	2.16	7.601346	5.57
10.		0.585337	2.16	7.601476	5.58
analy.		0.572956		7.200000	
45.	0.1	0.656928	1.92	8.426790	4.03
	1.0	0.656928	1.92	8.426794	4.03
	5.0	0.656929	1.92	8.426818	4.03
	analy.	0.644576		8.100000	
	50.	0.1	0.728921	1.78	9.283346
1.0		0.728921	1.78	9.283348	3.15
5.0		0.728921	1.78	9.283359	3.15
10.		0.728922	1.78	9.283376	3.15
analy.		0.716195		9.000000	
55.	0.1	0.801147	1.69	10.158390	2.61
	1.0	0.801147	1.69	10.158390	2.61
	5.0	0.801147	1.69	10.158390	2.61
	analy.	0.787814		9.900001	
	60.	0.1	0.873518	1.64	11.044950
1.0		0.873518	1.64	11.044950	2.27
5.0		0.873518	1.64	11.044950	2.27
10.		0.873518	1.64	11.044960	2.27
analy.		0.859434		10.800000	

cont'd from the previous page					
$t, s$	$\Delta t$	$w_{wb}, \times 10^{-2} m$	rel. error, %	$p_{wb}, MPa$	rel. error, %
65.	0.1	0.945982	1.60	11.938990	2.04
	1.0	0.945982	1.60	11.938990	2.04
	5.0	0.945982	1.60	11.938990	2.04
	analy.	0.931054		11.700000	
70.	0.1	1.018509	1.58	12.838040	1.89
	1.0	1.018509	1.58	12.838040	1.89
	5.0	1.018509	1.58	12.838040	1.89
	10.	1.018509	1.58	12.838040	1.89
	analy.	1.002673		12.600000	
75.	0.1	1.091079	1.56	13.740550	1.78
	1.0	1.091079	1.56	13.740550	1.78
	5.0	1.091079	1.56	13.740550	1.78
	analy.	1.074293		13.500000	
80.	0.1	1.163680	1.55	14.645520	1.70
	1.0	1.163680	1.55	14.645520	1.70
	5.0	1.163680	1.55	14.645520	1.70
	10.	1.163680	1.55	14.645520	1.70
	analy.	1.145912		14.400000	
85.	0.1	1.236303	1.54	15.552260	1.65
	1.0	1.236303	1.54	15.552260	1.65
	5.0	1.236303	1.54	15.552260	1.65
	analy.	1.217532		15.300000	
90.	0.1	1.307497	1.42	16.442230	1.50
	1.0	1.308942	1.54	16.460310	1.61
	5.0	1.308942	1.54	16.460310	1.61
	10.	1.308942	1.54	16.460310	1.61
	analy.	1.289151		16.200000	
95.	0.1	1.380148	1.42	17.351250	1.47
	1.0	1.381594	1.53	17.369350	1.58
	5.0	1.381594	1.53	17.369350	1.58
	analy.	1.360771		17.100000	
100.	0.1	1.452809	1.43	18.261030	1.45
	1.0	1.454255	1.53	18.279140	1.55
	5.0	1.454255	1.53	18.279140	1.55
	10.	1.454255	1.53	18.279140	1.55
	analy.	1.432390		18.000000	



Table 4.4:  $w_{wb}$  and  $p_{wb}$  between the different Chebyshev grid points.  $N$ . Early time.

$t, s$	$N$	$w_{wb}, \times 10^{-2} m$	$\delta w_{wb}, \times 10^{-4} m$	$p_{wb}, MPa$	$\delta p_{wb}, MPa$
5.	5	0.241225		7.553291	
	10	0.246896	0.567099	8.720428	1.167136
	15	0.247126	0.023036	9.342992	0.622564
	20	0.247689	0.056282	9.938881	0.595889
10.	5	0.270316		6.203807	
	10	0.269506	0.081012	7.141482	0.937675
	15	0.270588	0.108275	7.653911	0.512428
	20	0.271331	0.074315	7.990123	0.336213
15.	5	0.283579		5.386477	
	10	0.284159	0.057998	6.242867	0.856389
	15	0.285280	0.112030	6.724667	0.481800
	20	0.285918	0.063816	7.066731	0.342065
20.	5	0.325166		5.125809	
	10	0.318690	0.647539	5.656522	0.530713
	15	0.317256	0.143483	6.010087	0.353566
	20	0.316896	0.035945	6.266607	0.256519
25.	5	0.388044		5.466225	
	10	0.378299	0.974438	5.702083	0.235858
	15	0.375871	0.242847	5.898804	0.196721
	20	0.375148	0.072321	6.048135	0.149332
30.	5	0.457419		6.110969	
	10	0.444923	1.249599	6.163641	0.052672
	15	0.441710	0.321272	6.265243	0.101602
	20	0.440715	0.099581	6.350284	0.085042
35.	5	0.529455		6.895555	
	10	0.514442	1.501364	6.830769	-0.064786
	15	0.510531	0.391042	6.875101	0.044332
	20	0.509299	0.123179	6.922335	0.047234
40.	5	0.602739		7.748356	
	10	0.585330	1.740897	7.601284	-0.147072
	15	0.580768	0.456268	7.608872	0.007588
	20	0.579319	0.144827	7.632672	0.023800

Table 4.5:  $w_{wb}$  and  $p_{wb}$  by the different Chebyshev grid points,  $N$ . Late times.

$t, s$	$N$	$w_{wb}, \times 10^{-2} m$	rel. error, %	$p_{wb}, MPa$	rel. error, %
35.	5	0.529455	5.61	6.895555	9.45
	10	0.514442	2.61	6.830769	8.42
	15	0.510531	1.83	6.875101	9.13
	20	0.509299	1.59	6.922335	9.88
	analy.	0.501337		6.300000	
40.	5	0.602739	5.20	7.748356	7.62
	10	0.585330	2.16	7.601284	5.57
	15	0.580768	1.36	7.608872	5.68
	20	0.579319	1.11	7.632672	6.01
	analy.	0.572956		7.200000	
45.	5	0.676666	4.98	8.636921	6.63
	10	0.656928	1.92	8.426794	4.03
	15	0.651738	1.11	8.408935	3.81
	20	0.650084	0.85	8.417213	3.92
	analy.	0.644576		8.100000	
50.	5	0.750950	4.85	9.545521	6.06
	10	0.728921	1.78	9.283348	3.15
	15	0.723118	0.97	9.246529	2.74
	20	0.721264	0.71	9.243831	2.71
	analy.	0.716195		9.000000	
55.	5	0.825445	4.78	10.466000	5.72
	10	0.801147	1.69	10.158390	2.61
	15	0.794739	0.88	10.106510	2.09
	20	0.792689	0.62	10.095560	1.98
	analy.	0.787814		9.900001	
60.	5	0.900070	4.73	11.393870	5.50
	10	0.873518	1.64	11.044950	2.27
	15	0.866510	0.82	10.980460	1.67
	20	0.864266	0.56	10.962990	1.51
	analy.	0.859434		10.800000	
65.	5	0.974780	4.70	12.326520	5.35
	10	0.945982	1.60	11.938990	2.04
	15	0.938378	0.79	11.863470	1.40
	20	0.935942	0.53	11.840590	1.20
	analy.	0.931054		11.700000	

cont'd from the previous page					
$t, s$	$N$	$w_{wb}, \times 10^{-2} m$	rel. error. %	$p_{wb}, MPa$	rel. error. %
70.	5	1.049546	4.67	13.262370	5.26
	10	1.018509	1.58	12.838040	1.89
	15	1.010311	0.76	12.752570	1.21
	20	1.007684	0.50	12.725020	0.99
	analy.	1.002673		12.600000	
75.	5	1.124351	4.66	14.200440	5.19
	10	1.091079	1.56	13.740550	1.78
	15	1.082289	0.74	13.645870	1.08
	20	1.079471	0.48	13.614180	0.85
	analy.	1.074293		13.500000	
80.	5	1.199183	4.65	15.140070	5.14
	10	1.163680	1.55	14.645520	1.70
	15	1.154298	0.73	14.542150	0.99
	20	1.151291	0.47	14.506680	0.74
	analy.	1.145912		14.400000	
85.	5	1.274036	4.64	16.080840	5.10
	10	1.236303	1.54	15.552260	1.65
	15	1.226331	0.72	15.440590	0.92
	20	1.223133	0.46	15.401610	0.66
	analy.	1.217532		15.300000	
90.	5	1.348903	4.63	17.022440	5.08
	10	1.308942	1.54	16.460310	1.61
	15	1.298380	0.72	16.340620	0.87
	20	1.294993	0.45	16.298320	0.61
	analy.	1.289151		16.200000	
95.	5	1.423781	4.63	17.964680	5.06
	10	1.381594	1.53	17.369350	1.58
	15	1.370443	0.71	17.241840	0.83
	20	1.366866	0.45	17.196380	0.56
	analy.	1.360771		17.100000	
100.	5	1.498668	4.63	18.907390	5.04
	10	1.454255	1.53	18.279140	1.55
	15	1.442515	0.71	18.143980	0.80
	20	1.438749	0.44	18.095460	0.53
	analy.	1.432390		18.000000	

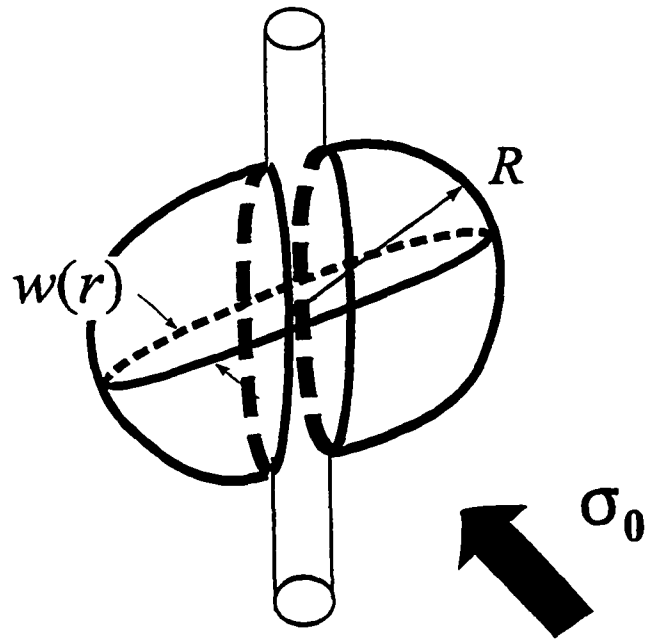


Figure 4.1: Sketch of the penny-shaped HF propagation.

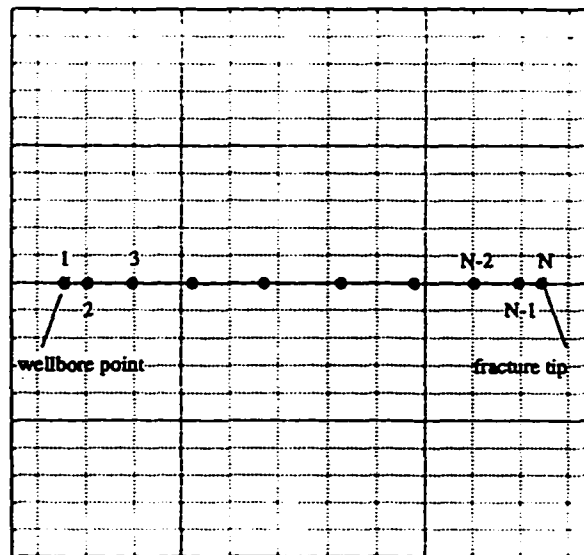


Figure 4.2: Nodal distribution of the Chebyshev grid.

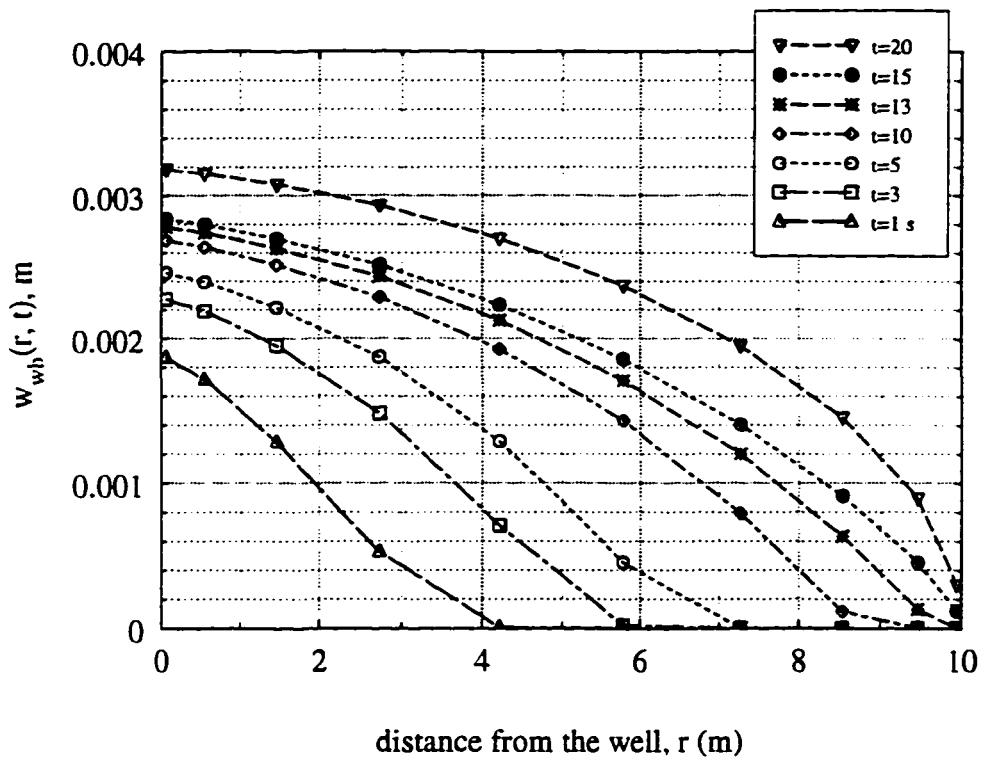


Figure 4.3: Fracture aperture profiles at early times before the fluid reaches the fracture tip.

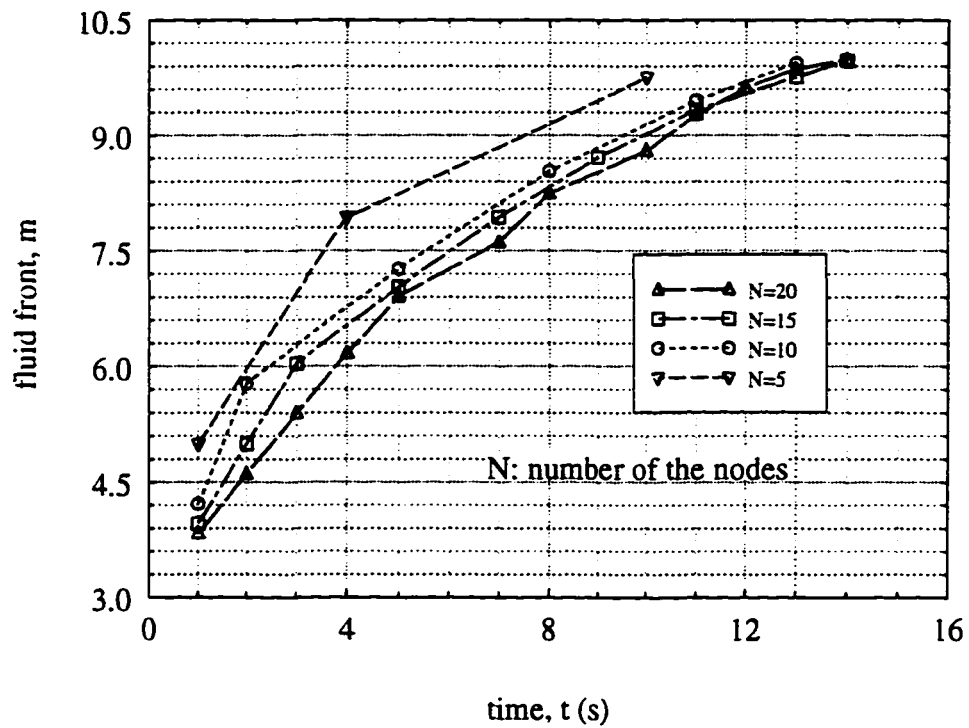


Figure 4.4: Fluid front position, measured in distance from the well, vs. time after different numbers of the Chebyshev grid nodes.

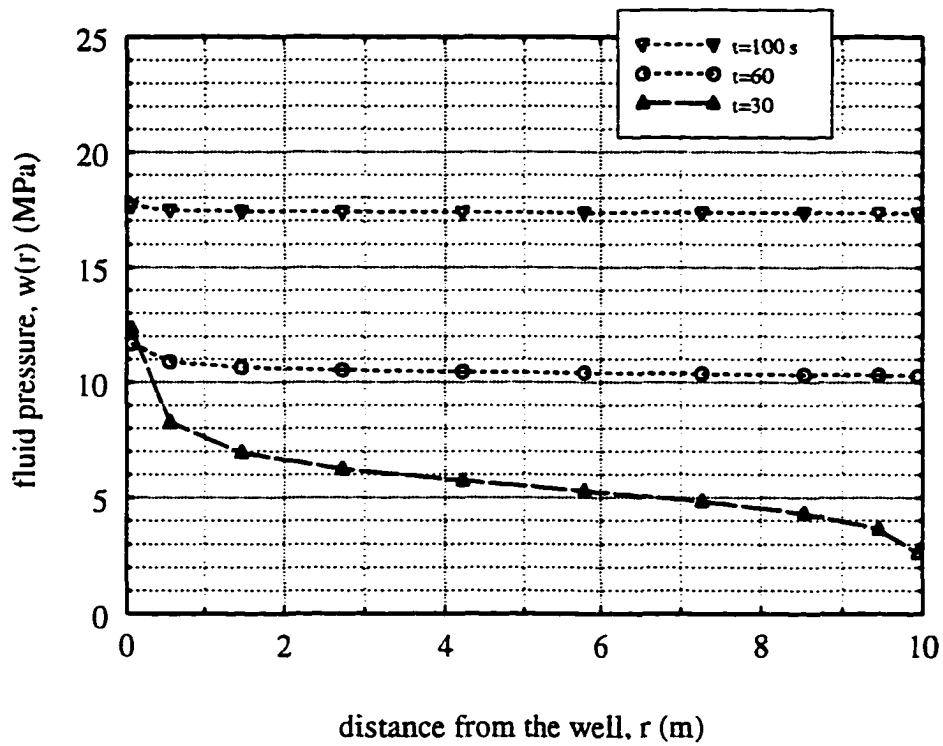


Figure 4.5: Pressure profiles along the fracture at late times.

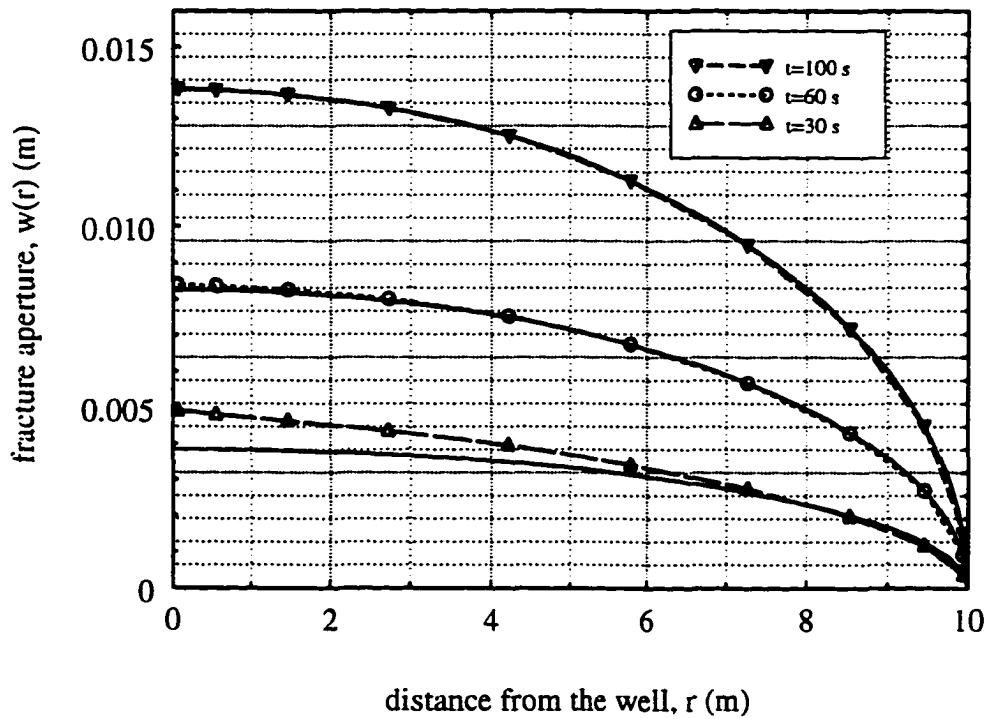


Figure 4.6: Fracture aperture profiles along the fracture at late times. The unmarked dotted lines are the predicted elliptical profiles based on the computed average pressures.

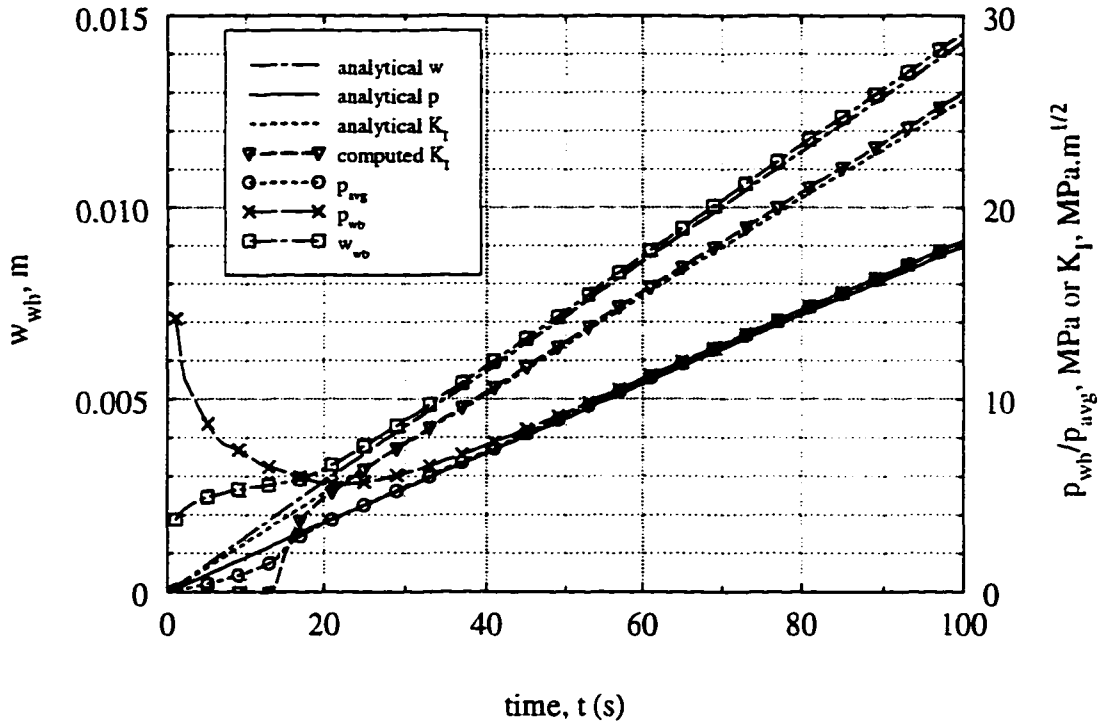


Figure 4.7: Evolution of the fracture aperture,  $w_{wb}$  and fluid pressure,  $p_{wb}$  at the wellbore; average pressure along the fracture,  $p_{avg}$  and stress intensity factor,  $K_I$ .

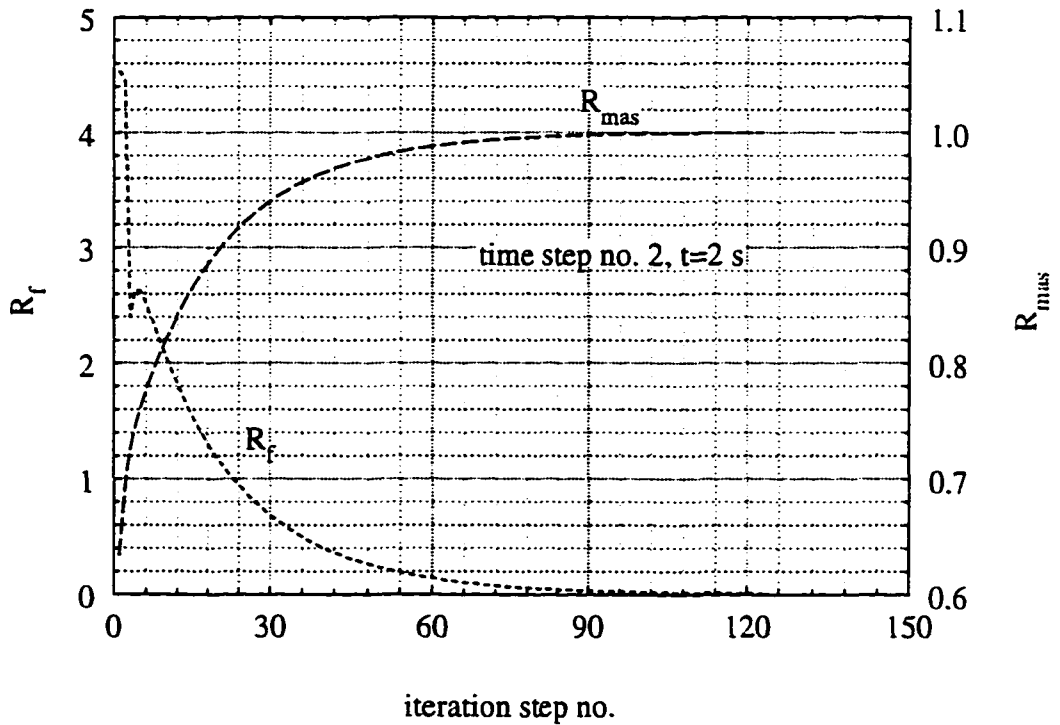


Figure 4.8: Evolution of  $R_f$  and  $R_{mas}$  during the iterations for time step no. 2.

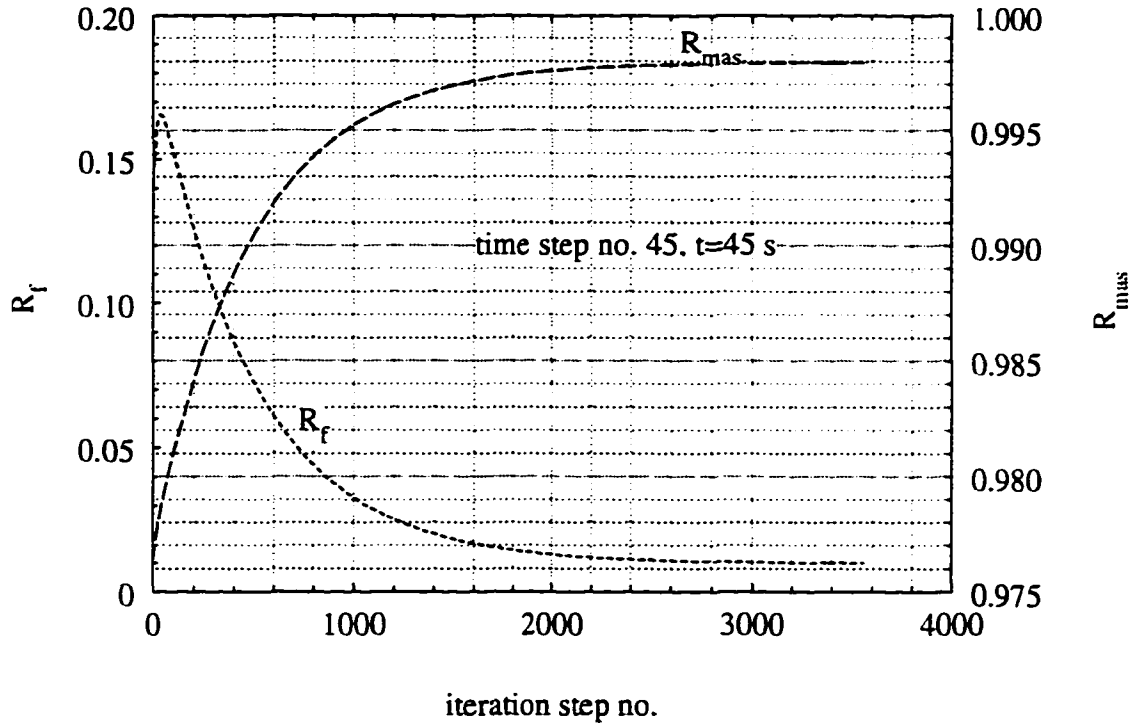


Figure 4.9: Evolution of  $R_f$  and  $R_{mas}$  during the iterations for time step no. 45.

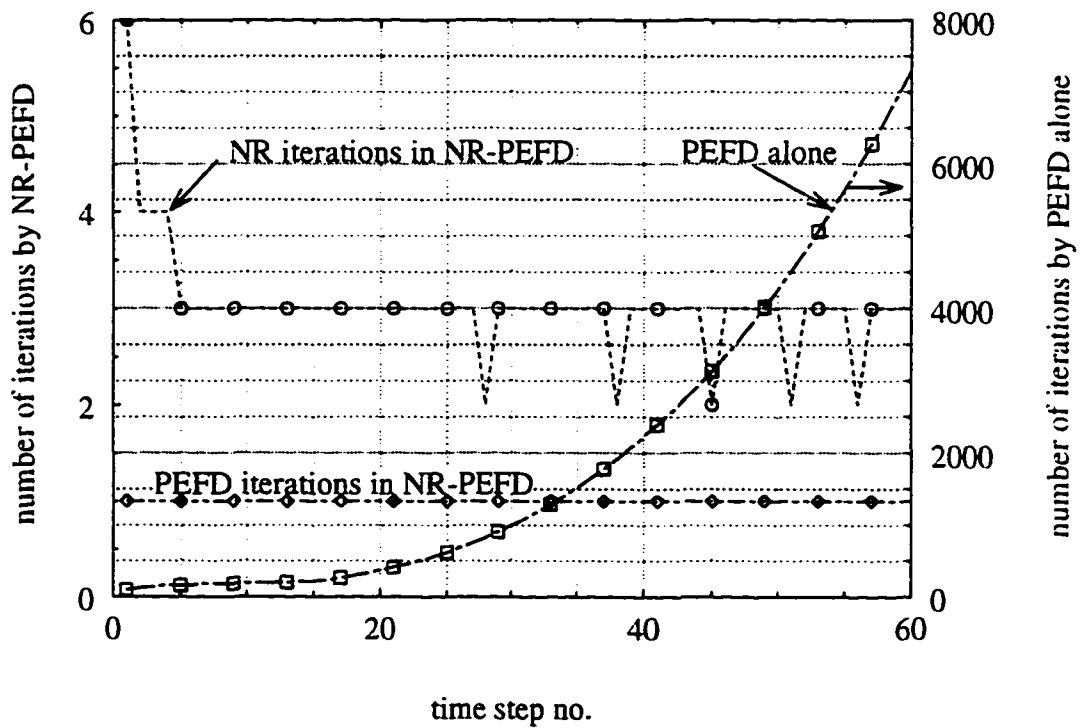


Figure 4.10: Number of iterations required for each time step if computed by the different numerical schemes.



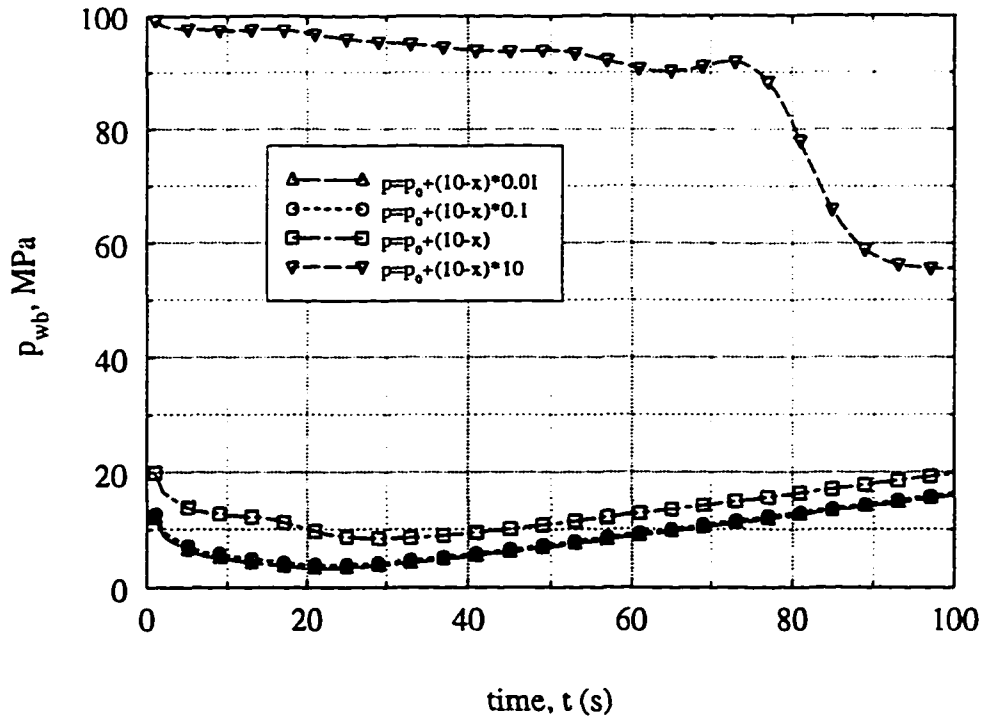
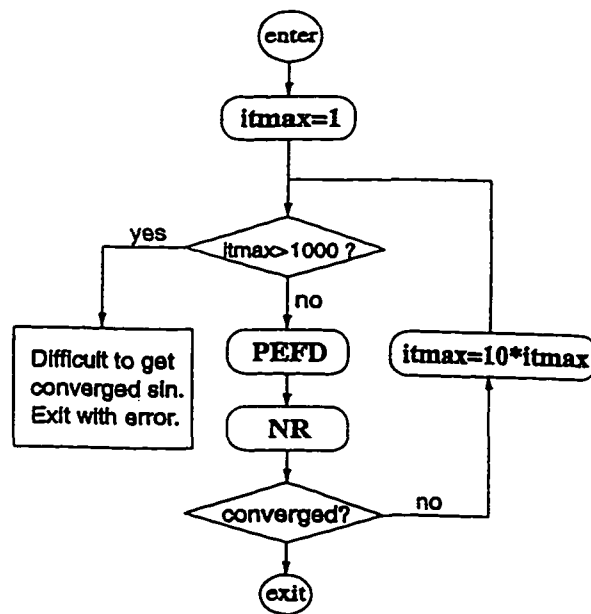


Figure 4.11: Evolution of the wellbore pressure computed by NR alone based on the different initial guesses for the pressure profile.



*itmax: maximum allowable iteration steps in PEFD.*

Figure 4.12: Relationship between the PEFD and NR algorithms.

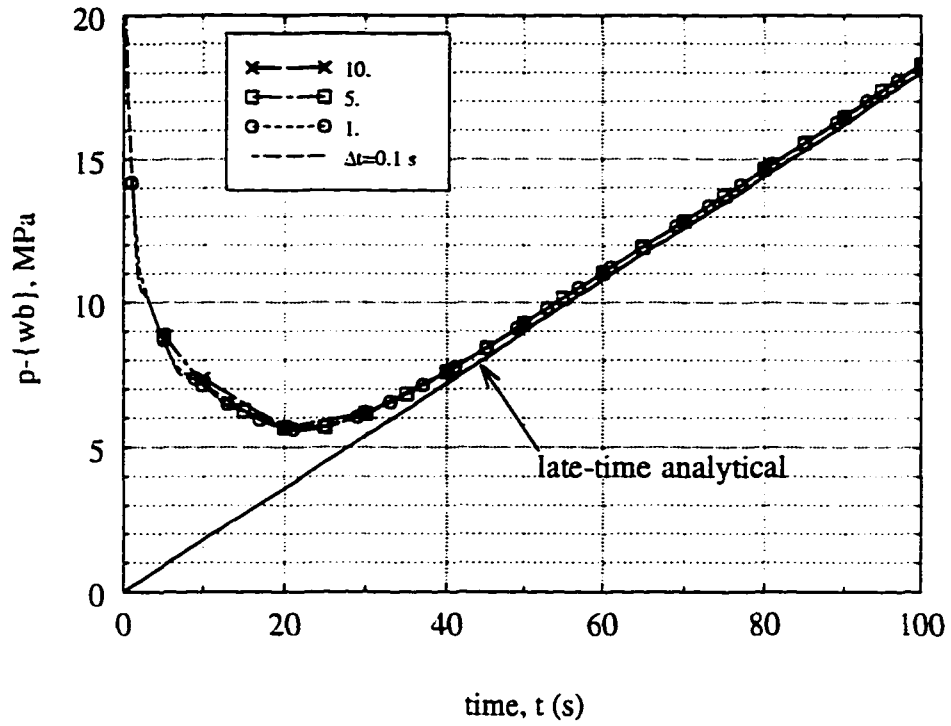


Figure 4.13: Influence of the time stepping size,  $\Delta t$  on the computed wellbore pressures,  $p_{wb}$ .

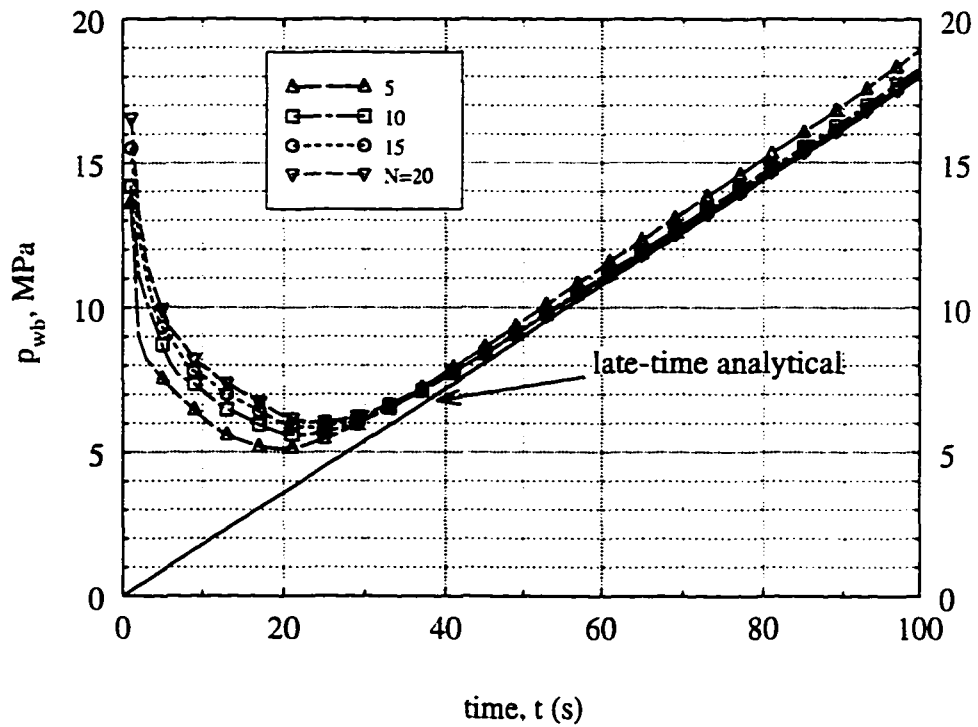


Figure 4.14: Influence of the different number of the Chebyshev nodes,  $N$ , on the computed wellbore pressure,  $p_{wb}$ .

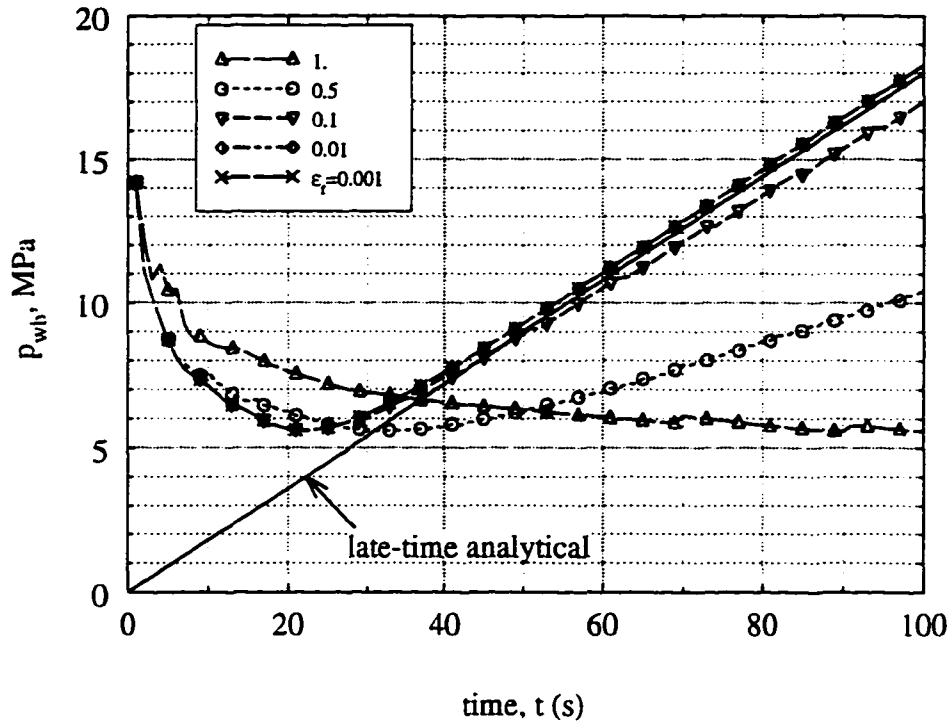


Figure 4.15: Influence of the different iteration measure values,  $\epsilon_f$ , on the computed wellbore pressure,  $p_{wb}$ .

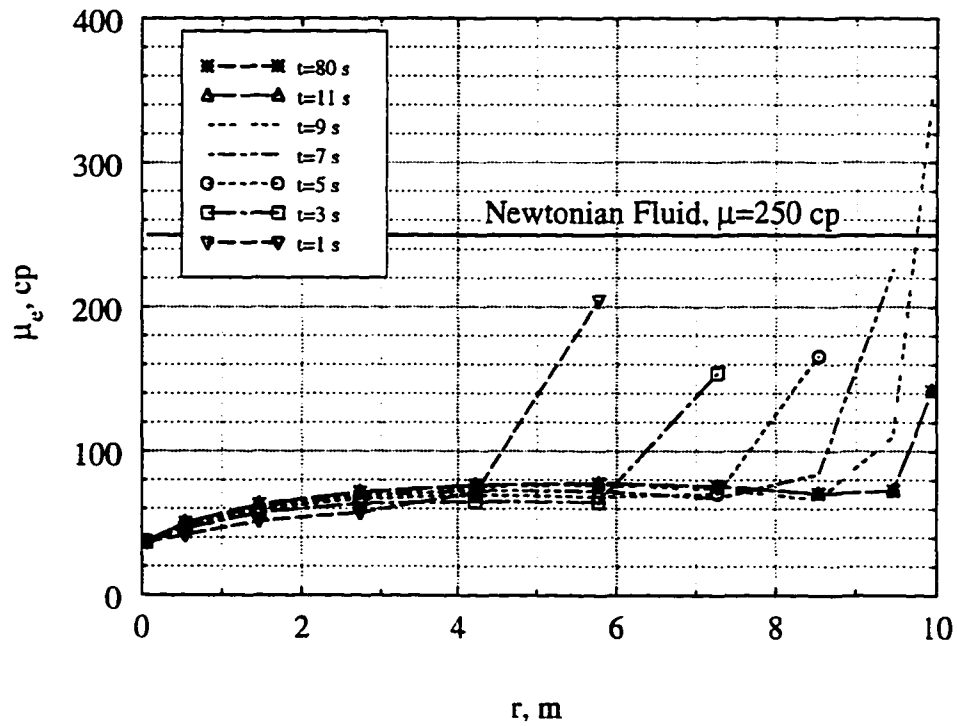


Figure 4.16: Distribution of the effective viscosity,  $\mu_e$ , along the fracture at different times.

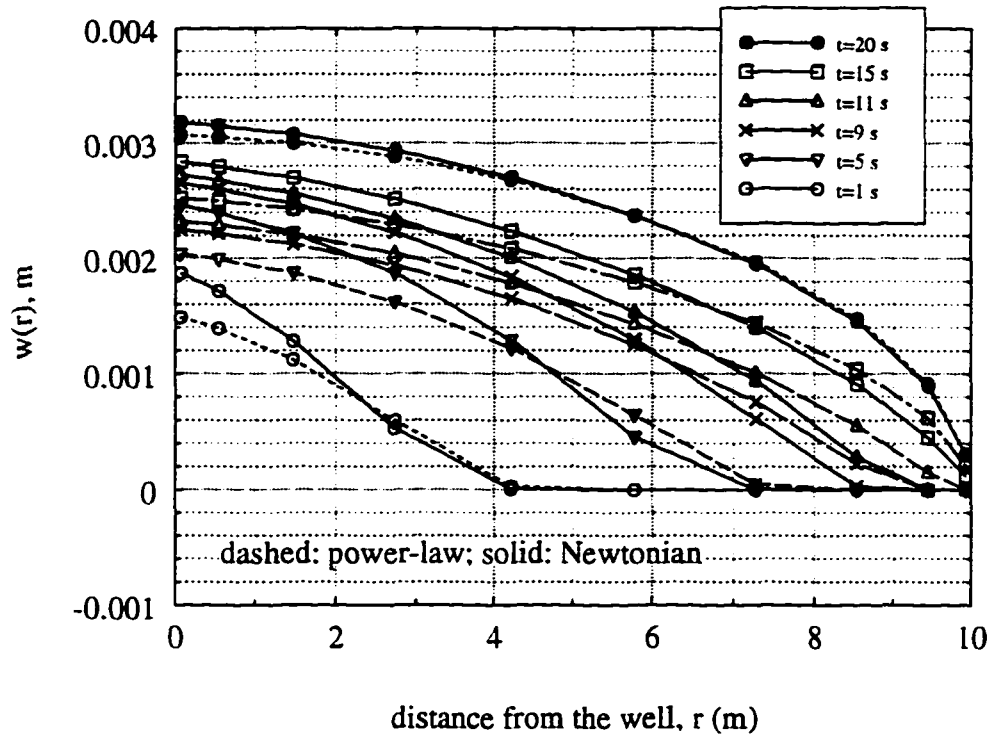


Figure 4.17: Fracture aperture profiles at early times and the comparison between the power-law and Newtonian rheology cases.

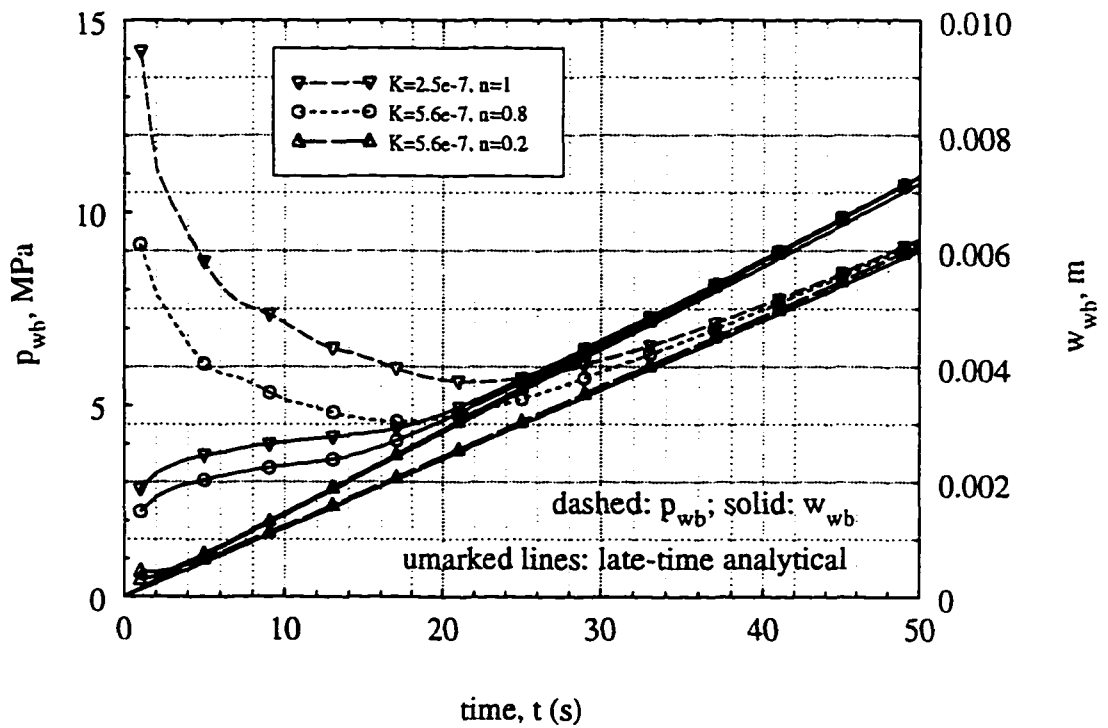


Figure 4.18: The wellbore responses for the power-law fluid cases.

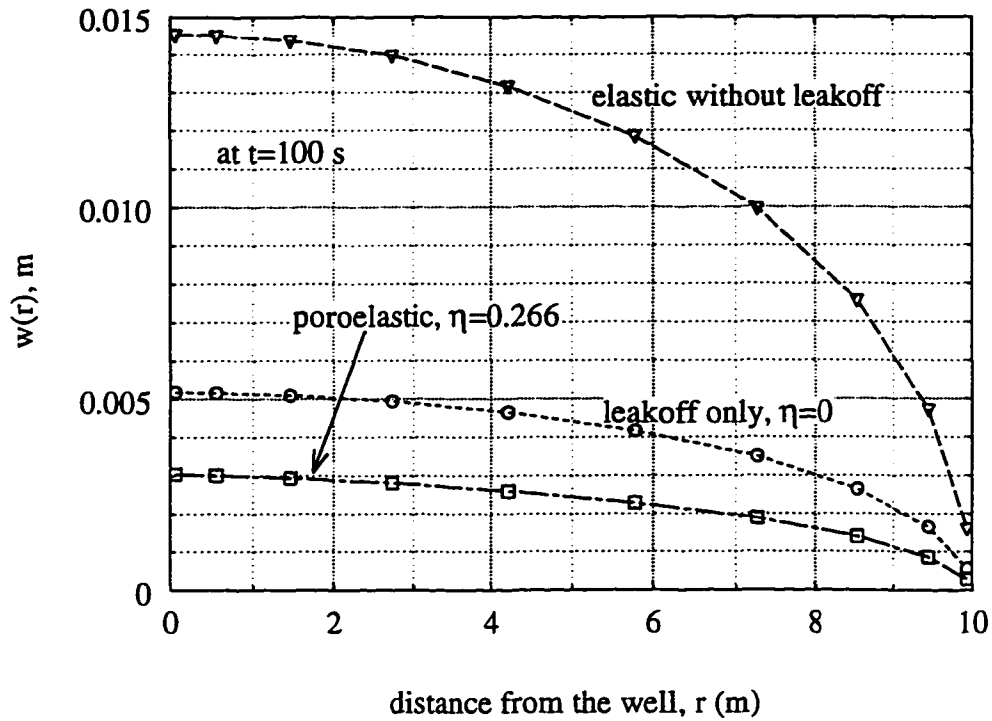


Figure 4.19: Poroelastic effect on fracture deformation as displayed by its profile along the fracture at  $t = 100$ s.

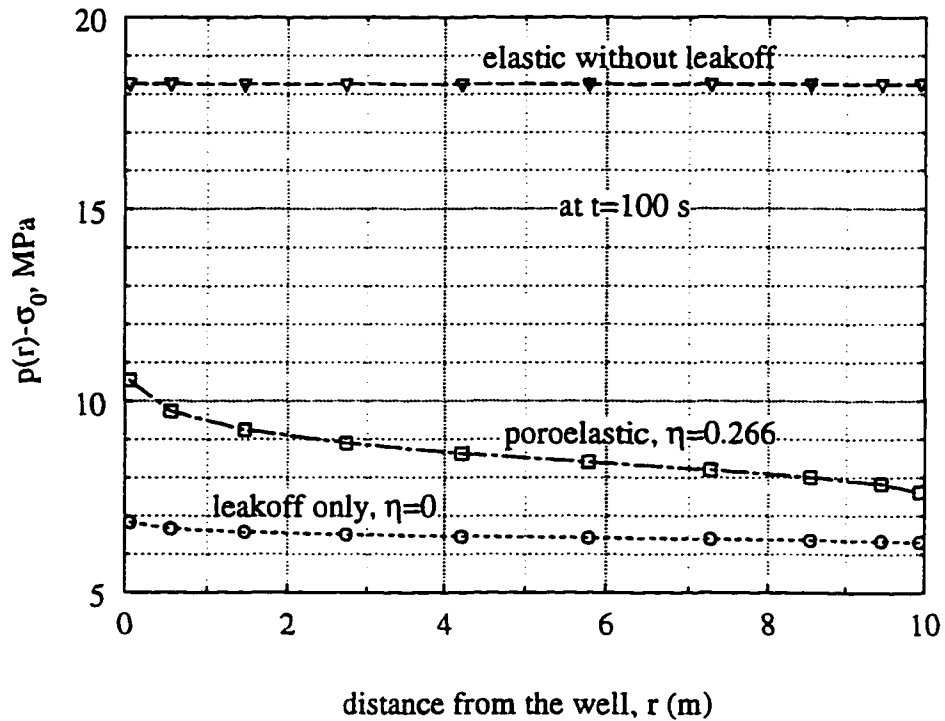


Figure 4.20: Pressure response due to the poroelastic effect as illustrated by its profile along the fracture at  $t = 100$ s.

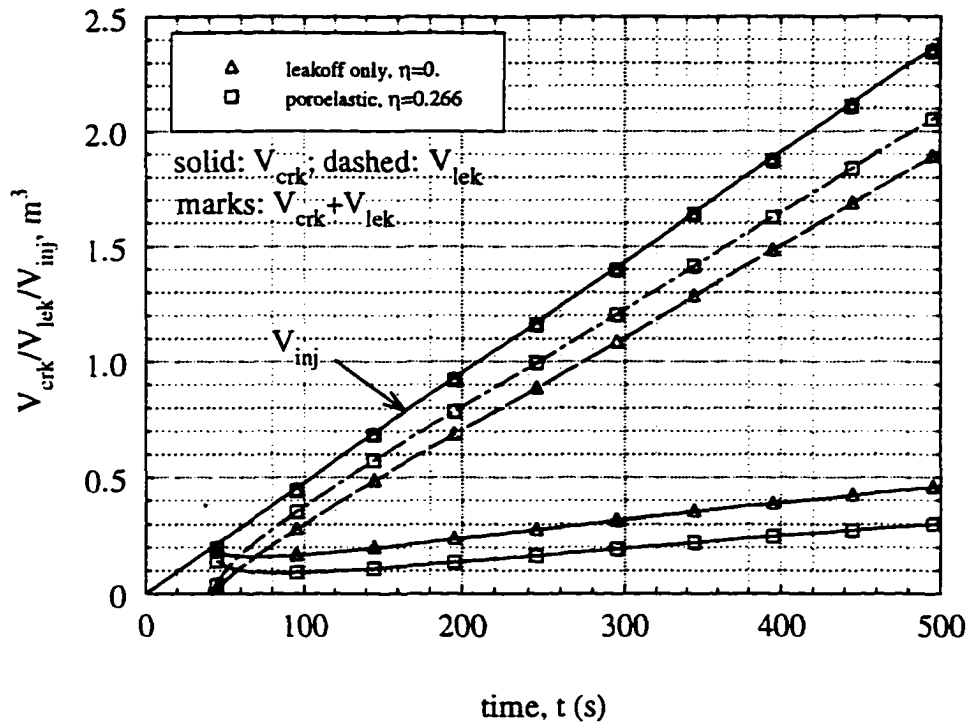


Figure 4.21: Evolution of the accumulated leakoff volume,  $V_{lek}$  and the created fracture volume,  $V_{crk}$ .

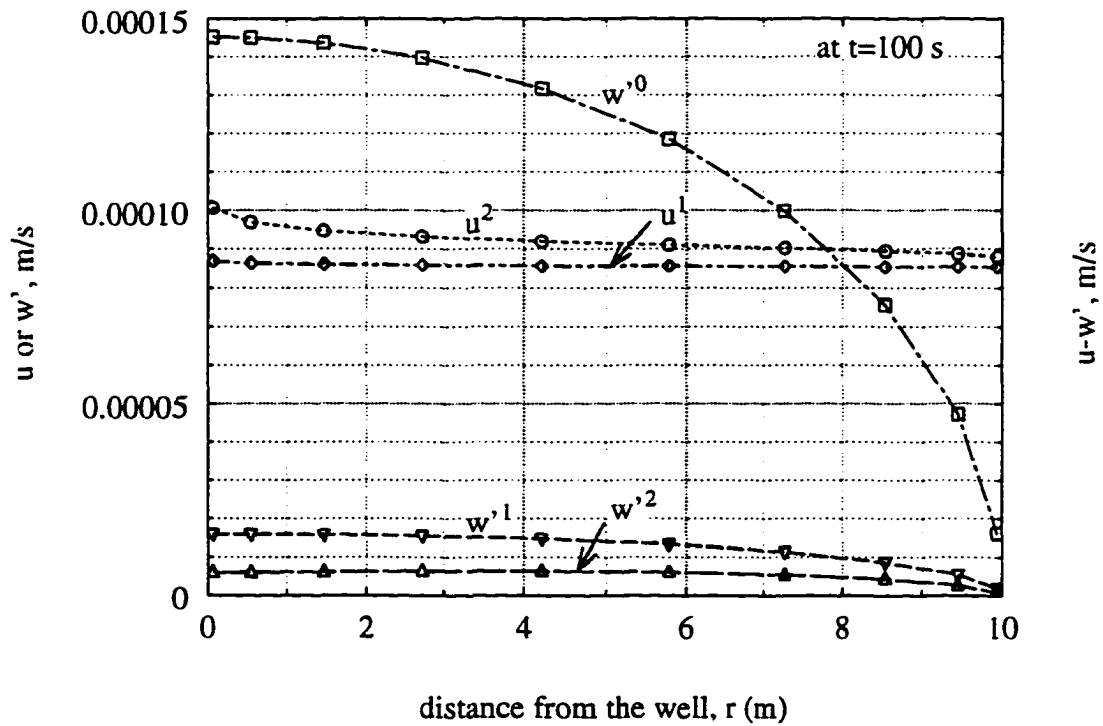


Figure 4.22: Comparison of the leakoff flux,  $u$ , with the fracture aperture change,  $w' = \frac{\partial w}{\partial t}$ , in the fluid mass balance equation.

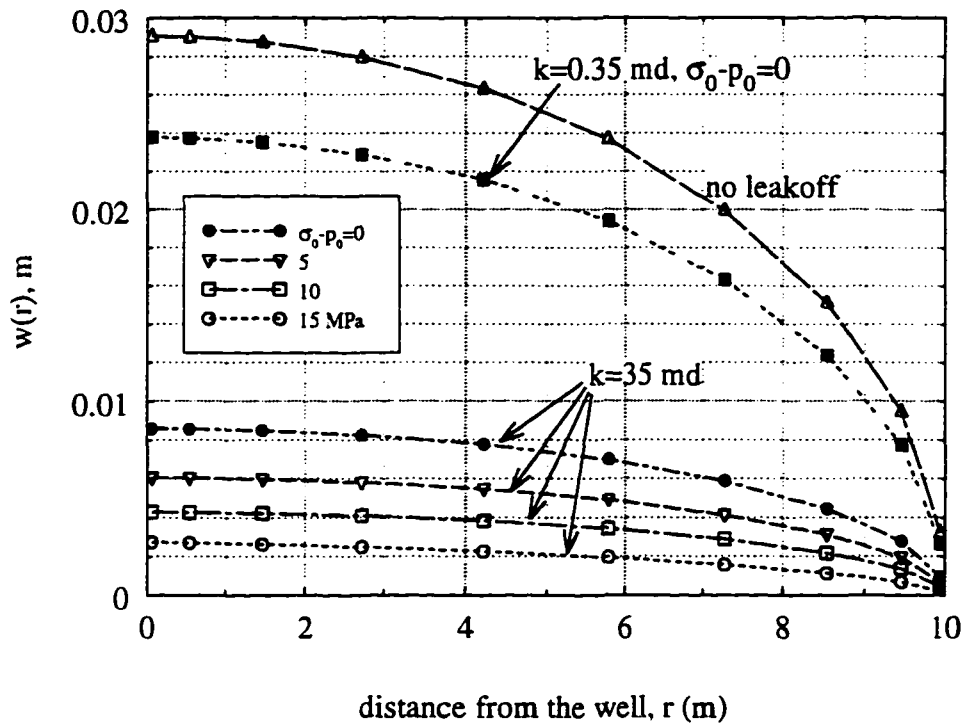


Figure 4.23: Poroelastic effect influenced by the  $\sigma_0 - p_0$  difference and the formation permeability as typified by the fracture aperture profile at  $t = 200s$ .

## Chapter 5

# Simulation of Fracture Propagation/Closure/Re-opening

HF was first investigated in Chapters 2 and 3 by prescribing a non-zero pressure boundary condition along the fracture. Chapter 4 related the pressure to fluid flow inside the fracture as well as its coupling with the fracture deformation. The only non-zero boundary condition therein is the fluid injection rate at the fracture inlet. Being confined to a stationary fracture, however, Chapter 4 has not considered the other boundary condition, i.e. the fracture propagation condition, Eqn. (4.7). In this chapter, this limitation is relaxed. Furthermore, the capacity of modeling multiple fracturing events, including the propagation/closure/re-opening (PCR) during multiple fluid injection/shut-in/flow-back (ISF) cycles, is implemented.

The first section is dedicated to the numerical calculation of fracture propagation during a single injection cycle. In the second section, the numerical strategy to model fracture closure is described, including the fracture remaining stationary upon stopping the fluid injection. In the third section, the fracture is allowed to re-open upon fluid re-injection. Validation examples are



given in each section whenever they become relevant and available. Finally, parametric analyses are carried out in regards to the poroelastic effect in the HF propagation, including the fracture closure/re-opening.

## 5.1 Fracture Propagation

Mathematically, allowance for the fracture propagation or closure creates a moving boundary value problem [160, 161, 162]. The condition to determine the fracturing behavior relies on the stress intensity factor-based fracture criterion, such as Eqn. (4.7). However, this equation is inherited from the purely elastic fracture mechanics theory. In the poroelastic domain, the effective pressure acting on the fracture includes the implicit poroelastic contribution which is not the boundary condition, but the computational outcome. Direct application of Eqn. (4.7) into the current poroelastic domain is thus not feasible. Therefore, special efforts in calculating the stress intensity factor are first elaborated. The numerical strategy to deal with the moving boundary is then discussed. Finally, several example problems are computed for validation purposes.

### 5.1.1 Calculation of the Stress Intensity Factor

Recently, Atkinson and Craster have published a series of papers on analytical derivations of fracturing behavior in poroelastic media, e.g., [163, 164, 165]. Therein, they found that in the near vicinity of the fracture tip, the Laplacian term,  $\nabla^2 p$ , is the dominant part in the fluid diffusion equation, such as Eqn. (2.10). Therefore, near the fracture tip, the poroelastic governing equations, Eqn. (2.9) and Eqn. (2.10), become de-coupled and mathematically equivalent to the uncoupled thermoelasticity. The asymptotic behavior of the stresses

towards the fracture tip is similar to their purely elastic counterparts, i.e. of the following form [163]:

$$\sigma_{ij} = \frac{K_{ij}f_{ij}(\theta)}{\sqrt{2\pi r}} \quad (5.1)$$

in which,  $K_{ij}$  is the stress intensity factor reflecting the contribution of the external loading condition as well as the fracture size and shape.  $f_{ij}$  summarizes the circumferential variation around the fracture tip.  $r$  is the radial distance to the tip. Atkinson and Craster (1991) further derived the asymptotic behavior of the pore pressure as:

$$p = K_p f_{ij}^p(\theta) \sqrt{2\pi r} \quad (5.2)$$

in which,  $K_p$  and  $f_{ij}^p$  have similar meaning as the above  $K_{ij}$  and  $f_{ij}$ , respectively. A similar asymptotic behavior was derived by Simmons (1977) [166] for a mode-II crack in poroelastic media, steadily moving with an either slow or high speed.

Therefore, based on the constitutive relation, Eqn. (2.4), the strain components can be easily shown to have a singularity of the order  $1/\sqrt{r}$ . Further, from the strain-displacement relationship, Eqn. (1.7), the displacement has an asymptotic variation of  $\sqrt{r}$  near the fracture tip. Particularly for the current axi-symmetric configuration, the total fracture aperture near the fracture tip has the following form:

$$w(r, t) = \left[ \frac{2(1-\nu)K_I(t)}{G} \right] \sqrt{R-r} \quad r \leq R \quad (5.3)$$

in which,  $r$  is now defined as the distance from the wellbore in order to agree with the notion carried out in the rest of this work. The  $K_I$  is specifically written as time-dependent. Numerically,  $K_I(t)$  can be computed based on

Eqn. (5.3) by using the total fracture aperture value,  $w_N$ , at the last node,  $N$ , in the Chebyshev grid via:

$$K_I = \frac{G}{2(1-\nu)} \frac{w_N}{\sqrt{R(1-s_N)}} \quad (5.4)$$

in which,  $s_N$  is the normalized coordinate of node,  $N$ .

### 5.1.2 $\Delta R$ -based Fracture Propagation Scheme

As pointed out earlier, the propagation of a discrete fracture is often numerically realized by a “snap-shot” scheme [67, 167]: the fracture is propagated by a certain amount,  $\Delta R$ . Iteration is then performed to adjust the time increment required to render the newly-propagated fracture tip to be at the critical condition again, i.e., Eqn. (4.7) holds. Numerically, this condition is equivalent to:

$$\left| \frac{K_I}{K_{Ic}} - 1 \right| \leq \epsilon_{K_I} \quad (5.5)$$

with  $\epsilon_{K_I}$  being given as input. This is called a  $\Delta R$ -based fracture propagation scheme. In McFrac, the  $\Delta R$  value at a new time step,  $n + 1$ , is given as:

$$\Delta R_{n+1} = R_n(1 - s_N) \quad (5.6)$$

which is the distance between the last node,  $N$ , and the true fracture tip at the previous time step,  $n$ . Therefore, in time increment from step  $n$  to  $n + 1$ , node  $N$  moves to the previous fracture tip. This arrangement is solely for the convenience of coding and there is no theoretical merits behind it.

The  $\Delta R$ -based scheme happens to be efficient in handling the time marching in fracture propagation. Fracture radius varies more rapidly at early times; therefore, it is beneficial, and important, to have smaller time increments in

the early history of the pumping-in. As shown in Eqn. (5.6), this condition is indeed met in the  $\Delta R$ -based scheme as the short fracture radius,  $R$ , at early times gives a smaller  $\Delta R$ .

The boundary condition, Eqn. (4.8), has already been explicitly implemented into the simulation by Eqn. (4.39). However, minor modifications are needed in the initial condition, Eqn. (4.9): An arbitrary, usually small, fracture radius at the beginning is given as input to initiate the computation. The initial width,  $w(r)$ , and pressure profiles,  $p(r)$  are still kept as zero.

### 5.1.3 Calculation of the Temporal Derivatives

To accommodate the moving boundary nature,  $R(t)$ , during the fracture propagation/recession, the time derivative appearing in the system of governing equations has to be adjusted accordingly. Analytically, the temporal derivatives are given by [168]:

$$\left. \frac{\partial}{\partial t} \right|_r = \left. \frac{\partial}{\partial t} \right|_\theta - \theta \frac{\dot{R}}{R} \left. \frac{\partial}{\partial \theta} \right|_t \quad (5.7)$$

Therefore, to implement this formula, spatial derivatives as well as the fracture propagation rate,  $\dot{R}$ , are needed. These quantities are generally not easy to accurately compute. In McFrac, this difficulty is overcome by looking at the physical coordinate, e.g.,  $r_i = R^{t+\Delta t} \theta_i$  which is the Chebyshev grid node,  $i$ , at the current time,  $t + \Delta t$ . The time derivative is discretized by the normal FD procedure, i.e.,

$$\left. \frac{\partial v}{\partial t} \right|_{r_i} = (v_i^{t+\Delta t} - v_i^t) / \Delta t \quad (5.8)$$

in which,  $v$  refers to the variable of interest. The superscript,  $t + \Delta t$  or  $t$ , denotes the value at the current time,  $t + \Delta t$ , or the previous time,  $t$ , respectively. At time  $t$ , the node,  $i$ , is no longer at the same physical coordinate.

$r_i$ , since  $R^t$  has propagated or receded to a new value,  $R^{t+\Delta t}$ . Therefore,  $v_i^t$  is interpolated from the  $v$  profile at time  $t$ .

Similar practices are carried out in computing the leakoff rate or the poroelastic displacements by Eqn. (3.46) or Eqn. (3.45). That is in computing  $u$  or  $w^p$  at  $\theta_i$  at the current time,  $t + \Delta t$ , the pressure histories since the fracture arrival time,  $\tau(r_i)$  at the same physical point,  $r_i = R^{t+\Delta t}\theta_i$ , are interpolated from the corresponding pressure profiles at that time.

#### 5.1.4 Validation Examples

Again, the example listed in Table 4.1 is re-computed by allowing the fracture to propagate if its stress intensity factor exceeds the fracture toughness,  $K_{Ic}$ . Two representative values of  $K_{Ic}=1$  and  $10 \text{ MPa}\cdot\sqrt{\text{m}}$  are used (Table 5.1).

Figure 5.1 shows the evolution of the pressure profiles along the fracture at early times for the high fracture toughness case,  $K_{Ic} = 10 \text{ MPa}\cdot\sqrt{\text{m}}$ . Initially, the fracture is very short so that its flowing velocity is large causing a high gradient pressure profile. As the fracture propagates, the fluid velocity becomes small. The high fracture toughness prevents easy extension of the fracture. As a result, a large amount of fluid volume has to be accumulated inside the fracture to bring the fracture tip to the critical condition. All these factors work to create a relatively uniform pressure profile at late times (Figure 5.1).

When the pressure profile becomes uniform, a similarity solution can be found from Abe et al.'s derivations [25], which use a concept of average pressure along the fracture. Assuming no fluid lag and negligible wellbore radius, the formulae for fracture length,  $R$ , fracturing pressure,  $p_{wb}$  and fracture aperture,  $w_{wb}$  at the wellbore can be inferred from Abe et al. (1976) [25]:

$$R(t) = K_R t^{2/5} \tag{5.9}$$

$$p_{wb}(t) = K_p t^{-1/5} \quad (5.10)$$

$$w_w(t) = K_w t^{1/5} \quad (5.11)$$

with:

$$K_R = \left[ \frac{3\sqrt{2}Q_0E}{16\pi(1-\nu^2)K_{Ic}} \right]^{2/5} \quad (5.12)$$

$$K_p = \frac{\pi K_{Ic}}{\sqrt{2}K_R} \quad (5.13)$$

$$K_w = \frac{8(1-\nu^2)K_R K_p}{\pi E} \quad (5.14)$$

Figure 5.2 shows that the late-time computations are indeed in excellent agreement with the analytical predictions.

For a low fracture toughness, i.e.,  $K_{Ic} = 1 \text{ MPa}\cdot\sqrt{\text{m}}$ , the pressure profile is not as uniform as in the case of high fracture toughness if the same injection rate,  $Q_0 = 0.03 \text{ m}^3/\text{s}$ , is used (Figure 5.3). Therefore, it is not expected that the computations agree with the foregoing analytical results. However, the non-dimensionalization exercise carried out in Chapter 4 has indicated that in a purely elastic formation without leakoff, the fracture propagation behavior in the dimensionless domain depends on the non-dimensionalized injection rate only. Taking the above high fracture toughness case as the base example (which has already been validated by comparing to the analytical solution), let us project the current small toughness case to the dimensionless domain by adjusting the injection rate (Table 5.1). Figure 5.4 indeed shows they coincide as expected.

Also shown in Figure 5.4 is the case of power-law fluid rheology (Table 5.1). It falls on the same growth line as the Newtonian cases. Note the huge difference in the injection rate required to render an identical dimensionless injection rate,  $Q_{0c}$  as in Eqn. (4.31). McFrac has handled them very easily without much difference in the convergence behavior.

## 5.2 Fracture Closure

When the fluid injection stops, fluid inside the fracture continues to leak into the formation. Therefore, the fracture volume gradually decreases, i.e., the fracture closes. Depending on the circumstances, the fracture may continue to propagate a little after the pumping-in ceases, or, it may remain stationary before its recession. As shown below, accurate simulation of this transition period is important in interpreting the wellbore pressure response such as in extracting the formation leakoff characteristics. This section is dedicated to modeling the fracture closure. A validation example is also given.

### 5.2.1 $\Delta t$ -based Fracture Propagation Scheme

The  $\Delta R$ -based scheme has no active control on the time increment,  $\Delta t$ .  $\Delta t$  is adjusted to accommodate the fracture propagation. In modeling the multiple pumping cycles, it is essential to truncate the time increment at the moment when the pumping activity changes, e.g., from pumping-in to shut-in, or vice versa. Hence, a  $\Delta t$ -based scheme is required in which McFrac could dictate the time increment to be used. The  $\Delta t$ -based scheme is also desired in modeling a stationary fracture.

The  $\Delta t$ -based scheme is similar to the  $\Delta R$ -based except that in the former, a  $\Delta t$  is manually given and McFrac iterates for different fracture radius increments,  $\Delta R$ , so that the newly propagated fracture tip lies at the imminent propagation state.

With the  $\Delta t$ -based scheme, it is also possible to model the continuous growth of the fracture after shut-in or continuous recession of the fracture after a new run of pumping-in. If the program detects that the fracture has entered

into a steady propagation or recession stage, the control is turned back to the  $\Delta R$ -based scheme.

When the computed SIF,  $K_I$ , is less than the fracture toughness, but larger than zero, the fracture is in a stable condition and no propagation will occur. i.e., a stationary fracture results. In McFrac, this condition is described as:

$$\epsilon_{K_I} \leq \frac{K_I}{K_{Ic}} \leq 1 \quad . \quad (5.15)$$

Furthermore, a negative  $K_I$ , or,

$$\frac{K_I}{K_{Ic}} < -\epsilon_{K_I} \quad (5.16)$$

signals that the fracture is to close. The fracture radius has to be reduced by a certain amount,  $\Delta R$ , so that the stress intensity factor,  $K_I$ , at the new fracture tip remains at zero. Numerically, this is equivalent to:

$$\left| \frac{K_I}{K_{Ic}} \right| \leq \epsilon_{K_I} \quad . \quad (5.17)$$

## 5.2.2 Determining Carter's Leakoff Coefficient from Pressure-Decline Curves

Nolte [96] proposed a theory of fracturing pressure decline analysis to estimate the formation characteristics, including Carter's leakoff coefficient. In the theory, Nolte assumes pressure-independent leakoff and no poroelastic effects. These assumptions can be realized in McFrac with a material property set such as the  $K_{Ic} = 10$  case in Table 5.1 except that now, a Carter's leakoff coefficient,  $C_l = 1.34 \times 10^{-4} \text{ m}/\sqrt{\text{s}}$ , is input. The high fracture toughness is chosen in order to render a relatively uniform pressure profile which is closer to Nolte's assumption. One pumping cycle is used with a pumping-in period of 100 seconds at  $Q = 0.3 \text{ m}^3/\text{s}$  and then shut-in until the fracture closes



completely. Based on the computed pressure decline and Nolte's theory, the Carter's leakoff coefficient can be computed. It is expected that the computed value should agree with the input one if the calculation is correct. This way, the validity of McFrac in computing the multiple fracturing events can be checked.

The computed wellbore pressure response as well as the fracture radius are shown in Figure 5.5. Figure 5.6 shows two pressure decline curves furnished from Figure 5.5 based on Nolte's theory [96]. A upper bound category was assumed because the given leakoff coefficient falls within the low leakoff range. One of the two curves in Figure 5.6 used a shut-in time of  $t_i = 100$  s when the pumping-in stops. At  $t_i = 100$  s, however, the fracture continues to propagate until 3 seconds later (Figure 5.7). Therefore, a shut-in time of  $t_i = 103$  s, when the fracture physically stops propagating, is used for the other curve in Figure 5.6. The  $t_i = 100$  s curve gives the Carter's leakoff coefficients of  $1.887 \times 10^{-4}$  m/ $\sqrt{s}$ , which results in 41% error relative to the input value. The  $t_i = 103$  s data set, however, gives a more accurate estimate of  $C_l = 1.282 \times 10^{-4}$  m/ $\sqrt{s}$ , which corresponds to 4% in the relative error.

This observation assures the validity of McFrac in computing the fracture closure. Meanwhile, it points out that it is important in pressure decline analysis to distinguish the times when the pumping-in stops or the fracture propagation ceases. It is more accurate to use the latter time as the  $t_i$  used in Nolte's theory. The necessity for such a correction can be easily recognized on the  $p^* - G(t_D)$  log curve. As shown in Figure 5.6, the  $t_i = 100$  s curve has a very high slope near the origin,  $G(t_D) = 0$ . Shortly after, the curve abruptly changes to another straight line which has a much smaller slope and is parallel to the  $t_i = 103$  s curve. This abrupt transition point is associated with the

time when the fracture has physically stopped extending. Translating this point to the origin by moving the  $t_i = 100$  s curve downwards along the  $p^*$  axis gives a new curve (the marked line in Figure 5.6) which almost coincides with the  $t_i = 103$  s curve and therefore, yields the correct value for the Carter's leakoff coefficient.

### 5.2.3 Fracturing Behavior after the Shut-in

With McFrac, one can look more closely into the fracturing behavior after shut-in. Figure 5.8 displays the evolution of pressure profiles immediately after shut-in. At  $t = 100$ s when the fracture still accepts the injected fluid, the pressure profile along the fracture has a relatively large gradient. Immediately thereafter, the fluid injection is stopped. But the pressure gradient, or the fluid momentum, inherited from the pre-shut-in period continues to push the fluid moving towards the fracture tip. As a result, the fluid pressure, or equivalently, the fracture aperture, near the tip continues to grow and the fracture propagates by an increment of  $\Delta R = 0.0769$ m one second after the shut-in. Meanwhile, the pressure near the wellbore decreases and its overall gradient along the fracture decreases as well. But the gradient is still sufficient to drive the fluid pressure to rise near the tip and the fracture to extend by a series of exponentially decreasing segment,  $\Delta R = 0.0393, 0.0034$  m consecutively during the next two one-second time increments till  $t = 103$  s. Starting from  $t = 103$  s, the fracture stops propagating further, i.e., remains in a stationary state. The fluid pressure along the fracture, including near the tip, decreases due to the fluid leakoff (Figure 5.8).

As more fluid leaks into the formation, the stiffness of the fracture, which is partly supplied by the accumulated or the pressurized fluid inside the fracture,

decreases. It is expected that the fracture will close, starting near the fracture tip and proceeding towards the wellbore until finally, the propped-up fracture radius becomes zero. This process is indeed shown in Figure 5.9.

As in the injection stage, the leakoff rate plays a decisive role in affecting the fracturing behavior during the shut-in. For example, by increasing the leakoff coefficient in the above example by an order, i.e.,  $C_l = 1.34 \times 10^{-3} \text{ m}/\sqrt{\text{s}}$ , the fracture propagation stops spontaneously upon the shut-in. Shortly after the shut-in, the fracture starts to recede and closes very rapidly (Figure 5.10).

Expectedly, the fracture toughness, or the mechanical strength of the rock mass, affects the fracture propagation as well. For example, a smaller fracture toughness allows the fracture to propagate longer after the shut-in, which is indeed seen in Figure 5.10 where the fracture keeps on propagating until about  $t = 120 \text{ s}$ . Correspondingly, the fracture recedes very slowly. However, the fracture starts to close earlier as compared to the high fracture toughness case.

Figure 5.11 shows another interesting point relevant to the HF stress measurement. When applied to the porous formation, the HF stress measurement technique often relies on the recognition of a characteristic pressure,  $p_{isip}$ , from the wellbore pressure log after the shut-in, e.g., [169, 170, 171, 172].  $p_{isip}$ , called the instantaneous shut-in pressure, is pinpointed by the abrupt turning point on the  $p_{wb}$  vs.  $t$  curve shortly after the shut-in. Often, the  $p_{isip}$  is assumed to be equal to the *in-situ* minimum stress,  $\sigma_0$ . However, both Figure 5.11 and Table 5.2 show that a large difference exists between them in the computed examples. A maximum difference of 5.5 MPa is found.

In the above discussion, the shut-in time,  $t_i$ , has already been defined in the pressure decline curve. Another characteristic timing can also be pinpointed to typify the time,  $t_{foc}$ , when the fracture starts to recede (Figure 5.5). Figure

5.5 suggests that  $t_{foc}$  is shown up on the  $p_{wb}$  vs.  $t$  curve as a inflexion point: the curve changes from convex to concave. In order to clarify this change, Figure 5.5 also plots the second time derivative,  $\partial^2 p / \partial t^2$ , of the wellbore pressure computed by Eqn. (2.80). In analytical mathematics, a convex curve has a positive second derivative while a concave one takes a negative value. At the transition point, the second derivative is zero. As shown in Figure 5.5,  $\partial^2 p / \partial t^2$  is obviously positive before  $t_{foc} = 339$  s and changes to mostly negative after  $t_{foc}$ . At  $t_{foc}$ , it attains an abrupt minimum (Figure 5.5)<sup>1</sup>. A  $t_{foc} = 108$  s can be readily picked by the same procedure for the case of higher leakoff coefficient,  $C_l = 1.34 \times 10^{-3}$  m/ $\sqrt{s}$ . For a low fracture toughness, however, the similar features are not so obvious, but can still be found which gives  $t_{foc} = 158$  s (Figure 5.12). Corresponding to  $t_{foc}$ , the pressure decline curves give a pressure reading,  $p_{foc}$ , i.e., the fracture closure pressure. Compared to  $p_{isip}$ ,  $p_{foc}$  is closer to  $\sigma_0$  (Table 5.2).

Determination of the timings,  $t_i$  and  $t_{foc}$ , are not only significant in the *in-situ* stress measurement, but could be indicative of more information. The preliminary results (Table 5.2) suggest that a small difference between them,  $t_{foc} - t_i$ , is representative of a very permeable formation and/or a small fracture toughness, or vice versa. But a small fracture toughness enables the fracture to propagate longer after shut-in (i.e.,  $t_i$  is much longer than the pumping shut-in time) while a very permeable formation causes the fracture propagation to cease instantly upon shut-in (i.e.,  $t_i$  coincides with the pumping shut-in time). In any case, the analysis shows that with a detailed rigorous simulation of the post-shut-in fracturing behavior, one may extract more information about the *in-situ* condition from the wellbore pressure recordings.

---

<sup>1</sup>  $\partial^2 p / \partial t^2$  is not strictly zero at  $t_{foc}$  because of the numerical artifact in computing the derivatives.

### 5.3 Fracture Re-opening

The fracture re-opens along the previously created trace during subsequent pumping-in's after the previous run of injection/shut-in. In McFrac, this condition is detected by the following criterion:

$$\frac{K_I}{K_{Ic}} \geq \epsilon_{K_I} \quad \text{and} \quad R(t) < R_{max} \quad (5.18)$$

in which,  $R_{max}$  is the maximum fracture length in its previous propagation history. The fracture reopening is modeled in a way similar to a fracture propagating through the intact formation. Except in the former, the fracture toughness is treated as zero.

Calculation of the leakoff rate is complicated by the fracture propagation/closure/reopening sequence. Leakoff calculation depends on the time at which the fracture surface is first exposed to the fracturing fluid, i.e., fracture arrival time,  $\tau$ . As sketched in Figure 5.12, a point at distance  $R_t$  from the wellbore is first exposed to the fracturing fluid at time  $t_0$ . At time  $t_1$ , however, the fracture is receding behind the same point. Theoretically, there is no fracturing fluid left around that point beyond  $t_1$ , i.e., from now on, there is no fluid ready to leak into the formation at this point. Subsequently at  $t_2$ , the fracture reopens and the fracturing fluid again passes beyond this point. The cycles could continue to  $t_3$  and so on. Herein, questions arise about which time to take as the time of fracture arrival in computing the leakoff and the associated poroelastic effects after the fracture re-opens. How does one correlate the fluid pressure at position,  $R(t)$ , during the time period of  $t \in [t_1, t_2]$ ? ... .

As no previous work has addressed these questions, this section is mainly dedicated to this issue. The treatment differs between the Carter's pressure-independent and the poroelastic pressure-dependent leakoff cases. For the

Carter's leakoff, a rigorous theoretical derivation is given based on the API standard filtration principle. For the 1-D pressure-dependent leakoff, an assumption has to be made as will be discussed below. For the 2-D pressure-dependent leakoff, however, more thorough research is needed before making any attempt, which is beyond the scope of the current dissertation work. Therefore, the 2-D poroelastic model is only used in computing the monotonic fracture propagation. When the fracture closes or re-opens, a 1-D model is used.

### 5.3.1 Carter's Leakoff Calculation in Multiple Fracturing Events

The pressure-independent leakoff (Carter's) is controlled by the buildup of a filtercake on the fracture surface. Its mathematical formula is derived based on the static filtration principle [173]. As fluid leaks into the formation, the solids or polymer contained in the fluid are stopped at the fluid-formation interface and gradually build up into a certain thickness  $h$ , i.e., a filtercake is formed. The total leaked-off fluid volume  $V_f$  up to current time  $t$  through a unit area of the cake can be computed according to Darcy's law [173]:

$$\frac{dV_f}{dt} = \frac{k\Delta P}{\mu h} \quad (5.19)$$

in which  $k$  is the cake permeability,  $\mu$  is the fluid viscosity and  $\Delta P$  is the pressure difference across the cake.

Consider a point where the cake has first built up to a thickness  $h_0$  up to time  $t_1$ , and then stops growing because no fluid supply exists. At a later time  $t_2$ , the solid-bearing fluid arrives again. Filtration restarts and the cake thickness

increases by  $\Delta h$ , i.e.,  $h = h_0 + \Delta h$ . Material balance gives:

$$f_{sm} (\Delta h + V_f) = f_{sc} \Delta h \quad (5.20)$$

in which  $f_{sc}$  and  $f_{sm}$  are the solid fraction in the cake and the fluid, respectively.  $V_f$  should be interpreted here as the incremental fluid volume leaked through the cake since the latest exposure time  $t_2$ . From Eqn. (5.20) it can be found that:

$$h_0 = \frac{V_0}{\frac{f_{sc}}{f_{sm}} - 1} \quad (5.21)$$

where  $V_0$  is the total leaked volume per unit area of the surface prior to  $t_2$  when fluid is reintroduced. Combining Eqn. (5.19) - Eqn. (5.21) yields:

$$V_0 V_f + \frac{1}{2} V_f^2 = 2C_l^2 \Delta t \quad (5.22)$$

in which  $\Delta t$  is the elapsed time after the latest exposure to the fluid: and,

$$C_l = \sqrt{\frac{k\Delta P}{2\mu} \left( \frac{f_{sc}}{f_{sm}} - 1 \right)} \quad (5.23)$$

is the Carter's leakoff coefficient. Solving the quadratic equation (5.22) (Only the plus solution is physically valid) gives the total leaked volume since the latest exposure  $t_2$  as:

$$V_f = \sqrt{V_0^2 + 4C_l^2 \Delta t} - V_0 \quad (5.24)$$

Taking the time derivative gives the leakoff rate as:

$$u = \frac{4C_l^2}{\sqrt{V_0^2 + 4C_l^2 \Delta t}} \quad (5.25)$$

in which, a factor "2" is added to account for the two fracture surfaces. Note that with  $V_0 = 0$ , Eqn. (5.25) reduces to the conventional Carter's leakoff formula, Eqn. (4.4). Contrary to  $u$ , which is estimated for both surfaces of the fracture,  $V_0$  is computed only for one side of the fracture.

### 5.3.2 1-D Pressure-dependent Leakoff Calculation in Multiple Fracturing Events

In computing the pressure-dependent leakoff, McFrac assumes that the fluid pressure at point,  $R_t$ , remains constant during the time interval of  $[t_1, t_2]$  when the fracture closes at this point (Figure 5.13). This assumption comes from the fact that there is no fracturing fluid available to leak into the formation after the fracture closes at this point. Therefore, it is solely based on physical intuition and could be modified in the future if more refined work comes forth.

### 5.3.3 An Example

Figure 5.14 shows the histories of fracture radius and wellbore pressure under three pumping cycles. The Carter's leakoff model is used and no poroelastic effect is considered. The relevant material properties are based on field data and listed in Table 5.3. Each pumping cycle consists of 5 minutes of pumping-in at a rate of 20 bpm and then 20 minutes of shut-in. For the current material property set, right at the beginning of shut-in, the fracture stops propagating and remains stationary for a short period. Afterwards, the fracture recedes rapidly. The fracture closes completely before the end of the shut-in period. During the late pumping-in cycles, the fracture reopens rapidly along the preexisting trace until it reaches the previously attained maximum radius. Thenafter, the propagation rate slows down, because from now on, the fracture extends through the intact formation.

The wellbore pressure response returns to the *in-situ* minimum stress value,  $\sigma_0$ , whenever the fracture closes completely no matter what pumping cycle it is in. Moreover, in this particular example, both  $p_{isip}$  ( $\sim 4280$  psi) and  $p_{foc}$  ( $\sim 4260$  psi) remain relatively constant between the consecutive pumping



cycles and very near the *in-situ* minimum stress,  $\sigma_0$  (=4200 psi). As pumping cycles increase, the pressure decline during the shut-in period becomes slower. Smaller leakoff rate during the late shut-in periods due to the longer exposure time is responsible for this phenomenon.

The staircase-like pattern in the fracture radius history profile in the third pumping-in cycle manifests the fracture re-opening (Figure 5.14). Correspondingly, the pressure profile shows a local increasing cusp in contrast to the general descending trend (Figure 5.14). After the fluid re-injection, the fracture propagates rapidly along the previously created trace. After it reaches the maximum length previously attained, the fracture hits the intact formation and a non-zero fracture toughness has to be overcome before the fracture propagates further. The fluid pressure inside the fracture builds up in order for the stress intensity factor to exceed the fracture toughness value of the intact formation. Therefore, the fracture propagation rate slows down dramatically. The increasing cusp in the wellbore pressure history reflects this pressure buildup process. After the pressure buildup stage, the fracture has gained new momentum and is in a phase of rapid propagation (although it is not as fast as in the fracture reopening phase). The longer the fracture, the more significant this feature becomes. For example, the slow propagation rate starts to show up in the second pumping-in cycle and becomes more significant in the third one (Figure 5.14).

As shown in Figure 5.14, at the transition from the general descending trend to the local increasing cusp in the wellbore pressure log curve during the third pumping-in cycle lies the fracture re-opening pressure,  $p_r$ , which has been also used in micro-HF jobs to equate to the *in-situ* minimum stress,  $\sigma_0$ . In this particular example,  $p_r \sim 4320$  psi which is indeed close to the  $\sigma_0$ . During the

second pumping-in cycle.  $p_r$  is marked by an abrupt change from the rapid pressure descending rate to a slow one. As shown in Figure 5.14, immediately after the fluid re-injection, the wellbore pressure increases instantly to a very high value (5280 psi in the second pumping-in cycles and 5230 psi in the third cycle). As the fluid flows inside the previously-created fracture trace, the wellbore pressure drops rapidly. When the fluid reaches the previous fracture tip, the wellbore pressure decrease greatly slows down (in the second cycle) or even locally reverses, changing to increase (in the third cycle).

Corresponding to  $p_r$ , one may define another characteristic timing,  $t_r$ , at which the previously created fracture is completely opened up. Obviously, the difference between  $t_r$  and the time when the most recent fluid re-injection starts is a good indicator about the fracture length previously created. In the third re-injection cycle of the current example, such a difference reaches to about 3 minutes while in the second cycle, it is only 1.2 minutes. The former corresponds to a fracture length of 100 m while the latter is associated with a fracture length of 86 m.

Therefore, in the post-shut-in pressure decline as well as in the wellbore pressure response during the subsequent pumping-in cycles, McFrac has been able to give the three characteristic pressures,  $p_{isip}$ ,  $p_{foc}$  and  $p_r$ , all of which have been used in micro-HF jobs to measure the *in-situ* stress,  $\sigma_0$ . Associated with these pressures can be defined three characteristic times,  $t_i$ ,  $t_{foc}$  and  $t_r$ . Comparison between these timings as well as the pumping schedule could reveal more information about the *in-situ* condition, such as the previously created fracture length, leakoff characteristics and formation strength.

## 5.4 Poroelastic Effects in HF Fracture Propagation

Herein, the poroelastic effects on fracture propagation are analyzed. In the monotonic fracture propagation history, the difficulty in dealing with the leakoff calculation during multiple PCR events does not show up. Therefore, the calculation is based on the modified 2-D poroelastic model. In calculating the multiple pumping cycles, however, the 1-D poroelastic model is used since the 2-D model is not mature enough to handle the complex situation as explained in Section 3.

### 5.4.1 Poroelastic Effect During the Monotonic Fracture Propagation

A series of parametric studies have been carried out to study the influence of *in-situ* stress and pore pressure difference, formation permeability via the poroelastic mechanism. The effect is manifested by the created fracture dimension (radius and fracture aperture) as well as the wellbore pressure response. The basic material property set is the  $K_{Ic} = 10$  case in Table 5.1 with the additional poroelastic parameters as  $\alpha = 0.798$ ,  $B = 0.678$  and  $\kappa = 3.5 \times 10^{-5}$  m<sup>2</sup>/MPa.s. The following observations can be summarized:

- (a) The wellbore pressure response increases due to the poroelastic mechanism (Figure 5.15). For example, the net pressure,  $p_f - \sigma_0$ , at  $t = 100$ , increases by over 150% as compared to the purely elastic case without leakoff (Table 5.4). The specific magnitude of the increase depends on the difference between the *in-situ* stress and the reservoir pressure. i.e.,  $(\sigma_0 - p_0)$ , as well as the formation permeability,  $k$ , among other effec-

tual parameters. A larger difference of  $(\sigma_0 - p_0)$  or a higher permeability results in a higher pressure at the wellbore (Figure 5.15 and Table 5.4).

- (b) There is a large difference in the created fracture length between the poroelastically-affected case and the purely elastic case without leakoff. Owing to the poroelastic effect, the fracture length is reduced (Figure 5.16). Similarly, a larger permeability or a larger difference in  $(\sigma_0 - p_0)$ , results in a larger amount of such a reduction.
- (c) Furthermore, the fracture aperture also decreases due to the poroelastic influence (Figure 5.17). Therefore, the resultant fracture volume, or the fracturing efficiency, in a poroelastic medium is much smaller than in low-permeability formations where the pressure-dependent leakoff and poroelastic effect are not significant. The fluid leakage has taken a large portion of the injected fluid volume so that the created fracture dimension is small in either its aperture or length.
- (d) The poroelastically-affected fracture dimension or the wellbore pressure response is linear proportional to the *in-situ* stress and pore pressure difference,  $(\sigma_0 - p_0)$  (Figure 5.18). However, the permeability effect on similar variables is a positive power function<sup>2</sup>(Figure 5.19).

#### 5.4.2 Poroelastic Effects during Fracture Propagation/Closure/Re-opening

Figure 5.20 shows the wellbore pressure response under pressure-dependent leakoff. Basic material properties are listed in Table 5.3. Two cases are considered to examine the poroelastic effects. The poroelastic stress coefficient,  $\eta = 0.3$ , denotes the poroelastic case while  $\eta = 0$  corresponds to a pure leakoff

---

<sup>2</sup>i.e., in the form of  $v \propto \kappa^e$  in which,  $v$  is the fracture width or length or the wellbore pressure;  $\kappa$  is the permeability coefficient;  $e < 1$  is a positive number.

case without considering the poroelastic effect. There are four pumping cycles consisting of 100 seconds of pumping-in at a rate of  $0.3 \text{ m}^3/\text{s}$  and 100 seconds of shut-in. Table 5.5 further lists two characteristic pressures,  $p'_{isip}$  and  $p'_{foc}$  in each pumping cycle for the two cases.  $p'_{isip}$  is taken exactly at the beginning of the shut-in and  $p'_{foc}$  right at the end of the shut-in. Therefore, they are not defined in a way similar to that used in HF stress measurement.

It is obvious that the poroelastic case always has a higher pressure value. As pumping cycles go on, the difference between the poroelastic and the leakoff-only cases increases. In the present example, the difference reaches nearly 3 MPa. In the leakoff-only case, the wellbore pressure converges to the *in-situ* minimum stress value when the fracture closes completely. In the poroelastic case, however, the wellbore pressure remains higher than the *in-situ* stress value by an increment of 2.5 MPa at the complete closure of the fracture.

## 5.5 Summary

This chapter documents the numerical strategies in simulating the fracture propagation, closure and re-opening. Particularly, it used the  $\Delta R$ -based scheme to model the monotonic fracture propagation/recession. It employed the  $\Delta t$ -based scheme to compute the fracturing behavior during the transition in the pumping activities. Comparison with the similarity solution [25] has validated the capability of computing the fracture propagation for purely elastic cases. Based on Nolte's theory, a Carter's leakoff coefficient is inferred from the computed fracture decline curve during the shut-in period. The leakoff magnitude obtained this way agrees very well with the input, which therefore further lends support to the validity of computing the fracture closure. To verify the calculation of the multiple fracture PCR events during the multiple ISF

cycles. a field example based on Carter's leakoff is also computed. The computations have been shown as physically valid although quantitative comparison has not been possible. With these, it is believed that a complete HF simulator, McFrac, which is able to compute fracture propagation/closure/reopening due to the fluid injection/shut-in, is developed.

McFrac is able to assist in detailed analyses of the fracturing behavior after shut-in and/or its subsequent fluid re-injection. Several examples have been computed to illustrate the capabilities of McFrac. For example, the three characteristic pressures,  $p_{isip}$ ,  $p_{foc}$  and  $p_r$  in relation to the HF stress determination, have been identified on the computed wellbore pressure history. It has been shown that, depending on individual circumstances,  $p_{isip}$  could be several MPa's higher than  $\sigma_0$ . High leakoff formation increases this difference. While a low material strength as realized by a small fracture toughness decreases this difference, it can be still as high as 4 MPa in the computed example. Moreover, corresponding to the three characteristic pressure readings,  $p_{isip}$ ,  $p_{foc}$  and  $p_r$ , there are three characteristic times,  $t_i$ ,  $t_{foc}$  and  $t_r$ . The analyses carried out in this work have revealed that these timings depend on the previously created fracture length, formation leakoff characteristics as well as its mechanical strength.

More parametric analyses have been performed in regards to the poroelastic effect in HF propagation. It has been shown that the poroelastic mechanism significantly increase the wellbore pressure and reduce both the fracture aperture and radius. The specific magnitude of such an increment or reduction depends on the *in-situ* stress and pore pressure difference,  $\sigma_0 - p_0$ , as well as the formation permeability,  $\kappa$ . The  $\sigma_0 - p_0$  influence is nearly linear while the  $\kappa$  effect is more like a positive power function. During the multiple

injection/shut-in cycles, the wellbore pressure increase due to the poroelastic effect becomes more significant in the late pumping cycles.

Table 5.1: Material properties for the propagating fracture.

case	$K$	$n$	$E$ , MPa	$\nu$	$\sigma_0$ , MPa	$p_0$ , MPa	$K_{Ic}$	$Q_0$ , m <sup>3</sup> /s
$K_{Ic} = 10$	250 cp	1	3.0E4	0.25	40.	N/A	10	0.03
$K_{Ic} = 1$	250 cp	1	3.0E4	0.25	40.	N/A	1	0.3E-7
power-law	2.5E-7 MPa.s <sup>n</sup>	0.8	3.0E4	0.25	40.	N/A	1	0.6E-6

$K_{Ic}$  is in MPa. $\sqrt{m}$ .

Table 5.2: Some characteristic values on the computed wellbore pressure log in pertinence to HF stress measurement.

case		$p_{istp} - \sigma_0$ , MPa	$p_{foc} - \sigma_0$ , MPa	$t_{foc} - t_i$ , s
$K_{Ic}$	$C_l$			
10	$1.34 \times 10^{-4}$	4	2.5	237
1	$1.34 \times 10^{-4}$	4	2.5	17
10	$1.34 \times 10^{-3}$	5.5	3	8

$K_{Ic}$  is in MPa. $\sqrt{m}$ .  $C_l$  in m/ $\sqrt{s}$ .

Table 5.3: Material Properties for the Examples with Multiple Pumping Cycles

parameter	$p$ -dependent leakoff	Carter's leakoff
dynamic permeability, $\kappa$	$8.36 \times 10^{-5}$ m <sup>2</sup> /MPa.s	N/A
diffusivity, $c$	0.4 m <sup>2</sup> /s	N/A
Young's modulus, $E$	$0.3 \times 10^5$ MPa	$1.5 \times 10^6$ psi
Poisson's ratio, $\nu$	0.25	0.25
Fracturing fluid viscosity, $K, n$	250 cp (Newtonian only)	$K=0.15$ lbf.s <sup>0.5</sup> /ft <sup>2</sup> , $n = 0.5$
$\sigma_0 - p_0$	1.7 MPa	1500 psi ( $p_0 = 2700$ psi)
Carter's leakoff coefficient, $C_l$	N/A	0.003 ft/ $\sqrt{min}$
Fracture toughness, $K_{Ic}$	1 MPa. $\sqrt{m}$	1000 psi. $\sqrt{in}$



Table 5.4: Poroelastic effect on the wellbore pressure response.

case	$p_{wb} - \sigma_0$ , MPa	rel. inc., %
no leakoff	6.05	0.
$k=0.35$ md, $p_0 = 40$ MPa	7.46	23.3
$k=3.5$ md, $p_0 = 40$ MPa	7.83	29.4
$k=35$ md, $p_0=40$ MPa	8.81	45.6
$k=350$ md, $p_0=40$ MPa	11.84	95.7
$k=35$ md, $p_0=40$ MPa	8.81	45.6
$k=35$ md, $p_0=35$ MPa	10.67	76.4
$k=35$ md, $p_0=30$ MPa	12.72	110.3
$k=35$ md, $p_0=25$ MPa	15.14	150.3

Table 5.5: Comparison of Wellbore Pressures during the Multiple Pumping Cycles. Poroelastic ( $\eta = 0.3$ ) vs. Leakoff-only Cases ( $\eta = 0.$ ).

$p'_{isip}$ , MPa			
cycle no.	$\eta = 0$	$\eta = 0.3$	$\Delta p'_{isip}$
1	5.53883	7.04015	1.50132
2	4.84622	7.12749	2.28127
3	4.52247	7.20590	2.68343
4	4.28523	7.24109	2.95586
$p'_{foc}$ , MPa			
cycle no.	$\eta = 0$	$\eta = 0.3$	$\Delta p'_{foc}$
1	0.86225	1.72610	0.86385
2	1.10563	2.04533	0.93970
3	1.16955	2.23766	1.06811
4	0	2.48004	2.48004

$\Delta$  denotes the difference between the cases of  $\eta = 0.3$  and 0.

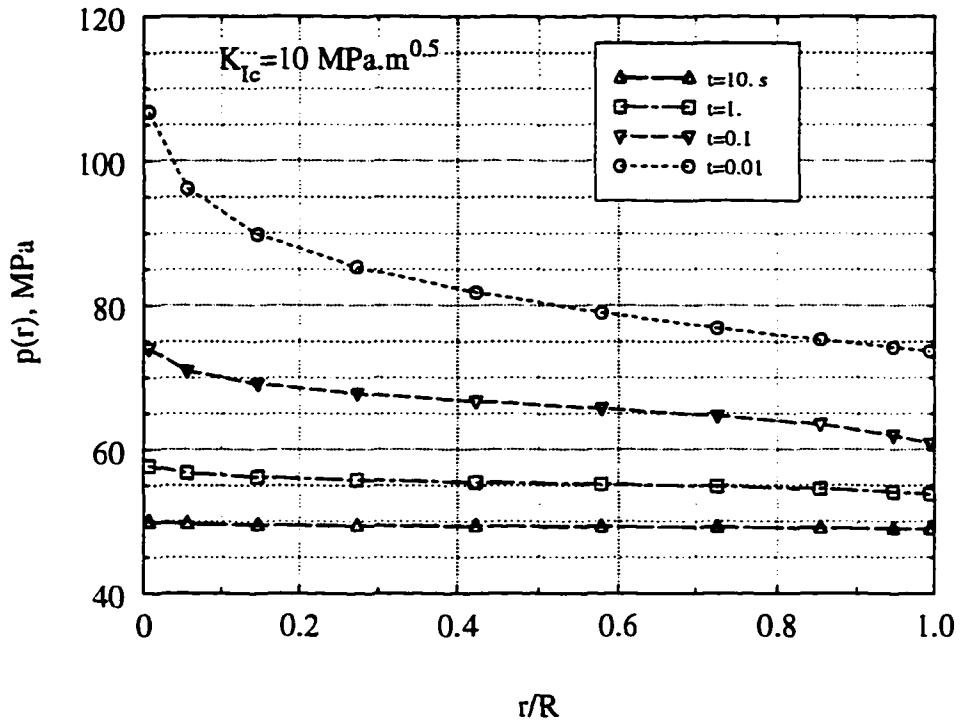


Figure 5.1: Evolution of the pressure profiles along the fracture.

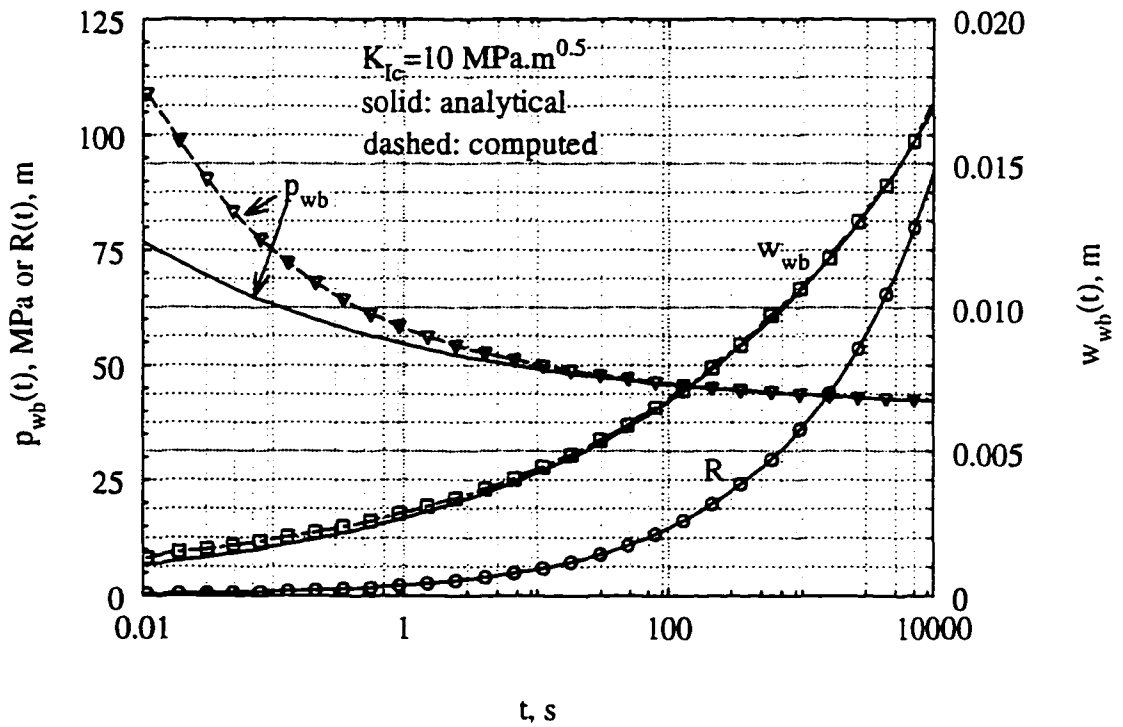


Figure 5.2: Computed wellbore pressure, aperture and fracture radius as well as their comparison with the similarity solution.

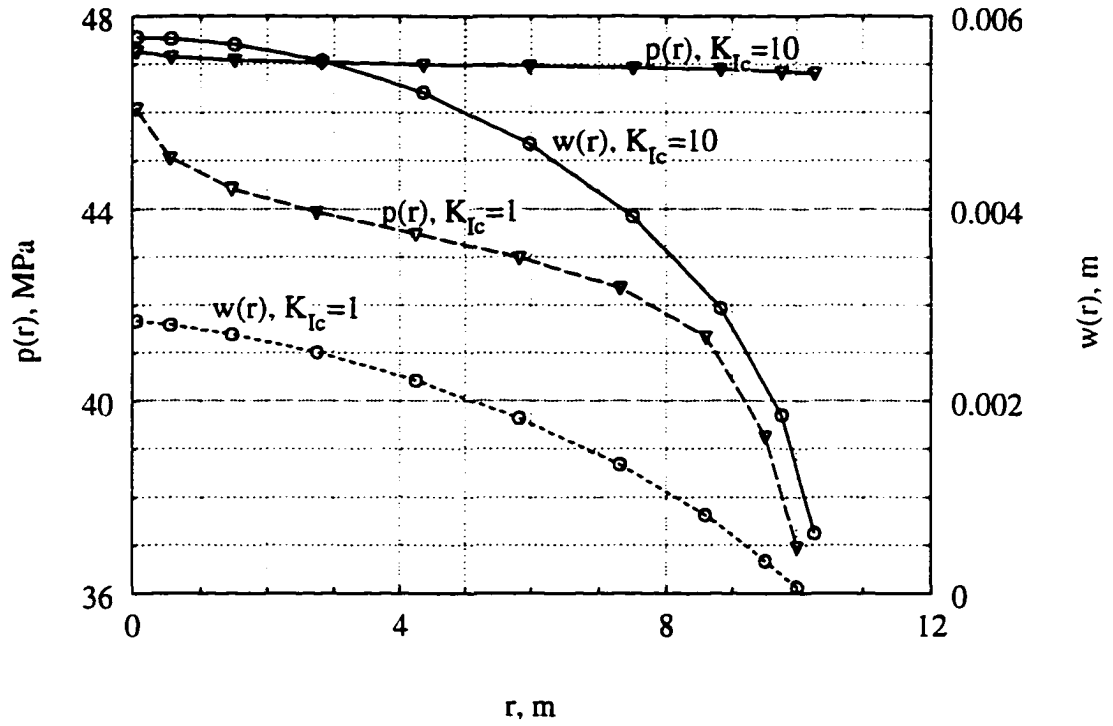


Figure 5.3: Comparison of pressure and aperture profiles between high and low fracture toughnesses.

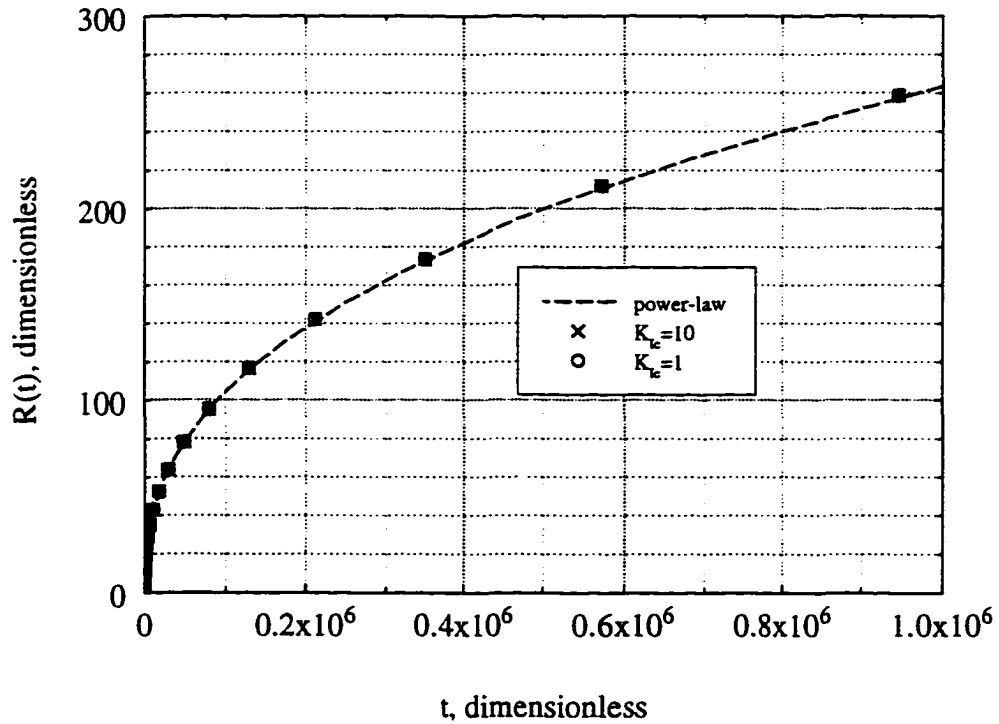


Figure 5.4: Fracture propagation history projected in the dimensionless coordinates.

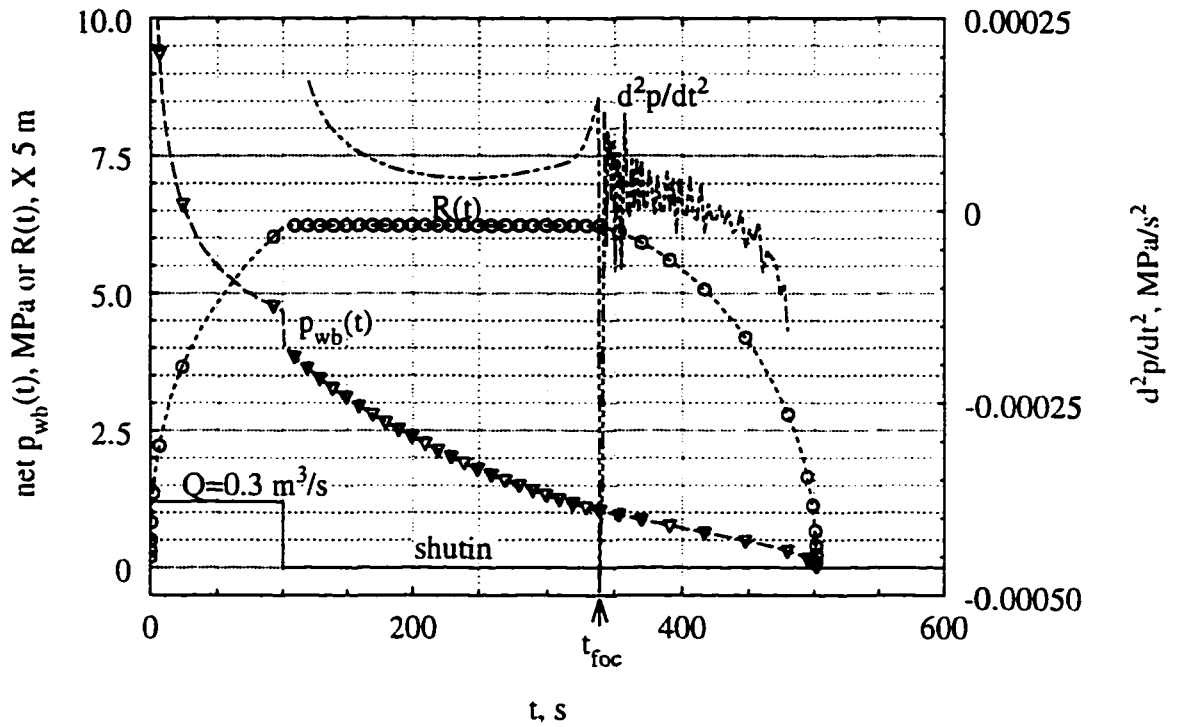


Figure 5.5: Evolution of the post-shut-in wellbore pressure and fracture radius. Carter's leakoff.

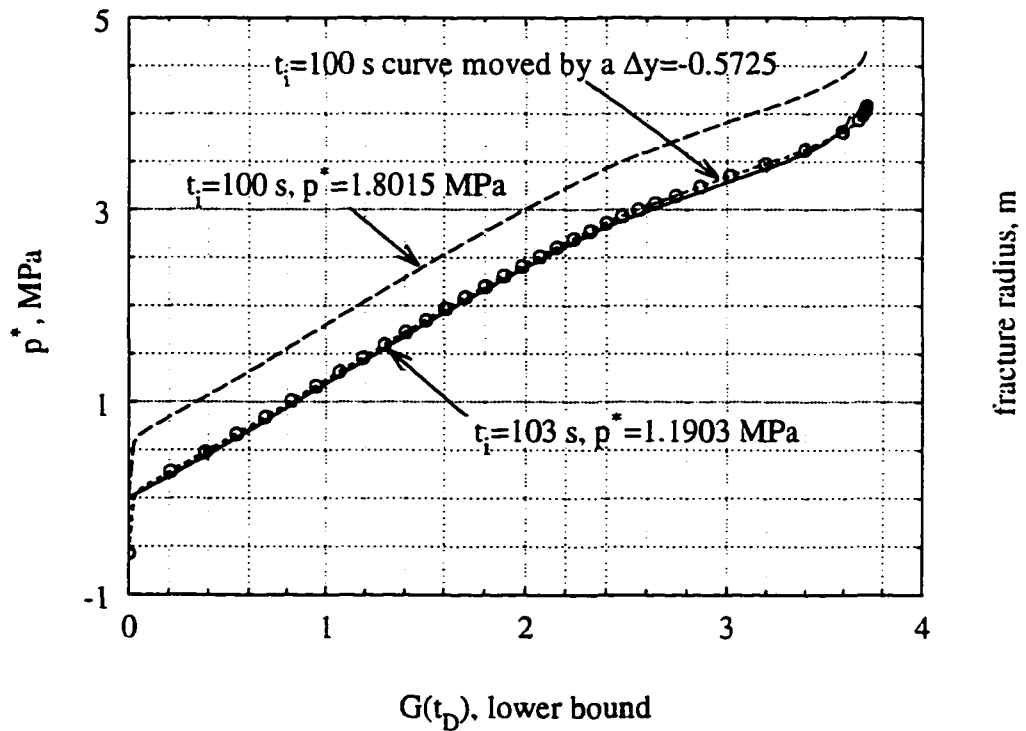


Figure 5.6: Nolte's pressure decline curve.

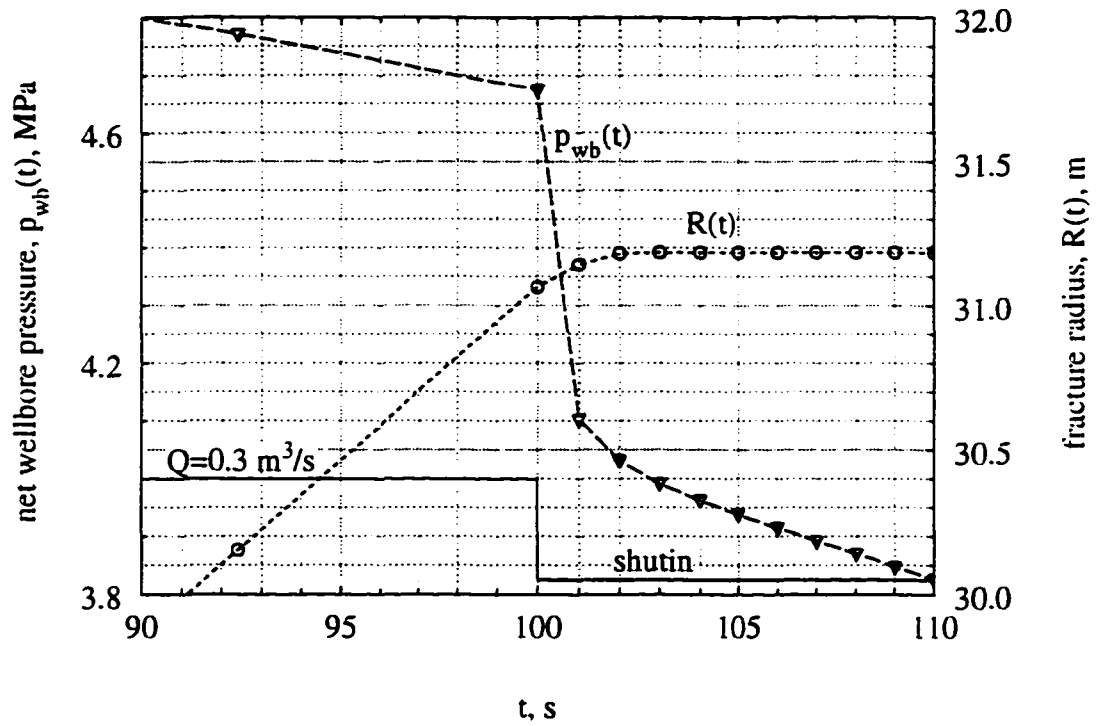


Figure 5.7: Zoom-up of Figure 5.5 near  $t = 100$  s to show the continuous fracture propagation after shut-in.

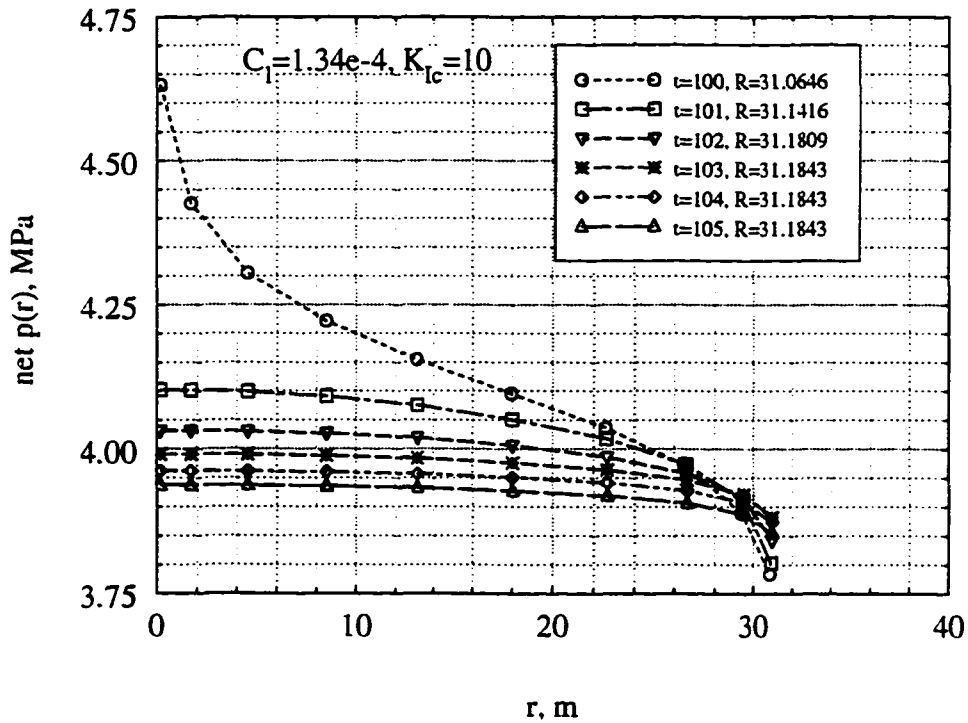


Figure 5.8: Evolution of the pressure profiles immediately after shut-in.

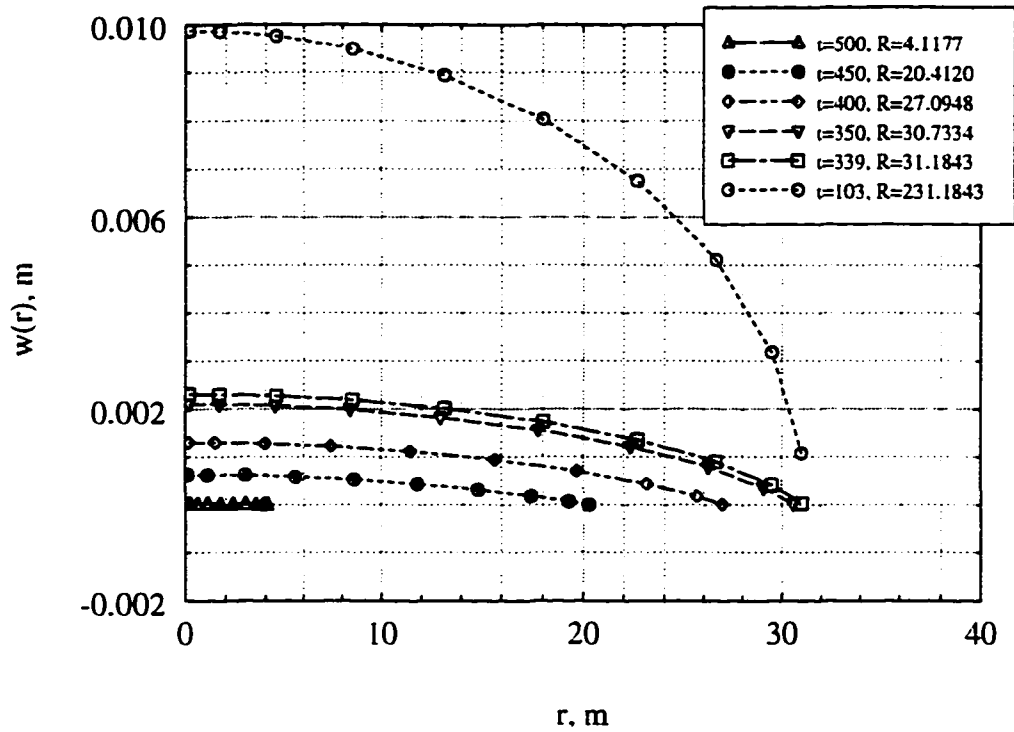


Figure 5.9: Evolution of the aperture profiles during the fracture closure.

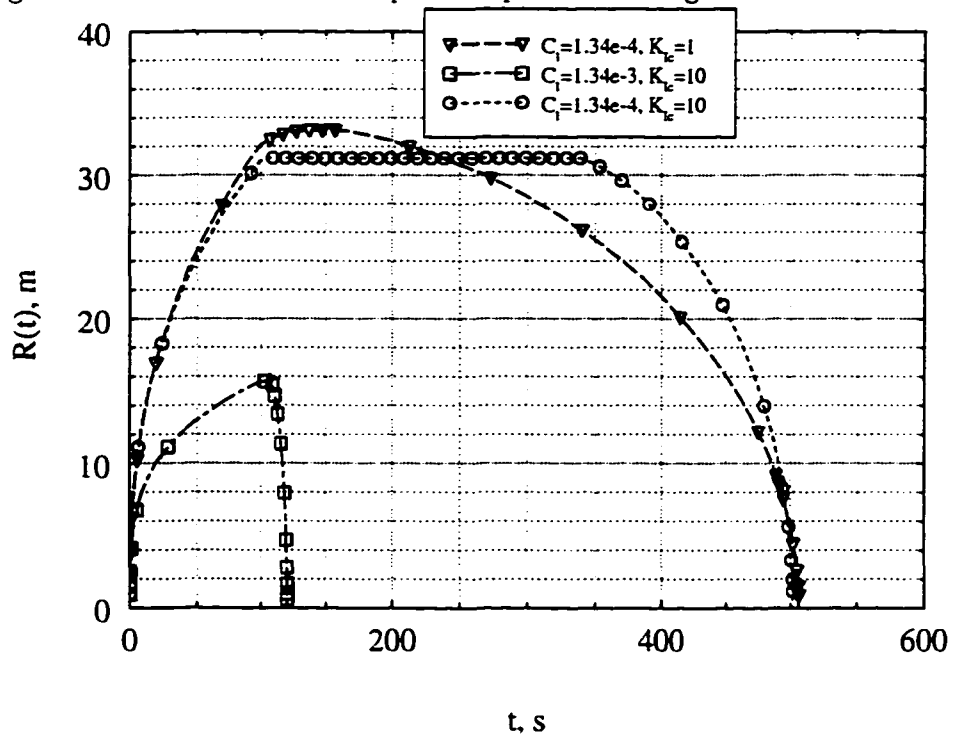


Figure 5.10: Comparison of the fracture radius among the different leakoff coefficients and/or fracture toughnesses.

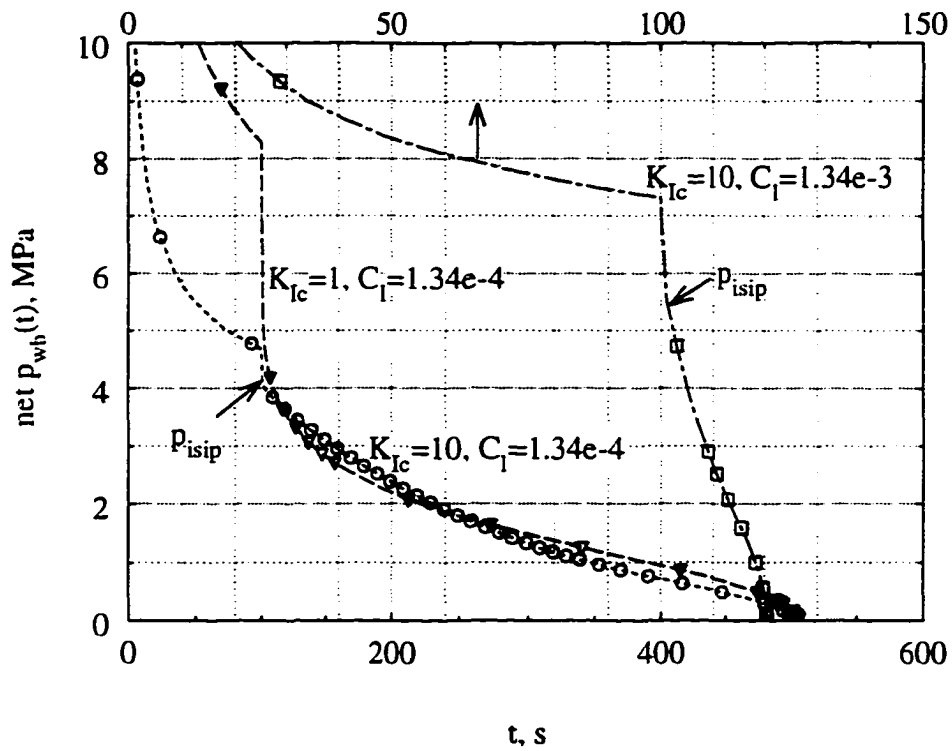


Figure 5.11: Zoom-up of the wellbore pressure evolution near the shut-in time to show up the  $p_{isip}$ .

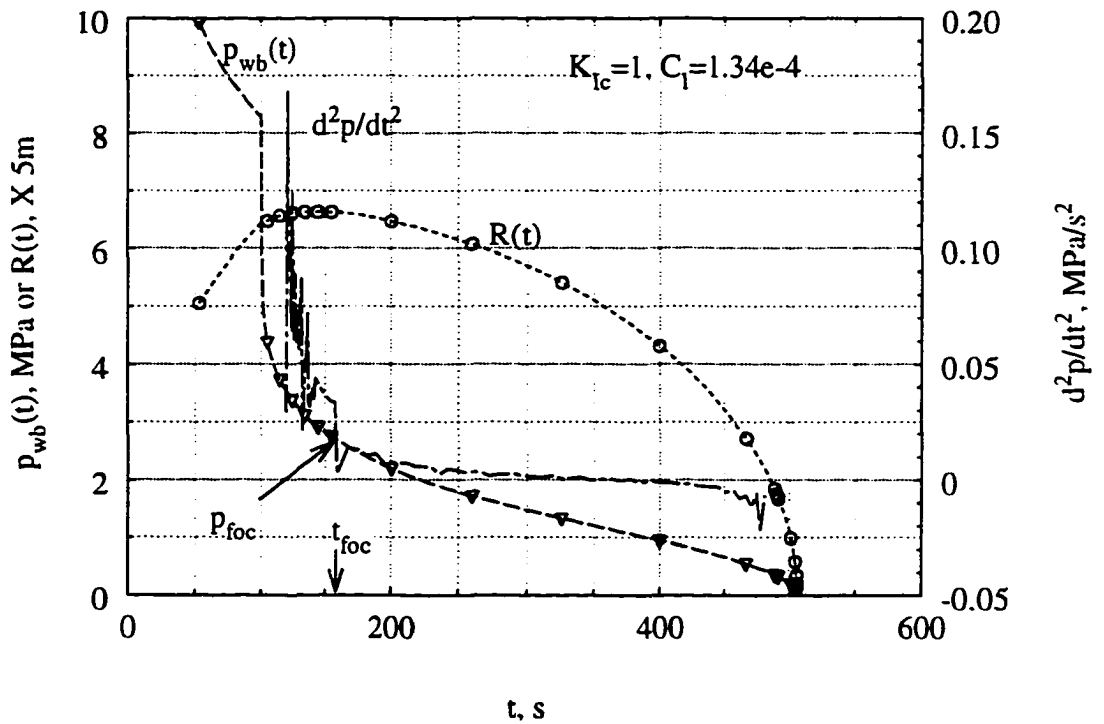


Figure 5.12:  $p_{foc}$  point on the wellbore pressure logs as reflected by its second time derivatives.

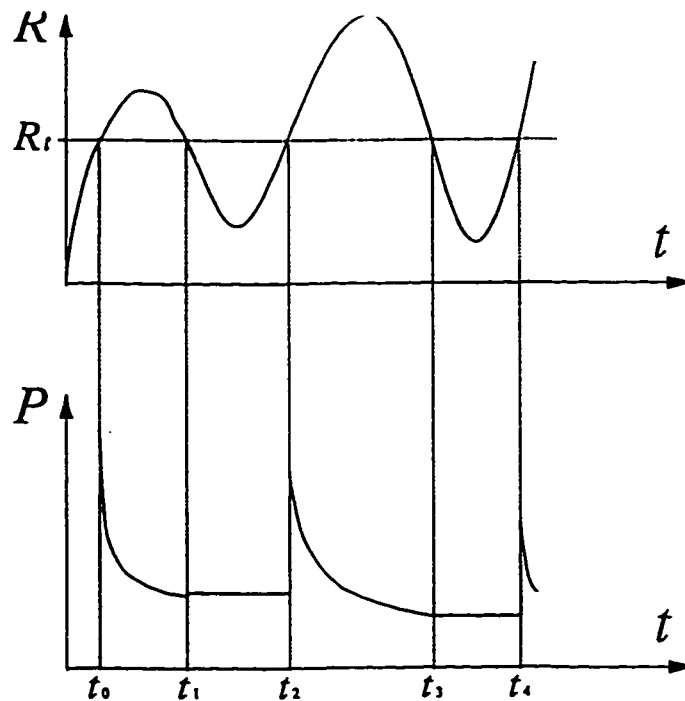


Figure 5.13: Calculating pressure-dependent leakoff in multiple fracturing events.

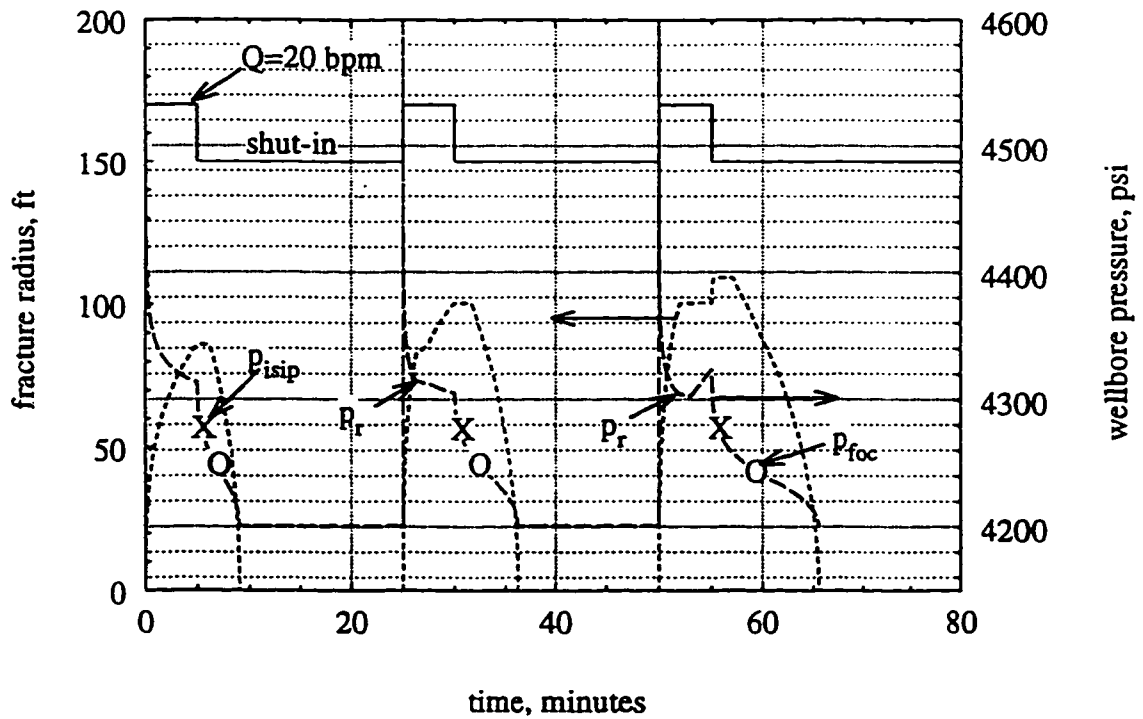


Figure 5.14: Evolution of fracture radius and wellbore pressure under multiple pumping cycles.



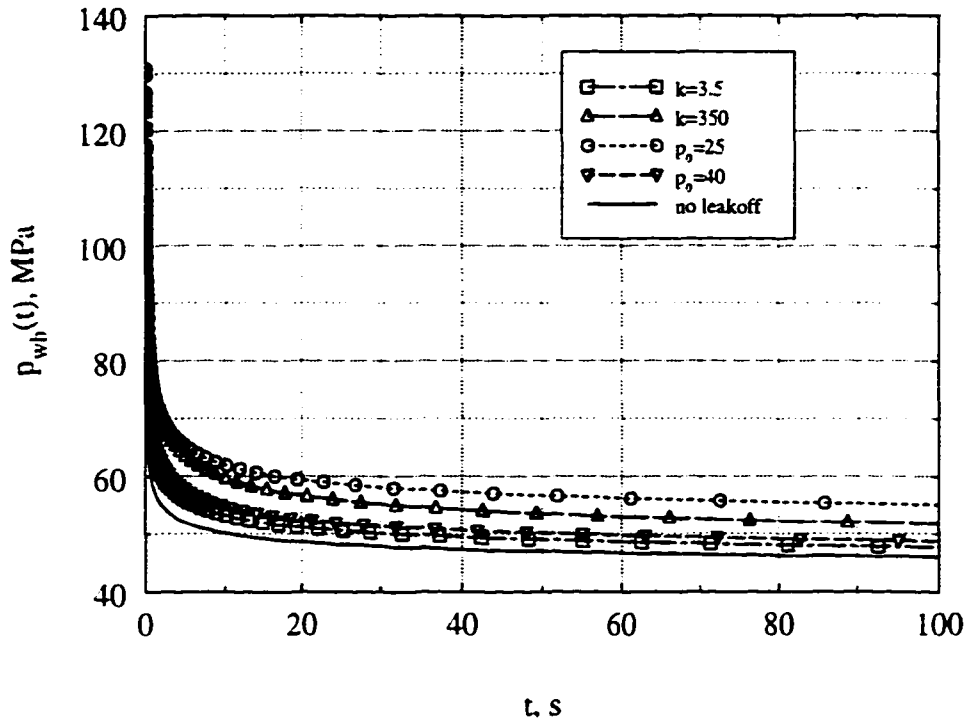


Figure 5.15: Poroelastic effect on wellbore pressure response and its parametric dependence.

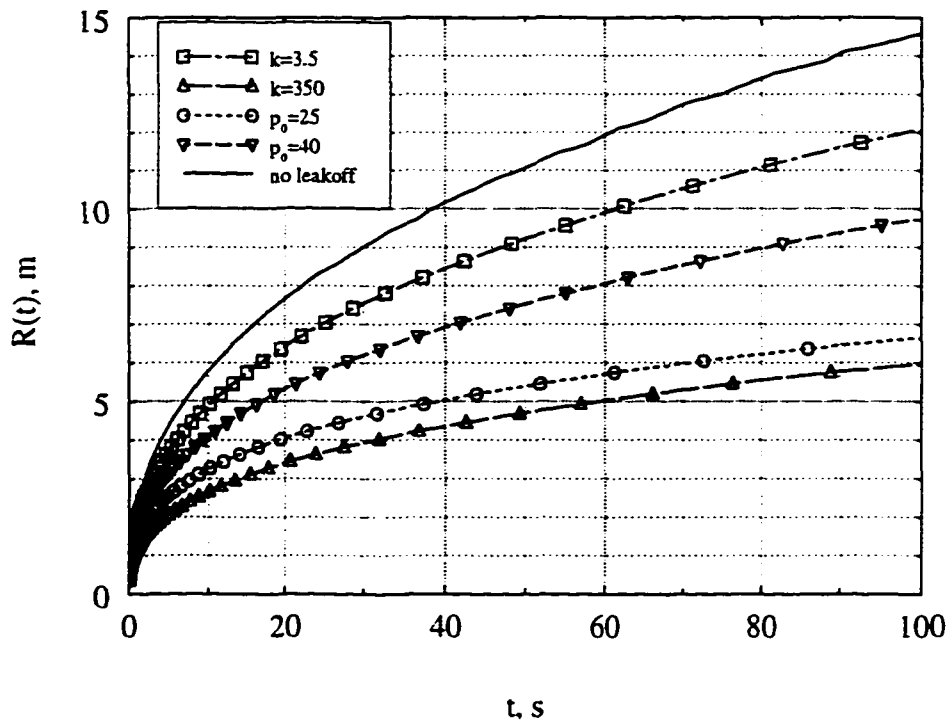


Figure 5.16: Poroelastic effect on the created fracture radius and its parametric dependence.

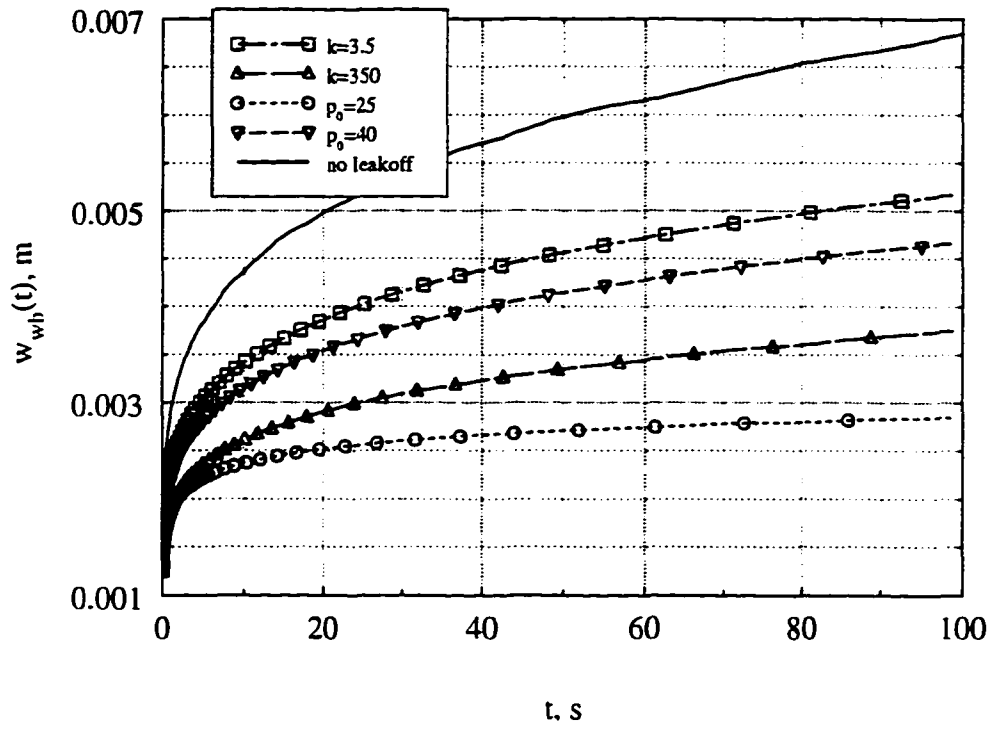


Figure 5.17: Poroelastic effect on wellbore fracture aperture and its parametric dependence.

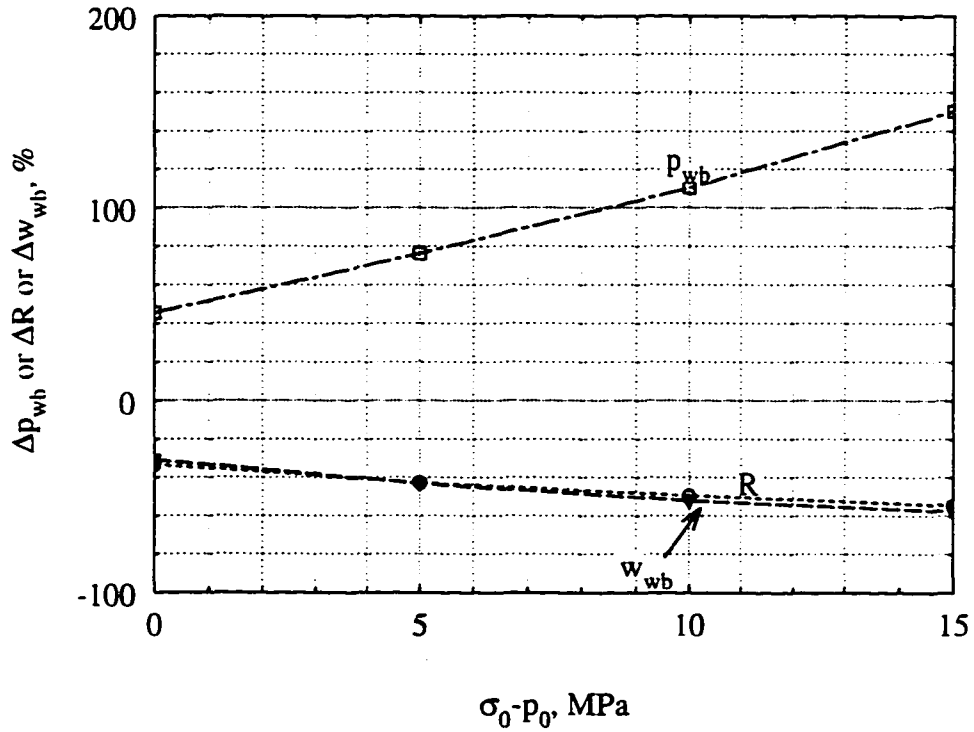


Figure 5.18: Effect of the *in-situ* stress and pore pressure difference,  $\sigma_0 - p_0$ , via the poroelastic mechanism.

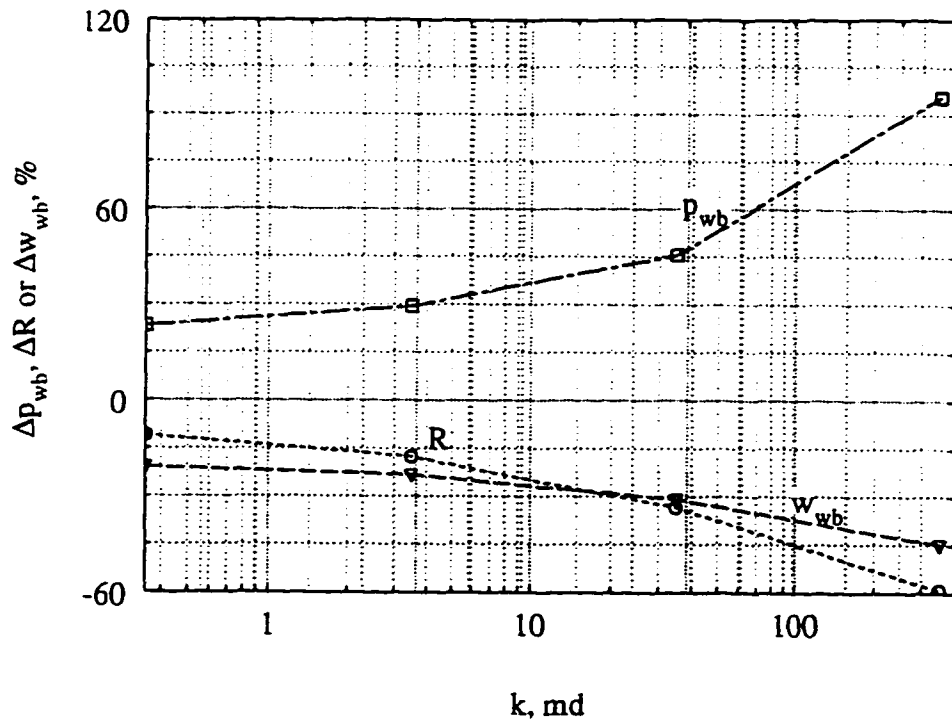


Figure 5.19: Effect of the formation permeability,  $k$ , via the poroelastic mechanism.

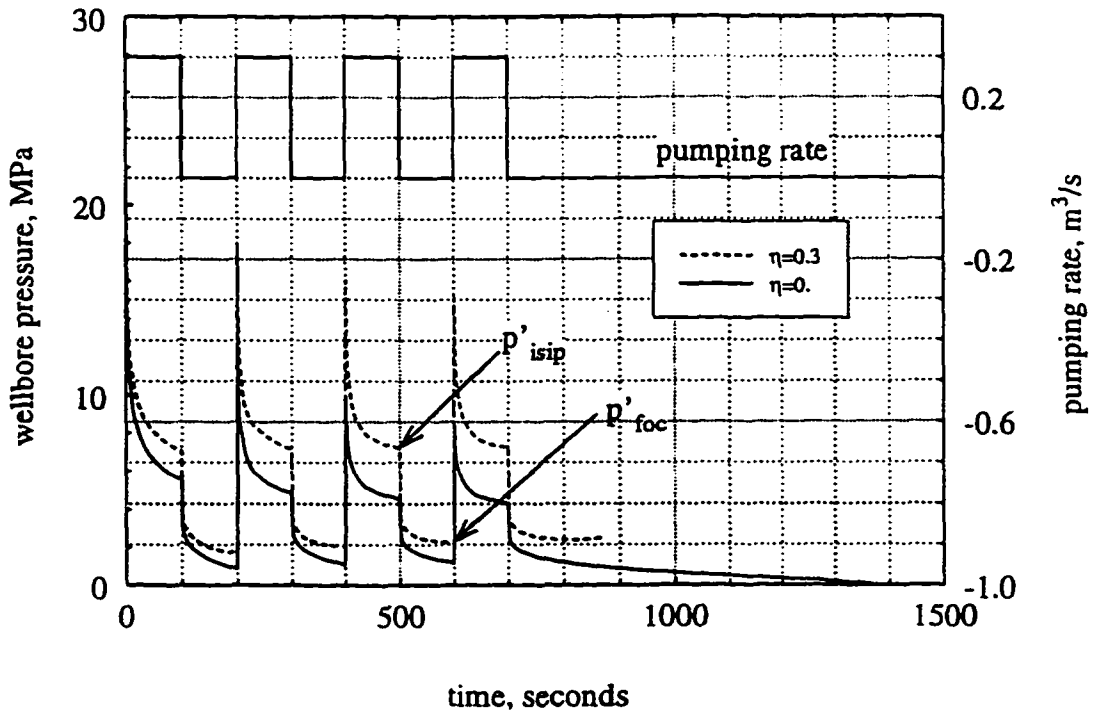


Figure 5.20: Evolution of wellbore pressure response during multiple pumping cycles under pressure-dependent leakoff.

# Chapter 6

## Conclusions and Recommendations for Future Work

In all, the following conclusions can be drawn:

- (a) The full poroelastic model can be approximated, to an adequately good accuracy, by the simplified 2-D poroelastic model derived in this work. It involves less than 10% relative error in the significant part of the poroelastic domain, when compared with the numerical computations by ABAQUS for the full poroelastic model. Equally importantly, the simplified model is computationally efficient and comparable to the 1-D model. Therefore, it provides an effective and efficient methodology to account for the poroelastic effect in the conventional HF simulations.
- (b) The size effect of the propagating fracture, which has not been included in the 1-D model, enhances the backstress-induced fracture deformation if the 2-D model is used. Therefore, in general, the 1-D model underestimates the poroelastic effect. A faster propagating fracture and/or a more permeable formation increases this contrast. Figures 3.27-28 help illustrating these points. In contrast, the 1-D poroelastic model predicted a

much more comparable leakoff rate to the 2-D model as shown in Figure 3.29.

- (c) The pseudo-explicit finite difference method has proven suitable to solve the coupled nonlinear integro-differential equation system. The numerical tests suggested that it is stable, consistent and convergent. Excellent accuracy has been obtained in the computed examples. With the help of the Newton-Raphson scheme for a nonlinear equation set, the efficiency of the PEFD scheme is believed to be remarkable. Additionally, the flexibility of the explicit FD method is inherited. Therefore, more complicated physics can be included with few additional difficulties, such as the current pressure-dependent leakoff and poroelastic effect. Similarly, thermal effects can be easily implemented.
- (d) McFrac, the resultant HF simulator after this work [157, 174, 175, 176], is able to model the complicated fracture propagation/closure/re-opening events during multiple injection/shut-in/flow-back pumping cycles. For example, several characteristic pressures,  $p_{isip}$ ,  $p_{foc}$  and  $p_r$  which are commonly used to determine the *in-situ* minimum stress in the micro-HF jobs, can be easily pin-pointed on the computed wellbore pressure logs.
- (e) Poroelastic effects, including the pressure-dependent leakoff and the backstress-induced fracture closure, significantly increases the wellbore pressure response. The increase relative to the purely elastic case without leakoff has reached a high of 150%. Meanwhile, the poroelastic mechanism causes more fluid leakoff into the formation and therefore, reduces both the fracture aperture and radius. The magnitude of the poroelastic effect is linearly proportional to the *in-situ* stress and pore pressure difference,  $\sigma_0 - p_0$ , and is a positive power function of the formation permeability,

$\kappa$ . The poroelastic effect increases with the number of pumping cycles.

The recommended future works include:

- (a) use McFrac to compute a variety of additional examples, particularly field cases, to relate various *in-situ*/formation characteristics to the wellbore pressure response. The author keenly believes<sup>1</sup> that there is good promise in using multiple pumping cycles to characterize, more accurately and in more details, the previously-created hydraulic fracture and the relevant *in-situ* parameters. The former includes the fracture dimension and detailed geometry such as surface roughness, multiple fracture strands, etc. The latter includes the *in-situ* minimum principal stress, leakoff characteristics, *in-situ* value of fracture toughness and other material parameters, which are otherwise difficult or impossible to obtain by conventional methods. There have been successful attempts made in industry along similar directions. But could more be forthcoming?
- (b) validate the mathematical accuracy of the principle of extending the stationary fracture-based 2-D model to the propagating fracture. Moreover, new avenues have to be derived to extend it to a receding fracture.
- (c) add additional improvements in modeling the fracture recession in the complicated poroelastic domain.

---

<sup>1</sup>The inspiration comes from the history of exploration seismology. In its early history, the recorded full seismic waveforms were only analyzed for two points: the P- or S-wave arrival times. Gradually, more information carried on the waveform is utilized, such as the incidence phase angle, shear-wave splitting, ..., until full waveform modeling. Multiple ISF cycles not only generate the wave-like wellbore pressure history; but also should carry more information about the formation properties and the fracturing behavior. It is hoped that the present study will open a way to this arena.

# Appendix A

## Proof of the 1-D Poroelastic Formulae

Proof of Eqn. (2.29) can be carried out by combining the various equations stated in the above. The procedure is illustrated here by taking mode 2 loading as an example. Integrating Eqn. (2.19) over  $x \in [0, \infty]$  and considering Eqn. (2.24) gives:

$$w^p(t) = -\frac{\eta}{G} \int_0^{\infty} p(x, t) dx \quad (\text{A.1})$$

while integrating Eqn. (2.27) over  $x \in [0, \infty]$  yields:

$$\left. \frac{\partial p}{\partial x} \right|_{x=0} = -\frac{1}{c} \int_0^{\infty} \frac{\partial p(x, t)}{\partial t} dx \quad (\text{A.2})$$

where the regularity condition at infinity,  $\left. \frac{\partial p}{\partial x} \right|_{x=\infty} = 0$  and  $w^p(x \rightarrow \infty) = 0$ , are applied. Therefore, via Darcy's law, the leakoff rate at  $x = 0$  is given by:

$$u(t) = \frac{\kappa}{c} \int_0^{\infty} \frac{\partial p(x, t)}{\partial t} dx \quad (\text{A.3})$$

Integrating the above equation over  $\tau \in [0, t]$  results in:

$$\begin{aligned} \int_0^t u(\tau) d\tau &= \frac{\kappa}{c} \int_0^t d\tau \int_0^{\infty} \frac{\partial p(x, \tau)}{\partial \tau} dx \\ &= \frac{\kappa}{c} \int_0^{\infty} p(x, t) dx \end{aligned} \quad (\text{A.4})$$

where the initial condition  $p(x, t = 0) = 0$  is substituted. Comparing Eqn. (A.1) with Eqn. (A.4) comes to Eqn. (2.28).

Similar derivations can be carried out for mode 1 loading, which shows the displacement field consisting of the following two parts:

$$\Delta w(x, t) = w(x, t) - w(x = 0, t) = \Delta w^e(x, t) + \Delta w^p(x, t) \quad (\text{A.5})$$

with

$$\Delta w^e(x, t) = \frac{1 - 2\nu_u}{2G(1 - \nu_u)} [p_f(t) - \sigma_0] x \quad (\text{A.6})$$

$$\Delta w^p(x, t) = -\frac{\eta c}{G\kappa} \int_0^t [u(x, \tau) - u(\tau)] d\tau \quad (\text{A.7})$$

Obviously,  $\Delta w^e(x, t)$  represents the undrained response to the mechanical loading,  $p_f(t) - \sigma_0$ .  $\Delta w^p(x, t)$  purely depends on the fluid leakoff into/out from the model, thus belonging to the poroelastic displacement. Note that in this part,  $w^p$  and  $u$  both tend to zero as  $x \rightarrow \infty$ ; and; therefore, Eqn. (A.7) can be reduced to Eqn. (2.28).

Eqn. (2.28) implies that  $w^p(t)$  is proportional to the total fluid leakoff volume into the media through  $x = 0$  until the current time,  $t$ . To arrive at Eqn. (2.28), the pressure boundary condition at  $x = 0$ , i.e.  $p(x, t) = 0$  or  $p(x, t) = p_f - p_0$ , is not required. Therefore, if the boundary condition there changes to a leakoff rate-prescribed boundary such as in Carter's leakoff model,  $u(x = 0, t) = u_0(t)$ , Eqn. (2.28) still holds.

Again, proof of the leakoff rate is given to Eqn. (2.30) only, which corresponds to mode 2 loading. Calculation of the leakoff rate needs the knowledge about the pore pressure field,  $p(x, t)$ , which is obtained by solving the diffusion equations (2.26) or (2.27). This can be readily found in the literature



such as [121]. Following the Green's function principle [122], the fundamental diffusion problem in semi-infinite domain:

$$\begin{cases} c \frac{\partial^2 p}{\partial x^2} - \frac{\partial p}{\partial t} = -\delta(x-s)\delta(t-\lambda) & x > 0, t > 0 \\ p(x, t) = 0 & x = 0, t > \lambda \end{cases} \quad (\text{A.8})$$

for given  $s, \lambda$  has a fundamental solution to  $p$ ,  $G_p(x, t; s, \lambda)$  and the associated leakoff rate at  $x = 0$ ,  $G_u(t; s, \lambda)$  as:

$$G_p(x, t; s, \lambda) = \sqrt{\frac{1}{4\pi c(t-\lambda)}} e^{-(x-s)^2/4c(t-\lambda)} - \sqrt{\frac{1}{4\pi c(t-\lambda)}} e^{-(x+s)^2/4c(t-\lambda)} \quad (\text{A.9})$$

$$G_u(t; s, \lambda) = -\frac{s\kappa}{\sqrt{4\pi[c(t-\lambda)]^{3/2}}} e^{-s^2/4c(t-\lambda)} \quad (\text{A.10})$$

The particular solutions to the problem:

$$\begin{cases} c \frac{\partial^2 p}{\partial x^2} - \frac{\partial p}{\partial t} = -f(x, t) & x > 0, t > 0 \\ p(x, t) = g(x) & x > 0, t = 0 \\ p(x, t) = h(t) & x = 0, t > 0 \end{cases} \quad (\text{A.11})$$

can be written as:

$$\begin{aligned} p(x, t) &= \int_0^t d\lambda \int_0^\infty G_p(x, t; s, \lambda) f(s, \lambda) ds + \int_0^\infty G_p(x, t; s, 0) g(s) ds \\ &\quad + c \int_0^t h(\lambda) \left. \frac{\partial}{\partial s} G_p(x, t; s, \lambda) \right|_{s=0} d\lambda \end{aligned} \quad (\text{A.12})$$

$$\begin{aligned} u(t) &= \int_0^t d\lambda \int_0^\infty G_u(t; s, \lambda) f(s, \lambda) ds + \int_0^\infty G_u(t; s, 0) g(s) ds \\ &\quad + c \int_0^t h(\lambda) \left. \frac{\partial}{\partial s} G_u(t; s, \lambda) \right|_{s=0} d\lambda \end{aligned} \quad (\text{A.13})$$

Particular for mode 2 loading, the various components corresponding to the differential equation set, (A.11), are:

$$\begin{cases} f(s, \lambda) = 0 \\ g(s) = 0 \\ h(\lambda) = p_f(\lambda) - p_0 \end{cases} \quad (\text{A.14})$$

Therefore, Eqn. (A.13) becomes:

$$u^2(t) = \int_0^t [p_f(\lambda) - p_0] \frac{\partial}{\partial t} \left[ \frac{\kappa}{\sqrt{\pi c(t-\lambda)}} \right] d\lambda \quad (\text{A.15})$$

Integrating by parts yields Eqn. (2.30).

## Appendix B

# Proof of the Steady-State Poroelastic Displacement Formula

Eqn. (2.42) can be proven by combining Eqn. (2.37) to Eqn. (2.39) and Eqn. (2.40). The key in the proof is to validate the equality of:

$$f(x) = \left[ \frac{(1-\nu)R_0}{G} \right] \eta p_f(x) \quad . \quad (\text{B.1})$$

Performing the integration-by-parts twice w.r.t.  $u$  in the second integral in Eqn. (2.40) yields:

$$q(\eta) = \frac{2}{\pi R_0} \left[ \frac{\sin \eta}{\eta} \int_0^1 \frac{y g_1(y) dy}{\sqrt{1-y^2}} - \frac{1}{\eta} \int_0^1 \frac{y^2 dy}{\sqrt{1-y^2}} \int_0^1 g_2(yu) \sin(\eta u) du \right] \quad (\text{B.2})$$

with:

$$g_1(v) = p_f(v) + s p'_f(v) \quad (\text{B.3})$$

$$g_2(v) = 2 p'_f(v) + s p''_f(v) \quad (\text{B.4})$$

and  $p'_f(v) = \frac{dp_f(v)}{dv}$  and  $p''_f(v) = \frac{d^2 p_f(v)}{dv^2}$ . Substituting Eqn. (B.2) into Eqn. (2.39) and utilizing the integral:

$$\int_0^\infty \frac{J_0(xt) \sin(yt) dt}{t} = \begin{cases} \frac{\pi}{2} & x \leq y \\ \sin^{-1} \left( \frac{y}{x} \right) & x \geq y \end{cases} \quad (\text{B.5})$$

leads to:

$$f(x) = \frac{(1-\nu)R_0\eta}{G} \left[ \int_0^1 \frac{v g_1(v) dv}{\sqrt{1-v^2}} - \int_x^1 du \int_0^1 \frac{v^2 g_2(uv) dv}{\sqrt{1-v^2}} - \frac{2}{\pi} \int_0^x \sin^{-1}\left(\frac{u}{x}\right) du \int_0^1 \frac{v^2 g_2(uv) dv}{\sqrt{1-v^2}} \right] \quad (B.6)$$

Eqn. (B.5) is obtained after manipulating the integral property [127]:

$$\int_0^\infty \frac{\sin(\eta)}{\eta} J_0(\rho\eta) d\eta = \begin{cases} \sin^{-1}\left(\frac{1}{\rho}\right) & \rho \geq 1 \\ \frac{\pi}{2} & \rho \leq 1 \end{cases} \quad (B.7)$$

Substituting the definition of  $g_1$  and  $g_2$  into Eqn. (B.6), performing a series of integration-by-parts and exchanging the integration variable finally gives:

$$f(x) = \frac{(1-\nu)R_0\eta}{G} \left[ \frac{2}{\pi} \int_0^1 \frac{v dv}{\sqrt{1-v^2}} \int_0^{vx} \frac{g_1(u) du}{\sqrt{v^2 x^2 - u^2}} \right] \quad (B.8)$$

Therefore, the burden of the proof is to show that the quantity in the bracket of the above equation satisfies the following equality:

$$I = \frac{2}{\pi} \int_0^1 \frac{v dv}{\sqrt{1-v^2}} \int_0^{vx} \frac{g_1(u) du}{\sqrt{v^2 x^2 - u^2}} = p_f(x) \quad (B.9)$$

Direct proof of Eqn. (B.9) is very difficult; hence, an analytical series approach is employed.

Assume that the pressure distribution function,  $p_f(u)$ , is analytical for  $u \in (0, 1)$ . Thus, it can be expanded into Taylor series w.r.t. to an interior point,  $u_0$ :

$$p_f(u) = \sum_{n=0}^{\infty} \frac{p_f^{(n)}(u_0)}{n!} (u - u_0)^n \quad (B.10)$$

which is absolutely convergent over the convergence circle,  $|u - u_0| < r_s^1$ .

$p_f^{(n)} = d^n p_f / du^n$ . Further expanding  $(u - u_0)^n$  into the power series of  $u$ :

$$(u - u_0)^n = \sum_{m=0}^n (-1)^m \frac{n(n-1)\dots(n-m+1)}{m!} u^{n-m} u_0^m \quad (B.11)$$

---

<sup>1</sup>Note that a particular convergence circle may not necessarily lead  $u$  to cover all the defined region  $(0, 1)$ . But based on the continuation of analytical expansion [122], a series of different  $u_0$  can indeed make the expansion, Eqn. (B.10), valid for any analytical points within the region  $u \in (0, 1)$ .

gives:

$$g_1(u) = \frac{d[up_f(u)]}{du} = \sum_{n=0}^{\infty} \frac{g^{(n)}(u_0)}{n!} \left[ \sum_{m=0}^n (-1)^m \frac{n(n-1)\dots(n-m+1)(n-m+1)}{m!} u^{n-m} u_0^m \right] \quad (\text{B.12})$$

The prototype integral of:

$$I_1 = \frac{2}{\pi} \int_0^1 \frac{v dv}{\sqrt{1-v^2}} \int_0^{vx} \frac{u^{n-m} du}{\sqrt{v^2 x^2 - u^2}} \quad (\text{B.13})$$

can be computed by changing the integration variable,  $u$ , to  $z$  via  $u = vxz$  and using the elementary integral property of:

$$\begin{aligned} \int_0^1 \frac{v^k dv}{\sqrt{1-v^2}} &= \int_0^{\pi/2} \sin^k t dt \\ &= \frac{k-1}{k} \int_0^{\pi/2} \sin^{k-2} t dt \\ &= \begin{cases} \frac{\pi}{4} \left[ \frac{(k-1)(k-3)(k-5)\dots 3}{k(k-2)(k-4)\dots 4} \right] & \text{if } k = 2l \\ \frac{(k-1)(k-3)(k-5)\dots 2}{k(k-2)(k-4)\dots 3} & \text{if } k = 2l + 1 \end{cases} \end{aligned} \quad (\text{B.14})$$

which finally yields:

$$I_1 = \frac{1}{n-m+1} x^{n-m} \quad (\text{B.15})$$

Therefore,

$$\begin{aligned} I &= \sum_{n=0}^{\infty} \frac{p_f^{(n)}(u_0)}{n!} \left\{ \sum_{m=0}^n (-1)^m \frac{n(n-1)\dots(n-m+1)(n-m+1)u_0^m}{m!} \left[ \frac{2}{\pi} \int_0^1 \frac{v dv}{\sqrt{1-v^2}} \int_0^{vx} \frac{u^{n-m} du}{\sqrt{v^2 x^2 - u^2}} \right] \right\} \\ &= \sum_{n=0}^{\infty} \frac{p_f^{(n)}(u_0)}{n!} \left[ \sum_{m=0}^n (-1)^m \frac{n(n-1)\dots(n-m+1)}{m!} x^{n-m} u_0^m \right] \\ &= \sum_{n=0}^{\infty} \frac{p_f^{(n)}(u_0)}{n!} (x - u_0)^{n-m} \\ &= p_f(x) \end{aligned} \quad (\text{B.16})$$

With  $I$  given by  $p_f(x)$ , it can be easily shown that Eqn. (B.1) is met. Substituting Eqn. (B.1) into Eqn. (2.38) and in turn into Eqn. (2.37) and using the integral property [127]:

$$\int_0^\infty \sin(\mu\eta)J_0(\rho\eta)d\eta = \begin{cases} 0 & \rho > \mu \\ \frac{1}{\sqrt{\mu^2-\rho^2}} & 0 < \rho < \mu \end{cases} . \quad (\text{B.17})$$

gives Eqn. (2.42).

## Appendix C

### Equations for Power-law Fluid Flow inside Fractures

Take a representative volume in the fluid which is flowing inside two parallel plates (Figure A.1). Let us first derive the momentum equation. The Newton's second law dictates the force balance as follows:

$$\frac{dp}{dr}(2\pi rz)\Delta r = (2\pi r\Delta r)\tau \quad (\text{C.1})$$

where the property of  $\tau = 0$  at  $z = 0$  due to the symmetry of the flow system is used. Also implied in this equation is a small Reynolds number so that a laminar flow exists and the inertial force is negligibly small. For a power-law fluid,

$$\tau = K \left( -\frac{du_r}{dz} \right)^n \quad (\text{C.2})$$

in which the property of a decreasing velocity profile in the  $z$ -direction is used so that  $-\frac{du_r}{dz}$  is positive.  $u_r$  is the flow velocity along the  $r$  direction. Combining Eqn. (C.1) and Eqn. (C.2) yields:

$$\frac{du_r}{dz} = - \left( \frac{1}{K} \frac{dp}{dr} \right)^{1/n} z^{1/n} \quad (\text{C.3})$$

Defining the fluid flux through the parallel plates,  $q$ , as the volumetric rate per unit circumference, i.e.,

$$q = \frac{Q}{2\pi r} = \frac{1}{2\pi r} \left[ 2 \int_0^{w/2} u_r(2\pi r) dz \right] \quad (\text{C.4})$$

integrating the R.H.S. of Eqn. (C.4) by parts and using Eqn. (C.3) gives:

$$q = 2 \left[ u_r z \Big|_{z=0}^{w/2} + \int_0^{w/2} \left( \frac{1}{K} \frac{dp}{dr} \right)^{1/n} z^{(n+1)/n} dz \right] \quad (\text{C.5})$$

i.e.,

$$q = \frac{n}{2n+1} \frac{1}{2^{(n+1)/n}} \left( \frac{1}{K} \frac{dp}{dr} \right)^{1/n} w^{(2n+1)/n} \quad (\text{C.6})$$

In the above, we have used the non-slip property of  $u_r = 0$  at the fracture wall ( $z = w/2$ ) and assumed that  $\frac{dp}{dr}$  does not change across the fracture in the  $z$ -direction. Note that the above derivation has not required any particular property about the fracture aperture,  $w$ , between the plates. Therefore, although Figure A.1 depicts a constant aperture, Eqn. (C.6) is valid for a changing aperture profile,  $w(r)$ .

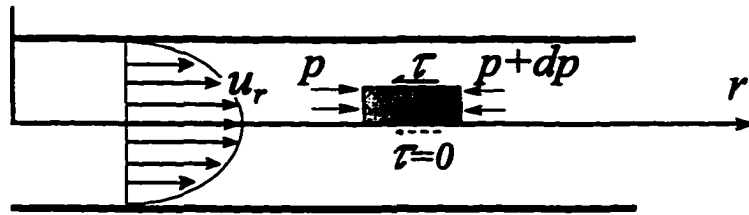
Now, let us proceed to derive the local fluid mass balance equation. Take another representative segment of  $r \in [r, r + \Delta r]$  along the fracture (Figure A.2). Adding up the various mass transfer components results:

$$-\frac{\partial Q}{\partial r} \Delta r \Delta t - u(2\pi r) \Delta r \Delta t - \frac{\partial w}{\partial t} (2\pi r) \Delta r \Delta t = 0 \quad (\text{C.7})$$

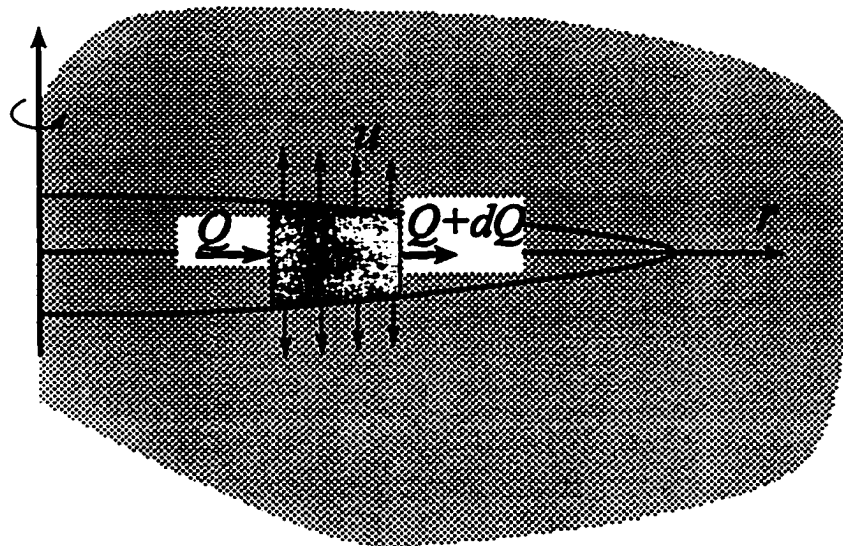
if the fluid is assumed to be incompressible.  $u$  consists of the leakoff from the upper and lower fracture surfaces. Noting  $Q$  is related to the fluid flux,  $q$ , via

$$Q = 2\pi r q \quad (\text{C.8})$$

yields the mass balance equation, Eqn. (4.2), in the text.



(a)



(b)

Figure C.1: Sketch of an elementary volume to derive: (a). the momentum equation and (b). mass balance equation for fluid flow inside parallel plates.



## Appendix D

### Matrix Coefficients in NR Algorithm

With the known solution at the end of iteration step  $m$  in time step  $n$ , the incremental pressure  $\delta p_{i,n}^m$  during the iteration step  $m + 1$  is computed via the following:

$$\alpha_{ij} \delta p_{j,n}^m = \beta_i \quad i = 1, 2, \dots, N \quad . \quad (D.1)$$

The coefficients are computed differently for cases of pressure-dependent and pressure-independent (Carter's) leakoff.

#### Pressure-dependent Leakoff

$$\begin{aligned} \alpha_{1j} &= \frac{c_{1j}^w}{\Delta t} + \left(1 - \frac{\eta c}{G\kappa}\right) \frac{4\kappa}{\sqrt{\pi c \Delta t}} \delta_{1,j} \\ &+ C_{1+1/2}^\alpha \left\{ \left(1 + \frac{1}{2n}\right) \left[ c_{2,j}^w + c_{1,j}^w - \frac{8\eta}{3G} \sqrt{\frac{c \Delta t}{\pi}} (\delta_{2,j} + \delta_{1,j}) \right] \frac{\partial p}{\partial \theta} \Big|_{1+1/2} \right. \\ &\left. + \frac{S_{1+1/2}^p w_{1+1/2}}{n(\theta_2 - \theta_1)} (\delta_{2,j} - \delta_{1,j}) \right\} \quad (D.2) \\ \alpha_{ij} &= \frac{c_{ij}^w}{\Delta t} + \left(1 - \frac{\eta c}{G\kappa}\right) \frac{4\kappa}{\sqrt{\pi c \Delta t}} \delta_{i,j} \\ &+ C_{i+1/2}^\alpha \left\{ \left(1 + \frac{1}{2n}\right) \left[ c_{i+1,j}^w + c_{i,j}^w - \frac{8\eta}{3G} \sqrt{\frac{c \Delta t}{\pi}} (\delta_{i+1,j} + \delta_{i,j}) \right] \frac{\partial p}{\partial \theta} \Big|_{i+1/2} \right\} \end{aligned}$$

$$\begin{aligned}
& + \frac{S_{i+1/2}^p w_{i+1/2}}{n(\theta_{i+1} - \theta_i)} (\delta_{i+1,j} - \delta_{i,j}) \Big\} \\
& - C_{i-1/2}^\alpha \left\{ \left(1 + \frac{1}{2n}\right) \left[ c_{i,j}^w + c_{i-1,j}^w - \frac{8\eta}{3G} \sqrt{\frac{c\Delta t}{\pi}} (\delta_{i,j} + \delta_{i-1,j}) \right] \frac{\partial p}{\partial \theta} \Big|_{i-1/2} \right. \\
& \left. + \frac{S_{i-1/2}^p w_{i-1/2}}{n(\theta_i - \theta_{i-1})} (\delta_{i,j} - \delta_{i-1,j}) \right\} \quad i = 2, 3, \dots, N-1 \quad (D.3)
\end{aligned}$$

$$\begin{aligned}
\alpha_{N,j} & = \frac{c_{N,j}^w}{\Delta t} + \left(1 - \frac{\eta c}{G\kappa}\right) \frac{4\kappa}{\sqrt{\pi c \Delta t}} \delta_{N,j} - C_{N-1/2}^\alpha \\
& \left\{ \left(1 + \frac{1}{2n}\right) \left[ c_{N,j}^w + c_{N-1,j}^w - \frac{8\eta}{3G} \sqrt{\frac{c\Delta t}{\pi}} (\delta_{N,j} + \delta_{N-1,j}) \right] \frac{\partial p}{\partial \theta} \Big|_{N-1/2} \right. \\
& \left. + \frac{S_{N-1/2}^p w_{N-1/2}}{n(\theta_N - \theta_{N-1})} (\delta_{N,j} - \delta_{N-1,j}) \right\} \quad (D.4)
\end{aligned}$$

with  $j$  ranges from 1 to  $N$ . And,

$$\begin{aligned}
\beta_1 & = -\frac{w_{1,n}^m - w_{1,n-1}^m}{\Delta t} - \left(1 - \frac{\eta c}{G\kappa}\right) u_{1,n}^m - C_{1+1/2}^\alpha \frac{\partial p}{\partial \theta} \Big|_{1+1/2,n}^m \\
& + \frac{C^q Q_{inj}}{2\pi R \theta_1 (\theta_{1+1/2} - \theta_{1-1/2})} \quad (D.5)
\end{aligned}$$

$$\begin{aligned}
\beta_i & = -\frac{w_{i,n}^m - w_{i,n-1}^m}{\Delta t} - \left(1 - \frac{\eta c}{G\kappa}\right) u_{i,n}^m - C_{i+1/2}^\alpha \frac{\partial p}{\partial \theta} \Big|_{i+1/2,n}^m \\
& + C_{i-1/2}^\alpha \frac{\partial p}{\partial \theta} \Big|_{i-1/2,n}^m \quad i = 2, 3, \dots, N-1 \quad (D.6)
\end{aligned}$$

$$\beta_N = -\frac{w_{N,n}^m - w_{N,n-1}^m}{\Delta t} - \left(1 - \frac{\eta c}{G\kappa}\right) u_{N,n}^m + C_{N-1/2}^\alpha \frac{\partial p}{\partial \theta} \Big|_{N-1/2,n}^m \quad (D.7)$$

In the above,

$$C_{i+1/2}^\alpha = \frac{\theta_{i+1/2} C^q w_{i+1/2}^{1+1/n} \left( \frac{\partial p}{\partial \theta} \Big|_{i+1/2} \right)^{1/n-1}}{R \theta_i (\theta_{i+1/2} - \theta_{i-1/2})} \quad i = 1, 2, \dots, N-1 \quad (D.8)$$

$$C_{i-1/2}^\alpha = \frac{\theta_{i-1/2} C^q w_{i-1/2}^{1+1/n} \left( \frac{\partial p}{\partial \theta} \Big|_{i-1/2} \right)^{1/n-1}}{R \theta_i (\theta_{i+1/2} - \theta_{i-1/2})} \quad i = 2, 3, \dots, N \quad (D.9)$$

All the pressure, fracture width and leakoff rate values are evaluated at  $n, m$  which are known prior to the current  $m + 1$ -th iteration.

## Pressure-independent (Carter's) Leakoff

$$\begin{aligned} \alpha_{1j} = & \frac{c_{1j}^w}{\Delta t} + C_{1+1/2}^\alpha \left\{ \left(1 + \frac{1}{2n}\right) (c_{2,j}^w + c_{1,j}^w) \frac{\partial p}{\partial \theta} \Big|_{1+1/2} \right. \\ & \left. + \frac{S_{1+1/2}^p w_{1+1/2}}{n(\theta_2 - \theta_1)} (\delta_{2,j} - \delta_{1,j}) \right\} \end{aligned} \quad (D.10)$$

$$\begin{aligned} \alpha_{ij} = & \frac{c_{ij}^w}{\Delta t} + C_{i+1/2}^\alpha \left\{ \left(1 + \frac{1}{2n}\right) (c_{i+1,j}^w + c_{i,j}^w) \frac{\partial p}{\partial \theta} \Big|_{i+1/2} \right. \\ & \left. + \frac{S_{i+1/2}^p w_{i+1/2}}{n(\theta_{i+1} - \theta_i)} (\delta_{i+1,j} - \delta_{i,j}) \right\} \\ & - C_{i-1/2}^\alpha \left\{ \left(1 + \frac{1}{2n}\right) (c_{i,j}^w + c_{i-1,j}^w) \frac{\partial p}{\partial \theta} \Big|_{i-1/2} \right. \\ & \left. + \frac{S_{i-1/2}^p w_{i-1/2}}{n(\theta_i - \theta_{i-1})} (\delta_{i,j} - \delta_{i-1,j}) \right\} \quad i = 2, 3, \dots, N-1 \end{aligned} \quad (D.11)$$

$$\begin{aligned} \alpha_{Nj} = & \frac{c_{Nj}^w}{\Delta t} - C_{N-1/2}^\alpha \left\{ \left(1 + \frac{1}{2n}\right) (c_{N,j}^w + c_{N-1,j}^w) \frac{\partial p}{\partial \theta} \Big|_{N-1/2} \right. \\ & \left. + \frac{S_{N-1/2}^p w_{N-1/2}}{n(\theta_N - \theta_{N-1})} (\delta_{N,j} - \delta_{N-1,j}) \right\} \end{aligned} \quad (D.12)$$

with  $j$  ranges from 1 to  $N$ . And,

$$\begin{aligned} \beta_1 = & -\frac{w_{1,n}^m - w_{1,n-1}^m}{\Delta t} - \left(1 - \frac{\eta c}{2G\kappa}\right) \frac{2C_l}{\sqrt{t + \Delta t - \tau u_1}} \\ & - C_{1+1/2}^\alpha w_{1+1/2,n}^m \frac{\partial p}{\partial \theta} \Big|_{1+1/2,n}^m + \frac{C^q Q_{inj}}{2\pi R \theta_1 (\theta_{1+1/2} - \theta_{1-1/2})} \end{aligned} \quad (D.13)$$

$$\begin{aligned} \beta_i = & -\frac{w_{i,n}^m - w_{i,n-1}^m}{\Delta t} - \left(1 - \frac{\eta c}{2G\kappa}\right) \frac{2C_l}{\sqrt{t + \Delta t - \tau u_i}} \\ & - C_{i+1/2}^\alpha w_{i+1/2,n}^m \frac{\partial p}{\partial \theta} \Big|_{i+1/2,n}^m + C_{i-1/2}^\alpha w_{i-1/2,n}^m \frac{\partial p}{\partial \theta} \Big|_{i-1/2,n}^m \end{aligned} \quad (D.14)$$

$$\begin{aligned} \beta_N = & -\frac{w_{N,n}^m - w_{N,n-1}^m}{\Delta t} - \left(1 - \frac{\eta c}{2G\kappa}\right) \frac{2C_l}{\sqrt{t + \Delta t - \tau u_N}} \\ & + C_{N-1/2}^\alpha w_{N-1/2,n}^m \frac{\partial p}{\partial \theta} \Big|_{N-1/2,n}^m \end{aligned} \quad (D.15)$$

In the above, factors  $C^\alpha$  are evaluated the same way as in pressure-dependent leakoff. The total width,  $w$ , consists of both the elastic and poroelastic parts

such as:

$$w_i = w_i^e - \frac{2\eta c C_l \sqrt{t + \Delta t - \tau_i}}{G\kappa} \quad (\text{D.16})$$

in the single pumping cycle; or:

$$w_i = w_i^e - \frac{2\eta c C_l}{G\kappa} \sqrt{\frac{V_{i,0}^2}{4C_l^2} + t + \Delta t - \tau_i} \quad (\text{D.17})$$

in the multiple pumping cycles.  $V_{i,0}$  is the total leaked volume at node  $i$  up to the latest exposure time  $\tau_i$ .

# Bibliography

- [1] Rice, J.R. 1976. The localization of plastic deformation. in *Theoretical and Applied Mechanics*. W.T. Koiter (ed.), North-Holland Publishing Co.. 207-220.
- [2] de Borst, R., Pamin, J., Schellekens, J.C.J. and Sluys, L.J. 1994. Instability in materials — computational aspects. in *Proc. 8th Int. Conf. Computer Meth. Adv. Geomech.*, Morgantown, WV, 91-102.
- [3] Ingraffea, A.R. 1977. Discrete fracture propagation in rock: laboratory tests and finite element analysis. *Ph.D. Dissertation, Univ. of Colorado*.
- [4] Barenblatt, G.I. 1962. Mathematical theory of equilibrium cracks in brittle fracture. *Adv. Appl. Mech.*, Vol. 7, 55-129.
- [5] Rice, J.R. 1968. Mathematical analysis in the mechanics of fracture. in *Fracture, Vol. II: Mathematical Fundamentals*, H. Liebowitz (ed.). Academic Press, New York, 191-311.
- [6] Weng, X. 1993. Fracture initiation and propagation from deviated wellbore. SPE paper 26597. 68th Annual Tech. Conf. Exhib. of SPE, Houston, TX, Oct. 3-6.
- [7] Erdogan, F. and Sih, G.C. 1963. On the crack extension in plates under plane loading and transverse shear. *ASME J. Basic. Engr.*. Vol. 85. 519-527.
- [8] Sih, G.C. 1973. Some basic problems in fracture mechanics and new concepts. *Eng. Fract. Mech.*, Vol. 5, 365-377.
- [9] Hussian, M.A., Pu, S.L. and Underwood, J. 1974. Strain energy release rate for a crack under combined mode I and mode II. *Fracture Analysis. ASTM, STP 560*, 2-28.
- [10] Shlyapobersky, J. and Chudnovsky, A. 1994. Review of recent development in fracture mechanics with petroleum engineering applications. *EUROCK'94*, 381-388.
- [11] Yuan, Y.G., Abousleiman, Y., Weng X. and Roegiers, J.-C. 1995. Three-dimensional elastic analysis on fracture initiation from a perforated borehole. SPE paper 29601, Joint Rocky Mountain Regional Meeting/Low-Perm. Res. Symp., Denver, CO, March 19-22.
- [12] Yuan, Y.G., Weng X., Abousleiman, Y. and Roegiers, J.-C. 1996. Poroelastic aspects in fracture initiation from a perforated borehole. *INGPET-126-96*.
- [13] Irwin, G.R. 1960. Fracture mode transition for a crack transversing a plate. *J. Basic Eng.*, Vol. 82, 417-425.

- [14] Irwin, G.R. 1962. Crack extension force for a part-through crack in a plate. *J. Apply. Mech.*, Vol. 29, 651-654.
- [15] Shlyapobersky, J., Wong, G.K. and Walhaug, W.W. 1988. Overpressure-calibrated design of hydraulic fracture stimulations. SPE 18194. Prof. 13th Annual Tech. Conf. and Exhib., Houston, TX.
- [16] Sousa, J.L., Carter, B.J. and Ingraffea, A.R. 1993. Numerical simulation of 3D hydraulic fracture using Newtonian and power-law fluids. *Int. J. Rock Mech. Min. Sci & Geomech. Abstr.*, Vol. 30. pp. 1265-1271.
- [17] Ghassemi, A. 1996. *Three-Dimensional Poroelastic Hydraulic Fracture Simulation Using the Displacement Discontinuity Method*. Ph.D. Dissertation, Univ. of Oklahoma, USA, 173 p.
- [18] Khristianovich, S.A. and Zheltov, Y.P. 1956. Formation of vertical fractures by means of highly viscous liquids. *Proc. 4th World Pet. Congress. Rome, Vol. II*, pp. 579-586.
- [19] Geertsma, J. and de Klerk, F.A. 1969. A rapid method of predicting width and extent of hydraulically induced fractures. *J. Petroleum Technology*, December, pp. 1571-1581.
- [20] Daneshy, A.A. 1973. On the design of vertical hydraulic fractures. *J. Petroleum Technology*, January, pp. 83-97.
- [21] Perkins, T.K. and Kern, L.R. 1961. Width of hydraulic fractures. *J. Petroleum Technology*, September, pp. 937-949.
- [22] Nordgren, R.P. 1972. Propagation of a vertical hydraulic fracture. *Society of Petroleum Engineering Journal*, August, pp. 306-314.
- [23] Barenblatt, G.I. 1956. On the formation of horizontal cracks in hydraulic fracture of an oil-bearing stratum. *Prikl. Mat. Mekh.*, Vol. 20, 475-486.
- [24] Barenblatt, G.I. 1959. The formation of equilibrium cracks during brittle fracture: general ideas and hypotheses: axially-symmetric cracks. *Prikl. Mat. Mekh.*, Vol. 23, 434-444.
- [25] Abe, H., Mura, T. and Keer, L.M. 1976. Growth rate of a penny-shaped crack in hydraulic fracturing of rocks. *J Geophys. Res.*, Vol. 81, 5335-5304.
- [26] Cleary, M.P. 1980a. Analysis of mechanisms and procedures for producing favorable shapes of hydraulic fractures. SPE 9260, 55th Fall Annual Tech. Conf. Exhib. of SPE, Dallas, TX, Sept. 21-24.
- [27] Advani, S.H. and Lee, J.K. 1982. Finite element model simulations associated with hydraulic fracturing. *Society of Petroleum Engineering Journal*, Vol. 22, pp. 209-218.
- [28] Van Eekelen. 1982. Hydraulic fracture geometry: fracture containment in layered formation. *Society of Petroleum Engineering Journal*, Vol. 22, pp. 341-349.
- [29] Cleary, M.P., Kavadas, M. and Lam, K.Y. 1983. Development of a fully three-dimensional simulator for analysis and design of hydraulic fracturing. SPE paper 11631, SPE/DOE Symp. on Low Perm., Denver, CO, March 14-16.
- [30] Palmer, I.D. and Carol, H.B., Jr. 1983. Numerical solution for height and elongated hydraulic fracture propagation. *Society of Petroleum Engineering Journal*, Vol. 223 pp. 870-878.

- [31] Settari, A. and Cleary, M.P. 1984. Three-dimensional simulation of hydraulic fracturing. *J. Petroleum Technology*, July, pp. 1177-1190.
- [32] Meyer, B.R. 1986. Design formulae for 2-D and 3-D vertical hydraulic fractures: model comparison and parametric studies. SPE paper 15240. Unconventional Gas Tech. Symp., Louisville, KY, May 18-21.
- [33] Meyer, B.R. 1989. Three-dimensional hydraulic fracturing simulation on personal computers: theory and comparison studies. SPE paper 19329. SPE Eastern Regional Meeting, Morgantown, WV, Oct. 24-27.
- [34] Meyer, B.R., Cooper, G.D. and Nelson, S.G. 1990. Real-time 3-D hydraulic fracturing simulation: Theory and field case studies. SPE paper 20658, 65th Annual Tech. Conf. Exhib. of SPE, New Orleans, LA, Sept. 23-26.
- [35] Clifton, R.J. and Abous-Sayed, A.S. 1979. On the computation of the three-dimensional geometry of hydraulic fractures. SPE paper 7943, SPE Symp. on Low Perm. Gas Res., May 20-22.
- [36] Clifton, R.J. and Abou-Sayed, A.S. 1981. A variational approach to the prediction of three-dimensional geometry of hydraulic fractures. SPE paper 9879, SPE/DOE Low Perm. Symp., Denver, CO, May 27-29.
- [37] Barea, R.D. 1983. A practical numerical simulator for three dimensional fracture propagation in heterogeneous media. SPE paper 12273, Reservoir Simulation Symp., San Francisco, CA, Nov. 15-18.
- [38] Cleary, M.P., Keck, R.G. and Mear, M.E. 1983. Microcomputer models for the design of hydraulic fractures. SPE paper 11628, SPE/DOE Symp. on Low Perm., Denver, CO, March 14-16.
- [39] Abou-Sayed, A.S., Sinha, K.P. and Clifton, R.J. 1984a. Evaluation of the influence of in-situ reservoir conditions on the geometry of hydraulic fractures using a 3-D simulator: Part I: technical approach. SPE paper 12877, SPE/DOE/GRI Unconventional Gas Recovery Symp., Pittsburgh, PA, May 13-15.
- [40] Abou-Sayed, Clifton, R.J., Dougherty, R.L. and Morales, R.H. 1984b. Evaluation of the influence of in-situ reservoir conditions on the geometry of hydraulic fractures using a 3-D simulator: Part I: case studies. SPE paper 12878, SPE/DOE/GRI Unconventional Gas Recovery Symp., Pittsburgh, PA, May 13-15.
- [41] Vandamme, L. and Curran, J.H. 1989. A three-dimensional hydraulic fracturing simulator. *Int. J. Num. Meth. Engrg.*, Vol. 28, pp. 909-927.
- [42] Lee, T.S., Advani, S.H. and Lee, J.K. 1990a. Three-dimensional modeling of hydraulic fractures in layered media: part I-finite element formulations. *J. Energy Resources Tech.*, ASME, Vol. 112, pp.1-9.
- [43] Lee, T.S., Advani, S.H. and Lee, J.K. 1990b. Three-dimensional modeling of hydraulic fractures in layered media: part II-calibration, parametric sensitivity and field simulations. *J. Energy Resources Tech.*, ASME, Vol. 112, pp.10-19.
- [44] Carter, R.H., Holditch, and Wolhart, S.L. 1996. Results of a 1995 hydraulic fracturing survey and a comparison of 1995 and 1990 industry practices. SPE 36483. 1996 Annual Tech. Conf. and Exhib., Denver, CO, Oct. 6-9.

- [45] Veatch, R.W. 1983a. Overview of current hydraulic fracturing design and treatment technology — Part 1. *J. Petroleum Technology*, Vol. 35, 677-687.
- [46] Veatch, R.W. 1983b. Overview of current hydraulic fracturing design and treatment technology — Part 2. *J. Petroleum Technology*, Vol. 35, 853-864.
- [47] Mendelson, D.A. 1984a. A review of hydraulic fracture modeling — Part I: general concepts, 2D models, motivation for 3D modeling. *J. Energy Resources Tech., ASME*, Vol. 106, 369-376.
- [48] Mendelson, D.A. 1984b. A review of hydraulic fracture modeling — II: 3D modeling and vertical growth in layered rock. *J. Energy Resources Tech., ASME*, Vol. 106, 543-553.
- [49] Veatch Jr., R.W. and Moschovidis, Z.A. 1986. An overview of recent advances in hydraulic fracturing technology. SPE 14085, SPE 1986 Int. Meeting on Petrol. Eng., Beijing, China, March 17-20.
- [50] Cleary, M.P.. 1988. The engineering of hydraulic fractures — state of the art and technology of the future. *J. Petroleum Technology*, Vol. 40, 13-21.
- [51] Howard, G.C. and Fast, C.R. 1970. *Hydraulic Fracturing*. SPE Monograph Series, Dallas, Vol. II.
- [52] Gidley, J.L., Holditch, S.A., Nierode, D.E. and Veatch, R.W. Jr. 1989. *Recent Advances in Hydraulic Fracturing*, SPE monograph series Vol. 12.
- [53] Valko, P. and Economides, M.J. 1995. *Hydraulic Fracture Mechanics*. John Wiley & Sons, 298 p.
- [54] Carter, R.D. 1957. Derivation of the general equation for estimating the extent of the fractures area. Appendix to “*Optimum Fluid Characteristics for Fracture Extension*”, by Howard, G.C. and Fast, Drill. and Prod. Prac., API. 261-270.
- [55] Settari, A. 1980. Simulation of the hydraulic fracture process. *Society of Petroleum Engineering Journal*, Vol. 20, pp. 487-500.
- [56] Hagoort, J., Weatherill, B.D. and Settari, A. 1980. Modeling the propagation of waterflood-induced hydraulic fractures. *Society of Petroleum Engineering Journal*, Vol. 20, pp. 293-303.
- [57] Settari, A. and Price, H.S. 1984. Simulation of hydraulic fracturing in low permeability reservoirs. *Society of Petroleum Engineering Journal*, Vol. 24, pp. 141-152.
- [58] Settari, A. and Warren, G.M. 1994. Simulation and field analysis of waterflood induced fracturing. EUROCK'94, pp. 435-445.
- [59] Castillo, J.L. 1987. Modified fracture decline analysis including pressure-dependent leakoff. SPE 16417, SPE/DOE Low Perm. Res. Symp., Denver, CO, May 18-19.
- [60] Abousleiman, Y. 1991. *A Poroelastic PKN Model with Pressure-dependent Leakoff and Formation Permeability Determination*. Ph.D. Dissertation, Univ. of Delaware, Newmark, USA, 150 p.
- [61] Settari, A. 1985. A new general model of fluid loss in hydraulic fracturing. *Society of Petroleum Engineering Journal*, August.



- [62] Settari, A and Mouritis, F.M. 1994. Coupling geomechanics and reservoir simulation models. *Proc. 8th Int. Conf. Computer Meth. Adv. Geomech.*, Morgantown, WV, pp. 2151-2158.
- [63] Clifton, R.J. and Wang, J.J. 1988. Multiple fluids, proppant transport and thermal effects in 3-dimensional simulation of hydraulic fracturing. SPE paper 18198, 63rd Annual Tech. Conf. Exhib. of SPE. Houston, TX, Oct. 2-5.
- [64] Zhu, D. and Hill, A.D. 1991. The effect of temperature on minifrac pressure decline. SPE paper 22874, 66th Annual Tech. Conf. Exhib. of SPE, Dallas, Tx, Oct. 6-9.
- [65] Jensen, T.B. 1994. Reservoir/rock mechanics modeling of waterflood behavior with thermally induced fracturing. *Proc. 8th Int. Conf. Computer Meth. Adv. Geomech.*, Morgantown, WV, pp. 2077-2082.
- [66] Johnson, E. and Cleary, M.P. 1991. Applications of recent laboratory experimental results for hydraulic fractures. SPE paper 21846, Rocky Mountain Regional Meeting and Low-Perm. Res. Symp., Denver, CO, April 15-17.
- [67] The SCR Geomechanics Group. 1993. On the modeling of near tip processes in hydraulic fractures. *Int. J. Rock Mech. Min. Sci & Geomech. Abstr.*, Vol. 30. pp. 1127-1134.
- [68] Cleary, M.P., Wright, C.A. and Wright, T.B. 1991. Experimental and modeling evidence for major changes in hydraulic fracturing design and field procedures. SPE paper 21494, SPE Gas Tech. Symp., Houston, TX, Jan. 23-25.
- [69] Papanastasiou, P. and Thiercelin, M. 1993. Influence of inelastic rock behavior in hydraulic fracturing. *Int. J. Rock Mech. Min. Sci & Geomech. Abstr.*, Vol. 30, 1241-1248.
- [70] Biot, M.A. 1941. General theory of three-dimensional consolidation. *J. Appl. Phys.*, Vol. 12, 155-164.
- [71] Rice, J.R. and Cleary, M.P. 1976. The stabilization of spreading shear faults by coupled deformation-diffusion effect in fluid-infiltrated porous materials. *J Geophys. Res.*, Vol. 81, 5322-5334.
- [72] Cleary, M.P. 1977, Fundamental solutions for a fluid-saturated porous solid. *Int. J. Solids Structures*. Vol. 13, 785-806.
- [73] Cleary, M.P. 1978. Moving singularities in elasto-diffusive solids with applications to fracture propagation. *Int. J. Solids Structures*. Vol. 14, 81-97.
- [74] Geertsma, J. 1966. Problems of rock mechanics in petroleum production engineering. *Proc. First Cong. Int. Soc. Rock Mech.*, Lisbon.
- [75] Haimson, B. and Fairhurst, C. 1969. Hydraulic fracturing in porous permeable materials. *J. Petroleum Technology*, Vol. 21, 811-817.
- [76] Ruina, A. 1978. Influence of coupled deformation-diffusion effects on the retardation of hydraulic fracture. *Proc. 19th US Rock Mech. Symp.*, Lake Tahoe, NV, 274-282.
- [77] Cleary, M.P. 1979. Rate and structure sensitivity in hydraulic fracturing of fluid-saturated porous formations. *Proc. 19th US Rock Mech. Symp.*, Austin, TX, K. Gray (ed.).

- [78] Boone, T.J. 1989. Simulation and Visualization of Hydraulic Fracture Propagation in Poroelastic Rock. Ph.D. dissertation, Cornell Univ., USA. 430 p.
- [79] Boone, T.J. and Ingraffea, R.A. 1990. A numerical procedure for simulation of hydraulically-driven fracture propagation in poroelastic media. *Int. J. Num. Anal. Meth. Geomech.*, Vol 8, 71-96.
- [80] Boone, T.J. and Detournay, E. 1990. Response of a vertical hydraulic fracture intersecting a poroelastic formation bounded by semi-infinite impermeable elastic layers. *Int. J. Rock Mech. Min. Sci & Geomech. Abstr.*, Vol. 27, 189-197.
- [81] Detournay, E. and Cheng, A.H.-D. 1991. Plane strain analysis of a stationary hydraulic fracture in a poroelastic medium. *Int. J. Solids Structures*. Vol. 27, 1645-1662.
- [82] Zhang, X. 1994. *A Study of Poroelasticity and Its Application to Petroleum Related Problems*. Ph.D. Dissertation, Univ. of Texas at Austin, USA. 123 p.
- [83] Cleary, M.P. 1980b. Comprehensive design formulae for hydraulic fracturing. SPE paper 9259, 55th Fall Annual Tech. Conf. Exhib. of SPE, Dallas, TX, Sept. 21-24.
- [84] Cleary, M.P., Crockett, A.R., Martinez, J.I. Narendran, V.M. and Slutsky, S. 1983. Surface integral schemes for fluid flow and induced stresses around fractures in underground reservoirs. SPE 11632, SPE/DOE Symp. on Low Perm., Denver, CO, March 14-16.
- [85] Detournay, E., Cheng, A.H.-D. and McLennan, J.D. 1990. A poroelastic PKN hydraulic fracture model based on an explicit moving mesh algorithm. *J. Energy Resources Tech., ASME*, Vol. 112, 224-230.
- [86] Clifton, R.J. and Wang, J.J. 1991. Modeling of poroelastic effects in hydraulic fracturing. SPE 21871, Rocky Mountain Regional Meeting and Low-Perm. Res. Symp., Denver, CO, April 15-17.
- [87] Boone, T.J., Ingraffea, A.R. and Roegiers, J.-C. 1990. Simulation of hydraulic fracturing propagation in poroelastic rock with application to stress measurement techniques. *Int. J. Rock Mech. Min. Sci & Geomech. Abstr.*, Vol. ??,
- [88] Cheng, A.H.-D., Abousleiman, Y. and Roegiers, J.-C. 1993. Review of some poroelastic effects in rock mechanics. *Int. J. Rock Mech. Min. Sci & Geomech. Abstr.*, Vol. 30, 1119-1126.
- [89] Detournay, E. and Cheng, A.H.-D. 1993. Fundamentals of poroelasticity. in *Comprehensive Rock Engineering. Vol. 1. Fundamentals*. Hudson, J.D. (ed.), 113-171.
- [90] Nierode, D.E. 1985. Comparison of hydraulic fracture design methods to observed field results. *Society of Petroleum Engineering Journal*, October, 1831-1839.
- [91] Smith, M.B. 1985. Stimulation design for short, precise hydraulic fractures — MHF. SPE paper 10313, 56th Annual Tech. Conf. Exhib. of SPE, Santonio, TX, Oct. 5-7.
- [92] Felsenthal, M. and Ferrell, H.H. 1971. Fracturing gradients in water-floods of low-permeability, partially depleted zones. *J. Petroleum Technology*, 727-730.

- [93] Salz, L.B. 1977. Relationship between fracture propagation pressure and pore pressure. SPE paper 6870, 52nd Annual Fall Tech. Conf. Exhib. of SPE, Denver, CO, Oct. 9-12.
- [94] Kry, P.R. 1989. Field observations of steam distribution during injection into the Cold Lake reservoir. in *Rock Mechanics and Rock Physics at great Depth*, ISRM-SPE Joint Symp., Pau, France.
- [95] Boone, T.J., Kry, P.R., Bharatha, S. and Gronseth, J.M. 1991. Poroelastic effects related to stress determination by micro-frac tests in permeable rock. *Proc. 32nd US Rock Mech. Symp.*, J.-C. Roegiers (ed.). 25-34.
- [96] Nolte, K.G. 1982. Fracture design considerations based on pressure analysis. SPE paper 10911, SPE Cotton Valley Symp., Tyler, TX. May 20.
- [97] McLennan, J.D. and Roegiers, J.-C. 1982. How instantaneous are instantaneous shut-in pressures?. SPE paper 11064, 57th Annual Tech. Conf. Exhib. of SPE, New Orleans, LA, Sept. 26-39.
- [98] Medlin, W.L. and Masse, L. 1985. Laboratory experiments in fracture propagation. *Society of Petroleum Engineering Journal*, Vol. 24, 256-268.
- [99] Zoback M.D., Rummel, F., Jung, R. and Raleigh, C.B. 1977. Laboratory hydraulic fracturing experiments in intact and pre-fractured rock. *Int. J. Rock Mech. Min. Sci & Geomech. Abstr.*, Vol. 14, 49-58.
- [100] Detournay, E. and Cheng, A.H.-D. 1988. Poroelastic response of a borehole in a no-hydrostatic stress field. *Int. J. Rock Mech. Min. Sci & Geomech. Abstr.*, Vol. 25, 171-182.
- [101] Detournay, E., Cheng, A.H.-D., Roegiers, J.-C. and McLennan, J.D. 1989. Poroelasticity considerations in *in situ* stress determination by hydraulic fracturing. *Int. J. Rock Mech. Min. Sci & Geomech. Abstr.*, Vol. 26, 507-513.
- [102] Carter, J. and Booker, J.R. 1982. Elastic consolidation around a deep circular tunnel. *Int. J. Solids Structures*, Vol. 18, 1059-1074.
- [103] Mandel, J. 1953. Consolidation des sols (étude mathématique). *Geotechnique*, Vol. 3, 287-299.
- [104] Cryer, C. 1963. A comparison of the three-dimensional consolidation theories of Biot and Terzaghi. *Quart. J. Mech. Appl. Math.*, Vol. 16, 401-412.
- [105] Verruijt, A. 1969. Elastic storage of aquifers. in *Flow through Porous Media*, DeWiest, R.J.M. (ed.), Academic Press, New York, 331-376.
- [106] Cleary, M.P. 1994. Discussion of comparison study of hydraulic fracturing models — test case: GRI staged field experiment No. 3. *SPE Production & Facilities*, February.
- [107] Terzaghi, K. 1923. Die berechnung der durchlässigkeitsziffer des tones aus dem verlauf der hydrodynamischen spannungserscheinungen. *Sitzungsber. Akad. Wissen., Wien Math. Naturwiss. Kl., Abt. IIa 132*, 105-124.
- [108] Biot, M.A. 1955. Theory of elasticity and consolidation for a porous anisotropic solid. *J. of Appl. Phys.*, **26**, 182-185.
- [109] Biot, M.A. 1962. Mechanics of deformation and acoustic propagation in porous media. *J. Appl. Mech.* Vol. 33, 1482-1498.
- [110] Crochet, M.J. and Naghdi, P.M. 1966. On constitutive equations for flow of fluid through an elastic solid. *Int. J. Eng. Sci.*, Vol. 4, 383-401.

- [111] Morland, L.W. 1972. A simple constitutive theory for a fluid-saturated porous solid. *J Geophys. Res.*, Vol. 77, 890-900.
- [112] Bowen, R.M. 1982. Compressible porous media models by use of the theory of mixtures. *Int. J. Eng. Sci.*, Vol. 20, 697-735.
- [113] Katsube, N. and Carrol, M.M. 1987. The modified mixture theory for fluid-filled porous materials: theory. *J. Appl. Mech.*, Vol. 54, 35-40.
- [114] Geertsma, J. 1957. The effect of fluid pressure decline on volumetric changes of porous rocks. *Trans. Am. Inst. Min. Metall. Pet. Eng.*, Vol. 210, 331-340.
- [115] Brown, R.J. and Korringa, J. 1975. On the dependence of the elastic properties of a porous rock on the compressibility of the pore fluid. *Geophysics*, Vol. 40, 608-616.
- [116] Carroll, M.M. 1979. An effective stress law for anisotropic elastic deformation. *J Geophys. Res.*, Vol. 84, B13, 751-7512.
- [117] Carrol, M.M. 1980. Mechanical response of fluid-saturated porous materials. in *Theoretical and Applied Mechanics, 15th Int. Congr. Theoretical and Appl. Mech.*, F.P.J. Rimrott and B. Tabarrok (ed.), 252-262.
- [118] Carrol, M.M. and Katsube, N. 1983. The role of Terzaghi effective stress in linearly elastic deformation. *J. Energy Resources Tech.*, ASME, Vol. 105, 509-511.
- [119] Yew, C.H. and Liu, G.F. 1992. Pore fluid and wellbore stability. SPE 22381, SPE Int. Meeting on Petrol. Eng., Beijing, China.
- [120] Abousleiman, Y. and Cheng, A.H.-D. 1992. Poroelasticity: Theory and Applications. Part I. Rock Mechanics Consortium report RMC-92-01. Univ. of Oklahoma, USA. 37 p.
- [121] Carslaw, H.S. and Jaeger, J.C. 1959. *Conduction of Heat in Solids*. Oxford at the Clarendon Press. 2nd ed. 510 p.
- [122] Morse, P. and Feshback, H. 1953. *Methods of Theoretical Physics*. Part I, McGraw-Hill, New York.
- [123] Warpinski, N.R., Abou-Sayed, I.S., Moschovidis, Z. and Parker, C. 1993. Hydraulic fracture model comparison study: complete results. GRI-93/0109. 163 p.
- [124] Nowacki, W. 1986. *Thermoelasticity*. Pergmon Press, 2nd ed. 565 p.
- [125] Olesiak, Z. and Sneddon, I.N. 1961. The distribution of thermal stress in an infinite elastic solid containing a penny-shaped crack. *Arch. Rat. Mech. Analysis*, Vol. 3, 238-254.
- [126] Sneddon, I.N. and Lowengrubd, M. 1969. *Crack Problems in the Classical Theory of Elasticity*. John Wiley & Sons, Inc. 198 p.
- [127] Sneddon, I.N. 1951. *Fourier Transforms*. McGraw-Hill Book Company, Inc. 531 p.
- [128] Sneddon, I.N. 1946. The distribution of stress in the neighborhood of a crack in an elastic solid. *Proc. Royal Soc. of London*, Vol. A 87, 229-260.
- [129] Gordeyev, Y.N., 1993. Growth of a crack produced by hydraulic fracture in a poroelastic medium. *Int. J. Rock Mech. Min. Sci & Geomech. Abstr.*, Vol. 30, 233-238.

- [130] Gradshteyn, I.S. and Ryzhik, I.M., 1965. *Table of Integrals, Series, and Products*, Academic Press.
- [131] Stroud, A.H. and Secrest, D. 1966. *Gaussian Quadrature Formulas*. Prentice-Hall, Inc., 374 p.
- [132] McNamee, J. and Gibson, R.E. 1960. Displacement functions and linear transforms applied to diffusion through porous elastic media. *Q. J. Mech. Appl. Math.*, Vol. 13., 210-227.
- [133] Biot, M.A. 1956a. General solutions of the equations of elasticity and consolidation for a porous material. *J. Appl. Mech. Trans. ASME*, Vol. 78, 91-96.
- [134] Biot, M.A. 1956b. Thermoelasticity and irreversible thermodynamics. *J. Appl. Phys.*, Vol. 27, 240-253.
- [135] Christian, J.T. 1968. Undrained stress distribution by numerical methods. *J. Soil Mech. Found. Div., ASCE*, Vol. 94, 1333-1345.
- [136] Sandu, R.S. and Wilson, E.L. 1969. Finite element analysis of seepage in elastic media. *J. Eng. Mech. Div., ASCE*, Vol. 95, 641-652.
- [137] Zienkiewicz, O.C. 1982. Basic formulation of static and dynamic behavior of soil and other porous media. in *Numerical Methods in Geomechanics* (ed. by J. Martinus), 39-56.
- [138] Cui, L.Z. 1995. *Poroelasticity with Application to Rock Mechanics*. Ph.D. Dissertation, Univ. of Delaware, Newmark, USA.
- [139] Cheng, A.H.-D. and Liggett, J.A. 1984. Boundary integral equation method for linear poroelasticity with applications to fracture propagation. *Int. J. Num. Meth. Engrg.*, Vol. 20, 279-296.
- [140] Badmus, T., Cheng, A.H.-D. and Grill, S. 1993. A Laplace-transform based three-dimensional BEM for poroelasticity. *Int. J. Num. Meth. Engrg.*, Vol. 36, 67-85.
- [141] Cheng, J.X., 1996. *An Elastoplastic Model of Fluid-saturated Porous Media*. Ph.D. Dissertation, Univ. of Oklahoma, USA. 198 p.
- [142] Yuan, Y.G. and Abousleiman, Y. 1993. *Poroelasticity Capacity in ABAQUS*. Rock Mechanics Consortium report RMC-93-05, Univ. of Oklahoma, USA. 35 p.
- [143] Vermeer, P.A. and Verruijt, A. An accuracy condition for consolidation by finite elements. *Int. J. for Num. Analy. Meths. in Geomechanics*, 5, 1-14, 1981.
- [144] Van Dyke, M. 1975. *Perturbation Methods in Fluid Mechanics*. Parabolic Press, Palo Alto, CA, USA.
- [145] Nayfeh, A.H. 1993. *Introduction of Perturbation Techniques*. John Wiley & Sons, Inc., 519 p.
- [146] Press, W.H., Teukolsky, S.A., Vetterling, W.T. and Flannery, B.P., 1990. *Numerical Recipes, the art of scientific computing (Fortran Version)*. Cambridge University Press, 702 p.
- [147] Rice, J.R. and Simons, D.A. 1976. The stabilization of spreading shear faults by coupled deformation diffusion effects in fluid infiltrated porous materials. *J Geophys. Res.*, Vol 81, 5322-5334.

- [148] Civan, F. and Engler, T. 1994. Drilling mud filtrate invasion — improved model and solution. *J. Petroleum Science and Eng.*, 183-193.
- [149] Yuan, Y.G. and Civan, F. 1996. Near-wellbore polymer invasion — a parametric study. submitted to *IN-SITU*.
- [150] Zazovskii, A.F. 1979a. Growth of coin-shaped crack produced by hydraulic fracture in an impermeable rock. *Izv. AN SSR. Mehkanika Tverdogo Tela.*, Vol. 14, 103-109.
- [151] Zazovskii, A.F. 1979b. Development of a disk-shaped hydraulic fault crack in a thick fluid-saturated stratum. *Izv. AN SSR. Mehkanika Tverdogo Tela.*, Vol. 14, 169-178.
- [152] Cleary, M.P. and Wong, S.K. 1985. Numerical simulation of unsteady fluid flow and propagation of a circular hydraulic fracture." *Int. J. Numer. Anal. Meth. Geomech.*, Vol. 9, 1-14.
- [153] Nilson, R.H. 1986. An integral method for predicting hydraulic fracture propagation driven by gases or liquids. *Int. J. Numer. Anal. Meth. Geomech.*, Vol. 10.
- [154] Nilson, R.H. 1988. Similarity solutions for wedge-shaped hydraulic fractures driven into a permeable medium by a constant inlet pressure. *Int. J. Numer. Anal. Meth. Geomech.*, Vol. 10, 477-495.
- [155] Settari, A. and Cleary, M.P. 1982. Development and testing of a pseudo-three-dimensional model of hydraulic fracturing geometry (P3DH). SPE paper 10505, 6th SPE Symp. on Res. Simulation. New Orleans, LA, Jan. 31-Feb. 3, 1982.
- [156] Petersen, D.R. 1980. *Numerical analysis of hydraulic fracturing and related crack problems*. M.Sc. thesis, Massachusetts Inst. of Technology. 314 p.
- [157] Abousleiman, Y. and Yuan, Y.G. 1993. *McFrac Simulator — Part I: Poroelastic Effect in Mini- and Micro-hydraulic Fracturing*. Rock Mechanics Research Center report, RMRC-93-11, Univ. of Oklahoma, 49 p.
- [158] Peaceman, D.W. and Rachford, H.H. 1955. The Numerical solution of parabolic and elliptic differential equations. *SIAM J. Appl. Math.*, Vol. 3, 28-41.
- [159] Douglas, J. and Rachford, H.H. 1956. On the numerical solution of heat conduction problems in two and three space variables. *Trans. Am. Math. Soc.*, Vol. 82, 421-439.
- [160] Crank, J. and Gupta, R.S. 1972. A moving boundary problem arising from the diffusion of oxygen in absorbing tissue. *J. Inst. Maths. Applics.*, Vol. 10, 19-33.
- [161] Bonnerot, R. and Jamet, P. 1977. Numerical computation of the free boundary for the two-dimensional Stefan problem by space-time finite elements. *J. of Computational Physics*, Vol. 25, 163-181.
- [162] Bonnerot, R. and Jamet, P. 1979. A third order accurate discontinuous finite element method for the one-dimensional Stefan problem. *J. of Computational Physics*, Vol. 32, 145-167.
- [163] Atkinson, C. and Craster, R.V. 1991. Plane strain fracture in poroelastic media. *Proc. R. Soc. London. A* **434**, 605-633.

- [164] Atkinson, C. and Craster, R.V. 1992. The application of invariant integrals in diffusive elastic solids. *Phil. Trans. R. Soc. Lond., A* **339**, 231-263.
- [165] Craster, R.V. 1992. Shear cracks in thermoelastic and poroelastic media. *J. Mech. Phys. Solids*. Vol. 40, 887-924.
- [166] Simmons, D.A. 1977. Boundary-layer analysis of propagating mode II cracks in porous elastic media. *J. Mech. Phys. Solids*, Vol. 25, 99-115.
- [167] Desroches, J. and Thiercelin, M. 1993. Modeling the propagation and closure of micro-hydraulic fractures. *Int. J. Rock Mech. Min. Sci & Geomech. Abstr.*, Vol. 30, 1231-1234.
- [168] Abousleiman, Y., Yuan, Y.G. and Roegiers, J.-C. 1993. Propagation/recession of a penny-shaped fracture in a permeable diffusive formation. EUROCK'94. 471-478.
- [169] Fairhurst, C. 1964. Measurement of in-situ rock stresses, with particular reference to hydraulic fracturing. *Rock Mech. and Engineering Geology*, Vol. 2, 129-148.
- [170] Haimson, B.C. 1978. The hydrofracturing stress measuring method and recent field studies. *Int. J. Rock Mech. Min. Sci & Geomech. Abstr.*, Vol. 15, 167-178.
- [171] McLennan, J.D. and Roegiers, J.-C. 1983. Do instantaneous shut-in pressures accurately represent the minimum principal stress?. *Proc. Workshop on Hydraulic Fracturing Stress Measurements*, 68-78, U.S. Natl. Comm. on Rock Mechanics, Washington, D.C.
- [172] Shlyapobersky, J. 1988. Hydraulic fracture determination of minimum in-situ stress from extended pressure falloff and from fracture reopening and flowback tests. *Proc. 2nd Int. Workshops on Hydraulic Fracturing Stress Measurements*, ed. Haimson, B.C., Roegiers, J.-C. and Zoback, M.D., 760-799.
- [173] Bourgoyne, A.T., Chenevert, M.E., Millherim, K.K. and Young, Jr., F.S., 1991. *Applied Drilling Engineering*, SPE Textbook Series, Vol. 2, 502 p.
- [174] Yuan, Y.G. and Abousleiman, Y. 1994. *McFrac Simulator — Part II: A Pseudo-Explicit Finite Difference Scheme*. Rock Mechanics Research Center report, RMRC-94-10, Univ. of Oklahoma, 64 p.
- [175] Yuan, Y.G. and Abousleiman, Y. 1996a. *McFrac Simulator — Part III: Newton-Raphson Scheme for Convergence.*, Rock Mechanics Research Center report, RMRC-96-01, Univ. of Oklahoma, 44 p.
- [176] Yuan, Y.G. and Abousleiman, Y. 1996b. *McFrac Simulator — Part IV: User Manual.*, Rock Mechanics Research Center report, RMRC-96-02. Univ. of Oklahoma, 23 p.